UNIVERSITÀ DEGLI STUDI DI PADOVA

Head Office: Università degli Studi di Padova

Dipartimento di Scienze Chimiche

Ph.D. COURSE IN: MOLECULAR SCIENCES

CURRICULUM: CHEMISTRY

SERIES XXXIV

SELF-ORGANIZED NANORECEPTORS FOR THE DETECTION OF METABOLITES

Coordinator: Prof. Leonard J. Prins

Supervisor: Prof. Fabrizio Mancin

Ph.D. student: Giordano Zanoni

Introduction

Gold nanoparticles

Gold atom nanoclusters are discrete assemblies of gold atoms with a precise molecular formula. Monolayer-protected gold nanoparticles are mixtures of gold nanostructures, with a defined size distribution, stabilized by a protective layer of organic ligands.[1] Thiolate is the most common functional group used to grant the adhesion of the ligands to the gold atoms because of the strong interaction of gold atoms with sulfur. The use of thiolate ligands hence allow a durable passivation of the metal surfaces, the synthesis of stable colloids and, by the use of multifunctional thiols, the effective grafting of desirable functional groups or molecules to the nanoparticle surface. Functionalized nanoparticles resulting from the use of multifunctional thiols are complex supramolecular systems where both the properties of the gold core and those of the organic monolayer can be tuned and exploited for several different application fields, ranging from molecular recognition and catalysis to biomedical[2] applications. Many different strategies have been developed to date for the synthesis of functionalized gold nanoparticles and the exact procedure which should be chosen depends on size, shape and final use of the colloid. In general, synthetic strategies can be differentiated into two categories: “top-down” approaches and “bottom-up” ones. “Top-down” methodologies are based on the disaggregation of macroscopic metallic gold, which can be done in physical ways, for example with the aid of lasers or mechanical friction. These methodologies can only be used when strict control on shape, size and polydispersity is not required as they allow very limited control over the colloid properties. When precise control is needed “bottom-up” strategies should be chosen. At difference with the previous ones, these strategies are based on the reduction of a gold precursor, usually a gold salt, in solution. For these reasons they are also included in the “wet syntheses” class. The reduction reaction can be controlled and directed toward the desired outcome by changing several experimental parameters such as stoichiometry of the reactants, temperature, reducing power of the reductant, reactant mixing order and rate of addition, and by addition of ligands for gold during the reduction step. Most of these parameters are easy to control and reproducible synthetic strategies can be developed. Methodologies for the direct synthesis even of atomically-precise gold clusters are available nowadays.[3] Some of the most common procedures, considered relevant for this work, will be illustrated in the following chapters.

Turkevich synthesis

The Turkevich synthesis is one of the most popular synthetic strategy in colloid science, and it is usually the commonly employed one for the synthesis of gold nanoparticles with diameters above 8-10 nm. This strategy, which allow good control over nanoparticles size and reproducibility, is based on the reduction of Au(III), introduced as tetrachloroaurate, with citrate in hot water. The reducing agent here acts also as buffer (pH = 6.5). In the last half century the mechanism of the Turkevich synthesis was demonstrated to be a seed-mediated growth process, which can be summarized in four main steps (schematized in Figure 1).

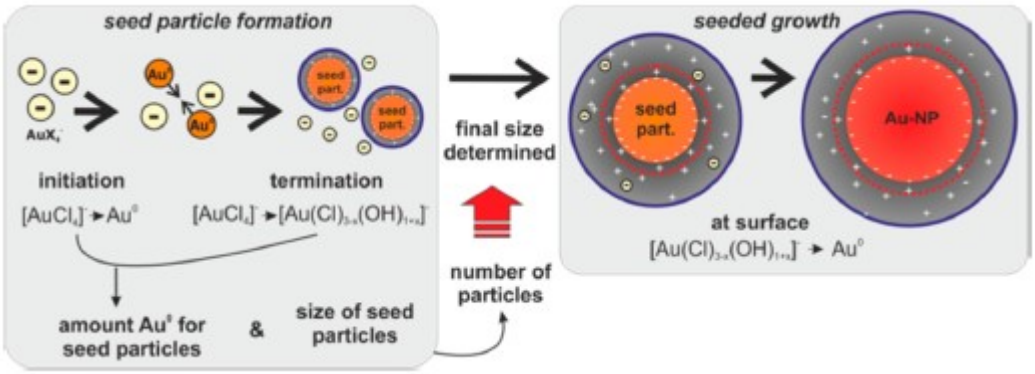

Figure 1: Summary of the Turkevich synthesis mechanism.[4]

Initially, the reduction of part of the Au(III) ions leads to the formation of small gold clusters which subsequently grow to generate seed particles with diameters greater than 3 nm. At this point the formation of the seeds stops (the reasons for this will be explained later) and during the third and fourth steps only the growth of these species is observed. This last process is attributed to the reduction of the remaining ionic gold species which are concentrated in the electrical double layer (EDL) of the seeds. The kinetics of the growth process is slow in the third step but becomes faster in the following one.[4] The reduction of gold ions on seed surface act as a size-focusing process, likely because small particles grow faster than large ones, creating a relatively monodisperse colloid starting from a polydisperse seed one. The formation of large structures has been often proposed in the past to explain the transient bluish color of the solution, but these have been proved not to be present at any time in the Turkevich synthesis. This coloration, instead, is most likely caused by a change of the nanoparticle electronic properties due to the attachment of gold ions in the EDL of the seed particles.[5] As the final number of nanoparticles is equal to the number of seed particles initially produced, the kinetics of the reduction process is irrelevant for the final size determination. The formation of seeds occurs in the first half minute in a standard Turkevich protocol and less than 2 % of the total gold is utilized for this process. The final colloid size

depends on the amount of remaining unreacted gold ions and on the number of seeds present to which this gold will be reduced on. The number of seeds formed is influenced by their dimension, as larger seeds need a larger amount of gold atoms fewer of them will be formed and this leads to bigger final nanoparticles. The solution acidity affects the Au(III) complexes that constitute the gold atoms source. An increase in pH leads to chloride displacement forming $[AuCl_{4-x}OH_x]^-$ species. The reduction of these hydroxo-species with highly deprotonated citrate forms is much slower than that of $[AuCl_4]^-$. After the initial mixing of the tetrachloroaurate and citrate solutions, the protonation and hydrolytic equilibria are immediately shifted away from these two highly reactive species, but thanks to their high reactivity, a small amount of $[AuCl_4]^-$ is reduced quickly enough during this mixing time to form the initial clusters, which will then evolve forming the seeds. As soon as hydroxo-species $[AuCl_{4-x}OH_x]^-$ are formed by tetrachloroaurate hydrolysis, gold clusters are not formed anymore and these hydrolyzed species can only be reduced on the surface of the already formed seeds, leading to their growth (step 3 and 4). The accumulation of dicarboxy acetone (DCA), a direct oxidation product of citrate (and a stronger reductant), will facilitate the deposition of Au^0 from $[AuCl_{4-x}OH_x]^-$ in the growth steps. This compound is present only in traces during the initial steps and at these concentrations it has been proven not to affect seeds formation. This compound has therefore no effect on the final nanoparticle size. The amount of initial $[AuCl_4]^-$ can be changed also by alteration of the reactant addition order. In an inverse method, where concentrated $HAuCl_4$ is added to the citrate solution, the higher local concentration of tetrachloroaurate ions (when droplets mix with the reductant solution) leads to the formation of a larger number of seeds and therefore of smaller nanoparticles. The fortunate interplay of all these complex reactions allows the synthesis of finely tuned monodisperse colloids of the desired size. The concentration of citrate, as long as it is sufficient to ensure pH buffering, has negligible effect on the nanoparticles size. The solution pH, however, has a very important role on the synthesis outcome as seed-mediated growth can occur only in a limited pH region (Figure 2, blue region) and, as previously discussed, if this process is prevented then control over size and polydispersity is no longer possible. Temperature has a complex effect as this parameter affects the kinetics of all the occurring processes in solution, a change of the system thermal energy leads to a different colloid stability region. The temperature dependence of the Turkevich method is therefore non-linear. Anyway, it has been observed that a size minimum is present at 60 °C. While Turkevich method is suitable when greater than 10 nm nanoparticles are needed, if smaller ones are desired then different synthetic strategies are required.

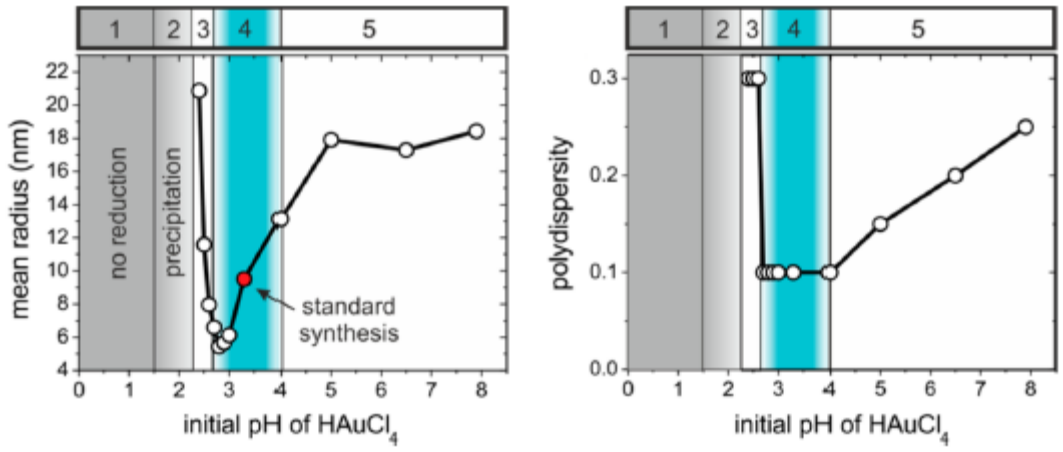

Figure 2: pH dependence of Turkevich synthesis; only in the blue region seed-mediated growth can occur.[4]

Borohydride as reductant – synthesizing smaller NPs

By employing reductants of different strength it is possible to modify the colloid synthetic mechanism affecting the final nanoparticles size. A common and inexpensive strong reducing agent is sodium borohydride. When this compound is used for the reduction of tetrachloroaurate, the nanoparticles formation mechanism does not follow a seed-mediated process as, in this case, the reduction process of the gold precursor is so fast that it is no longer involved in the actual particle growth. In this situation nanoparticle growth is caused only by aggregation or coalescence of pre-formed nuclei.[6] In tetrachloroauric acid reduction with sodium borohydride the nanoparticle growth process has been demonstrated to be based on coalescence only (Figure 3).[7]

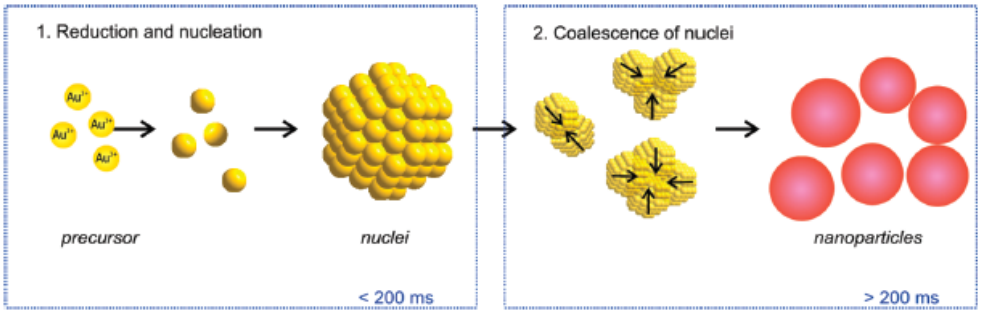

Figure 3: gold nanoparticle formation with borohydride as reductant.[7]

With such a strong reductant, the reduction process of the metal precursor is completed in just a hundred of milliseconds and leads to the formation of a large number of primary clusters. These clusters then coalesce forming the final nanoparticles in a second and

separate process, which is not related to the metal reduction one.[6] In this situation three scenarios are possible:

i) Long-term stable nanoparticles (2-5 nm radius) are formed (as in [Ag] reduction with $NaBH_4$)

ii) Metastable nanoparticles (2-3 nm radius) are formed, which are not stable and slowly grow further (as in [Au] and [Pd] reduction with $NaBH_4$)

iii) The particles exceed the length scale of nanoparticles and precipitate (as in [Cu] reduction with $NaBH_4$)

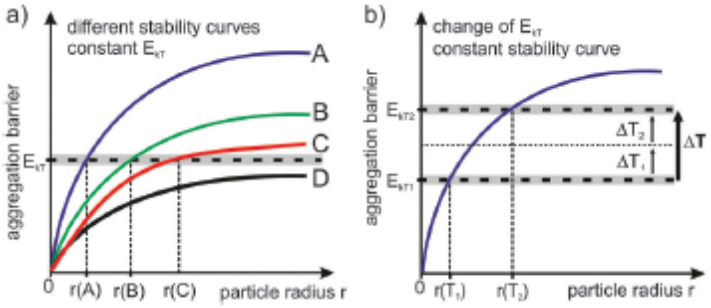

Figure 4: schematics of particles growth; a) change of the stability curve; b) change of the thermal energy.[6]

Using an excess of borohydride it is possible to reach a metastable state after the first coalescence step. The residual borohydride is however hydrolyzed within several minutes and this change in solution composition alters the surface chemistry of the nanoparticles, decreasing the colloid stability (the stability curve is changed). A second coalescent growth step is therefore observed. The final size of the nanoparticles and the presence of eventual successive coalescent steps in their formation mechanism depend on all the parameters which affect the stability curve of the colloid.

Brust and Schiffrin synthesis

The use of stabilizers (ligands for gold) in the synthesis such as long-chained alkylamines or thiols, is a great practical way to alter the colloid stability curve and to control nanoparticles size and shape. Brust and Schiffrin in 1994 developed a single-step protocol for the synthesis of small gold nanoparticles which can't be accessed with the Turkevich synthesis.[8] Tetrachloroaurate, the gold ions source, is initially transferred from aqueous solution to an organic phase (toluene), with the aid of tetraoctylammonium bromide as phase transfer agent, where is then reduced in presence of the free thiol (the stabilizer) by addition of a freshly prepared aqueous solution of sodium borohydride. The aqueous phase has been

demonstrated to act only as tetrachloroaurate and borohydride ion source and the chemical reactions take place in the organic one. The mechanism of the synthesis is schematized in Figure 5.[9] The thiol, once added, acts as a reductant for $[AuCl_4]^-$:

$$TOA^+[AuCl_4]^-_{(O)} + 2RSH_{(O)} \rightleftarrows TOA^+[AuCl_2]^-_{(O)} + RSSR_{(O)} + 2HCl_{(W)}$$

The formation of polymeric $[Au(I)SR]_n$ species during the synthesis depends on the reaction conditions: the presence of a retained aqueous phase when the thiol is added to the reaction mixture favours it.

$$TOA^+[AuCl_2]^-_{(O)} + RSH_{(O)} \rightleftarrows Au(I)SR_{(O)} + TOA^+Cl^-_{(O)} + HCl_{(W)}$$

The formation of these polymeric species is also favoured when it is employed a concentration of thiol higher than that of $[AuCl_4]^-$ (RSH/Au ratio > 2), and they can also be formed directly from the reduction of $[AuCl_4]^-$.

$$TOA^+[AuCl_4]^-_{(O)} + 3RSH_{(O)} \rightleftarrows Au(I)SR_{(O)} + RSSR_{(O)} + TOA^+Cl^-_{(O)} + 3HCl_{(W)}$$

Au ions reduction by borohydride has been proven not to be an interfacial reaction, but to occur only in the organic phase.

$$TOA^+[AuCl_2]^-_{(O)} + BH_4^-_{(O)} \rightleftarrows Au_{(O)} + TOA^+Cl^-_{(O)} + HCl_{(W)} + B(OH)_4^-_{(W)}$$

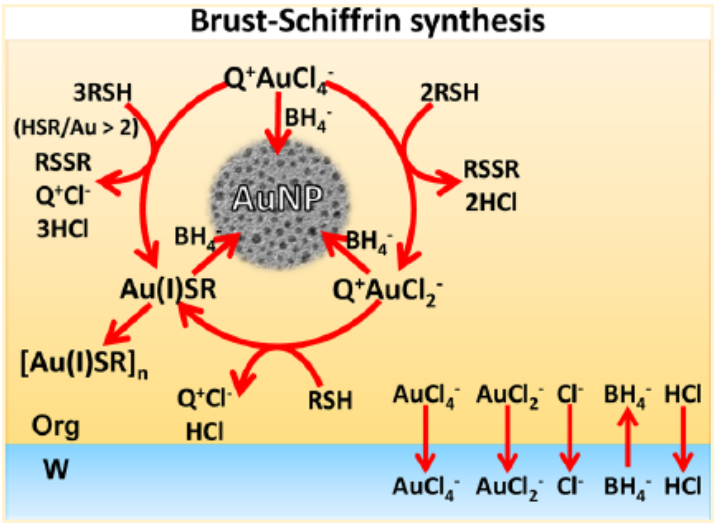

Figure 5: Scheme of the Brust and Schiffrin synthesis[9]

At a low thiol/gold ratio (from 1 to 3) the nanoparticles size and distribution was not affected by a delayed addition of the borohydride, 5 h after the preparation of the reaction mixture. However, at a higher thiol/gold ratio (from 4 to 8), the number of synthesized particles decreased progressively in the aged sample. The difference in behaviour is caused by the progressive consumption of gold by the formation of insoluble $[Au(I)SR]_n$ polymers, which

are no longer available for the nanoparticles formation. The size of the obtained AuNPs depends therefore on the employed thiol/gold ratio and on the mixing duration (which affects the accumulation of $[Au(I)SR]_n$ polymer). Higher concentrations of 1.0-1.5 nm nanoparticles were formed when low RSH/$[AuCl_4]^-$ ratios between 1 and 2 were employed.[9] Perala and Kumar demonstrated that the control over size and dispersion of the colloid is due to a continuous nucleation-growth-passivation mechanism (Figure 6).[10] The continuous nucleation of AuNPs caused by the reduction of gold ions by borohydride would, in theory, lead to a polydisperse colloid, since nuclei continuously form and grow over the whole reaction time. Thanks to the presence of a passivating agent (the thiol), however, the nanoparticles are progressively capped as they grow, forming eventually fully capped ones, which are stable and do not grow anymore.

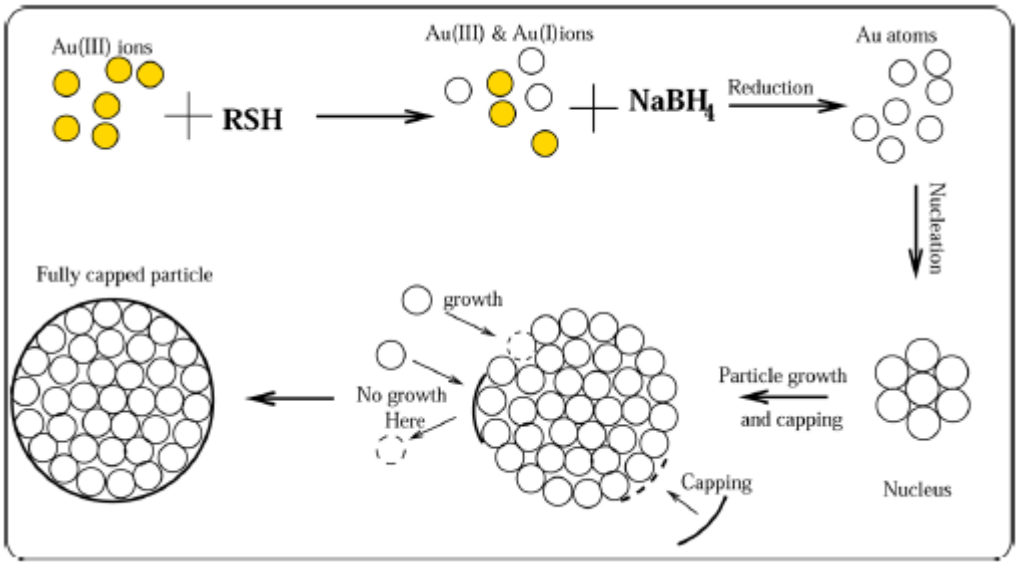

Figure 6: Scheme of the Brust and Schiffrin synthesis mechanism[10]

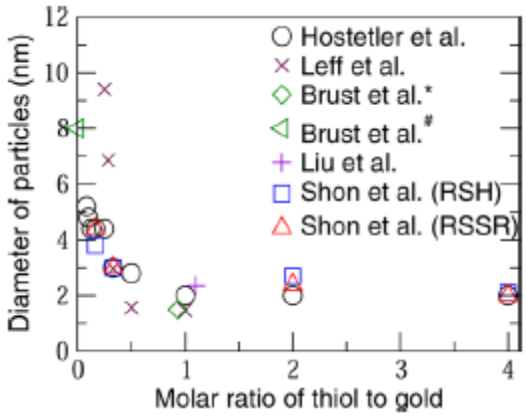

Figure 7: Effect of the thiol to gold ratio on the AuNPs size

Therefore, it is the control over the capping process which allow to control over size and dispersity of the colloid. It is possible to effectively change the nanoparticle size by altering the thiol to gold ratio, with an increase of the thiol amount leading to smaller AuNPs (Figure 7). Depending on the nature of the ligand employed, the nanoparticles (in the 1-3 nm diameter range) can be purified by precipitation from appropriate solvents and are generally stable enough to be handled as a novel compound. As the role of the thiols is to cap the particles as they form, preventing further growth, it is possible also to substitute them with other ligands, such as disulfides, without losing the advantages of the Brust and Schiffrin synthesis.

Two-steps methods – decoupling gold core from organic monolayer synthesis

As previously discussed, the Brust and Schiffrin method employs sodium borohydride for the gold precursor reduction, which is performed in the organic phase in the presence of the desired thiol. This reductant, however, is quite harsh and can be incompatible with many functionalized thiols (such as peptides, saccharides, or thiols bearing reducible moieties, as an example). This incompatibility issue can be a huge problem when the interest is not purely focused on the nanoparticle gold core but the synthesis of expressly designed monolayers is required and labile functionalities have to be included. The Brust and Schiffrin method might not be flexible enough for this scenario and different synthetic strategies are needed. A two-step method has been developed in 2008 by Lay and Scrimin which enable to separate the gold core synthesis process from its functionalization with the desired thiols.[11] In this procedure, a modification of the original Brust and Schiffrin one, a defined amount of di-n-octylamine is added to the tetrachloroauric acid solution prior to the reduction step to Au^0. This secondary amine initially reduces Au(III) to Au(I) and then, during the actual nanoparticle formation step with $NaBH_4$, it binds on the cluster surface, acting as a stabilizer, and allows to achieve a great control over the nanoparticles size. The affinity of gold for thiols is greater than that for amines and therefore, by ligand exchange, the amine can be easily substituted with the desired thiol, forming the final desired monolayer. The amount of dioctylamine added, which overall acts as a “transient” stabilizer, allows to control the nanoparticles size. The larger the amount of added DOA it is, the smaller and more size-focused the nanoparticles will be (see Figure 8). Other amines can also be used as “transient” ligands for the synthesis of gold nanoparticles. A similar procedure to the previously discussed one has been developed in 2018 with oleylamine (OAm) in combination with tBAB as reducing agent.[12] In this procedure core size tuning was performed controlling the reaction

temperature (Figure 9). Higher temperatures yielded smaller nanoparticles up to 40°C, where a minimum size was reached.

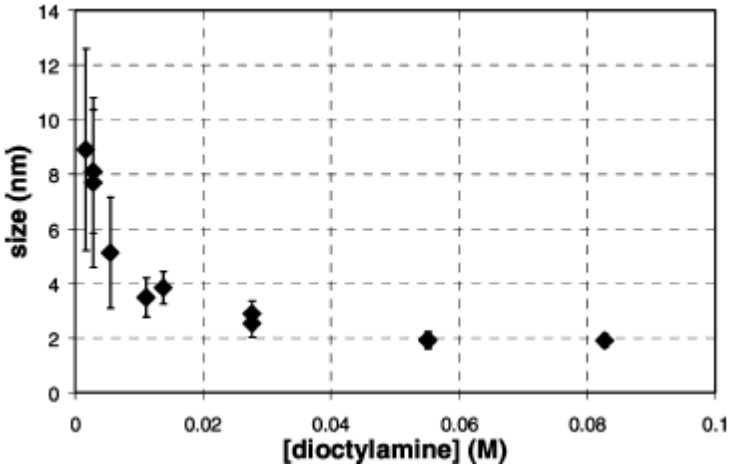

Figure 8: relation between AuNPs size and DOA concentration.[11]

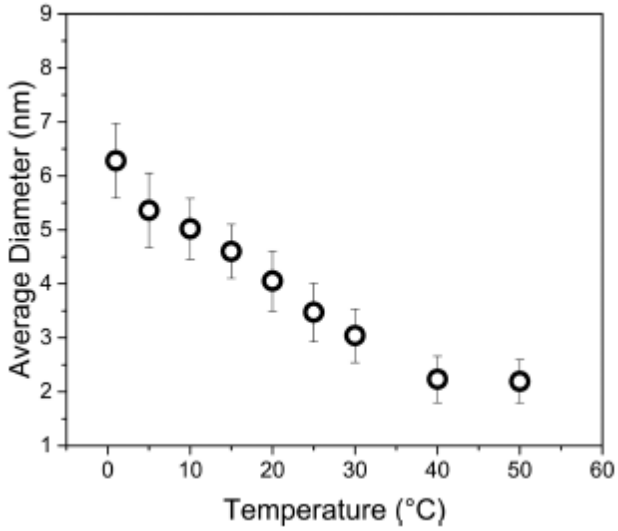

Figure 9: core size dependence on reaction temperature with the two-steps procedure involving OAm and TBAB[12]

Cluster mixture and Au-S bond

Gold nanoparticles below a certain size limit show different properties than those of bulk metal. Plasmonic absorption, due to a resonant oscillation of the valence electrons with the electromagnetic field of the incident light, is the most popular. Below a certain threshold (around 4 nm), metal nanoparticles are no longer plasmonic and at very small sizes molecularly precise clusters with a characteristic shape and mass can even be found (Figure 10 and Figure 11).[13] Nanoparticles samples are usually found as mixture of nanostructures of

different size and shape, while at very small sizes (in the range of few nanometers) such colloids are composed of mixtures of atomically-precise clusters. Gold clusters can be considered as chemically-modified "superatoms" as they show different and characteristic properties than those of larger nanoparticles, such as discrete energy levels and relative characteristic absorption bands.[14] The notion of superatom also explain the long standing question about the oxidation state of the gold atoms. Indeed, to compensate the charge of the thiolates bound to the surface, part of the core atoms must bear a positive charge and have a +1 oxydation state. Part of these atoms coincide with the "staples" structures which we will discuss later, but the rest should belong to the core, which appears to be as a mixture of Au(I) and Au(0) atoms. In reality, electrons are located in the superatom orbitals and intermediate oxidation states are shared by all the core atoms. The nature of gold-sulfur bond in these clusters have been elucidated and oligomeric structures of $RS(AuSR)_n$ units, where bridiging gold atoms are in the +1 oxidation state, have been proved to be present at the gold-sulfur interface.[15] $Au_{144}(SR)_{60}$, with a core weight of 29kDa and a diameter of 1.6 nm, is one of the most ubiquitous gold cluster and has abundantly been synthesized and studied. A model has been determined for it and this species would be best described as $Au_{114}[RS(AuSR)_{30}]$.[16] This cluster shows an icosahedral symmetry (I) and has a core of 144 gold atoms disposed in three concentric shells of 12, 42 and 60 atoms. The 60 atoms of the outer shell, which is remarkably spherical (with a deviation of only 0.04Å on the 7.10Å radius), are protected by 30 thiols arranged in RS-Au-SR equivalent units (referred also as staple-motif) (Figure 12). The arrangement of these RS-Au-SR units is chiral and the cluster can be found as two enantiomeric isomers.

fraction[a]	M_w[b]	chemical composition	core mass (kDa)[c]	D (nm)[d]
I	12,318	$Au_{38}(SC12)_{24}$	8	1.1 ± 0.1
II	29,547	$Au_{104}(SC12)_{45}$	21	1.4 ± 0.3
III	35,675	$Au_{130}(SC12)_{50}$	26	1.5 ± 0.3
IV	40,447	$Au_{144}(SC12)_{60}$	29	1.6 ± 0.1
V	50,528	$Au_{187}(SC12)_{68}$	38	1.8 ± 0.3
VI	~59,820	$Au_{\sim 226}(SC12)_{\sim 76}$	45	2.0 ± 0.5
VII	~68,000	$Au_{\sim 253}(SC12)_{\sim 90}$	53	2.1 ± 0.4
VIII	~81,760	$Au_{329}(SC12)_{84}$	66	2.2 ± 0.4
IX	~92,630	$Au_{\sim 356}(SC12)_{\sim 112}$	75	2.2 ± 0.3
X	~128,700	$Au_{\sim 520}(SC12)_{\sim 130}$	108	2.4 ± 0.2
VI′	~55,570	$Au_{\sim 226}(SC8)_{\sim 76}$	46	–
VII′	~62,940	$Au_{\sim 253}(SC8)_{\sim 90}$	53	–
IX′	~86,350	$Au_{\sim 356}(SC8)_{\sim 112}$	75	–
X′	~121,300	$Au_{\sim 520}(SC8)_{\sim 130}$	108	–

Figure 10: Au clusters composition and size[13]

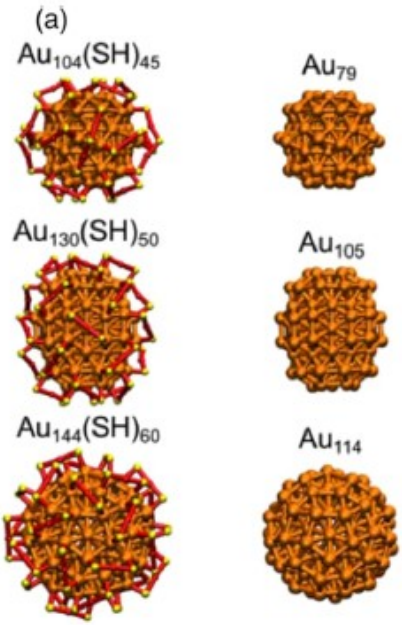

Figure 11: Gold clusters have different and characteristic shapes[13]

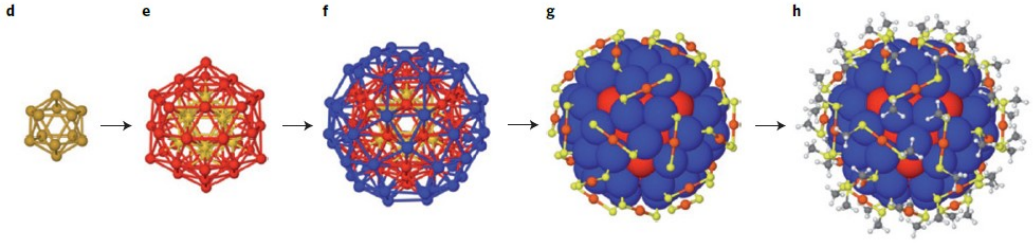

Figure 12: ***d-f****, The concentric 12-atom (hollow), 42-atom and 60-atom Au shells of the 144-atom gold core of* $Au_{144}(SCH_3)_{60}$ *respectively;* ***g****, S-Au-S arrangement of the 30 RS-Au-SR unit covering the surface (blue) of the 114-atom gold core;* ***h****, with all the atom shown.*[16]

Gold nanoparticles protecting monolayer

Monolayer-protected gold nanoparticles as multivalent receptors

Gold nanoparticles, or, more in general, metal nanoparticles functionalized with organic ligands, provide a great way to take advantage of cooperativity between the attached ligands. Indeed, these are kept in close proximity on the surface and organized in a dynamic but partially ordered arrangement. In this way, interacting groups inserted in the ligand structure can be considered as pre-organized for the interaction with multivalent species. The first example of this approach was provided by L. Pasquato and P. Scrimin who demonstrated that nanoparticles functionalized by mixed monolayer composed of a methylimidazole-terminated thiol and a neutral alkyl thiol show multivalency in the interaction with bis- and tris-porphyrins (Figure 13).[17] The apparent binding constant of the tris-porphyrin 4 was three orders of magnitude greater than that of an analogue mono-

porphyrin and the actual concentration of methylimidazole on the nanoparticle surface showed negligible effect on the binding. This demonstrated that the mobility of the thiol chains can compensate for the lack of complementarity without introducing a significative entropic cost. The gold core can therefore be seen as a template which allows a partial preorganization of the functionalities grafted through Au-S bonds.

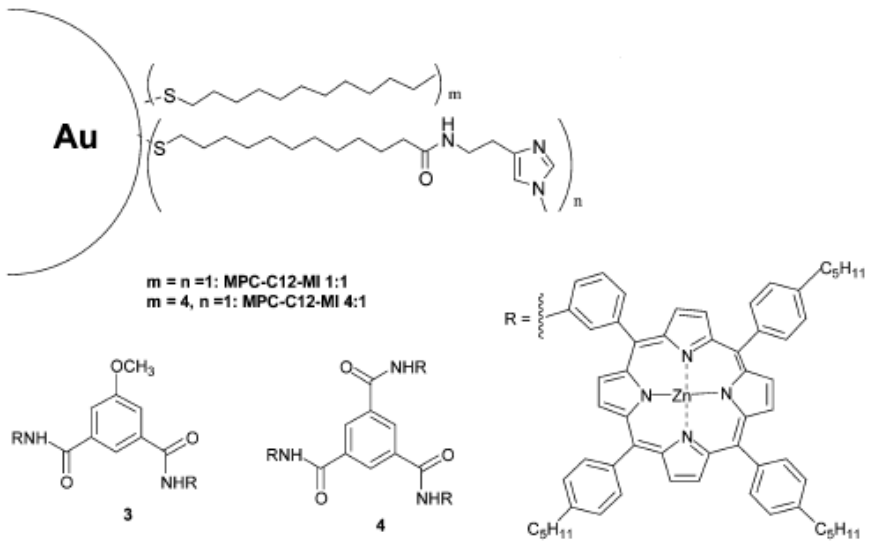

Figure 13: multivalency was demonstrated using methylimidazole functionalized nanoparticles and porphyrin arrays 3 and 4.[17]

Another system showing multivalency was developed by V. Rotello to work as receptor for flavin.[18] Ligands functionalized with diacyldiaminopyridine, as hydrogen-bonding donor and acceptor, and pyrenes, for aromatic stacking interactions, were employed for the functionalization of gold nanoparticles (Figure 14). The binding constant (K_a) of colloid 2 was 323 M^{-1}, twice of that for colloid 3 (193 M^{-1}) where diacyldiaminopyridines were diluted in neutral octanethiol ligands, in absence of pyrene moieties, showing that both the two interactions play an important role in the flavin recognition. To explore the self-assembly of binding pockets on the surface of the nanoparticles a system where the two ligands employed for H-bonding and aromatic stacking were diluted with inactive alkyl ligands was synthesized (colloid 4). This receptor showed a K_a of 235 M^{-1}, with an enhancement of 71% over that of colloid 3, where no pyrene was present.

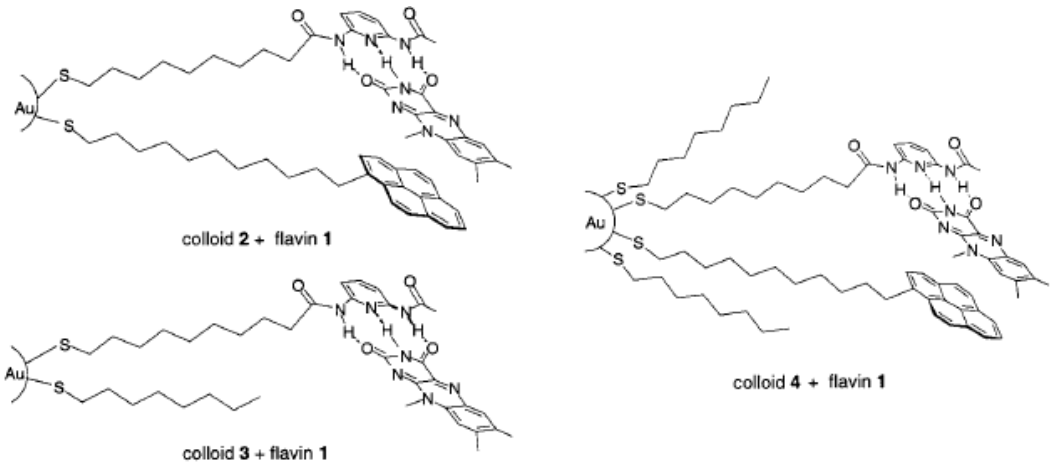

Figure 14: receptors for flavins show multivalency[18]

These results show that the monolayer is flexible and different moieties can assume the correct conformation to cooperate and improve the binding sites affinity for a target molecule. Environments with features similar to those of the organic monolayers on the surface of metal nanoparticles can be created with the use of surfactants. In Figure 15 the simulated structures of an SDS micelle and that of an $Au_{144}SR_{60}$ cluster are compared. Indeed, we will see later that micelle-assisted DOSY experiments have been developed making use of SDS micelles in a similar way to the AuNPs-assisted ones.[19] However, when the system needs to be accurately studied and/or finely tuned, more "rigid" and less dynamic structures such as those provided by functionalized gold nanoparticles offer a huge advantage.

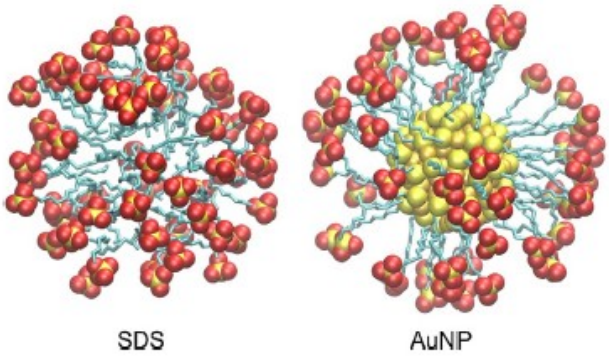

Figure 15: comparison between MD-simulated structures of SDS micelle (left) and $Au_{144}(SR)_{60}$ cluster functionalized with mercaptoundecane-1-sulfonate[20]

A large variety of different ligands can be attached on the gold surface with different synthetic procedures. Functionalized AuNPs are currently of great interest for the development of supramolecular receptors.[1,21] Such systems are known to form transient pocket-like binding sites on their surface which resemble, in some ways, the ones found in

proteins.[22,23] Selectivity of such binding sites can be tuned by changing the structure of the ligands employed or by mixing different ones bearing different functionalities. Thanks to the simplicity provided by their self-assembly based synthetic strategy, such systems are of great interest for the development of both sensors and catalysts where recognition of a molecule (or a class of molecules of interest) is needed. NMR-chemosensing techniques are currently being developed using such supramolecular systems as receptors.[20,24–27] Historically, thiols are used for the functionalization of gold nanoparticles as the strong bond formed between the ligand and the gold surface allows the synthesis of stable and resilient nanostructures. Recently, N-heterocyclic carbenes (NHC) have also started to attract interest due to their even stronger interaction with the metal surface.[28–33]

The importance of nanoparticle size

Gold core size has been demonstrated to significantly affect the bound ligands spatial arrangement and packing, on which depend both the binding properties and solvation of the nanoparticle ligand monolayer.[34] Differences in thiol packing have been demonstrated through several different studies. Hydrophobic nitroxide radical 2 (Figure 16) was used as ESR probe to study its partition between water and the monolayer of AuNPs of different sizes (from 1.6 to 5.3 nm) protected with thiol 1.[34]

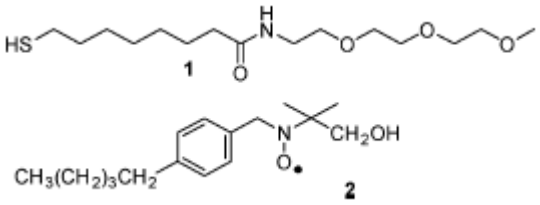

Figure 16: Thiol used for the functionalization of AuNPs and hydrophobic radical used as ESR probe[34]

The ratio between the concentration of the partitioned radical and that in the free state was found to correlate with the nanoparticles size (Figure 17) and the partition equilibrium constant was observed to increase decreasing the nanoparticle size (from 34.4 for 5.3 nm AuNPs to 104 for 1.6 nm ones), showing that the interaction with small organic molecules is more favoured in monolayers of smaller nanoparticles. This suggests a lower steric hindrance on the surface of smaller nanoparticles. Thiols that could undergo Norrish type II reaction were also used as a probe to study their reactivity when bound to AuNPs surface.[35] This reaction can proceed through two different pathways, one leading to cyclization and the other to elimination of an alkene and a ketone (Figure 18). When these thiols were bound to

nanoparticles only the fragmentation pathway was observed, and a 30% decrease in the extent of the reaction was found increasing the size of the AuNPs from 1.7 to 4.5 nm. This can be explained by the fact that thiols can be located in different micro-environments inside a nanoparticle monolayer: in terrace regions (similar to monolayers of 2D gold surfaces) or in vertex sites (defects). Terrace regions are more abundant in larger nanoparticles, while in smaller ones the fraction of vertex sites is larger. Thiols in the latter position are less sterically hindered and, thanks to their increased mobility, are more likely to assume the correct conformation for the fragmentation reaction to occur.

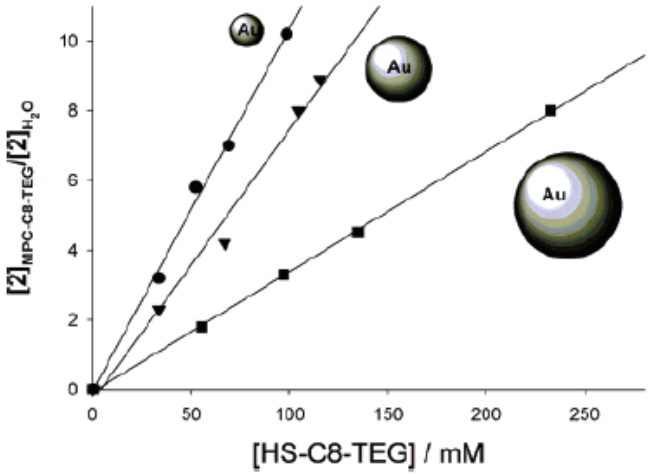

Figure 17: plot of the ratio between the concentration of partitioned analyte in the monolayer and that of the free species. HS-C8-TEG protected gold nanoparticles of 1.6 nm, 3.4 nm and 5.3 nm[34]

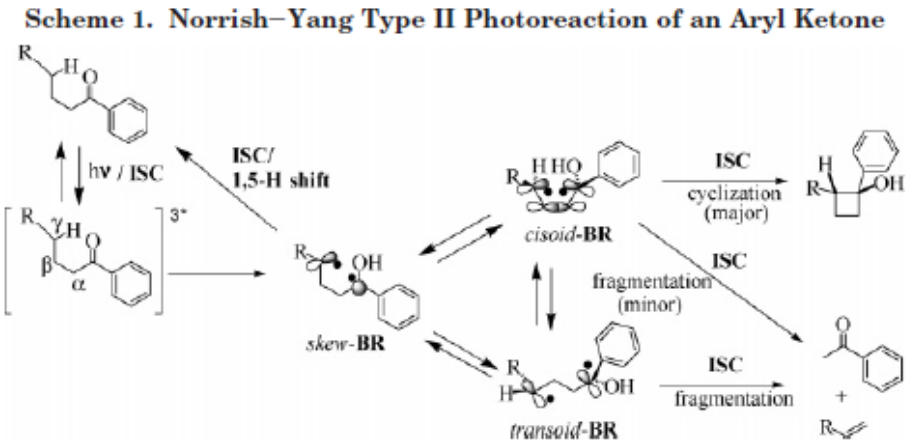

Figure 18: Norrish Type II reaction mechanism.[35]

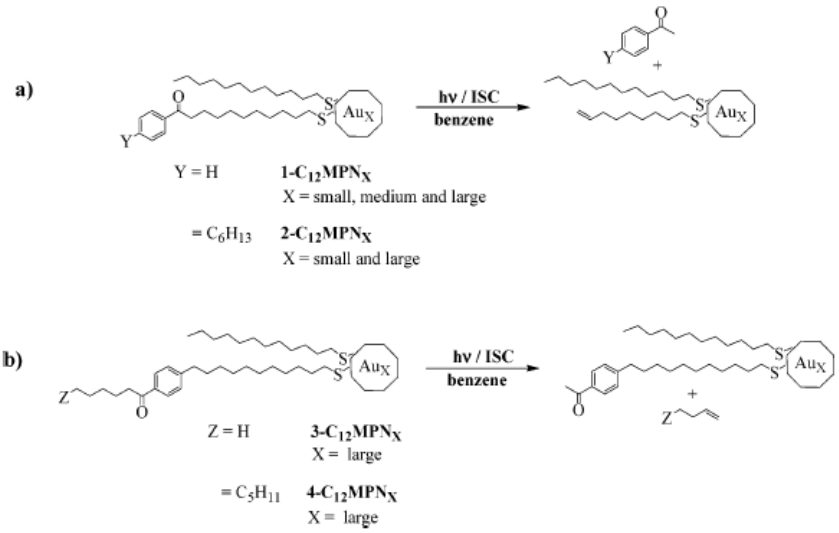

Figure 19: Norrish II type reaction used as probe for thiol reactivity on differently sized gold nanoparticles; reactions on smaller nanoparticles show an higher reaction yield[35]

AuNPs of different sizes and functionalized with cationic thiols have been studied in detail through NMR experiments, following chemical shift of the cationic headgroup and T_2 relaxation rates, and by MD simulations.[36] Ligands were found to be progressively more disordered and mobile moving from 13 nm to 1.2 nm nanoparticles, suggesting that a more pronounced surface curvature, characteristic of smaller gold cores, leads to less sterically hindered and more accessible monolayers.

Chemical sensors with functionalized AuNPs

The organic monolayer of gold nanoparticles can be conveniently exploited as platform for the development of chemical sensors. Several examples based on different analytical methods can be found in literature. Thiols bearing exposed Zn^{2+} complexes have been bound to nanoparticles and their charge exploited for the detection of small anionic molecules, using AuNPs functionalized with metallated triazacyclononane (with both zinc, TACN-Zn^{2+}, and copper, TACN-Cu^{2+}) the resulting sensors were able to discriminate nucleotides in water via fluorimetric displacement assay.[37] When fluorescent probes are bound to the monolayer their fluorescence is quenched by the nanoparticle gold core. Then, when nucleotides are recognized, the probes are displaced according to their affinity and the detachment restores their fluorescence, which can be easily measured. The fluorescence fingerprint is related to the nucleotide identity (affinity for the monolayer) and to its concentration. By using two metals and different fluorescent probes it was possible to create a sensors array able to discriminate between 8 nucleotides in micromolar concentration (Figure 20). This effectively

demonstrates the possibility to tune the selectivity of a supramolecular detector to detect the desired analytes.

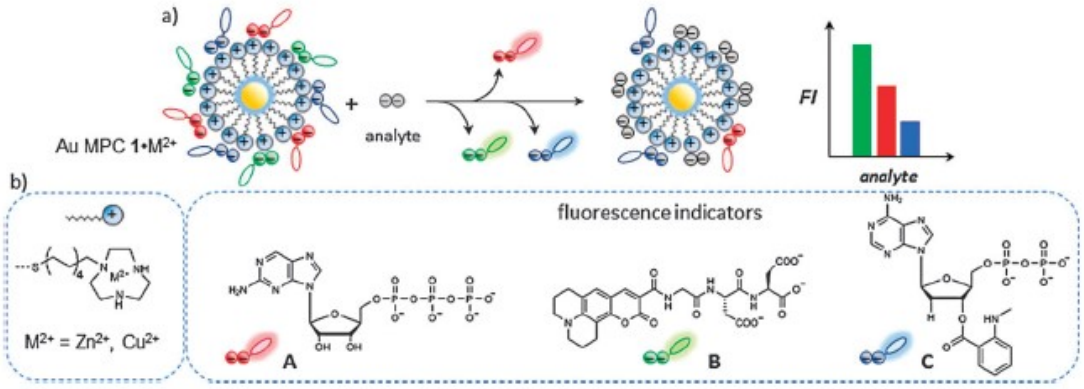

Figure 20: supramolecular sensor for fluorimetric displacement assay of nucleotides.[37]

The binding of anionic biomolecules to TACN*Zn^{2+}-functionalized AuNPs has been demonstrated to be strongly affected by both ionic interactions and hydrophobicity.[38] The introduction of a hydrophobic MANT group on ATP derivatives increased the binding constant of the guest more than the addition of supplementary negative charges in place of the hydrophobic group. The hydrophobicity of such group favours its insertion inside the internal hydrophobic portion of the nanoparticle monolayer increasing the affinity for this guest (Figure 21). This characteristic binding mode was confirmed by monitoring the change in chemical shift of the proton signals of MANT when from a free state it is allowed to interact with the nanoparticles.

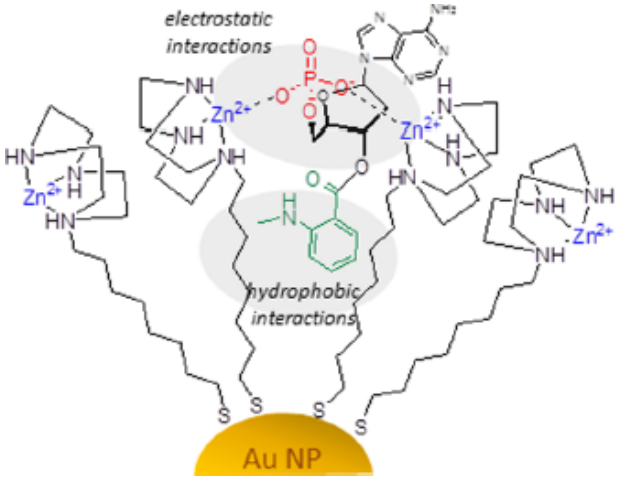

Figure 21: hydrophobicity plays an important role even in the recognition of charged molecules.[38]

Computer assisted monolayer design

Even if endowed with a certain degree of structural organization, nanoparticle-coating monolayer remains a dynamic object, and this mobility hampers the on-demand design of their binding properties. To investigate monolayer behaviour and binding properties, molecular dynamics (MD) studies were performed on thiol-protected clusters.[22,27] In one case, functionalized nanoparticles with thiols bearing both an internal alkyl and external oligoethylenglycol portion were studied for their recognition properties (Figure 22). While it may seems that the interaction of small molecules with such monolayers is purely driven by a partition of the guest between the apolar environment of the monolayer and the polar one of the bulk solvent, as initially suggested by Pasquato and Lucarini[34], the nature of these interactions is actually different and much more complex. While nanoparticle **1** (in Figure 22) can selectively interact with salicylic acid, which is the most hydrophobic (higher octanol/water partition coefficient) of the analytes set, nanoparticle **2**, which has an alkyl chain four carbons longer, can recognize both the most hydrophobic (salicylate, 3) and the most hydrophilic (tosylate, 6) molecules of the set without detecting the two in between. Computational simulations (MD) performed on 1 and on 7-10, supported by experimental data, showed that the superficial environment is not homogeneous and that the packing of the thiols strongly affects the properties of the system.[22] For example, when nanoparticles protected with long alkyl chain (as thiols 9 and 10) are dispersed in water, the alkyl portions of the ligands exclude water molecules and pack together. This ligand clustering phenomenon induces a change in the nanoparticle shape (Figure 23), which drifts from a spherical one (which can be observed with the more “hydrophilic” thiol **1**, bearing a shorter alkyl chain and an amide group) to a more irregular and elongated one (for thiols bearing longer aliphatic chains). The resulting thiols organization forces a fraction of the ligands to expose their hydrophobic moiety to the aqueous environment, disfavouring the nanosystem solvation. Rigidification of the monolayer and aggregation of the nanoparticles were confirmed by ^{1}H-NMR spectra, where a significative broadening was observed in the signals of less solvated monolayers, indicating a correlation between solvation and rigidification of the environment.

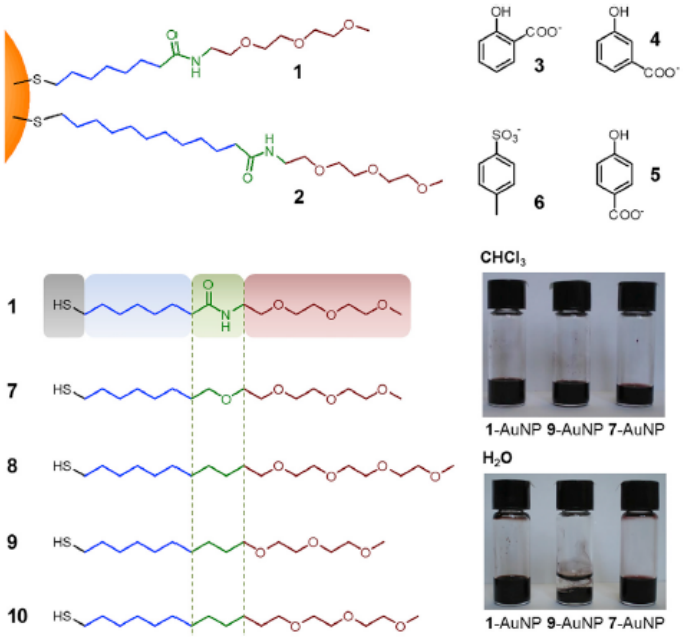

Figure 22: Effect of ligand structure on nanoparticle binding and solvation properties.[22]

Broadening was observed even for signals from the outermost portion of the oligoethylenglycol chain, providing evidence, further confirmed by DLS measurements, that longer alkyl chains lead to nanoparticles clustering in water dispersions. If the alkyl portion of the chain becomes too long or the solubilizing one too short or inadequate, aggregation is so severe that nanoparticles can no longer be dispersed in water (**10** in Figure 23). The presence of an amide group between the alkyl and the OEG portions of the thiol **1** facilitates the intercalation of water molecules, increasing the disorder of the monolayer and allowing the reaching of a more homogeneous and spherical organization. When these nanosystems are dispersed in less polar solvents, such as chloroform, hydrophobicity plays no longer a role and the interaction between the internal alkyl portion of the monolayer and the solvent is no longer disfavoured by an entropic contribute. In these solvents the monolayer of nanoparticles functionalized with long alkyl chains can be permeated by the solvent molecules and it assumes again a homogeneous spherical conformation (see **10** in Figure 23). MD simulations showed that transient pockets form inside the organic monolayer and that the formation of such structures is compulsory for the recognition of target molecules. The recognition ability of the system therefore depends on the nature of the pockets the monolayer is able to form.[22] In particular, deep an large pockets are needed for effective target binding, and such pockets are formed only in monolayers featuring sufficient mobility and "defects", resulting from reduced intramolecular interactions, solvation and altered conformational preferences of the ligands.

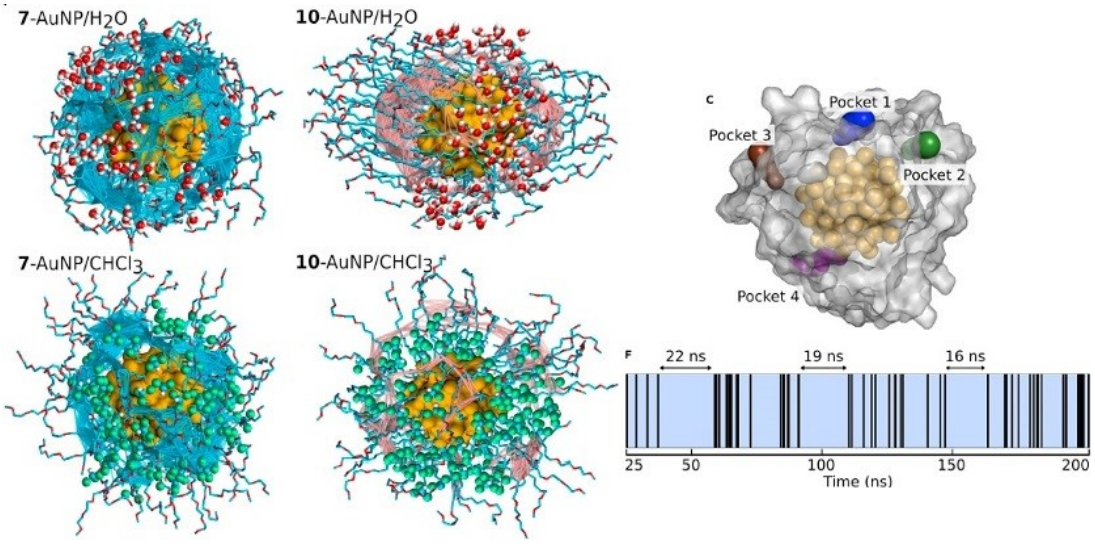

Figure 23: MD simulation of transient binding pockets in a nanoparticle monolayer.

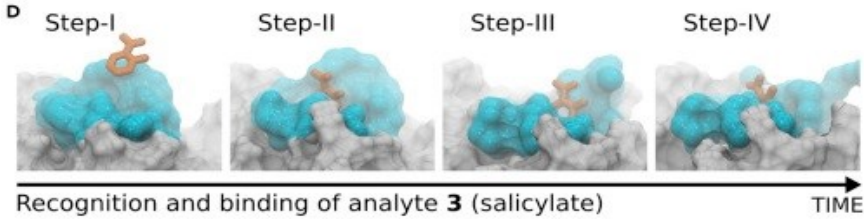

Figure 24: MD simulation of the binding of salicylate to a transient pocket.[22]

Nicely the presence of such pockets is correlated with long analytes predicted residence time inside a binding pocket (Figure 25), which in turn correlate well with the experimental recognition trend of the nanoreceptor.

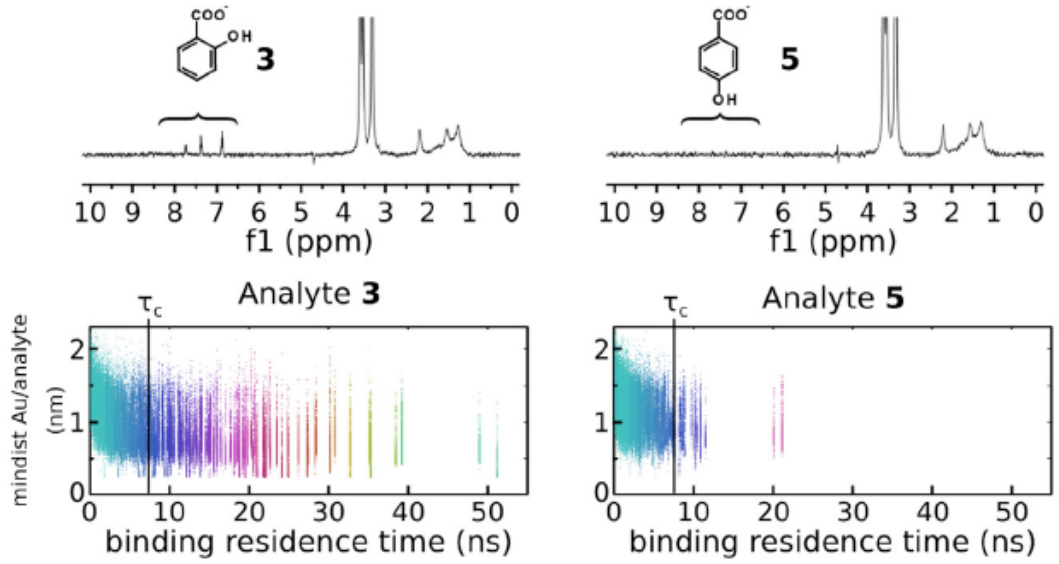

Figure 25: A) NOE pumping experiments of Salicylate and p-hydroxybenzoate, B) binding residence time of these two analytes inside the AuNPs monolayer pockets.

To understand whether MD simulation can bring the level of control of the nanoparticles properties from the explanation of their behavior to its design, a set of similar nanoparticles with a mutated hydrogen bond donor group was studied (Figure 26).[27] Amide of nanoparticle 1 was substituted in nanoparticle 2 with urethane, a weaker H-bond donor, and with urea in 3, which is instead a stronger one. Thiol 4 is a modification of thiol 3 where an ether group was introduced in the internal alkyl chain. All the mutated nanoparticles proved to have a spherical shape and to form a similar number of hydrogen bonds with the solvent. Regarding the intermolecular interactions, the two urea nanoparticles formed significantly more ligand-ligand hydrogen bonds with respect to the others, leading to a more rigid inner portion. Simulations of the population profile showed an increased amount of salicylate at a small distance (1.25 nm) from the gold core in presence of thiol 3 (Figure 27) but a strong reduction in the presence of thiols 2 and 4. This prediction was confirmed by the experimental calculation of the binding constants, which resulted to be 120 M^{-1} for 1, 1100 M^{-1} for 3, and >10 M^{-1} both for 2 and 4.

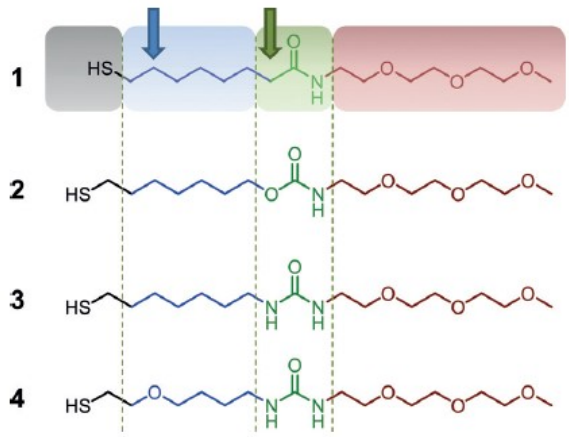

Figure 26: thiols used for nanoparticles functionalization; the arrows indicate the mutation points.[27]

Binding pocket analysis showed the presence of deep pockets in AuNPs 1 and 3, but not in AuNPs 4.[23] Hence, while the urea is able to form H-bonds with salicylate, nanoparticle 4 does not bind it while nanoparticle 3 does, because only the second one can form pockets capable to accommodate the substrate in the monolayer. Surprisingly, the reason of such difference is the internal ether group, which increases the preference of the ligand for folded conformations (more gauche angles) and hence for more compact monolayers. Selectivity of 1-AuNP was not altered by the substitution of amide with urea in 3-AuNP and this nanoparticle, developed with the aid of in-silico simulations, demonstrated to be an improved receptor for salicylate.

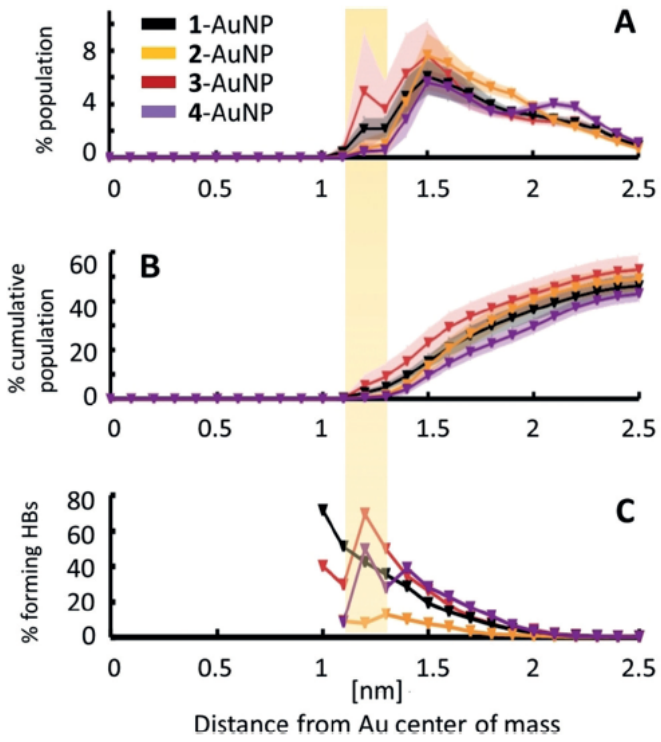

Figure 27: Salicylate penetration in the nanoparticle monolayer. A) salicylate distribution around the nanoparticles. B) Cumulative sum of the populations reported in A. C) Probability of an H-bond between salicylate and monolayer (relative to the analyte contacts with the monolayer). [27]

Results from these works clearly show the complexity of nanoparticles organic monolayer and demonstrate the necessity of a computational aid in the development of such systems. Without the ability to accurately simulate the dynamics of these supramolecular species in silico, the design of improved chemosensors for a defined analyte is likely to require large investments in time and resources without any guarantee of success.

Nanoparticle-assisted NMR-chemosensing

Nanoparticle-assisted NMR-chemosensing is a very powerful technique which allows to analyze even complex mixtures, such as human urine[24], for the detection of an analyte or a class of molecules of interest. This technique is based on the use of functionalized gold nanoparticles in combination with NMR experiments capable to exploit differences in molecular size. These include DOSY, diffusion filters, NOE-pumping, STD, waterLOGSY and the newly developed HPwater-STD. Usually, in standard NMR experiments, all the molecules in solution are magnetized with a non-selective pulse and the signals of every single species present is recorded in the spectrum. The complexity of such spectra greatly increases when mixtures of molecules are being analyzed as almost all of the signals may result to be

superimposed in a single spectrum. This situation can easily lead to very difficult to interpret spectra and, in most situations, even for relatively simple mixtures, the detection of molecules of interest can become impossible. Nanoparticle-assisted NMR-chemosensing exploits the size and the molecular recognition ability of functionalized nanoparticles to provide a way to selectively magnetize only a subset of the molecules present in the mixture, greatly reducing the complexity of the recorded spectrum.

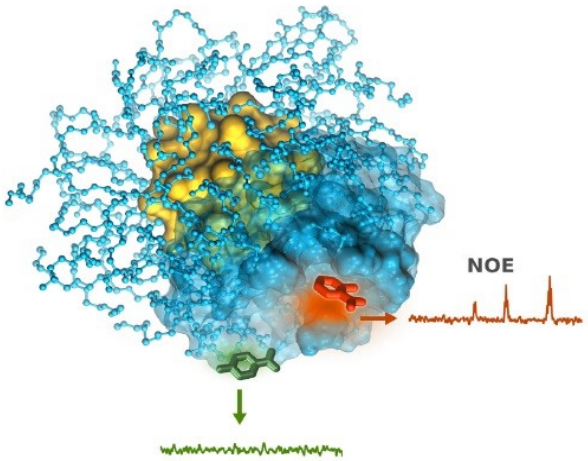

Figure 28: NMR-chemosensing experiment with a functionalized gold nanoparticles in presence of a detected analyte (red) and an unrecognized molecule (green)

As the result of the analysis is a complete NMR spectrum of the detected molecule, this analytical technique is inherently free from false positives, which are otherwise a big problem with standard chemical sensors (Figure 29). The reliability of the analytical technique is no longer affected by the selectivity of the sensor, as long as it is able to recognize the molecule of interest, and the operator no longer relies on trusting an indirectly obtained outcome value. With a supramolecular nanoreceptor able to recognize an entire class of molecules it is therefore possible to both quantify and unambiguously identify even unknown analogs of the analyte of interest. The first NMR-chemosensors were designed to detect small organic anions (Figure 30) in water.[24] AuNPs 1, functionalized with a thiol bearing an internal hydrophobic portion and an external hydrophilic triethylenglycol chain, were known to incorporate hydrophobic molecules inside the internal aliphatic portion of the monolayer and were conveniently chosen as a starting point for the development of a supramolecular nanoreceptor.

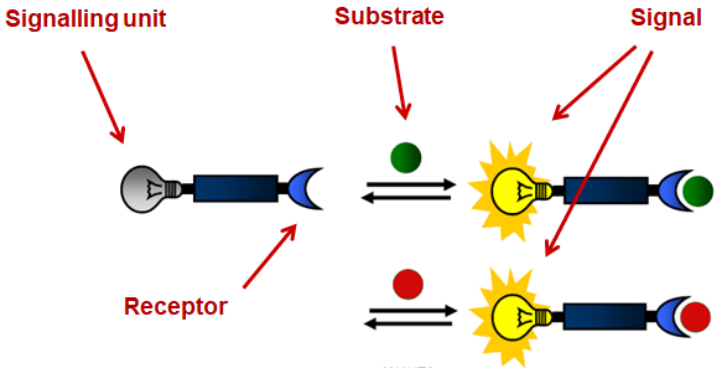

Figure 29: false positives are an important problem which affects standard chemical sensors: different recognized molecules trigger the same signal, which does not carry information about the detected guest

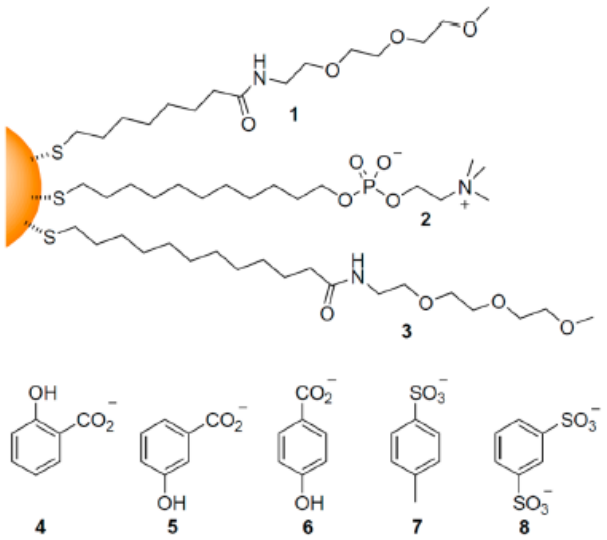

Figure 30: First NMR chemosensors (1-3) for small organic anions (4-8)[24]

AuNPs 1 were tested for the detection of analytes 4-8 via NMR chemosensing and proved to be able to recognize selectively salicylate, even when mixed to the other four molecules in equimolar concentration. The NOE-pumping experiment (Figure 28, d) allowed to extrapolate only the subset of signals of the recognized analyte, simplifying the ^{1}H-NMR spectrum (Figure 28, c), which would be otherwise very difficult to analyze due to the presence (and even superposition) of all the signals of every single molecule present in solution.

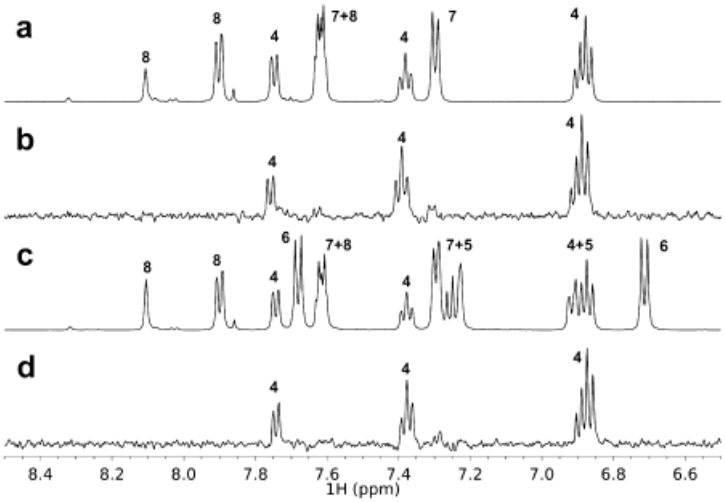

Figure 31: a) 1H-NMR of a mixture of molecules 4, 7 and 8 (7 mM, D_2O). b) NOE-pumping spectrum of the same sample in the presence of AuNPs 1 (1 mM in thiol). c) ^{1}H- NMR spectrum of a mixture of molecules 4-8 (7 mM in carbonate buffer 100 mM, pD = 10). d) NOE-pumping spectrum of the sample from c in the presence of AuNP 1 (70 µM)[24]

These results confirmed that with NOE-pumping experiments it is possible to effectively identify target molecules in complex mixtures. AuNPs 1 have a binding constant of 120 M^{-1} for salicylate, which allowed a detection limit of 2.5 mM for this analyte in carbonate buffer (pD = 10). As can be seen in Figure 32 the area of the analyte signals in the NOE-pumping spectrum correlates well with its concentration, making possible its simultaneous identification and quantification.

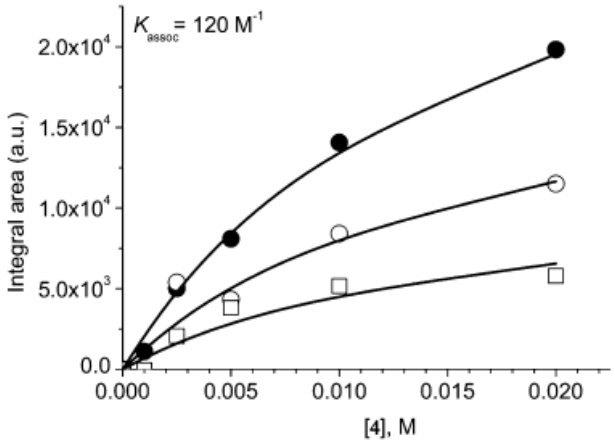

Figure 32: Relative area of the aromatic signals of 4 (black circle 6.8 ppm, white circle 7.4 ppm, square 7.75 ppm) in the NOE-pumping experiment as function of its concentration. AuNPs 1 (70 µM), carbonate buffer 100 mM, pD = 10[24]

Modifications in the thiol structure were then introduced to study their effect on affinity and selectivity of the system. Thiol 2, functionalized with a longer alkyl chain and a zwitterionic

phosphatidylcholine, was used as ligand to synthesize AuNPs 2, while AuNPs 3 were synthesized with just a longer alkyl chain but with the same triethylenglycol chain present also in AuNPs 1. With AuNPs 2 a decreased selectivity was observed, as it was possible to detect analyte 4 together with 7 and 8, while AuNPs 3 showed a selectivity in between that of AuNPs 1 and AuNPs 2. This behaviour demonstrated that both the size of the hydrophobic region and the specific interactions with the thiol headgroup affect the binding affinity. To demonstrate the applicability of chemosensing for the analysis of biological fluids, AuNPs 1 were used for the detection of salicylate in human urine at a concentration similar to those found after the administration of a standard dose of acetylsalicylic acid (Figure 33)

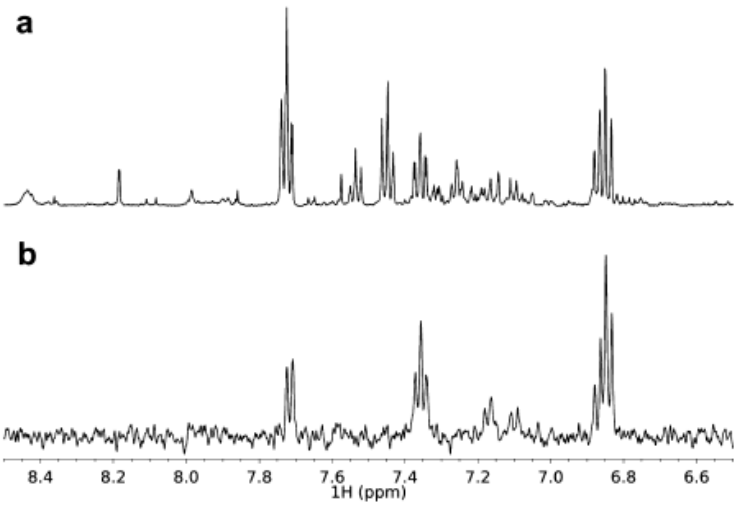

Figure 33: a) ^{1}H NMR spectrum of human urine containing sodium salicylate 5 mM, b) NOE-pumping spectrum of the same sample in presence of AuNPs 1 (70 µM).[24]

In a follow-up study, the effect of an increased binding affinity for the analytes on the NMR-chemosensing sensitivity was explored. Nanoparticles with different charged headgroups, 2 AuNPs and 4 AuNPs (Figure 34), were synthesized and compared with AuNPs 1.[39] The charged group was introduced to add a second effective interaction with the analyte (salicylate, negatively charged) other than the hydrophobic one already exploited in 1 AuNPs. 2 AuNPs proved to be effective for the detection of salicylate and allowed to detect its signals at lower concentrations (AuNPs 15 µM, salicylate 1 mM, S/N = 5.3). However, detection limit decreased only from 2.5 to 1 mM notwithstanding AuNPs 2 were able to bind salicylate with a K_a of $4*10^4$ M^{-1}, 2 order of magnitude greater than that of AuNPs 1 (120 M^{-1}).

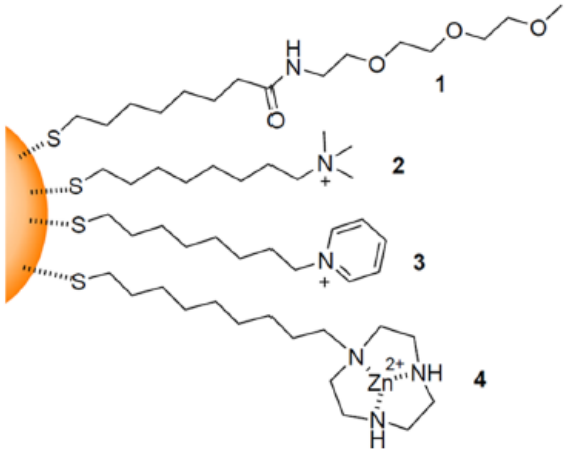

Figure 34: Second generation (2-4) of nanoreceptors for the detection of small organic anions

The observed affinity increase suggests that the ion pairing contribute was at least as effective as the hydrophobic interaction in the binding of the analyte. Indeed, repeating the same experiment in presence of acetate (having a negligible hydrophobic contribute) a K_a of 140 M^{-1} was found. A series of carboxylic acids with different chain lengths were used to explore further the concurrence of ion pairing and hydrophobic interaction and it was found that only in the case of sodium hexanoate it was possible to clearly detect all the signals of the analyte. Only some weak signals were present with sodium butyrrate and no signals at all were present in the NOE-pumping spectrum of sodium acetate, showing that the hydrophobic contribute of an alkyl chain at least 5 carbon atoms long was required for low concentration recognition. 2 AuNPs were also able to detect other anionic molecules more hydrophilic than salicylate, that were not detected by AuNPs 1 (Figure 35). Signal intensities followed the order 5 > 12 > 11 but a clear correlation to the hydrophobicity (logD) of the analytes was not observed, indicating that the interaction is more complex than a simple partition into a hydrophobic phase. 3 AuNPs and 4 AuNPs were synthesized to explore the possibility to detect hydrophilic carboxylates (such as acetate) at low concentration by NMR chemosensing, 4 AuNPs were able to effectively detect the analyte while with AuNPs 2 the signals were weak and completely absent with 3 AuNPs. The higher sensitivity of 4 AuNPs with respect to 2 and 3 AuNPs is likely to be caused by an additional metal-ligand coordination between carboxylates and Zn^{2+} ions. Cooperative binding of a carboxylate to two metal centers might also play a role. These nanoparticles were able to detect both the anionic molecules of the set (acetate, 6 and dimethylphosphate, 13).

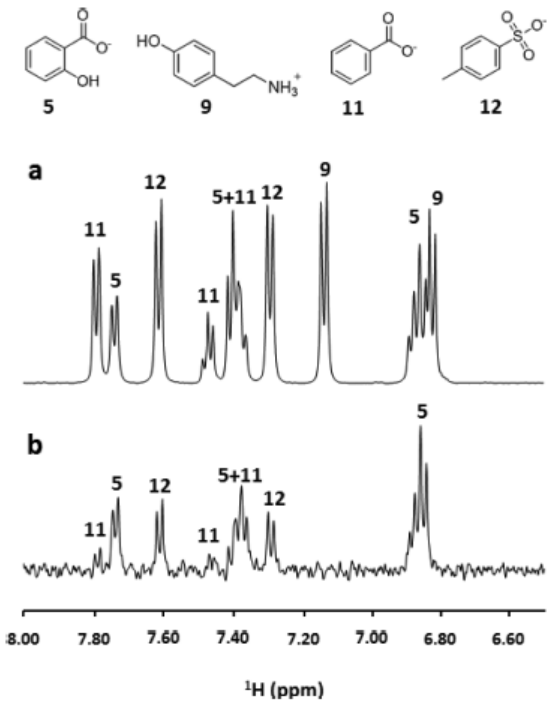

Figure 35: a) [1]H NMR of a mixture of analytes 5-12 (2 mM each) with AuNPs 2 (15 µM) in HEPES buffer 10 mM, pD = 7.0

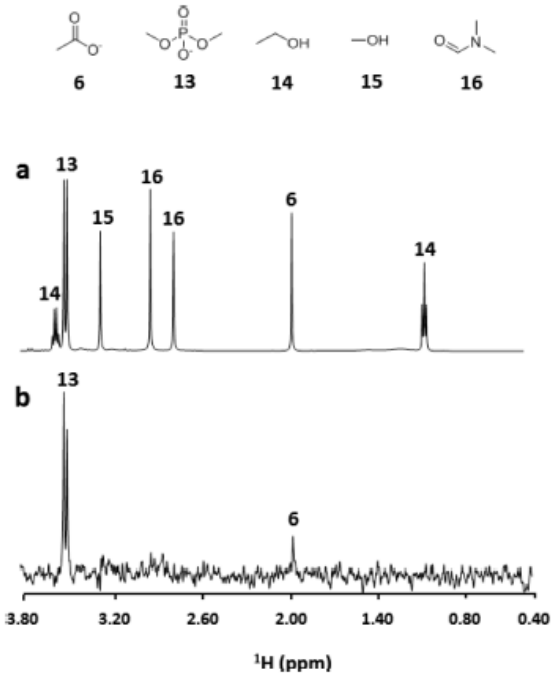

Figure 36: a) [1]H NMR spectrum of analytes 6, 13, 14, 15 and 16 10 mM each in D_2O, b) NOE-pumping CPMGz spectrum of the same sample in the presence of 4 AuNPs (15 µM)[39]

By modification of the thiols, nanoreceptors with different selectivity were developed: AuNPs 1 were effective for hydrophobic species, 2 AuNPs for moderately (and highly) hydrophobic

organic anions and 4 AuNPs for highly hydrophilic organic anions. 2 AuNPs were effectively used also to discriminate the analytes via 2D DOSY based "NMR-chromatography" (Figure 37). NMR chemosensors for the detection of organic cations have also been developed.[26] This time, at difference from the receptors previously described where the binding pockets are self-assembled during the nanoparticles functionalization, pre-synthesized organic receptors (crown ethers) were employed and grafted to AuNPs through the same amide linker used in the previous systems (Figure 38).

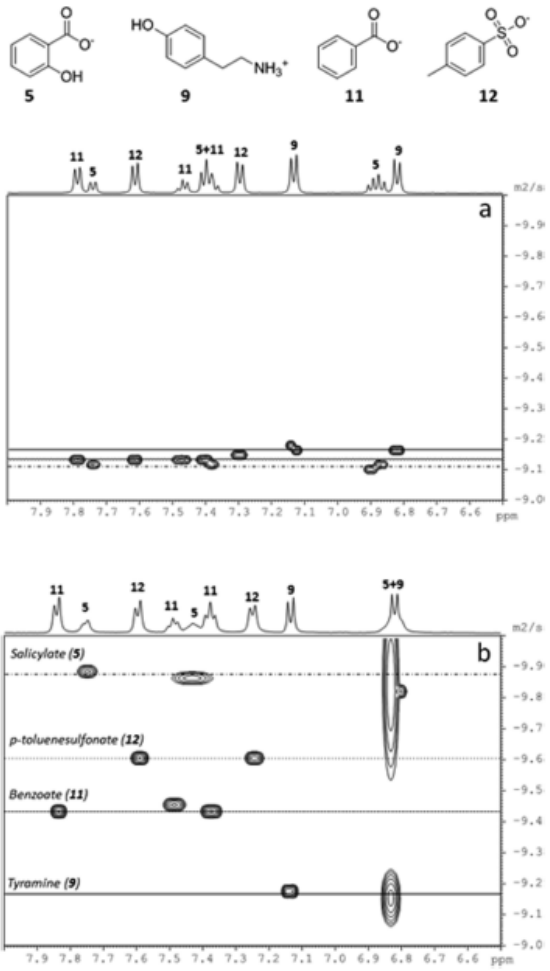

Figure 37: DOSY experiments performed on a mixture of analytes 5, 9, 11 and 12 in absence (a) or in presence (b) of AuNPs 2 (90 μM) in HEPES buffer 10 mM, pD = 7.0.[39]

18-crown-6 was chosen as it is a well-known receptor able to bind ammonium and protonated primary amines, forming three NH^+-O hydrogen bonds. This nanoreceptor (crown AuNPs) selectively detected analyte 2 from the substrates set 2-8 (Figure 39). The selectivity of crown AuNPs resulted to be even greater than that of the crown ether in the free state, and even α-aminoacids were not detected by the nanoparticles. This improved selectivity is

likely to be caused by steric effects of the analyte substituents which are amplified by the crowding of the crown ether moieties on the nanoparticle surface.

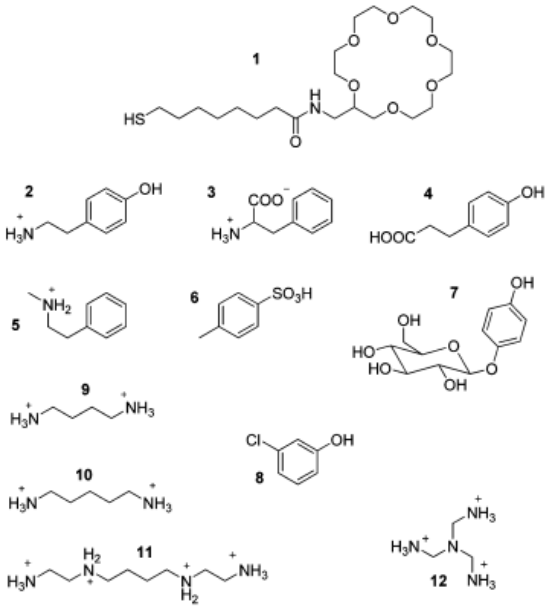

Figure 38: crown ether thiol (1) employed in the synthesis of crown NPs and the substrates tested.[26]

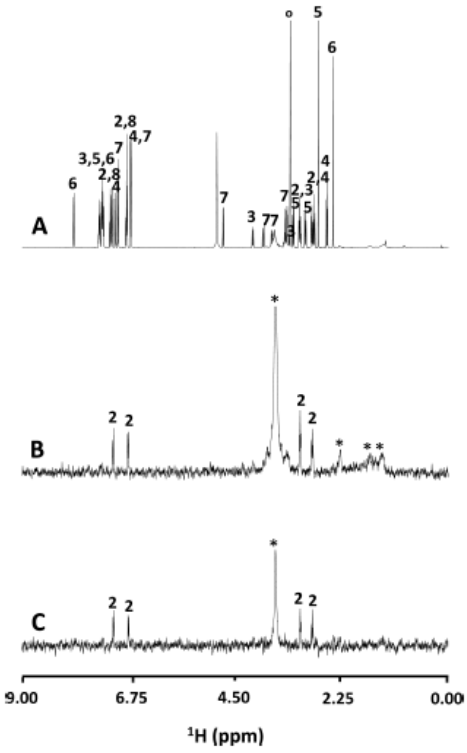

Figure 39: A) ^{1}H NMR of a mixture of compounds 2-8 10 mM each in MeOD. B) NOE- pumping spectrum of the same sample in presence of crown AuNPs (29 µM). C) NOE-pumping CPMGz spectrum of the same sample as in B.[26]

Indeed, the K_a for substrate 2 resulted to be $1.6*10^{-2}$ M^{-1}, an order of magnitude smaller than that of the free crown ether. The signals of the alkyl protons of substrate 2 resulted broader than those of the aromatic ring which suggest that the alkylammonium portion is closer to the nanoparticle than the aromatic one, as it is expected in a typical interaction with a crown ether. When the experiments were repeated in presence of a base (DBU), tyramine signals were no longer visible in the NOE-pumping spectrum confirming the need for a protonated primary amine. Diamines 9 and 10 were detected by the system with a lower detection limit. The affinity constant was higher with respect to that of substrate 2 but decreased to similar values when the analytes were in a mono-protonated state, demonstrating an interaction of one diamine with two crown ethers (1:2) when both the amines of the analyte are protonated. The higher sensitivity for diamines is likely caused by a closer spatial proximity of their spins with those of the crown ether moiety, and by longer residence times of the guest inside the monolayer, which both lead to increased magnetization transfer by NOE. Chemosensors for the detection of amphiphilic organic cations in water, in particular for phenethylamine derivatives (designer drugs), were also developed by exploiting both ion pairing and hydrophobic interactions.[25] Thiols bearing a negative charge, provided by a sulfonate group, and an hydrophobic chain were employed (Figure 40, S1-S4). The hydrophobic portion was modified in S2, S3 and S4 to explore its effect on the system selectivity (the dimethylsilane group in S4 was introduced for STD purposes, which will be discussed in a later chapter).

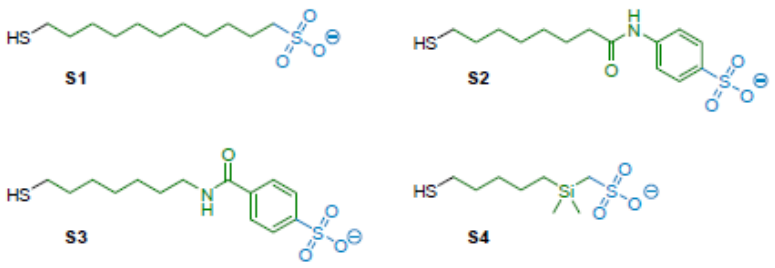

Figure 40: Thiols employed for the development of nanoreceptors for amphiphilic organic cations

S1-AuNPs detected all the phenethylamine derivatives tested (Figure 41) with association constants in the range 10^5-10^6 M. No signals were detected from molecules not having a cationic head group (except phloretic acid, probably recognized by hydrophobic interactions only).

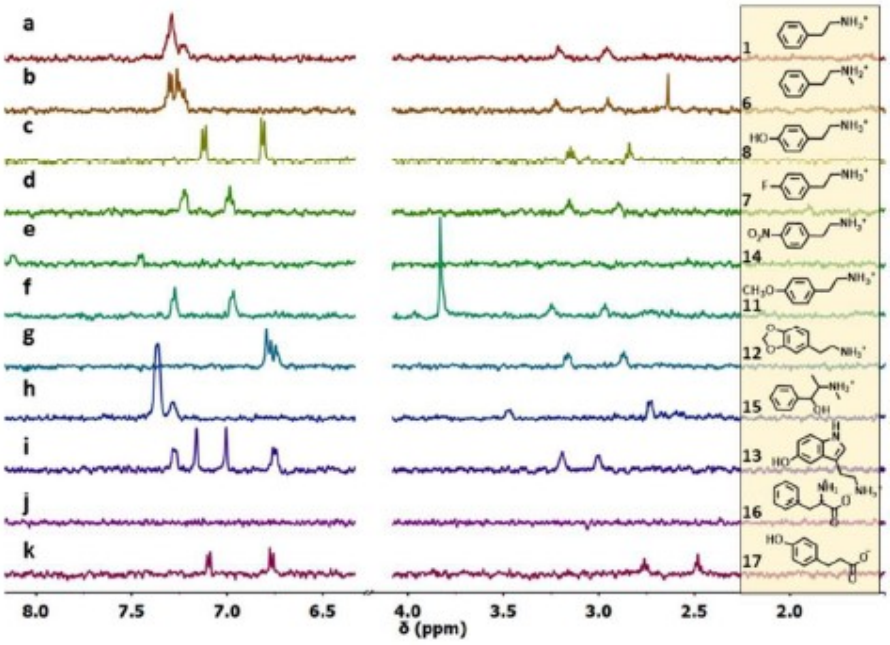

Figure 41: NOE pumping experiments with S1-AuNPs (1 mM in thiol) on several phenethylamine derivatives (2 mM) in HEPES buffer (10 mM), D_2O[40]

A linear correlation was found between the binding constants (K_a) and the n-octanol/water partition coefficients (logD at pH 7.4) of the analytes, demonstrating that the interaction is modulated by hydrophobicity. Modification of the hydrophobic portion in thiols S2-S4 always led to a decrease of the affinity constant with respect to S1-AuNPs, without affecting the correlation between K_a and logD. Therefore, the decrease in affinity is likely to be caused by a weaker ion pairing interaction with the analytes due to a decrease in charge density on the sulfonate groups. In S2-AuNPs a stronger sensitivity to analyte hydrophobicity was observed, demonstrating that the presence of an aromatic residue can increase the stabilization of the hydrophobic interactions, increasing their relative weight in the energetics of the binding event and allowing to tune the selectivity of such systems. S2-AuNPs proved to be able to detect N-methylphenethylamine (2 mM) in a hypothetical designer drug tablet containing phenylalanine (2 mM) as a masking agent and glucose (20 mM) as a possible excipient (Figure 42). The system was able to identify MDMA (the active component of ecstasy) also in a real seized “street” sample (Figure 42) proving that NMR-chemosensing is an effective method for the analysis of designer drugs in a real-world scenario.

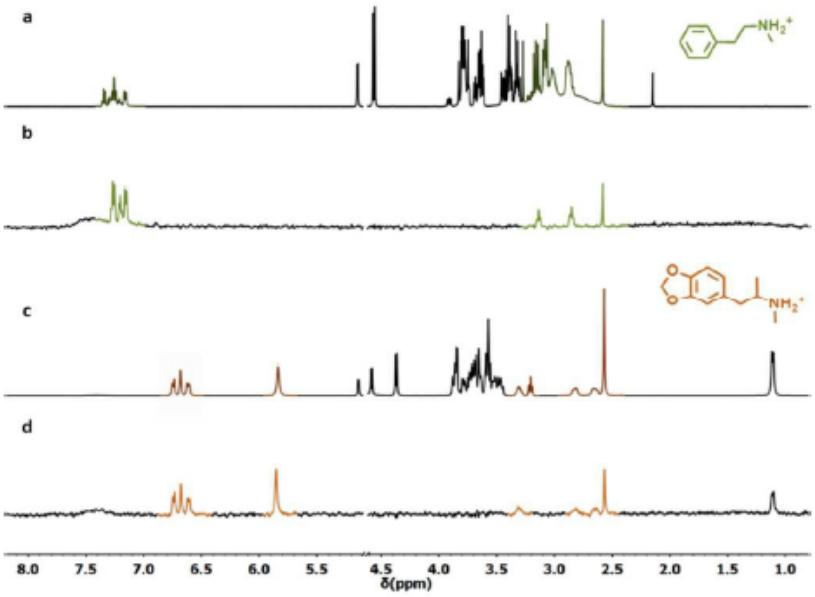

Figure 42: NMR-chemosensing of designer drugs; a) ^{1}H-NMR spectrum of N-methylphenethylamine hydrochloride (2 mM), phenylalanine (2 mM) and glucose (20 mM) in D_2O, b) NOE-pumping CPMGz spectrum of the same sample in presence of S2-AuNPs (3072 scan, 4h), c) ^{1}H-NMR spectrum of a drug tablet dissolved in D_2O, d) NOE-pumping CPMGz spectrum of the same sample in presence of S2-AuNPs (3072 scan, 4h). S2-AuNPs 1 mM (in thiol), HEPES buffer 10 mM, pD = 7.0.[40]

NOE-pumping experiment

The NOE-pumping is an experiment based on a pulse sequence originally developed by Shapiro in the framework of drug discovery for the screening of drug candidates capable of binding macromolecules.[41] This sequence relies on the significative decrease of the observed translational diffusion coefficient of small molecules when these interact with relatively large macromolecules. This decrease happens because the observed translational coefficient is the weighted average of the translational coefficients of the free and bound species. The larger the fraction of bound ligand it is, the lower the observed diffusion coefficient will be. This phenomenon can be exploited by the use of a diffusion filter which dephases selectively the magnetization of small molecules depending on their observed diffusion coefficient. If a cut-off which separates the macromolecules from the small molecules in solution is employed, then a situation where only the supramolecular nanoreceptors are magnetized can be reached. After the application of the filter, the previously dephased small molecules which interact with the nanoreceptors are progressively re-magnetized via NOE. A fast guest turnover on the receptor surface leads to an increased amount of magnetization transferred to the free analyte population, the receptor works therefore as a signal amplifier. As the

detected analytes are now magnetized, all their signals are recorded with the acquisition of the FID. A scheme of the pulse sequence can be seen in Figure 43. If the residual magnetization on the supramolecular systems needs to be removed, for example when the nanoparticle-originated signals are superimposed with those of the analytes and interfere with the data analysis, it is possible to apply a CPMGz filter in sequence after the NOE-pumping (Figure 43, below). This filter removes the signals from the fast relaxing species[42] and the FID now recorded will contain only signals from the small interacting molecules.

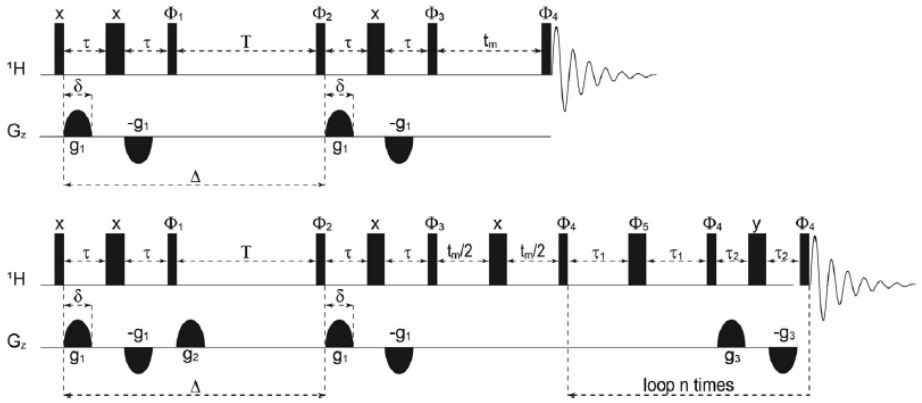

Figure 43: Pulse sequences for NOE-pumping[41] (above) and NOE-CPMGz[42] (below)

NOE-pumping based NMR-chemosensing

NOE pumping can be used for nanoparticles assisted NMR chemosensing if nanoparticle-based receptors of tailed selectivity are used in place of the proteins originally used by Shapiro.

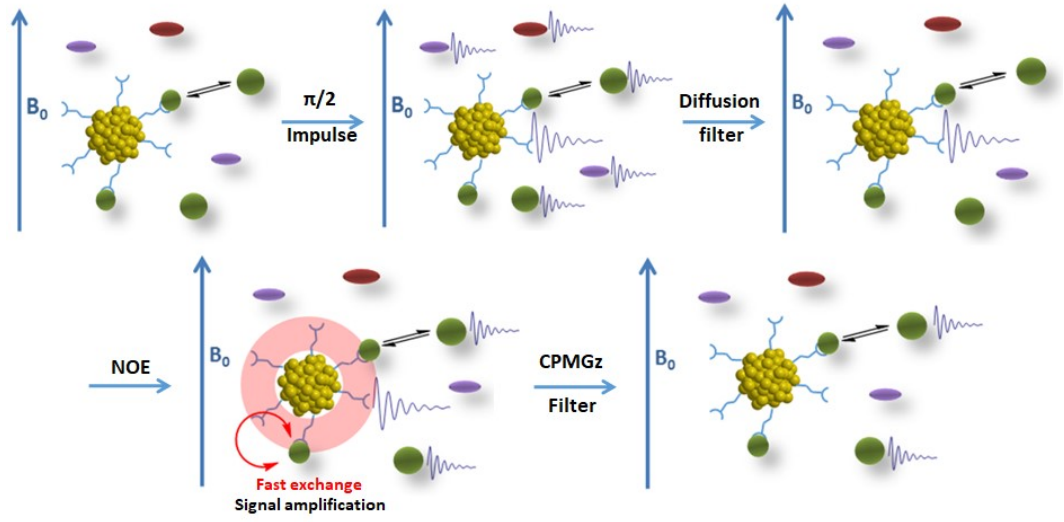

Figure 44: NOE-pumping based NMR-chemosensing experiment scheme

The NMR-chemosensing experiment is schematized in Figure 44. As can be seen, what happens overall in the sample during the experiment is that only a subset of the molecules present in solution is magnetized. From a very complex mixture it is therefore possible to acquire a clean spectrum of the nanoreceptor guests (green in Figure 44), which allow not only to quantify but also to fully identify the species detected.

STD experiments based NMR-chemosensing

STD has been originally developed in drug discovery to study the interaction between small analytes and relatively large macromolecules.[43] If resonances of the macromolecule (which are not superimposed with the analytes ones) are saturated with an appropriate rf pulse, then the accumulated saturation can be transferred to the interacting molecules (Figure 45).

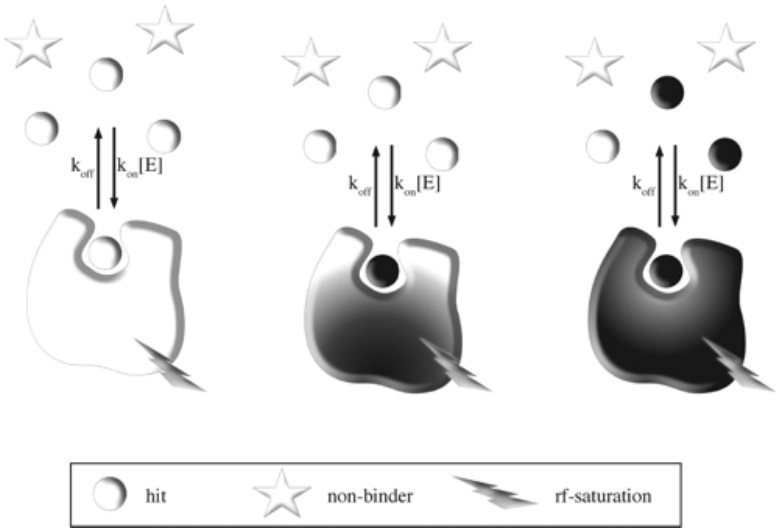

Figure 45: saturation transfer during rf irradiation[43]

By subtraction between two spectra where in the first the macromolecule is saturated and in the second the rf pulse is sent in a region where no resonances are present, it is possible to reach a similar situation to NOE-pumping experiments where only signals of interacting molecules appear (Figure 46). However, thanks to the active saturation of the receptor resonances, signals much more intense can be recorded. While NOE-pumping NMR-chemosensing is very effective when it comes to analyze a complex mixture it is also true that this technique suffers from low sensitivity, an issue generally shared between NMR-based techniques. A single analysis performed with a diffusion filter-based sequence can take several hours in order to have a sufficient signal to noise ratio to allow an analysis to be performed, and the detection limit is at the best around 500 µM for a 4h experiment. Saturation Transfer Difference can be combined to NMR-chemosensing to positively affect

the sensitivity of the technique. This was demonstrated in the development of NMR-chemosensors for the detection of amphiphilic organic cations (designer drugs) in water.[25] Nanoparticles functionalized with S1-S3 (**Errore. L'origine riferimento non è stata trovata.**) were developed for the detection of these analytes via NOE pumping experiments, as explained in an earlier chapter, but a decrease in the limit of detection was needed for the analysis of biological samples.

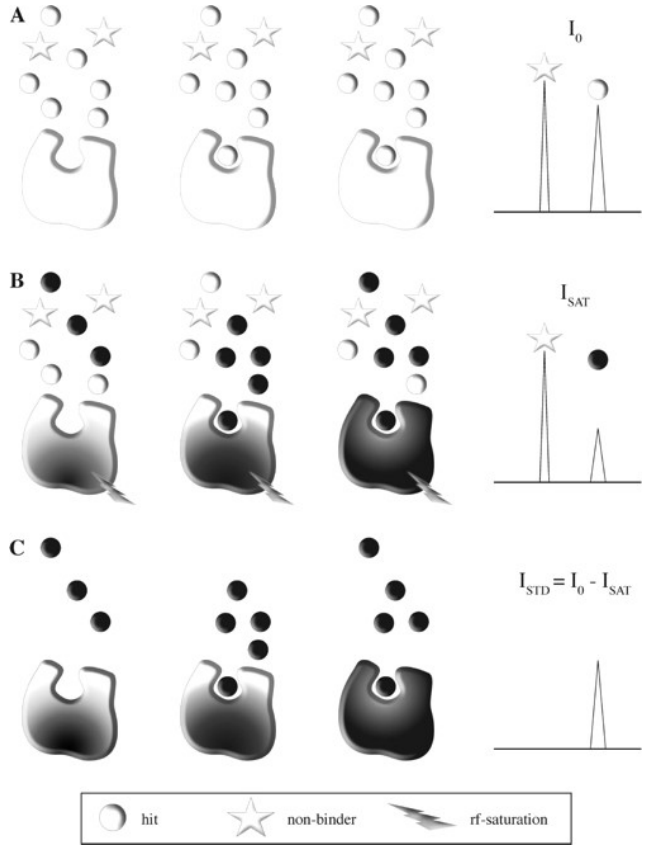

Figure 46: STD experiment scheme[43]. A) off-resonance spectrum, B) on-resonance spectrum, C) difference spectrum (A-B)

Thiol S4 was therefore designed as an analog of S1 bearing a methylsilyl group, which can be saturated without affecting the analyte resonances, thanks to its characteristic signals at 0.1 ppm, in a region where no signal overlapping with the analytes can be observed. With this thiol it was possible to functionalize AuNPs for STD experiments. While this modification caused a relatively small decrease in the affinity for the analytes, probably caused by a decrease of the charge density on the sulfonate group, moving from NOE-pumping experiments to STD ones improved the sensitivity of the NMR-chemosensing technique, decreasing the limit of detection from around 500 µM to 30 µM.

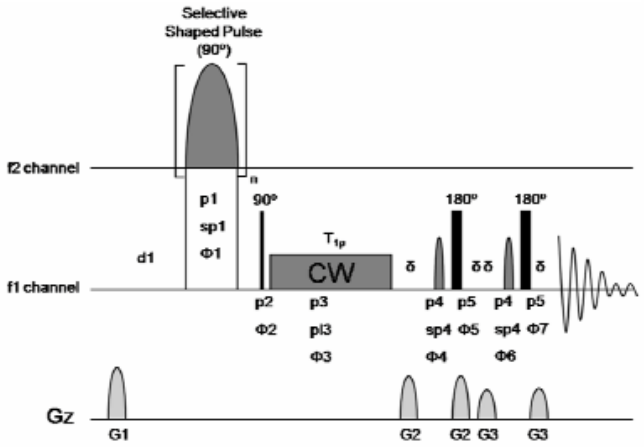

Figure 47: STD pulse sequence form NMRGuide4.0, Bruker BioSpin, 2004.

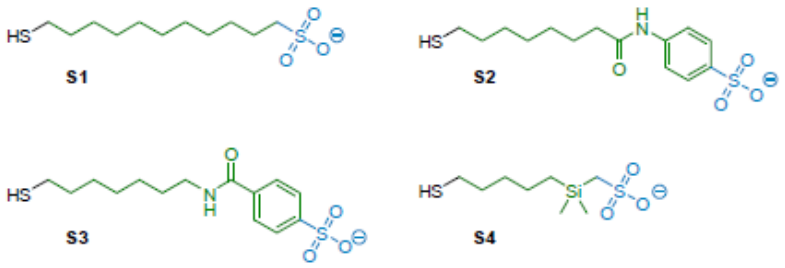

Figure 48: AuNPs developed for the detection of amphiphilic organic cations.[25]

As can be seen in Figure 49, the area of the analyte signals was linearly proportional to its concentration, allowing its quantification. It should be noticed that the signals of the analyte are completely undetectable in the proton spectrum (a, Figure 49) as they are superimposed with the phenylalanine ones, which is present at a concentration 20 times higher. A drawback of this technique, with respect to NOE pumping, is that being based on a spectra subtraction, subtraction errors can affect the experiment. STD-experiments, and partially also NOE-pumping ones, have also limitations when the binding constant is very high or very low. With high affinity ligands (k_{off} = 0.1 – 0.01 s^{-1}) there is no fast exchange of guest molecules on the nanoparticle surface and saturation cannot be transferred effectively to the free analyte population, leading to very weak detected signals. Small ligands bound to a receptor have also a faster relaxation rate than those in the free state and the guest has therefore to detach from the receptor rapidly enough not to lose all of its magnetization. Assuming k_{on} to be diffusion-limited, the lower K_D limit for STD is 10^{-8} M. When the binding constant is very low, however, the amount of bound ligand is too low to generate strong enough STD signals to be detected. Indeed, in order to have intense STD signals k_{off} should be large enough to allow

fast exchange but not too large to leave the binding site too soon to receive enough saturation.

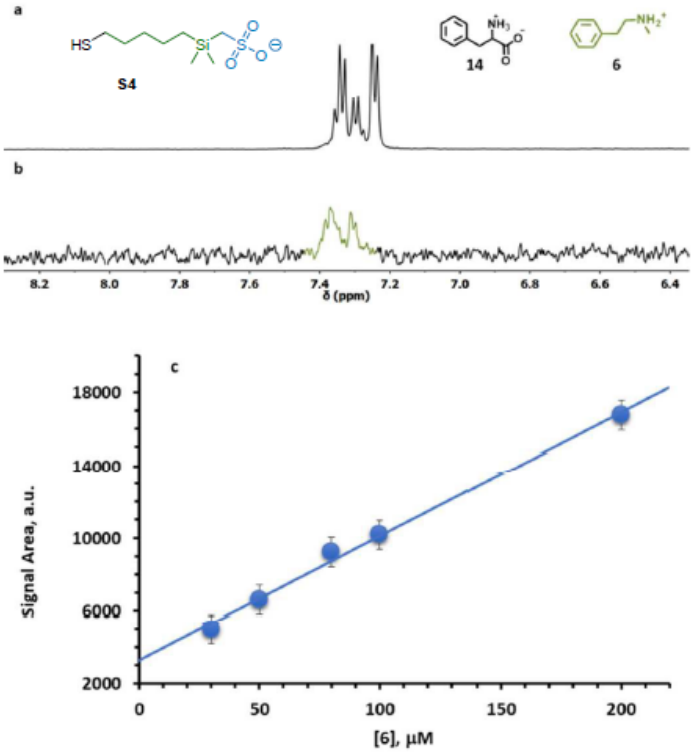

Figure 49: STD experiments with S4-AuNPs for the detection of N-methylphenethylamine (6, 50 µM) and phenylalanine (14, 1 mM) in HEPES buffer (pD = 7.0); a) 1H NMR spectrum, b) STD experiment (1024 scan, 3h) in presence of S4-AuNPs (1 mM in thiol), c) plot of the integrated signal area of the aromatic signals of 6 in the STD spectra.[25]

If k_{on} is diffusion controlled then the upper K_D limit for STD is 10^{-3} M.[44] In addition, the average number of analytes saturated per molecule of receptor (at a determined saturation time) can be calculated as STD amplification factor (A_{STD}).

$$A_{STD} = \frac{I_0 - I_{sat}}{I_0} * (\frac{L}{P} molar\ ratio)$$

Where [L] is the concentration of guest and [P] is the concentration of host. Again, to have a significant amplification we need a significant number of bound molecules. As a consequence, the best setting found so far for the STD detection of analytes at low (50 mM) concentration is the use of supramolecular nanoreceptors with high affinity at relatively low concentration. Indeed, elevated ones would increase the analyte bound fraction which would lead to a broadening of the recorded analyte signals. Note however that the efficiency of STD experiments depends not only on the free and bound analyte populations but also on the magnetization transfer efficiency from the receptor itself.[45]

High-Power Saturation (HP wSTD)

NOE pumping and STD are not the only NMR experiments developed for drug discovery. Another ones is the water-LOGSY (Water-Ligand Observation with Gradient SpectroscopY) experiment.[46] Here, the spins of the water molecules are used as magnetization source for the nanoreceptors. Consequentely, the solvent used is actually 90% protonated water and only 10% deuterium oxide. The pulse sequence used for water-LOGSY consists of a selective 1D NOESY on water with additional solvent suppression (double pulsed field gradient perfect-echo). The resonances of binding and non-binding analytes have opposite signs depending on their interaction with the water molecules. The magnetization transfer in water-LOGSY is most efficient for analytes in early-binding as the magnetization drops significantly due to relaxation in the case of late binding events. This is a disadvantage with respect to STD, where, instead, any binding event generates the same signal enhancement after the monolayer is saturated.[45] Yet, waterLOGSY is reported to be more sensitive than STD.

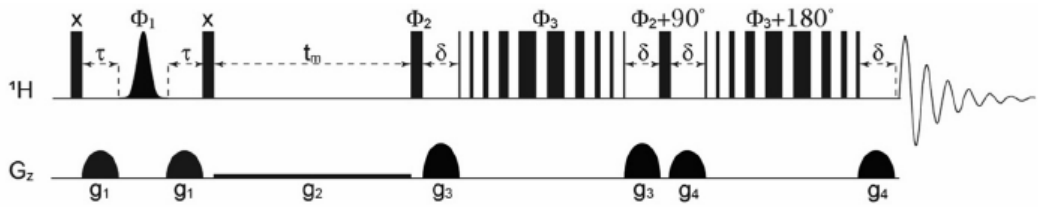

Figure 50: e-PHOGSY pulse sequence for water-LOGSY experiments[45]

An alternative to waterLOGSY is water-STD. In this technique the signals which are saturated are the ones of water molecules (solvent, also in this case a mixture of H_2O/D_2O 9:1 is used) instead of the nanoparticle resonances, as it was the case in standard STD experiments.[45] The experiment consists in the acquisition of multiple spectra with saturation alternately on and off-resonance on water signals. A train of 50 ms Gaussian shaped rf pulses is utilized with the power calibrated to deliver a 180° rotation. This rf pulse allows to selectively saturate the resonances close to the rf carrier and therefore only those of the solvent (water). The experiment incorporates then a solvent-suppression sequence (DPFG-"perfect echo" (PE) with W5 clusters as refocusing element) to remove the very intense signal of the saturated water. The PE allows to eliminate the antiphase magnetization, reducing the subtraction artifacts and improving the line shape. In general, similar signal enhancement to those obtained with water-LOGSY experiments can be recorded. The advantage of water-STD over water-LOGSY is that in this experiment any binding event generates the same enhancement regardless of the early or late nature of the analyte binding event.

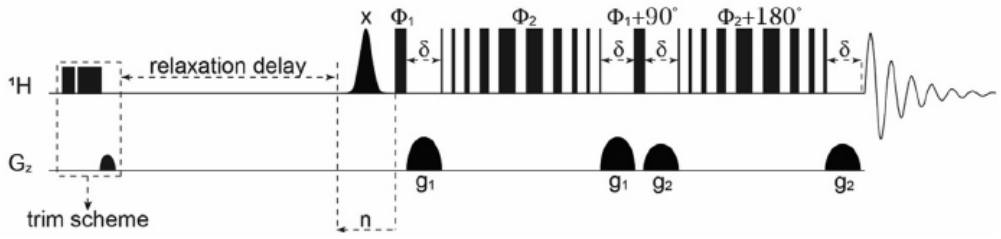

Figure 51: STD pulse sequence for wSTD[20]

When applied to nanoparticle-assisted NMR chemosensing, both the water-LOGSY and the wSTD experiments did provide substantial advantages over STD. The main limitation of both these protocols is the different sign that analyte signals can have in the recorded spectra as this could result in the cancellation of superimposed signals. These techniques can therefore be affected by false negatives: an analyte could remain undetected even if present in a sufficiently high concentration if its signals are cancelled out by a superimposed signal of a second species. This problem was addressed by increasing the power of the Gaussian pulses in the water-STD experiment. In this way, each pulse will have decreased selectivity generating a "leak" of rf which can cause partial saturation of the analyte signals. This affects primarily weak signals of non-interacting analytes, while the effect on the signals of interacting species is negligible.[45] This rf "leak" can also saturate the nanoparticle monolayer increasing the amount of magnetization which can be transferred to the analyte molecules. HP wSTD allows the recording of spectra with an increased signal intensity in the order of 300% with respect to water-LOGSY and water-STD, and to reach these results it requires only acquisition times of 10 minutes.[45] The sensitivity of this technique allow the detection of analytes down in the micromolar range. An excessive amount of saturation of the analytes should be avoided though as this might lead to the appearance of false positives.

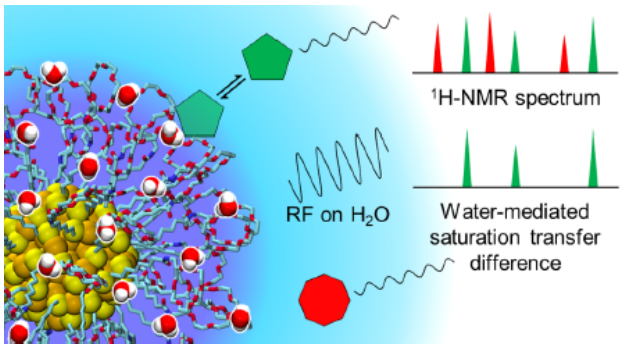

Figure 52: High power water-mediated Saturation Transfer Difference experiment

Additionally, the benefits of STD and water-STD techniques can be combined by splitting the saturating pulse in two sidebands. One of the pulses is used to saturate the water molecules

while the other is placed close to resonances of the organic monolayer, for example on the resonances of the thiol alkyl chain. The application of such saturation method increases the signal to noise ratio even further with respect to water-STD.[45] This protocol was effectively tested using anionic nanoparticles early developed for designer drug sensing. In a proof-of-concept experiments, 3-AuNPs (Figure 53) could selectively detect serotonin at 50 µM concentration in the presence of 50 µM phenylalanine.

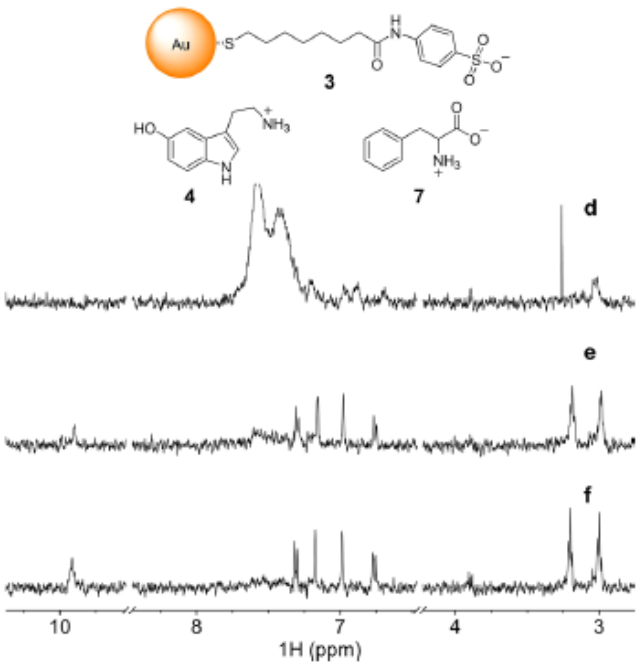

Figure 53: HP water-STD spectra of 50 µM serotonin (4) and 50 µM phenylalanine (7) with (d) 500 µM 3-AuNPs, (e) 50 µM 3-AuNPs and (f) 25 µM 3-AuNPs. Solvent medium is H2O/D2O = 90/10 with 10 mM phosphate buffer.[45]

Hybrid nanoreceptors for NMR-chemosensing (HP wSTD)

The optimization of the NMR protocol is not the only possible approach to increase the sensitivity of NMR detection. For example, stronger STD signals can be in principle recorded if the size of the nanoreceptor is increased. Indeed, the efficiency of magnetization transfer through NOE increases with the decrease of the tumbling rate of the nanosystem.[47] Using monolayer-protected gold nanoparticles of larger size though is not a viable option as the increased packing of the ligands would prevent the binding of the analytes (see earlier). A new strategy to increase the size of the nanoreceptor, avoiding these issues, has been developed by deposition of charged thiol-protected gold nanoparticles on bigger silica nanoparticles bearing superficial charges of the opposite sign.[47] These systems, without requiring any further synthetic effort, combine the currently employed 1.8 nm gold

nanoparticles for NMR-chemosensing and commercial 17 nm LUDOX (HS or CL, depending on the charge required) silica nanoparticles, which can be dispersed in water and mixed directly in the NMR tube. In this way it was possible to combine the recognition properties of the functionalized gold nanoparticles with the decrease in tumbling rate provided by the rigid silica support, leading to a significative decrease in the analyte detection limit, down to around 10 µM when used for HP wSTD experiments.

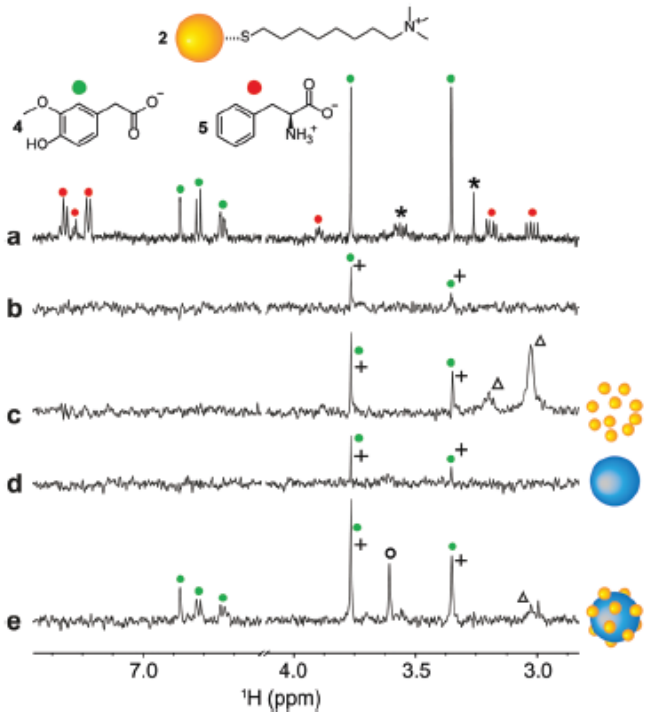

Figure 54: a) ^{1}H NMR spectrum of homovanillic acid 10 µM and L-phenylalanine 10 µM in $H_2O:D_2O$ = 90:10; (b-e) HP wSTD spectra (4k scans, 4h acquisition time); b) in absence of nanoparticles; c) in presence of AuNPs 20 µM in thiol; d) in presence of LUDOX HS, e) in presence of the nanoconjugates.[47]

Para-hydrogen hyperpolarization

One of the main issues of NMR-based techniques is their intrinsic low sensitivity. This is caused by the fact that the energy of nuclear magnetic moments in a field smaller than 10^4 T is smaller than the total thermal energy of the system at room temperature. The magnetic moments are nearly randomly oriented with respect to the applied magnetic field cancelling each other out and decreasing the recordable signal to only few parts per million of the potentially available one.[48] Non-Boltzmann spin populations can be artificially produced by taking advantage of hyperpolarization. Several hyperpolarization-based techniques have been recently developed which allow to record NMR signals with a massive increase in intensity, up to several orders of magnitude with respect to standard equilibrium

experiments. These non-equilibrium populations can be reached by different strategies such as: dynamic nuclear polarization (DNP)[49], optical pumping and hydrogenative p-H_2 induced polarization (PHIP).[50] The aim of hyperpolarization-based strategies is the creation of fast bursts of hyperpolarized substrate which can be rapidly analyzed with an increased sensitivity. Such methodologies are attracting a lot of interest not only for chemical applications, hyperpolarization-based techniques can be conveniently exploited also for in-vivo MRI imaging, which is of fundamental importance for biomedical purposes.

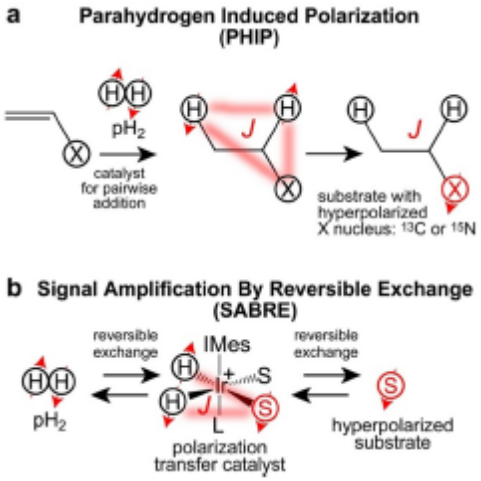

Figure 55 PHIP and SABRE[50]

If the analyte bears insaturations which can be hydrogenated, then PHIP can be chosen as hyperpolarization technique. When p-H_2, in its singlet state, is added in a pairwise way to an insaturation of an asymmetric molecule (as schematized in Figure 55 a), the symmetry of the hydrogen nuclei in the reaction product is broken and this causes an enhanced nuclear spin polarization, called hyperpolarization.[51–53] The polarization can be intramolecularly transferred via spin-spin coupling from the parahydrogen protons to other proton resonances or even to other nuclei, such as ^{13}C.[54]. While being a powerful technique, the main limitation of PHIP is the requirement for a chemical modification of the substrate, which has to take part in an irreversible addition of p-H_2. This requirement limits the applicability of the technique only to a small number of molecules and, by exploiting an irreversible chemical reaction, only a limited number of experiments can be performed on a single sample. For this reason PHIP is not suitable for multidimensional NMR experiments.

SABRE

A non-hydrogenative p-H_2 based hyperpolarization strategy, which allow to overcome many PHIP limitations, has been recently developed and called Signal Amplification by Reversible Exchange (SABRE).[55–57] SABRE is a very powerful strategy which allow to reversibly hyperpolarize a great number of analytes starting from para-hydrogen by using an hydrogenation catalyst as hyperpolarization transfer agent (Figure 55 b). As soon as the p-H_2 gas is introduced in the sample the catalyst reacts with it and the hyperpolarization can be transferred from the two hydrides generated by oxidative addition to other ligands of the hyperpolarization catalyst. If the analyte is able to act as ligand for the metal centre it is therefore possible to hyperpolarize it. Both ligand exchange and oxidative addition processes are reversible and can be repeated over and over without degradation. Depending on the applied magnetic field during the hyperpolarization step, which can be experimentally set in a relatively easy way, it is possible to enable polarization transfer to several different heteronuclei of the analyte. By applying magnetic fields in the millitesla range it is possible to hyperpolarize ^{1}H nuclei, while decreasing the field in the microtesla region enable polarization transfer to heteronuclei such as: ^{13}C [58], ^{15}N [59], ^{19}F [60], ^{31}P [61], ^{29}Si [62] and others.

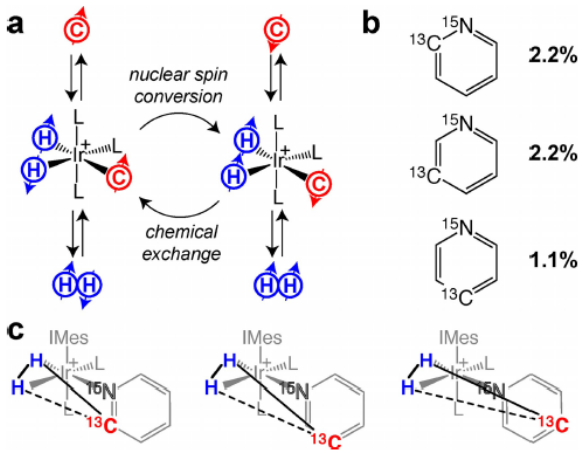

Figure 56: a) coherent transfer of spin order from parahydrogen-derived hydride protons to ^{13}C heteronuclei via SABRE; b) natural abundance of ^{13}C in ^{15}N labelled pyridine; c) most probable structures responsible for the polarization transfer. [58]

Thanks to the gain in sensitivity, by employing SABRE, it is possible in just 81 seconds to perform experiments which would otherwise require 20 h of acquisition time with standard thermal polarization.[63] This massive increase in sensitivity opens the door to the use of NMR for detection of trace analytes. Catalysts having a high ligand exchange rate should be employed to maximize the signal enhancement. As an example, for the hyperpolarization of pyridine with Ir-based catalysts, moving from Crabtree's catalyst [Ir(COD)(PCy_3)(py)][BF_4][64],

where a phosphine spectator ligand is employed, to a complex where this is replaced by Imes [Ir(COD)(IMes)Cl][65] (Figure 57), the stronger sigma-donating capability of the latter leads to a faster pyridine exchange rate. This increased the recorded signal intensity gain from more than two order of magnitude in the former case to more than three in the latter. The magnitude of pyridine ^{1}H signals obtained with Imes catalyst reached an impressive 8600-fold enhancement over standard proton experiments.

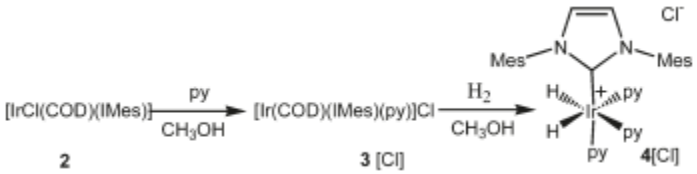

Figure 57: in-situ formation of the actual hyperpolarization catalyst (4)[65]

The development of effective catalysts which can simultaneously interact with the analytes in a fast exchange regime and easily react with hydrogen is therefore of fundamental importance. It has been demonstrated that SABRE can be used for the quantification of trace molecules[66] and applications in analytical chemistry are currently being developed. Several molecules have already been successfully detected with this technique, such as piperazine derivatives (designer drugs)[67] and molecules of biomedical interest in biological fluids, such as drugs[68] and tagged oligopeptides.[69] High-throughput continuous-flow systems have also been developed for the application of SABRE in analytical chemistry.[70]

Analytes of interest

NMR-chemosensing has already been successfully applied to the detection of small organic anions[22,39], primary amines[24] and designer drugs[25]. Thanks to its intrinsic capability to analyze complex mixtures, NMR-chemosensing could be a powerful technique to investigate biological fluids for medical purposes. Dopamine is a biologically relevant small molecule, it is synthesized in the human body from tyrosine degradation by three different pathways (Figure 58).[71]

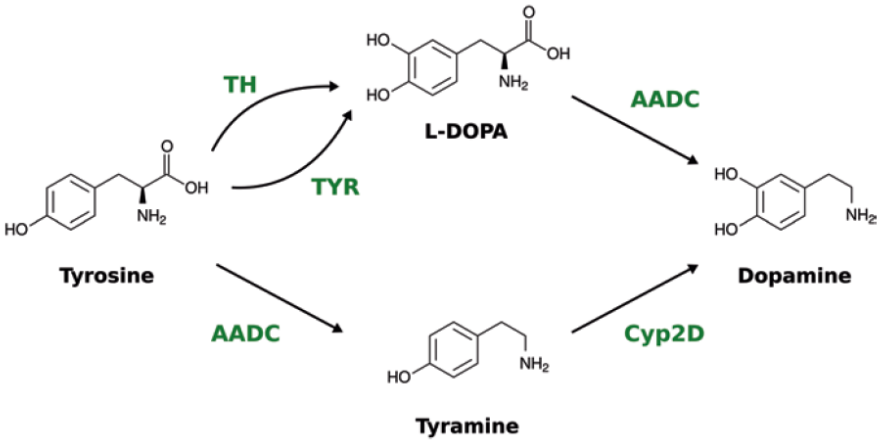

Figure 58: dopamine biosynthesis[71]

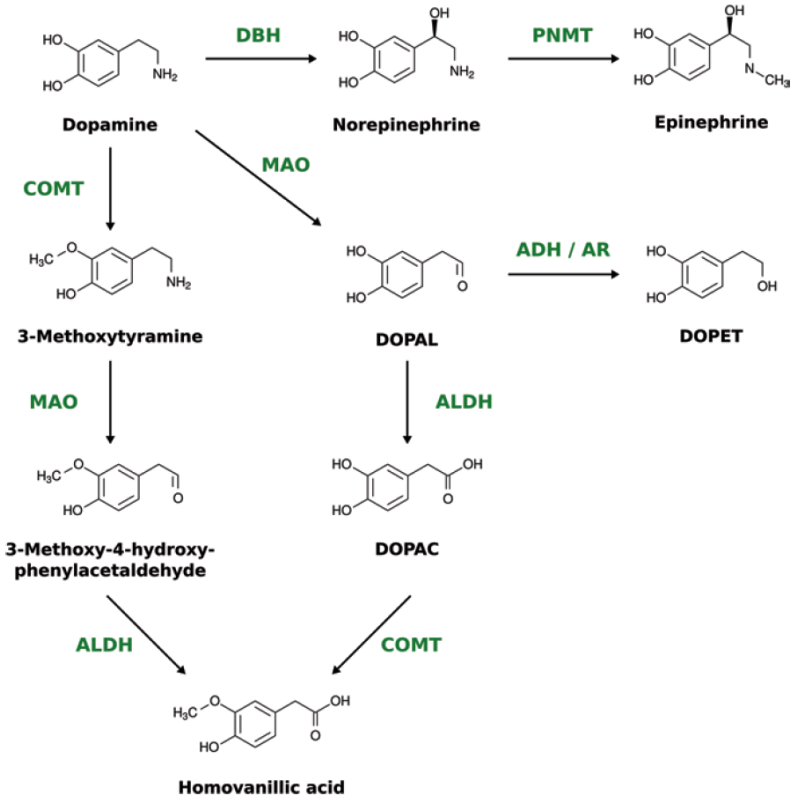

Figure 59: dopamine degradation[71]

Several metabolites are derived from the degradation of this molecule (Figure 59).[71] Some of these species have recently gained attention in biomedicine as they were proven to be useful biomarkers for the diagnosis of both cancer and metabolic disorders. Neuroblastoma is a neoplasm of the sympathetic nervous system, it is the most common solid tumour in infancy and the second most common extracranial malignant tumour of childhood.[72] Homovanillic acid (HVA, Figure 60) has been proposed as biomarker for neuroblastoma[73] and

functionalized nanoparticles for NMR-chemosensing with the ability to detect this molecule[74] and phenethylamines[40] in water have already been developed.

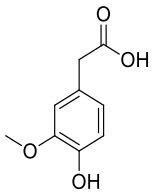

Figure 60: homovanillic acid

It has been found also that elevated levels of 3-methoxytyramine (MeOTyr, Figure 61) in the urine is a prognostic biomarker for the identification of neuroblastoma patients with poor clinical outcome.[75] This metabolite has therefore been chosen as analyte of interest and this work is aimed to the development of an effective receptor for the detection of this target via NMR-chemosensing.

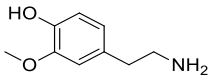

Figure 61: 3-methoxytyramine

Sarcosine (Figure 62), a N-methyl derivative of glycine produced by glycine-N-methyl transferase, was identified by metabolomic alteration profiling as a differential metabolite which is highly increased during prostate cancer progression to metastasis.[76] This molecule, which is therefore a potentially important intermediary of cancer cell invasion and aggressivity, can be easily analysed non-invasively in the patient urine as well. This makes it a good candidate for NMR-chemosensing too.

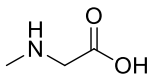

Figure 62: sarcosine

Designing NMR-chemosensors

Ligands for AuNPs – alternatives to thiols

N-heterocyclic carbenes (NHCs) are defined as heterocyclic species containing a carbenic carbon and at least one nitrogen atom within the ring structure.[77] The presence of one or two nitrogen atoms adjacent to the carbene carbon provides a great electronic stabilization both inductively, by lowering the sigma-orbital energy, and mesomerically, by donating

electron density to the carbon empty p-orbital. NHCs are found in a singlet ground state electronic configuration, their HOMO and LUMO can be described respectively as a sp^2-hybridized lone-pair and as an unoccupied p-orbital on the C2 atom (Figure 63).

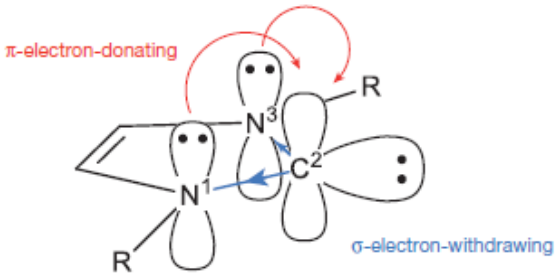

Figure 63: effect of adjacent nitrogen atoms[77]

In general, bulky substituents on the nitrogen atoms help in stabilizing the carbene by introducing a steric barrier for the dimerization process, thus preventing it, which would otherwise lead to the formation of a C=C bond (Wanzlick equilibrium, Figure 64).

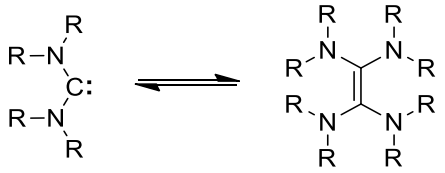

Figure 64: Wanzlick equilibrium

The cyclic nature of NHCs further favors the sp^2-like arrangement of the carbenic carbon. The partial aromaticity of heteroaromatic compounds enhances further the stability of NHCs. For example, the presence of the C=C bond on the imidazole adds a stabilization contribute of 25 kcal/mol in imidazol-2-ylidenes.[78] The presence of this partial aromaticity decreases the importance of bulky groups on the nitrogen atoms, and even N-methyl derivatives can be persistent species. The lone pair on the carbenic carbon renders these species nucleophilic, at difference with the usually electrophilic transient carbenes, and strong sigma-donor ligands. NHCs can bind to a large variety of metallic and non-metallic species. As an example, Au-C bond of the compound in Figure 65 has a bond dissociation energy of 67 kcal/mol, which is more than 20 kcal/mol greater than that of an average Au-S bond.[79] Metal-C2 coordination of NHCs is generally drawn as a single bond, rather than double one, and the π-delocalization is restricted within the heterocyclic ring. NHCs steric properties are inherently highly anisotropic and rotation around the M-C bond can occur to minimize steric hindrance.

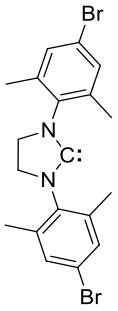

Figure 65: NHC example

One attractive advantage of NHCs over traditional sigma-donor ligands, such as phosphines, is that their electronic and steric properties can be tuned independently one from another by changing the N-substituents, backbone and heterocycle. Several NHC complexes have been synthesized with all the transition metals[80] and many similar adducts with alkali metals and alkali earths.[81] NHC are relatively easy to synthesize and several synthetic pathways from different precursors are available. Usually, however, the corresponding heterocyclic azolium salt is chosen as precursor as these species are very stable and easy to handle. By deprotonation of these compounds with common bases the carbene can be formed, in mild conditions. While the largest application of NHCs nowadays is in homogeneous catalysis and organocatalysis, these species are starting to attract interest also for the functionalization of metal surfaces and for the stabilization of metal colloids. Functionalization of gold surfaces with resilient organic monolayers is highly desirable for various applications including: nanoelectronics[82], sensing[83], nanofabrication[84] and nanotechnology[85]. Thanks to NHCs strong Au-C bond, they might be more effective than sulfur-based ligand for such applications.

Surface functionalization with NHCs

NHCs have been studied as ligands for the functionalization of Au(111) surfaces. It was demonstrated that substituents on the nitrogen atoms strongly affect how benzimidazolylidene ligands bind to the surface and how they organize.[86] When isopropyl groups are employed the carbenes attach to gold in an upright position, lifting the gold atom from the equilibrium position (Figure 66). If the bulkiness of the nitrogen substituents is decreased, the carbene no longer binds in an upright position, but forms dicarbenic complexes with superficial gold atoms. This can already be observed when one of the isopropyl groups of iPrNHC is substituted with an ethyl one (Figure 67). On the other side, when bulkier substituents are employed (such as tBu) the ligands retain the upright position but significantly weaker Au-C bonds are formed due to steric hindrance (Figure 68).

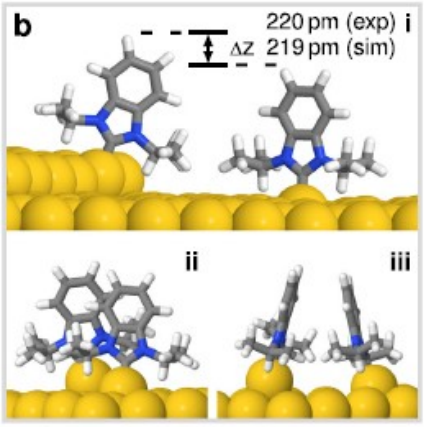

Figure 66: iPrNHC on Au(111) surface[86]

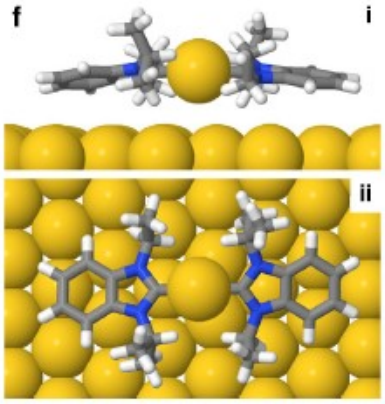

Figure 67: Et-NHC-iPr on an Au(111) surface[86]

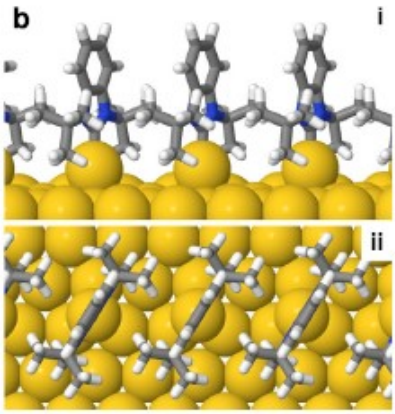

Figure 68: tBu-NHC on an Au(111) surface[86]

The effect of N-substituents on the binding mode is better illustrated in Figure 69, which shows that decreasing bulkiness from iPr lead to an inversion in the favoured binding mode.

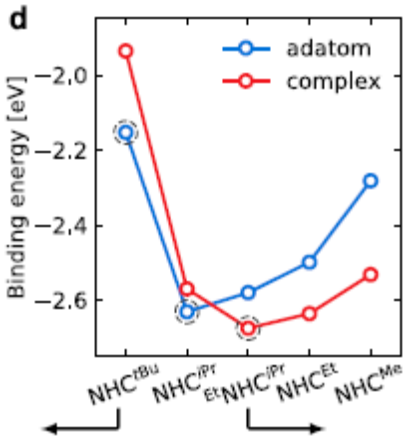

Figure 69: N-substituent effects on the binding energy[86]

Although iPr-NHC binds exclusively in an upright position forming zig-zag patterns, when the system is annealed at temperature greater than 50°C, an irreversible transition to dicarbenic complexes is observed. NHC-functionalized gold surfaces were demonstrated to be stable toward ligand substitution with sulfides and even thiols.[33]

NHC-protected gold nanoparticles

Several stable NHC-protected nanoparticles have been synthesized to date. In one of the first works, Pt nanoparticles were stabilized by employing NHCs with negatively charged sulfonate groups placed on the nitrogen substituents. These charged functionalities provided an effective electrostatic repulsion for the stabilization of the colloid.[28] Electrostatic repulsion is not the only way to prevent nanoparticles aggregation and, in a different work, carbenes functionalized with a long chained polyethylenglycol moiety were used. The use of this hydrophilic chain allowed to achieve both steric stabilization and solubilization in polar solvents. Stable NHC-coated gold nanoparticles were obtained with this method (Figure 70) which proved to be stable in a wide pH range and salinity conditions, including biologically relevant ones. These nanoparticles resulted to be stable even in aqueous H_2O_2, which is otherwise able to oxidize thiol-protected AuNPs leading to their degradation.[87] A simple protocol for the synthesis of size-tunable benzimidazolylidene-AuNPs was developed starting from AuCl, benzimidazolium bromide and a reductant.[30] This protocol allows to control the nanoparticle size by using reductants of different strength: sodium borohydride lead to the synthesis of nanoparticles in the 3-6 nm range, while 6 to 12 nm ones were prepared employing $tBuNH_2BH_3$. Lateral chains of 6 to 12 carbon atoms have been installed on the NHC to allow steric stabilization.

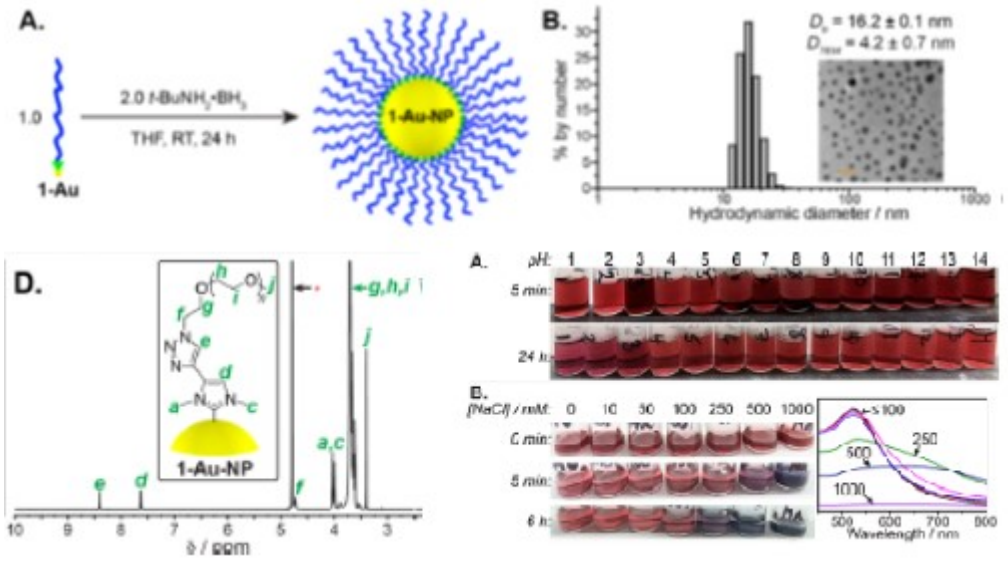

Figure 70: long chain PEG-NHCs for AuNPs stabilization[87]

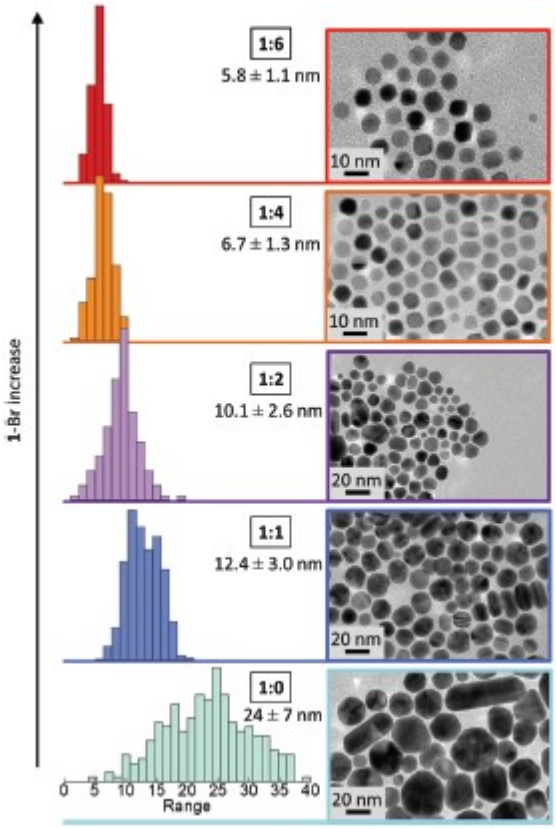

Figure 71: TEM images and size distribution of NHC-protected gold nanoparticles synthesized with an excess of NHC-precursor (from 0 to 6 eq.) and $tBuNH_2BH_3$ as reducing agent.[30]

A different strategy for the synthesis of size focused NHC-protected nanoparticles was developed starting from an aqueous solution of a dicarbenic gold complex and supplementary gold ions added as tetrachloroaurate.[32] This solution was reduced with borohydride at room temperature and the reaction was stopped after 5h (Figure 72). While

the yields are not exceptionally high, this protocol allows a good control over nanoparticles size and it is very easy to perform. In order to increase colloid stability, multidentate NHC ligands were synthesized and used for the synthesis of 3-5 nm AuNPs (Figure 73).[31] Such ligands proved to be more effective for the stabilization of the nanoparticles than monodentate benzimidazolylidene ones. These systems proved to be stable even after being exposed to a 5 mM dithiothreitol solution for 48h.

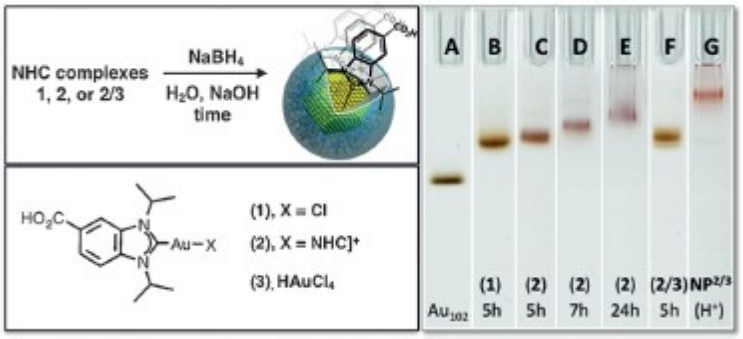

Figure 72: NHC protected AuNPs synthesis by reduction of a dicarbenic gold complex in presence or absence of supplemental tetrachloroaurate; gel electrophoresis of the synthesized colloids on the right[32]

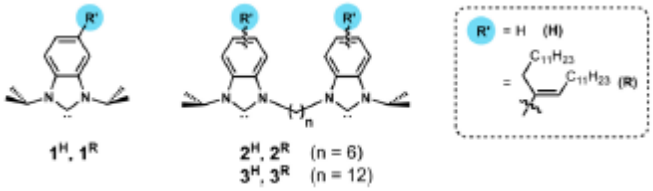

Figure 73: multidentate NHC ligands

Two different synthetic methods were explored (Figure 74) and the "top-down" one, where NHCs are grafted by ligand exchange on previously formed AuNPs (through Brust and Schiffrin method), proved to be consistently superior. Nanoparticles synthesized through the "bottom-up" approach, by direct reduction of NHC-Au(I) complexes, resulted less stable to both heating and treatment with thiol solutions. Hence, the way NHC-protected nanoparticles are synthesized has a relevant impact on the obtained material and needs to be carefully considered.

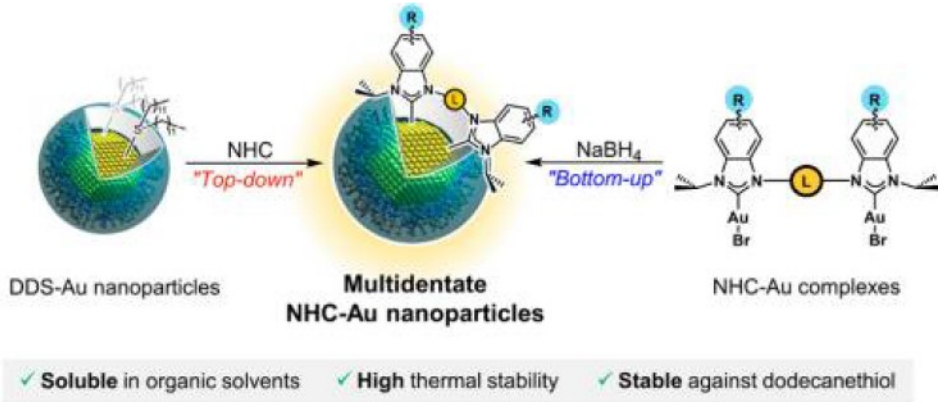

Figure 74: AuNPs protected with bidentate NHC synthesized via "top-down" and "bottom-up" approaches[31]

Aim of the thesis

Improving the effectiveness of NMR-chemosensors

As we've discussed in the previous chapters, ligand shell protected gold nanoparticles offer a straightforward strategy for the realization of self-organized macromolecular receptors. This strategy has found several different applications but, so far, selectivity reached is quite limited. In general, nanoparticle receptors are capable to recognize classes of molecules focusing on specific structural features, as highly chargers polyanions (ATP) or polycations (biogenic amines), amphiphilic anions (FANS) or cations (phenethylamines). In specific cases, some selectivity has been reached by taking advantage of specific supramolecular interactions, as the phosphate preference of TACN·Zn(II) functionalized nanoparticles, or the primary amines preference of 18[crown]6 bearing ones. Only in the early example of Rotello of flavin binding nanoparticles, at the best of our knowledge, a true selectivity due to multisite specific interaction was reached. In addition, affinity of the nanoparticles for the target analytes, when multiple ion pairing is not at play, rarely exceeds the micromolar range. Of course, these limitations may affect the possible application of the nanoparticles primarily for NMR sensing but also for other possible uses, either in sensing or in other fields. The main obstacle encountered in addressing this limitation is that the design of a monolayer with tailored binding properties is limited by the dynamic nature of the monolayers themselves. Indeed, the recognition properties of the nanosystem are not really correlated to the chemical nature of the single ligands, but strongly depend on the arrangement of those molecules on the nanoparticle surface.[22 27] The recognition ability is therefore a "collective property" of the bound ligands, which means that not only intermolecular interactions and solvation play an important role but also that the dynamics of the thiols is important. Moreover, the recognition pockets have already been demonstrated to be "transient",[22] and this nature not only makes difficult their design and optimization, as already discussed, but can also decrease the target affinity, as the costs for their opening contribute to the energetic balance of the recognition process. The possibility to computationally simulate the properties of a novel monolayer could be of great help allowing to perform an in-silico screening and a pre-optimization of the structure prior to the synthesis of the actual chemosensors. As we discussed, MD simulations had so far provided an extremely valuable insight on the monolayer dynamics and the recognition at the monolayer events. Yet, they are quite expensive in term of computational resources and time, and effective strategies for a computer assisted nanoreceptors design have not been developed.

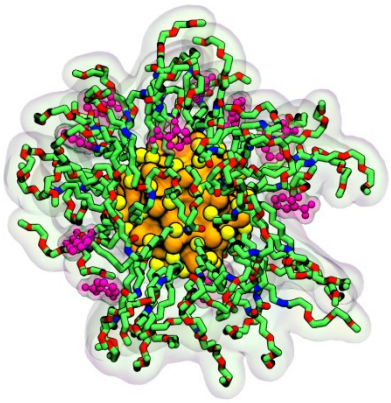

Figure 75: simulated chemosensor structure in presence of the analyte (in pink)

Computer aided design is not the only possible strategy that can be pursued to improve and expand the properties and application of nanoreceptors. As we have seen in the introduction, other possible strategies include: i) increasing the structural rigidity of the monolayers by using different coatings, ii) conjugate nanoparticles with supramolecular receptors, iii) increase the sensitivity of NMR-based methods. In this thesis work I tried to address these issues with a comprehensive approach aimed to increase the effectiveness of nanoparticles receptors and NMR chemosensing while maintaining the self-assembled nature of the used nanosystems. In chapter 1 I will report the results obtained toward the realization of a protocol for automated design and synthesis of nanoparticle receptors, based on solid phase ligand synthesis and computer-aided design. In chapter 2 I will report the results obtained in the realization of noncovalent nanoparticle-cavitand hybrids as receptors for NMR chemosensing. In chapter 3 I will discuss the attempts performed to individuate an alternative to thiols for the realization of rigid monolayers based on the use of carbene ligands.

Coupling SABRE to NMR-chemosensing

SABRE is another promising strategy for high sensitivity NMR detection but it is still affected by an important limitation: the analyte must bind to the hyperpolarization catalyst. It would be extremely interesting to combine in a single experiment p-H_2 hyperpolarization, with its massive enhancement in sensitivity, and nanoparticle-based NMR-chemosensing, with its tunable selectivity. This could lead to a further generalization of the SABRE technique, not being limited anymore to the sole analytes which can directly bind to the hyperpolarization catalyst. As in nanoparticle-based NMR-chemosensing it is the organic monolayer to act both as receptor and as magnetization carrier, being able to hyperpolarize the monolayer by

SABRE should allow to decouple the substrate recognition capability from the sensitivity enhancement process. This hypothetical technique would be based on a simultaneous two-step process where one would see the hyperpolarization catalyst simultaneously interacting with both p-H_2 and the nanoreceptor, hyperpolarizing the monolayer, while the other would involve a transfer by NOE of this enhanced polarization to the analyte inside the monolayer pockets. If it is possible to increase the sensitivity of NMR-chemosensing of several order of magnitude, as it has been already demonstrated with standard SABRE, then it would be possible to detect and fully characterize trace molecules in very complex mixtures, such as biological fluids, possibly leading to the development of innovative analytical and biomedical techniques. As monolayer protected gold nanoparticles can be designed to be biologically compatible and hydrogen gas is non-toxic and can easily permeate and diffuse in tissues, this technique could also be interesting for in-vivo applications. In chapter 4 I'll report the progresses made toward this goal.

Results and Discussion

1. Tripeptide nanoparticles

Aim

In this chapter, I'll report the results obtained toward the development of a fully automated protocol for nanoreceptor design and synthesis. The research was performed in collaboration with prof. De Vivo's group (ITT, Genova). Our working hypothesis was that small peptide-based ligands could provide the possibility to explore a large chemical space and to develop fast and possibly automated synthetic protocols. These features, when conjugated with in silico predictive molecular dynamics-based screening methods, could allow the straightforward and fully automated synthesis of nanoreceptors on demand.

Receptor design

In biological systems evolution led to the formation of greatly sophisticated recognition sites in proteins by using mainly L-aminoacids as building blocks. The same building blocks can be conveniently used for the scope of this work as techniques such as solid phase synthesis (SPS) have been widely developed and optimized to create large libraries of peptides with minimal effort. Employing SPS in the ligand synthesis would dramatically help in decreasing the time requirement of the synthetic step, which can even be automated, if necessary. Oligopeptide-based thiols were chosen for the functionalization of gold nanoparticles of around 1.8 nm of diameter, the standard size for NMR-chemosensing applications. 3-Methoxytyramine (Figure 76) was selected as analyte of interest as this molecule is one of the human metabolites which have been proposed as tumor markers.[75] Clearly, if successful, this approach can be extended to a large variety of different substrates.

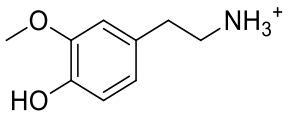

Figure 76: 3-methoxytyramine

The analyte, at physiological pH, bears a positive charge on the trimethylammonium head group. An ion pairing interaction can therefore be easily exploited for the development of a receptor. Accordingly, a negative charge was placed on the outermost portion of the ligands by inclusion of an aspartate as terminal amino acid. The placement of a charge at the

extremity of the chain allow to tune the internal portion of the thiol, and therefore of the resulting pocket, for a better interaction with the more hydrophobic portion of the analyte. For example, amino acids bearing aromatic rings or H-bond donor/acceptor moieties can be introduced in the internal positions to add different interactions which can improve the affinity (and/or the selectivity) for the analyte. The presence of a charge also enhances the water solubility of the nanoparticles and electrostatically stabilizes the colloid. In particular, we decided to use aspartate and glutamate as external amino acid, taking advantage of the charge naturally present on their lateral chains, and protecting the terminal acid group as methyl ester. This pathway allows flexibility on the charge placement along the peptidic chain and different positions can be later explored, if required. Two more amino acids were included in the chain and the tripeptide was attached to the gold core through an alkyl amide linker, which, in previous works, proved to be effective for nanoparticle stabilization. The use of tripeptides, and the possibility to change the size of the linker, provides a sufficiently large chemical space to be explored for the development of a computational screening method. Indeed, the possible combinations of tripeptides (starting from 20 aminoacids) and 3 chain lengths provide 24000 different molecules, a number that exceeded the available computations resources. To reduce the number of peptides which needs to be simulated, a size reduction strategy was studied. First, the length of the amide linker was set to 8 carbon atoms, which was already used for many of the previously developed receptors. Second, the charge of the ligands was set to -1 and assigned to the outer position only (introduced as aspartate only). Finally, for the remaining two positions we selected aminoacids with a higher occurrence in the recognition pockets of enzymes which naturally interact with the class of metabolites targeted (crystal structures of 172 proteins have been considered). These criteria reduced the ligand library explored to 100 different molecules.

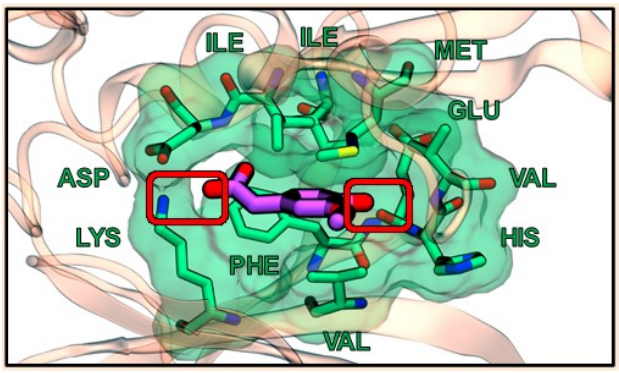

Figure 77: homovanillic acid in the binding pocket of 5MOH Casein kinase 2

On this basis, De Vivo's group (IIT Genova) set up a screening method based on short and repeated MD simulations where the release of 3-methoxytyramine from the nanoparticles was followed. In principle, the release rate observed should be inversely related to the monolayer affinity for the target molecule. This protocol was first trained by using all the available affinity data for the nanoreceptors studied so far and then used to screen the set of 100 AuNPs functionalized with tripeptide-based anionic thiols. The first and last 10 entries of the ranking are listed in Figure 78. Seven thiols from the complete list, covering the whole ranking, were chosen and synthesized.

Inner amino acid	Outer amino acid	ΔG (kcal/mol)	ranking
Pro	Leu	-17.27	1
Phe	Gln	-16.13	2
Phe	Ser	-14.50	3
Ile	Gln	-14.28	4
Ile	Trp	-12.97	5
Gln	Gly	-12.84	6
Gly	Ile	-12.77	7
Trp	Phe	-12.76	8
Ala	Tyr	-12.63	9
Pro	Pro	-12.22	10

Inner amino acid	Outer amino acid	ΔG (kcal/mol)	ranking
Ile	Ile	-5.89	91
Ser	Tyr	-5.87	92
Phe	Tyr	-5.54	93
Leu	Tyr	-5.33	94
Tyr	Gln	-5.25	95
Tyr	Trp	-5.08	96
Phe	Phe	-4.75	97
Gly	Pro	-4.39	98
Trp	Ser	-3.38	99
Leu	Gln	-3.05	100

Figure 78: predicted most and least active tripeptide-functionalized AuNPs. Inner amino acid is the one attached to the thiol linker while outer amino acid is the one before the aspartate terminal group.

Thiol synthesis

A solid phase synthetic procedure based on standard Fmoc protection and 2-chlorotrityl resin was set up. The general synthetic procedure is illustrated in Figure 79.

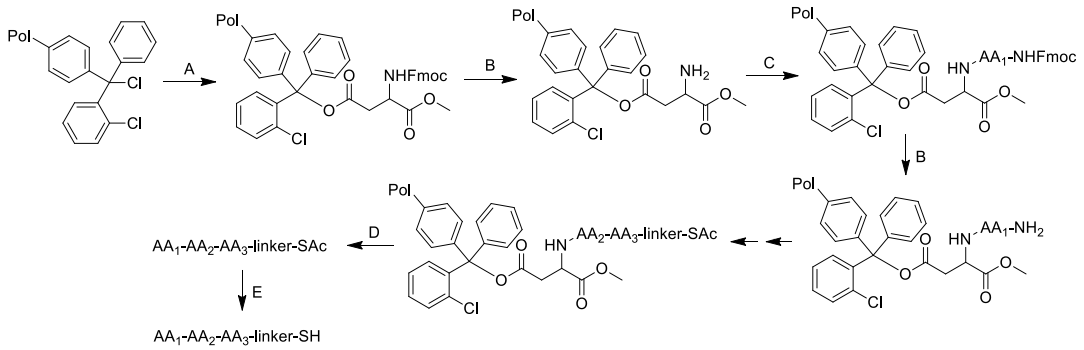

Figure 79: Synthetic scheme for the tripeptide-thiols. A) first amino acid immobilization; B) Fmoc deprotection; C) n^{th} N-Fmoc amino acid coupling; D) resin cleavage; E) thioacetate deprotection in solution

To attach the first amino acid to the resin, the carboxylate of the aspartate lateral chain was reacted directly with 2-chlorotrityl resin in presence of DIPEA as a base (Figure 80). This step

allowed also to simultaneously protect the carboxylate group until detachment of the ligand from the resin.

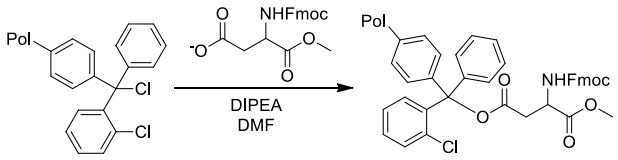

Figure 80: first N-Fmoc amino acid coupling

Fmoc protecting group was removed by treating the resin with a 20% solution of 4-methylpiperidine in dry DMF (Figure 81, above). The required Fmoc-protected amino acid was activated by mixing it with HBTU and DIPEA in DMF and this activated amino acid solution was then directly added to the resin (Figure 81, bottom).

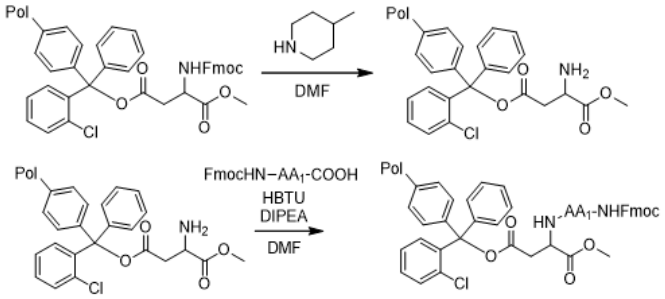

Figure 81: Fmoc deprotection step and N-Fmoc amino acid coupling

The C_8 linker was introduced with the thiol group protected as thioacetate in order to avoid oxidation and 1,1,1,3,3,3-hexafluoro-2-propanol was used for the tripeptide cleavage (Figure 82).

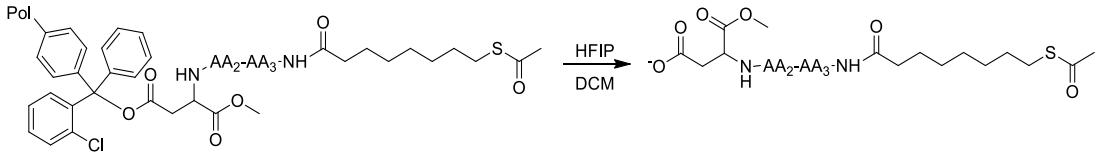

Figure 82: resin cleavage

The thiol was finally deprotected with sodium methoxide at room temperature (Figure 83).

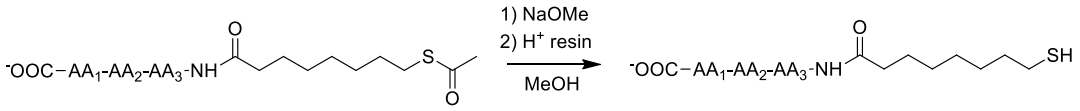

Figure 83: thioacetate deprotection

Gold nanoparticles synthesis

The gold core of the nanoparticles was synthesized by a modified Brust and Schiffrin procedure developed by Scrimin[11] (Figure 84). The Au(III) source is tetrachloroaurate which is initially extracted in toluene using tetraoctylammonium bromide as phase transfer reagent. The Au(III) was reduced to Au(I) at room temperature with a well-defined excess of dioctylamine (DOA) which then, during the further reduction to Au(0) with sodium borohydride, acts as surface stabilizing agent allowing to control the final nanoparticle size. By using 20 equivalents of DOA, nanoparticles with an average diameter of 1.8 nm are obtained. The thiol was then attached in the last step by ligand exchange. Both the reduction and ligand exchange steps were performed in an ice bath, allowing to avoid degradation of the DOA-protected nanoparticles which are much less stable than the thiol-protected ones. The ice bath permits also to work at a constant and reproducible temperature of 0°C and avoids the introduction of an eventual seasonal dependence on the synthesis outcome.

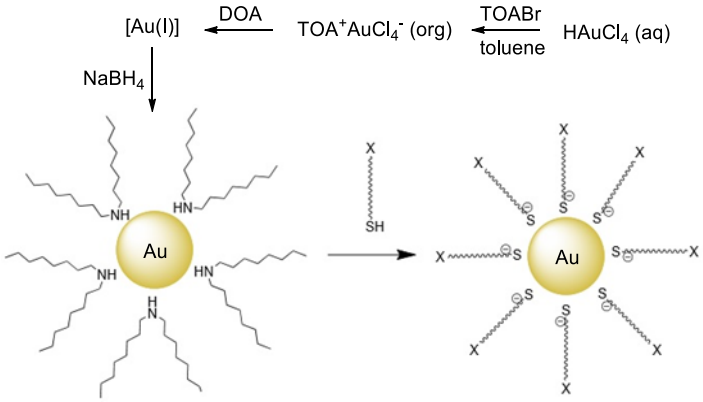

Figure 84: scheme of the standard procedure for thiol-protected AuNPs synthesis

Depending on the nature of the ligand used, the nanoparticles can be purified by centrifugation and extraction with organic solvents, by ultrafiltration or by size exclusion chromatography. The tripeptide nanoparticles synthesized in this work precipitated from the toluene mixture used for the synthesis and were purified by dissolution in methanol and precipitation by subsequent addition of diethyl ether as antisolvent. The nanoparticles were easily collected on the bottom of the flask by centrifugation at 5000 rpm for 8 minutes. The dissolution/precipitation step was repeated at least 3 times and then the residue was further purified three times by size exclusion chromatography in ultrapure water (on Sephadex G-25 resin). The structure of the seven synthesized chemosensors are reported in Figure 85. The two-steps procedure utilized for the gold AuNPs synthesis allows to decouple the gold core synthesis from the nanoparticle monolayer functionalization. It is possible therefore to synthesize a great variety of size-consistent NPs dispersions regardless of the nature of the

selected thiol, which could otherwise influence the obtained gold core size. In addition, the ester group present in the thiols used here is not compatible with the presence of sodium borohydride, which can both slowly reduce it and favor its transesterification.

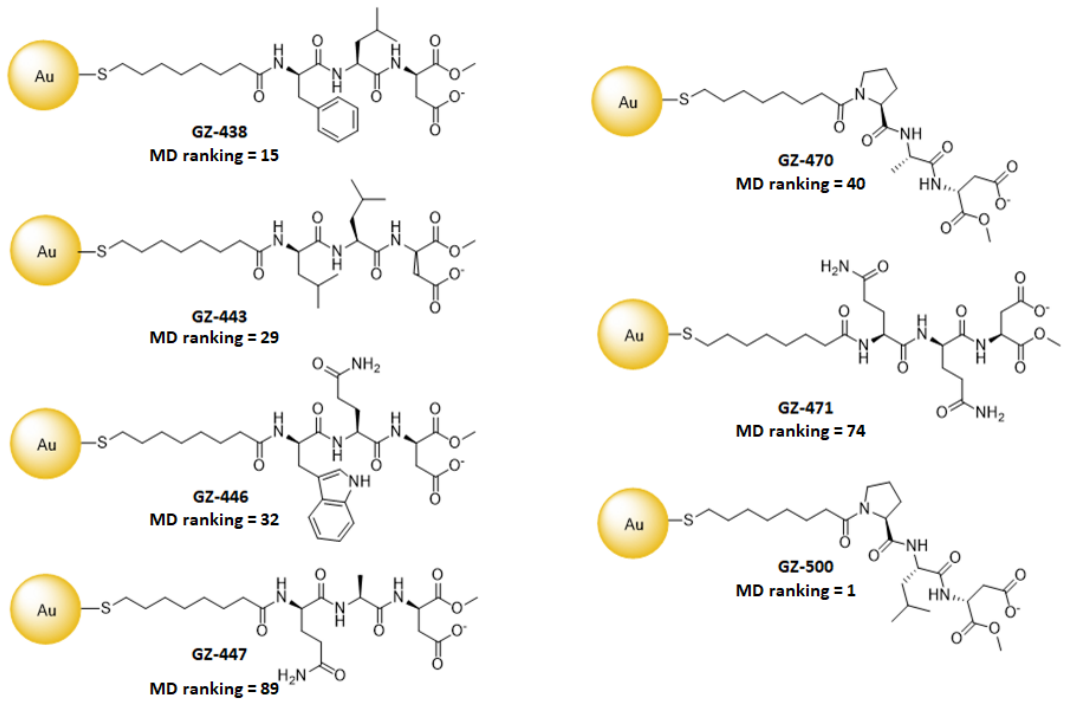

Figure 85: tripeptide-coated nanoparticles

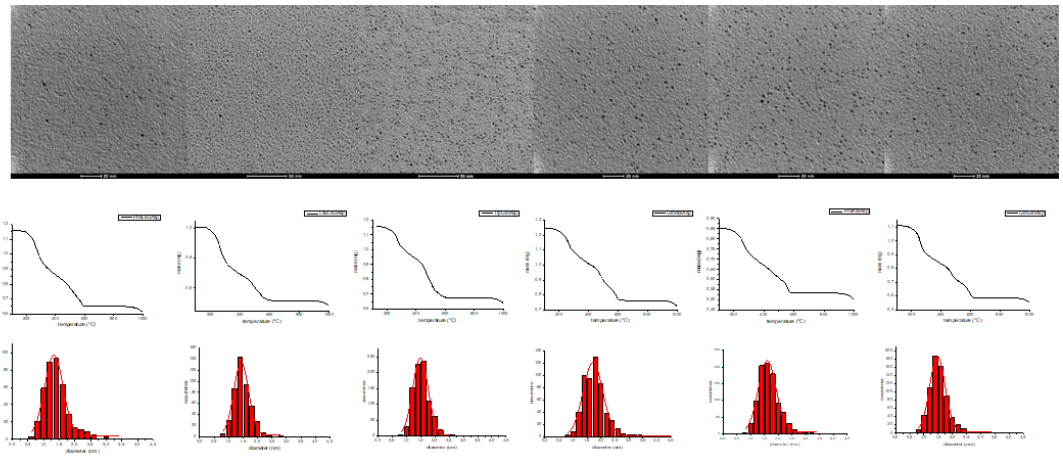

Figure 86: Comparison between TEM images, TGA weight loss curve and size distribution histogram (in scale) of 6 batches of AuNPs

To check the average diameter and the size distribution of the synthesized nanoparticles, TEM analysis has been performed. As can be seen from Table 1, the size distribution resulted to be comparable in each sample and well monodisperse, reflecting the desired average size for NMR-chemosensing applications. TGA analysis (also reported in Figure 86) allowed to measure the amount of organic mass attached to the nanoparticles and, in combination with

the TEM analysis, it has been possible to calculate a footprint of the ligands on the gold surface. The obtained data, reported in Table 1, shows that the nanoparticle batches are comparable in size and distribution confirming the effectiveness of the two-step synthetic methodology. It was possible to obtain the desired nanoparticles with each of the seven thiols employed.

Table 1: TGA weight loss, average diameter, mean cluster formula, thiol footprint and zeta potential of the nanoparticles

		TGA (%)	diameter (nm)	average formula	footprint (nm^2)	Zeta potential (mV)
GZ-438	**PheLeuAsp**	44.28	1.3 ± 0.3	$Au_{72}SR_{20}$	$2.16*10^{-1}$	/
GZ-443	**LeuLeuAsp**	49.15	1.4 ± 0.3	$Au_{91}SR_{33}$	$1.77*10^{-1}$	/
GZ-446	**TrpGlnAsp**	44.06	1.5 ± 0.3	$Au_{102}SR_{26}$	$2.45*10^{-1}$	-23.3
GZ-447	**GlnAlaAsp**	38.83	1.7 ± 0.4	$Au_{155}SR_{39}$	$2.07*10^{-1}$	-21.3
GZ-470	**ProAlaAsp**	37.27	1.6 ± 0.3	$Au_{127}SR_{31}$	$2.23*10^{-1}$	-22.6
GZ-471	**GlnGlnAsp**	47.27	1.5 ± 0.3	$Au_{99}SR_{31}$	$1.92*10^{-1}$	-21.3
GZ-500	**ProLeuAsp**	47.73	1.4 ± 0.3	$Au_{88}SR_{31}$	$1.87*10^{-1}$	-36.9

Tripeptide-based NMR-chemosensors

The tripeptide coated nanoparticles were tested for the detection of both 3-methoxytyramine and tyramine through NMR-chemosensing. The nanoparticles were dispersed into a D_2O solution 1 mM in analyte and 10 mM in HEPES buffer and the NOE pumping experiments (4000 scans, 4 h) were performed. The signal to noise ratio of the analyte aromatic protons was used to rank the recognition ability of the NMR chemosensors. Those signals were chosen as they are located in a free region of the spectrum where no interfering signals are present. NOE-pumping spectra are reported stacked in Figure 87 and Figure 88 with the associated signal/noise ratio calculated on the most intense signal of the analyte aromatic protons. Figure 89 reports the signal to noise ratio obtained for the two analytes (Tyr and 3-MeOTyr). In order to compare the recognition efficiency, the signal to noise ratios were corrected for the number of protons the signal is originated from. In the tyramine set the s/n ratio was therefore divided by 2. The trend which can be observed for 3-methoxytyramine reflects the one seen also for tyramine, showing that there is no noticeable difference in the selectivity of this nanoparticle set.

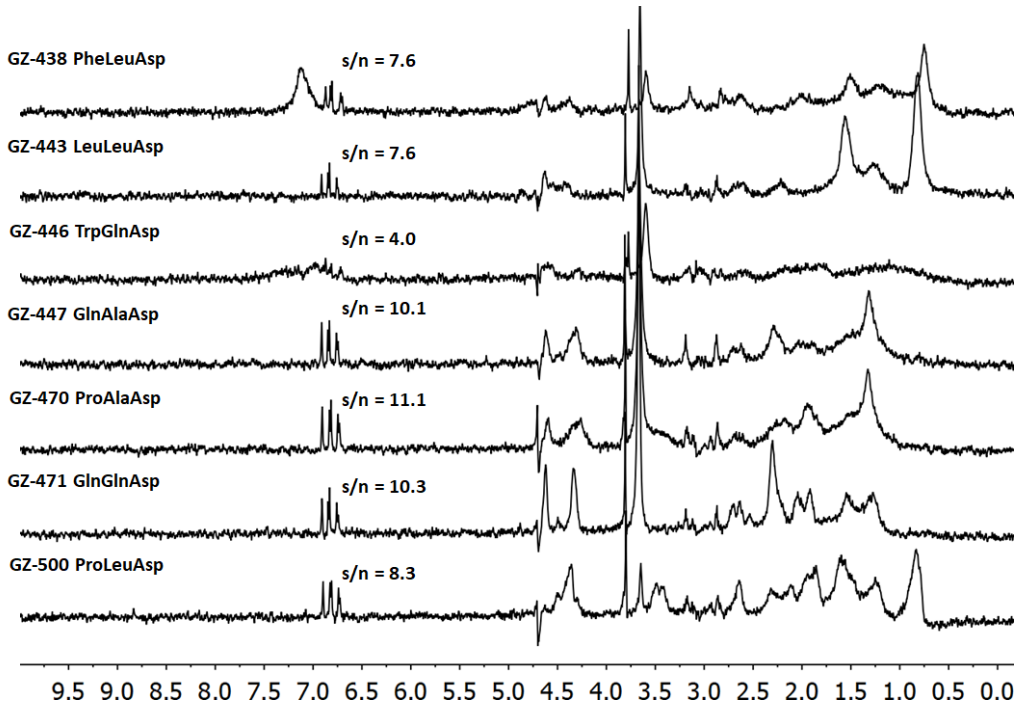

Figure 87: NOE-pumping experiments for the detection of 3-methoxytyramine with the tripeptide-AuNPs. 1 mM NPs (in thiol), 3-methoxytyramine 1 mM and HEPES 10 mM in D_2O. 3072 scans

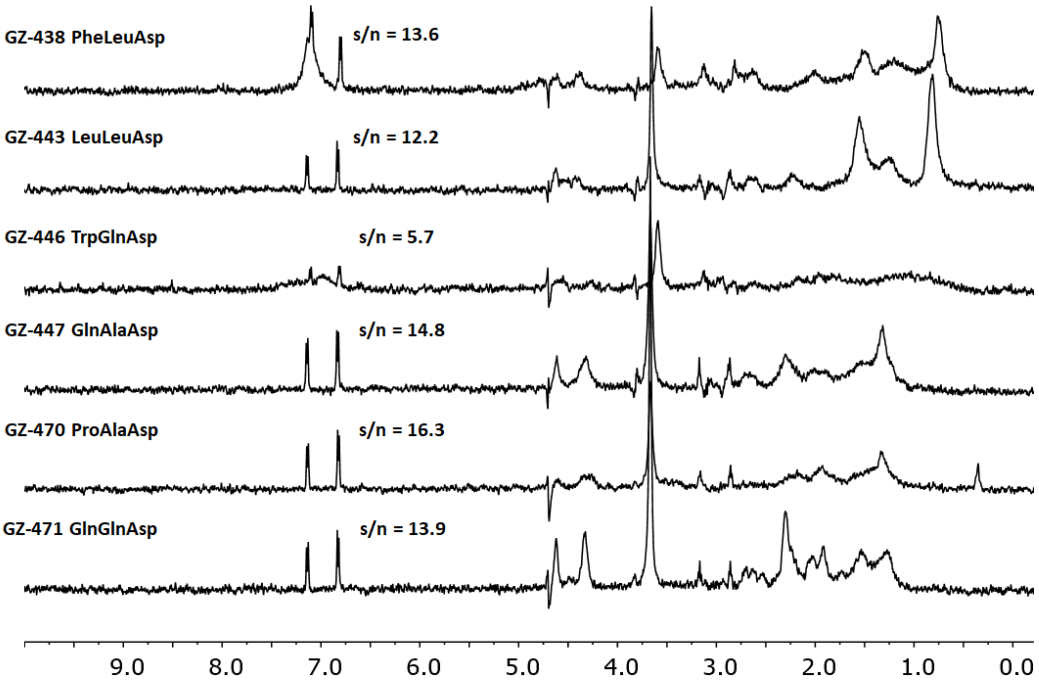

Figure 88: NOE-pumping experiments for the detection of tyramine with the tripeptide-AuNPs. 1 mM NPs (in thiol), tyramine 1mM and HEPES 10mM in D_2O. 3072 scans

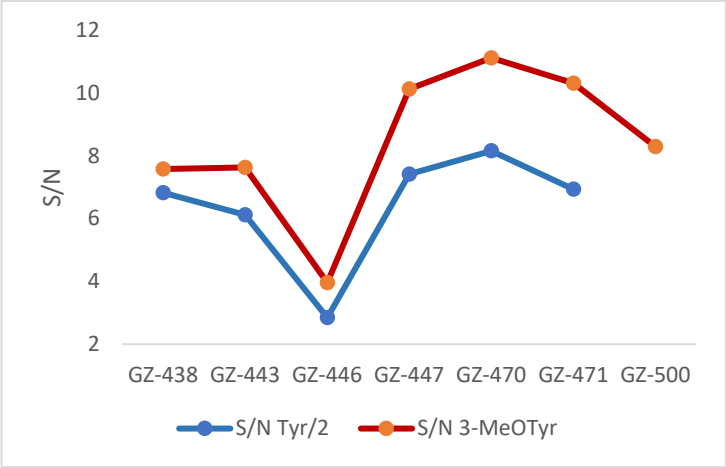

Figure 89: Comparison of the s/n ratio of the NOE experiments; the ratio is normalized for the number of protons originating the signal. s/n(Tyr)/2 in black and s/n(3-MeOTyr) in red

Each nanoparticle tested showed a higher detection efficiency for the analyte of interest with respect to tyramine, with an increase from 1 to 3 units of the signal to noise ratio. However, the difference in detection efficiency is limited in absolute value and, with the exception of GZ-446, they seem to perform very similarly. In addition, as can be seen in Figure 90, the efficiency as NMR-chemosensors does not seems to be correlated with the computationally derived affinity ranking.

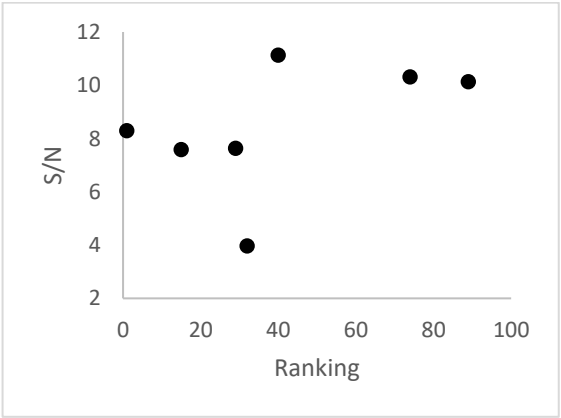

Figure 90: NOE s/n ratio for the detection of 3-MeOTyr

If the peptide chain contains amino acids bearing aromatic groups there could be a resulting superposition of signals with those of the chosen analyte, as can be seen in GZ-446 (and partially in GZ-438). When this needs to be avoided a CPMGz filter can be applied at the end of the experiment to remove all the residual signals from the species bound to a nanoparticle, leading to a clean NMR spectrum of the interacting species only. A comparison between a NOE-pumping experiment and one followed by CPMGz filter can be seen in Figure 91.

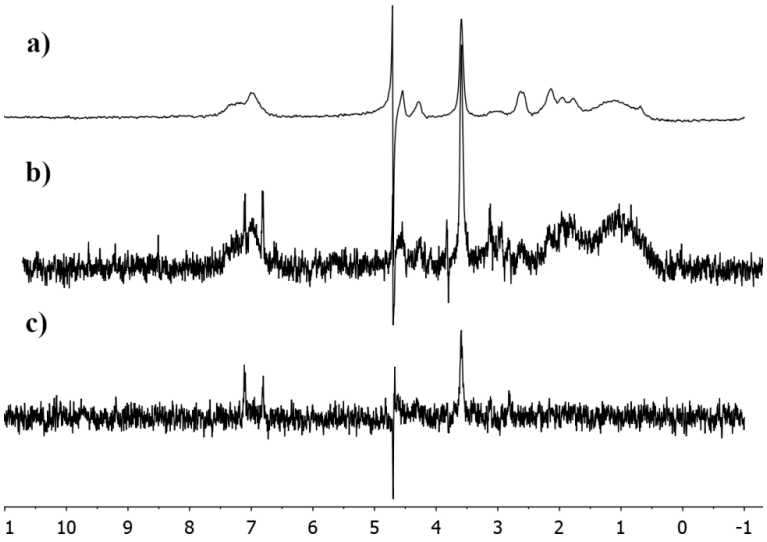

Figure 91: a) diffusion filter of GZ-446; b) NOE pumping experiments; c) NOE pumping experiments followed by CPMGz filter; both the two NOE experiments are performed on the same sample GZ-446 1 mM, tyramine 1 mM, HEPES 10 mM

DOSY experiments were also performed to obtain more information on the substrate binding properties. As apparent diffusions coefficients are the average between that of the free and bound state weighted for the relative population of the two states, the difference between the diffusion coefficient of the free analyte and that of the analyte in presence of a chemosensor indicates how strongly it is bound to the receptor. As it is shown in Figure 92, the diffusion coefficient D of the analyte is significantly decreased when the nanoreceptor is present in solution. In addition, apparent analyte diffusion rates appears to correlate with the nanoparticle computational ranking. However, remarkable differences are observed only for nanoparticle GZ-500 (ranking 1) and possibly for GZ-430 (ranking 15), while all the other particles seem to have similar affinities.

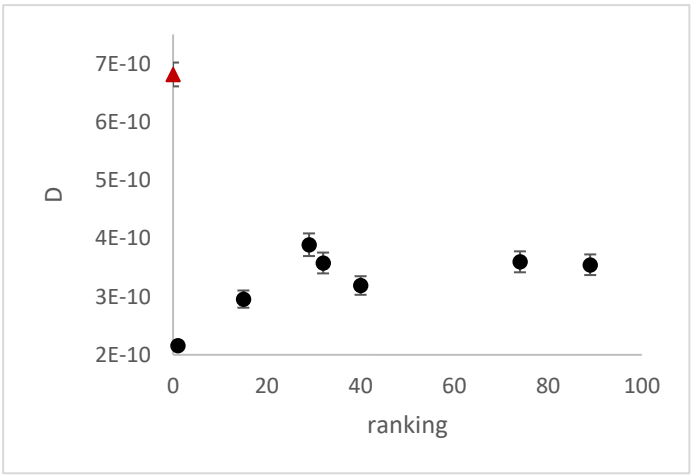

Figure 92: diffusion coefficients of 3-MeOTyr 0.5 mM in presence of AuNPs 2 mM (in thiol), HEPES buffer 10 mM in D_2O. The red triangle at "ranking 0" is the analyte (3-MeOTyr) in absence of nanoparticles

From DOSY experiments it is possible to calculate the binding constant of the receptor for the analyte (Figure 93). Again, there seems to be a weak correlation between the ranking and the experimentally obtained association constants, but the difference in absolute value is fairly modest, especially if compared to the relatively broad range of the computationally predicted ΔG values for the binding event.

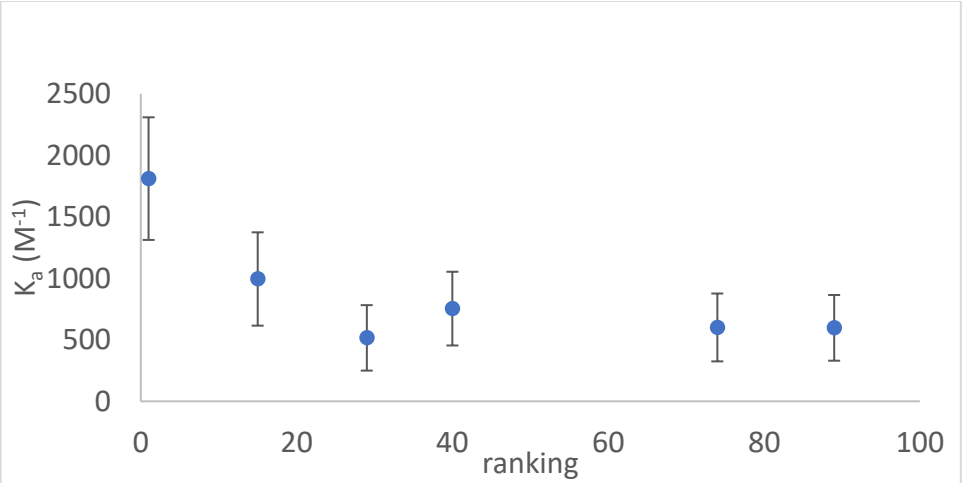

Figure 93: Binding constants (K_a) of the AuNPs for 3-MeOTyr obtained from DOSY experiments

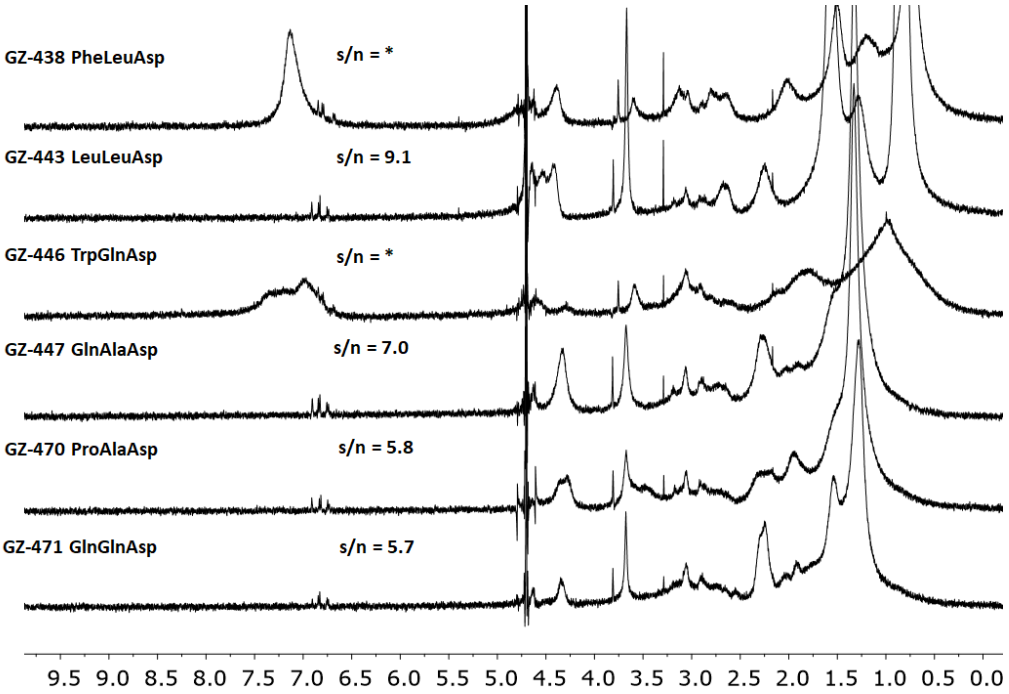

Figure 94: STD experiments irradiating on the alkyl portion of the nanoparticle monolayer. NPs 1 mM (in thiol), 3-methoxytyramine 1 mM and HEPES 10 mM in D_2O. For GZ-438 and GZ-443 it was not possible to calculate s/n as the analyte signals are superimposed with the receptor ones

The nanoparticles sensing performance was then investigated using saturation transfer difference (STD) experiments. Using this protocol, it was possible to increase the sensitivity

of the NMR-chemosensing, decreasing to 1/8 (30 min) the time required to have comparable signal to noise ratios to those obtained with NOE-pumping. Also, in this case, all the nanoparticles appeared to have similar performances, with GZ-446 providing the less intense signals and all the others providing signals with similar intensities. In the case of GZ-438 and GZ-446, in addition, overlap with the nanoparticles signals is very disturbing, hampering a reliable quantification of the signals. At difference with NOE pumping, however, no experimental sequence is available to avoid this problem.

HP wSTD experiments

The chemosensors were finally tested with the most recent NMR-chemosensing technique: the high power water-STD (HP wSTD). NMR tubes were prepared in 90% H_2O and 10% D_2O, 0.5 mM in chemosensor (in thiol), 0.1 mM in 3-methoxytyramine and 1 mM in HEPES.

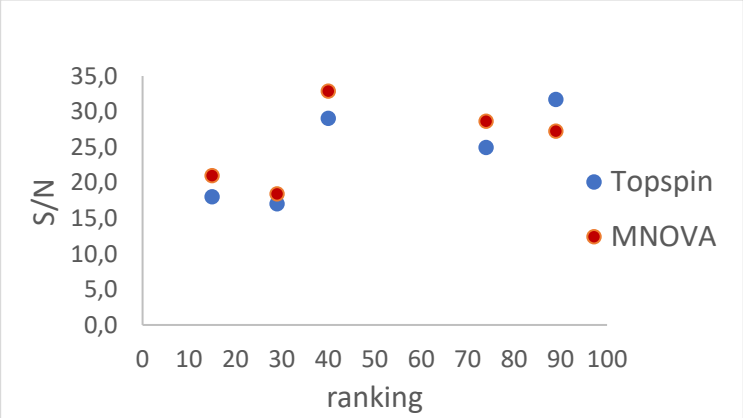

Figure 95: s/n ratios of HP wSTD experiments compared to the computational ranking. The values were calculated with two different software (TopSpin and MestreNOVA)

Again, as can be seen in Figure 95, no correlation can be seen between the signal to noise ratio of wSTD experiments and the computational ranking. However, this time the s/n value resulted to be very high (see Figure 95). Surprisingly, the relatively low affinity of these nanoparticles for the analyte makes them very effective for HP wSTD experiments. Indeed, as discussed in the introduction, lower binding constants may allow the detection of analytes in a broader range of concentrations. When the affinity constant is high what happens is that the analyte binds strongly to the receptor pockets saturating them, and it usually ends up being in a slow exchange regime. Signals from bound molecules are therefore very broad due to their slower mobility and the problem with broader signals is that their intrinsic s/n ratio is much lower than that of narrow ones. In order to be able to use receptors with a high affinity constant (10^5-10^6 M^{-1}) they must be used at very low concentration. This means that

the operator should already know at least the order of magnitude of the constant for the analyte, and also the concentration at which is present in the sample, which is a very undesirable feature for an analytical technique. On the other hand, receptors with low affinities (10^1-10^2 M^{-1}) are simply ineffective in detecting analytes at low concentrations since the fraction of bound analyte is always too low to produce a detectable signal. Hence, the best possible compromise is the use of a receptor with an intermediate (10^3-10^4 M^{-1}) binding constant so that narrow signals can be obtained even at high receptor concentrations, which correspond to a broader detection range of analyte concentrations in the sample. This effect of the binding constant on the signal broadness can be appreciated in Figure 96. DRG-14 is a receptor with a very high K_a for 3-methoxytyramine (≈10^5 M^{-1}), when this nanoparticle is used for MeOTyr detection at 100 mM concentration, very broad signals were obtained with a s/n of 3 (which is commonly accepted as being the bottom edge of what can be considered detectable). With tripeptide-AuNPs, in the same conditions, the same signals can be easily detected with a S/N of 25 thank to their much greater sharpness.

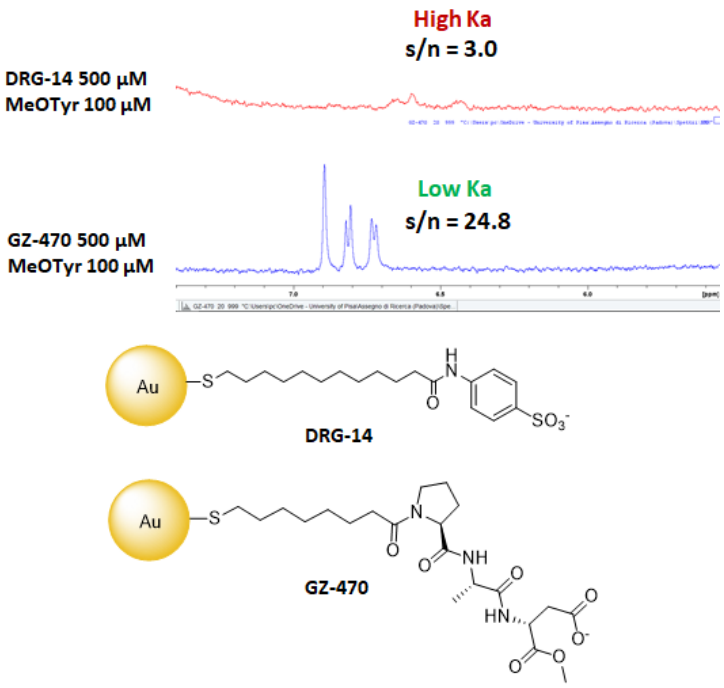

Figure 96: effect of the binding constant on the s/n ratio in HP wSTD experiments for the detection of 3-methoxytyramine

Discussion

One of the possibilities of the discrepancy observed between the experimental data and the predicted outcome is the fact that the efficiency for NMR detection is not really correlated

to the binding constant. A too high binding constant decreases the amount of magnetization on the analyte as the guest molecule, after being magnetized, remains bound inside the nanoparticle transient pockets. The inability of the free and bound guests of being in fast exchange prevents the spreading of the magnetization among the predominant unbound fraction of the analyte. In addition, different nanoparticles may have different magnetization transfer ability, with the results of altering the affinity/effectiveness correlation. Anyway, even the correlation between the observed diffusion coefficients and the binding affinity ranking is quite weak. The computational screening method seems therefore to greatly overestimate the ΔΔG of the binding events. These tripeptide-based chemosensors, however, seems to be well suited for NMR-chemosensing if used in combination with the high-power water-STD sequence, and offer valuable improvements over precedent generations of NMR-chemosensors. Their ability to sense the analytes in a broad range of concentrations is a key advantage toward the development of a real-world analytical technique based on this new technique.

Conclusions

More work is required in order to understand and be able to predict the behaviour of these peptide-based NMR-chemosensors. Apparently, the current computational method is still too inaccurate and not of much relevance for an in-silico screening of NMR-chemosensors, their development is therefore still a “trial and error” process. In order to be able to work also on the system selectivity, improvements on the MD simulations are required. Sensitivity of NMR-chemosensing based techniques can still be improved further and a novel strategy will be discussed in a later chapter.

2. Cavitand-functionalized NMR-chemosensors

Aim - cavitands as preorganized binding pockets

As discussed earlier, an important problem which currently limits the development of the NMR-chemosensing technique is the difficulty to design nanoparticle thiol monolayers having the right selectivity for the desired analyte. This is caused by the fact that the influence of the thiol structure on the binding properties of the nanoparticle is very complex. Indeed, “collective properties” arise from the specific spatial organization of the thiols that self-organize on the nanoparticle surface. If it were possible to attach some sort of pre-

synthesized molecularly-precise binding pocket to the nanoparticle, then it would be much easier to control the recognition ability of the resulting supramolecular system. This approach would also benefit from "operative advantages" typical of modular systems: as the analyte recognition ability is now independent from the nanoparticle core (intended here not only as the metallic gold core, but including also the binding-inactive thiols used both to graft the cavitands and to solubilize the nanoparticle in the desired solvent) it should be possible to design a standardized gold module to be used in a defined solvent, and then a second module, the desired "molecularly-precise pocket", would be grafted to tune the system selectivity accordingly. This principle was already demonstrated in the group of F. Mancin by the used of 18[crown]6 functionalized nanoparticles, as discussed in the introduction, which proved to be selective receptors for primary amines (also over amino acids) and cooperative receptors for polyamines. In this approach, however, each supramolecular receptor used needs to be functionalized with a thiol group for nanoparticles grafting. A nanoparticle functionalization approach not relying on the covalent modification of the supramolecular receptor, which might not always be trivial, would be highly desirable. Cavitands are a well-known class of molecules which are widely used as receptors for the realization of various types of chemical sensors.[88] Thanks to their interesting rigid vase-like shape, they allow to easily form an hydrophobic pocket which can accommodate hydrophobic portions of a guest molecule, shielding them from an otherwise polar environment. The cavitand structure can be functionalized on both the upper and lower rim to tune its recognition and physicochemical properties. Thanks to its peculiar properties, this class of molecules could be conveniently exploited as pre-formed and molecularly precise binding pockets to be grafted to AuNPs.

Cavitand-functionalized AuNPs

The easiest way to graft a cavitand to a nanoparticle is by employing a self-assembly process driven by ionic interactions, which are particularly convenient as they are not influenced by directionality, which would otherwise add unnecessary and difficult to predict conformational constrains to the system. In order to test cavitand-functionalized AuNPs suitability for NMR-chemosensing, phosC (Figure 97), a cavitand bearing four phosphonate groups on the upper rim and four positive charges linked to the lower one was obtained from prof. Dalcanale group (University of Parma). This molecule is known to selectively bind N-methyl ammonium cations, as N-methyl lysine (Figure 98).[89]

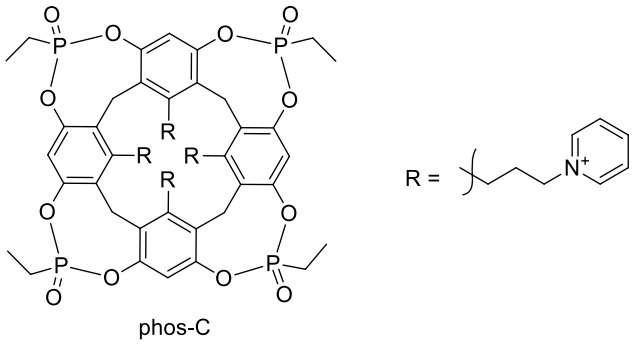

Figure 97: phosC cavitand structure

To prepare the self-organized nanoreceptors a solution of this cationic cavitand was mixed with a dispersion of AuNPs functionalized with an anionic monolayer in an appropriate molar ratio. Anionic nanoparticles functionalized with sulfonate groups (NP-SO_3) were chosen as they are well soluble in water and provide the negative charge necessary for the ionic interaction with the cationic tails of the cavitand. Sulfonate groups are also insensitive to protonation in a wide pH range. Nanoparticles with mixed monolayers (NP-mix), where the negatively charged thiol was diluted with a neutral one bearing a polyethylene glycol chain (47% of the thiols are charged), were also tested as chemosensors to explore the effect of the monolayer on the binding of the cavitand and to the sensing properties of the system (Figure 99).

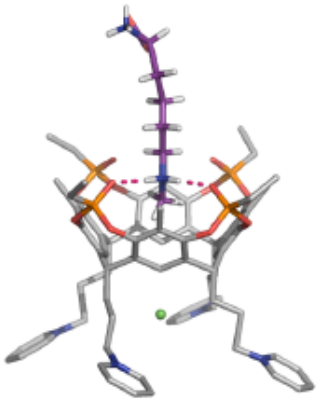

Figure 98: phosC interacting with N-methyl lysine hydrochloride[89]

The stock AuNPs dispersions were mixed with the phosC solution in phosphate buffered D_2O (pD = 7) directly in an NMR tube, and the experiments were then performed. Cavitand was added to the nanoparticles at a 1:8 ratio with respect to the sulfonic ligands. Indeed, binding of the cavitand to the particles surface might change their properties by neutralizing the negative charge and making the particle surface less polar. With the ratio used, only 50% of the particles surface is modified in the worst case.

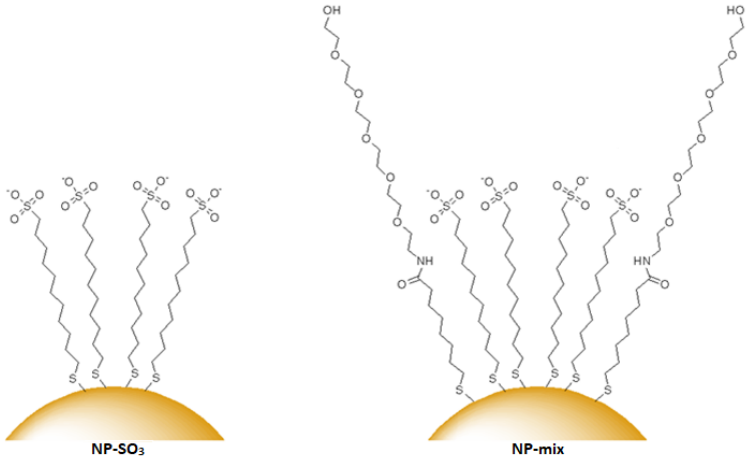

Figure 99: Anionic nanoparticles

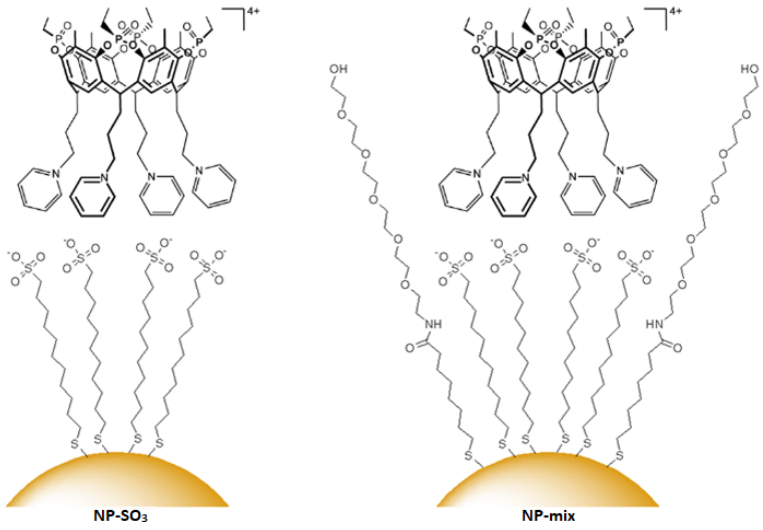

Figure 100: Anionic nanoparticles functionalized with cavitands

Effective binding of the cavitand to the nanoparticles was confirmed by NMR spectroscopy. Signals of the aromatic rings of the cavitand were detected after a diffusion filter in presence of NP-SO_3 (Figure 101). Dynamic Light Scattering (DLS) analysis of the nanoparticles showed no variation in hydrodynamic diameter after addition of the cavitand (Table 2). This effectively demonstrated that the presence of a cavitand with four positive charges on the lower rim tails is not inducing crosslinking and aggregation of the sulfonate-functionalized nanoparticles, suggesting that a single cavitand is not interacting with multiple nanoparticles.

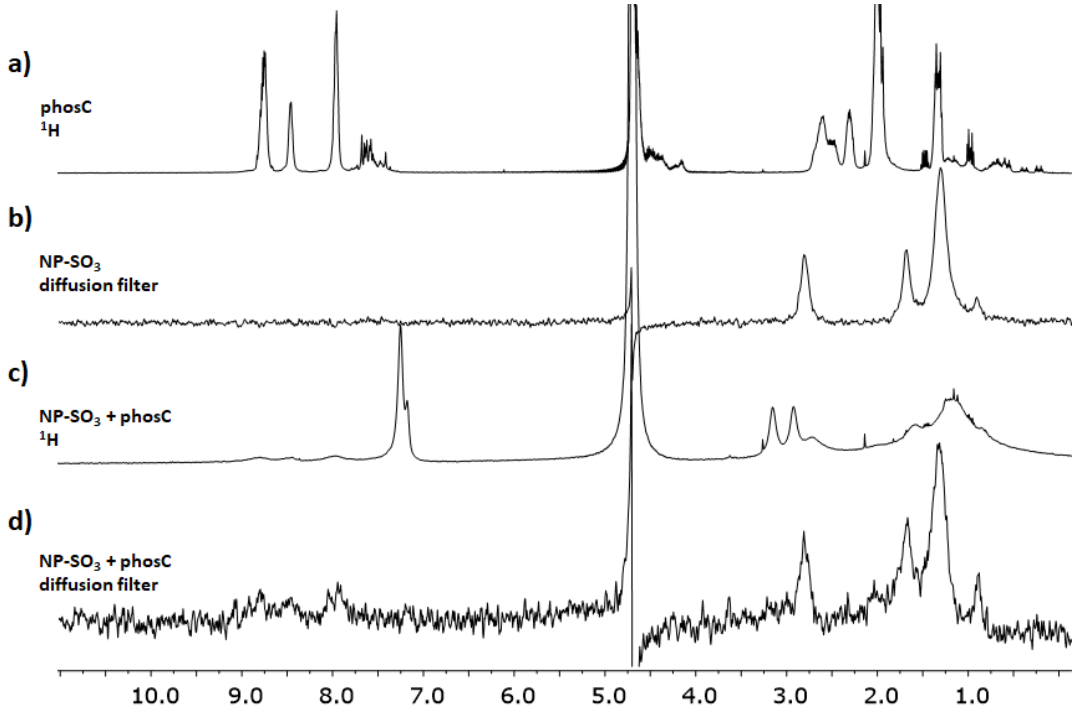

Figure 101: Binding of phosC to AuNP-SO$_3$ in D$_2$O. a) ^{1}H NMR of phosC, b) diffusion filter of NP-SO$_3$, c) ^{1}H NMR spectrum of NP-SO$_3$ (2 mM in thiol) and phosC (0.125 mM), d) diffusion spectrum of NP-SO$_3$ (2 mM in thiol) and phosC (0.125 mM)

Table 2: DLS and Zeta potential analysis of the AuNPs in presence and in absence of phosC cavitand. Buffer carbonate 10 mM (pH = 7) was used.

	AuNPs (µM)	phosC (µM)	size (nm)	err.std. (nm)	Zeta (mV)	err.std. (mV)
NP-SO3	20	0	**9**	3	**-21.5**	0.7
NP-SO3	20	1.25	**8.5**	0.5	**-25**	2
NP-mix	20	0	**6.0**	0.6	**-19**	2
NP-mix	20	1.25	**6.4**	0.4	**-27**	2

When phenNMe is mixed with phosC, the significative up-field shift and broadening of the analyte N-methyl group signals confirm that the receptor is able to recognize this molecule (Figure 102, second spectrum), while broadening of the aromatic signals is negligible. As can be expected, phenNMe interacts also with the anionic sulfonate nanoparticles NP-SO$_3$, and in this case signals are shifted to higher fields, but the shift and the broadening of the methyl group are less relevant than in the previous case (Figure 102, 3rd spectrum). The perturbation caused by the interaction with anionic nanoparticles seems to be more pronounced on the aromatic part of the analyte than on the N-methyl group, which undergoes a less relevant broadening. It is likely that the aromatic ring of phenNMe can enter in the inner hydrophobic

part of the monolayer leaving the charged cationic headgroup more free to move. When the phosC cavitand is present on the nanoparticles surface (Figure 102) the effects observed appear the combination of the previous ones. The broadening of the signals is greater than what is obtained with the nanoparticles alone, the methyl signal also undergoes a less relevant downfield shift, but a larger broadening, than with the sole nanoparticles. The most likely justification of these observations is that both nanoparticles and cavitand participate to the interaction with the analyte performing a multipoint interaction (i.e. the aromatic moiety is embedded in the monolayer and the methyl group is bound to the cavitand). This is quite noticeable since when phosC is grafted on the nanoparticles surface it partially "neutralizes" the negative charges of the monolayer preventing it to be available for ionic interactions with the methylammonium head group of the analyte. This effect alone should, in theory, disfavor the interaction of phenNMe directly with the anionic monolayer.

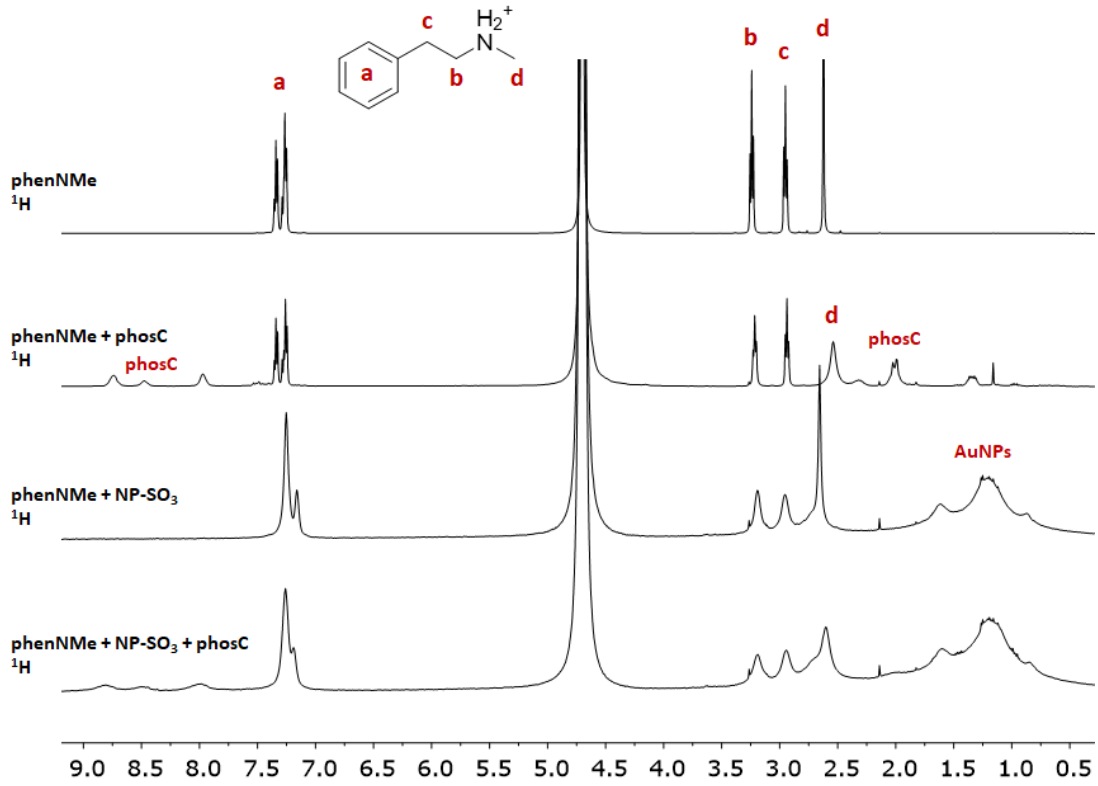

Figure 102: ^{1}H NMR spectra of phenNMe 1 mM, phosC 0.125 mM, NP-SO$_3$ 2 mM (in thiol) and phosphate buffer 10 mM (pD = 7) in D$_2$O

Diffusion filter and NOE-pumping experiments were then performed. The application of a diffusion filter removes the signals of the fast-diffusing species in solution leaving only the ones of nanoparticle-bound molecules. As can be seen in the third spectrum in Figure 103, cavitand and nanoparticle signals are retained after the application of the filter. This is a clear indication that the ionic interactions of the four charged tails with the monolayer are strong

enough to allow permanent cavitand grafting to the nanoparticle surface. On the other hand, analyte signals are not present suggesting a small decrease of the apparent diffusion rate of the analyte, and hence a small fraction of analyte bound.

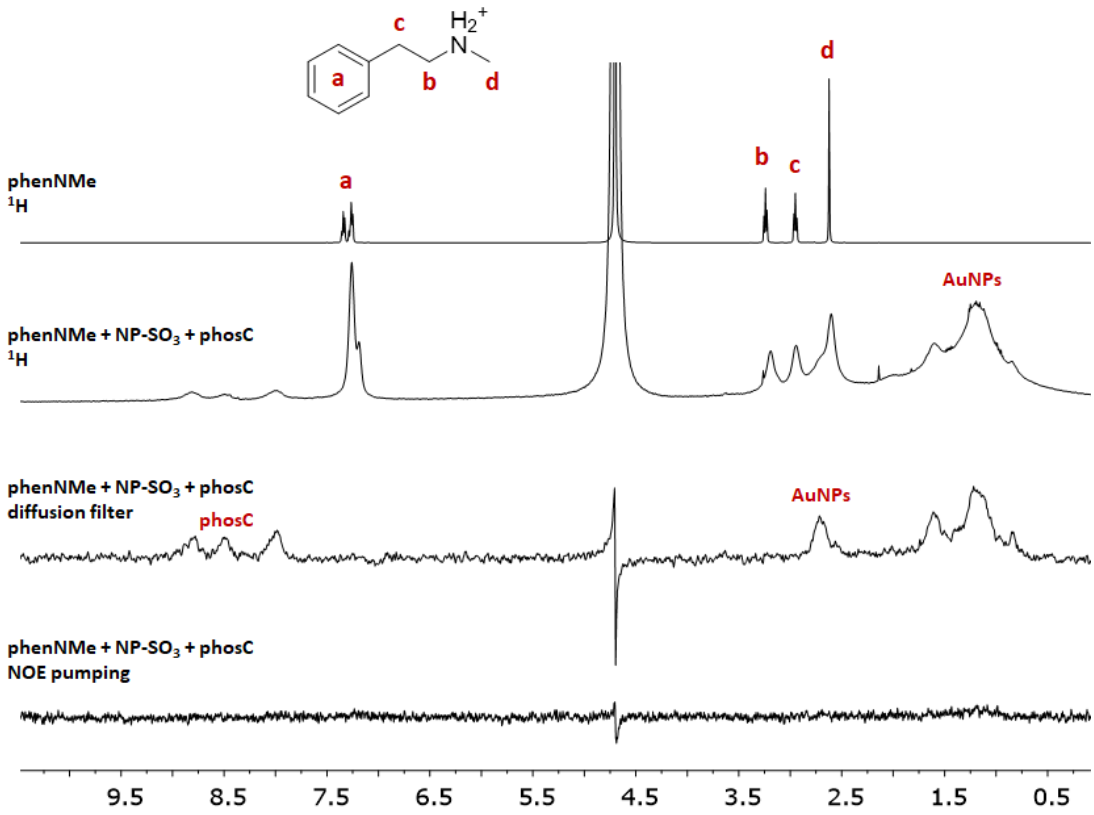

Figure 103: 1H, diffusion filter and NOE-pumping spectra with phenNMe. N-methylphenethylamine 1 mM, phosC 0.125 mM, NP-SO_3 2 mM (in thiol) and phosphate buffer 10 mM (pD = 7) in D_2O.

Unfortunately, it was not possible to detect any signal of the analyte with NOE-pumping experiments. The same experiments were repeated also with epinephrine as analyte, this time HEPES buffer was used instead of phosphate one, but the pD of the solution was kept identical. Epinephrine has a similar structure to phenNMe but has three hydroxy groups, two on the aromatic ring and one on the benzylic position. These three functional groups increase the hydrophilicity of this analyte and the two groups on the ring should disfavor the introduction of this portion inside the inner hydrophobic part of the monolayer. On the other side, the hydroxy group in the benzylic position could also disfavor the hydrogen bonding between the phosphonates and the methylammonium head group which drives the recognition at the cavitand upper rim. Epinephrine, similarly to phenNMe, gave the same negative result with the NOE-pumping experiment (Figure 104). However, by looking at the spectra it is evident that this supramolecular system is able to strongly interact with both of the two analytes since also the aromatic signals of epinephrine are massively broadened and

also shifted. There are two possible explanations for this negative result: the first is that the affinity of this system for the analytes is too high for NOE-pumping based NMR-chemosensing to be effective. This could explain why phenNMe and epinephrine are not detected in the previously described experiments. The second is that contacts between the monolayer and analytes spins are too few, or not close enough, to allow an effective transfer of the magnetization.

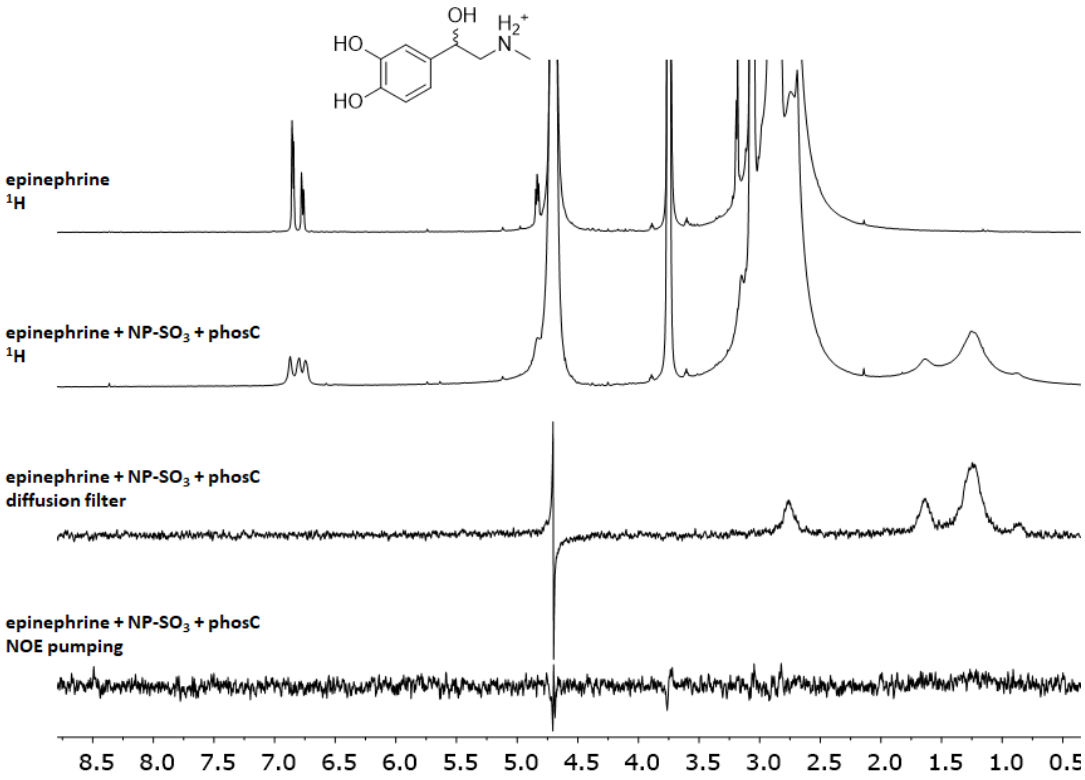

Figure 104: epinephrine (racemate) 1 mM, phosC 0.125 mM, NP-SO_3 2 mM (in thiol) and HEPES buffer 10 mM (pD = 7) in D_2O.

These supramolecular receptors were tested also for the detection of sarcosine, whose presence in urine was proven to be linked with the occurrence of prostate cancer[76], as phosC was already demonstrated to bind N-methyl aminoacids.[89] This molecule is zwitterionic at neutral pH and does not feature hydrophobic moieties, so it should not be recognized by the anionic nanoparticles in absence of the cavitand. In Figure 105 the proton NMR signals of sarcosine are compared with those of the molecule in presence of phosC and cavitand grafted to the anionic nanoparticles NP-SO_3. Both the two proton signals of the analyte resulted to be shifted and broadened in presence of the cavitand, especially those of the N-methyl group, suggesting it to be located inside the cavitand pocket after the binding event. The shift and broadening of these signals indicate that the cavitand is interacting with the analyte and thus confirming that it is an effective receptor for sarcosine. Unexpectedly

though, when phosC cavitand was grafted to NP-SO_3 nanoparticles, the analyte signals no longer exhibited the previously observed shift and broadening (Figure 105, last row).

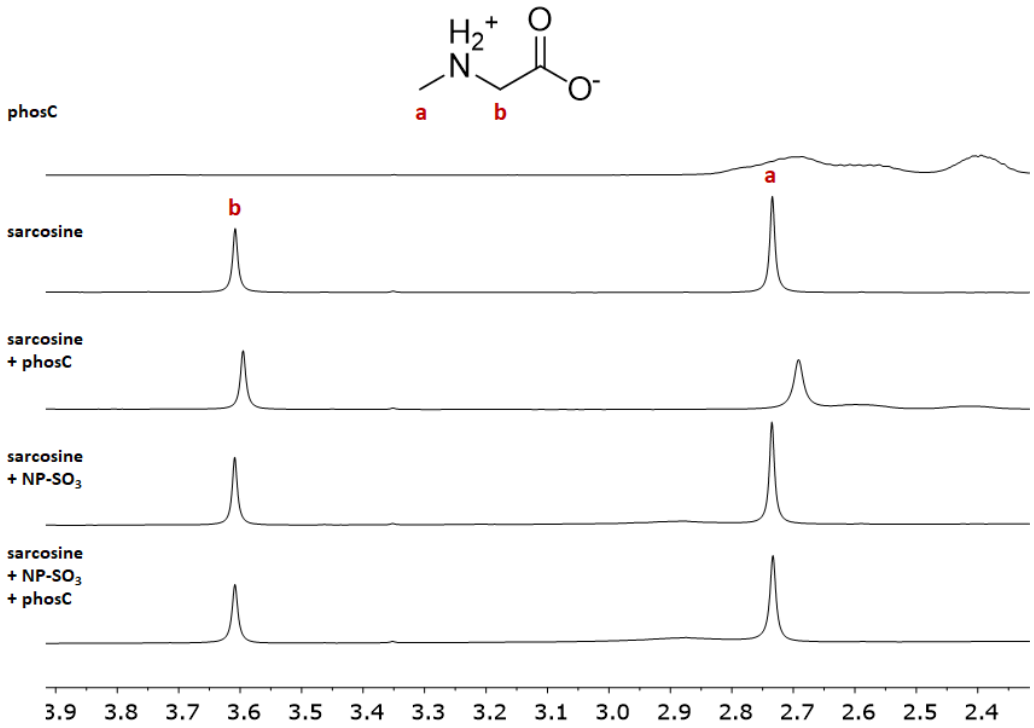

Figure 105: ^{1}H NMR signals of sarcosine in presence of phosC and NP-SO_3; sarcosine 1 mM, phosC 0.125 mM, NP-SO_3 2 mM (in thiol) and phosphate buffer 10 mM (pD=7) in D_2O

This is very curious considering that sulfonate nanoparticles should not interact with zwitterionic analytes, which is also confirmed by the fourth row of the same image. The presence of the anionic nanoparticles seems therefore to prevent the cavitand from recognizing sarcosine, which is apparently caused by the grafting of phosC to the nanoparticle surface. A possible explanation for this effect is that the cavitand conformation is changed when this species interacts with the nanoparticle monolayer, and that the new conformation is no longer able to bind methylammonium ions. However, considering that the cavitand upper rim is conformationally blocked by covalent phosphonate bridges, it is unlikely that the structure can be deformed enough to prevent the methylammonium recognition. It is more plausible that the cavitand, once its cationic tails interact with the sulfonate groups of the monolayer, expose to the aqueous environment not its upper rim but its lower one. If the upper rim faces the monolayer then the nanoparticle physically blocks the cavitand recognition site, preventing the molecular recognition from happening. This binding mode of the cavitand to the nanoparticle monolayer could also confirm why in the case of phenNMe it was possible to observe further broadening of the aromatic signals when in solution were present not only the nanoparticles but also the cavitand (as previously

discussed the free cavitand seems not to affect those signals). In this case it is possible that the cavitand is grafted "upside down" with the upper rim facing the monolayer and that the analyte bind to the cavitand phosphonates with the methylammonium head pointing "up" while its aromatic tail, much more hydrophobic than the carboxylate group of sarcosine, is inserted inside the alkyl portion of the monolayer. If this is the case, then there isn't an easy solution to prevent this binding mode and modifications of the cavitand and/or of the monolayer would be required. Standard NOE-pumping based NMR chemosensing experiments were then performed and again, even with this substrate, it wasn't possible to detect the analyte signals after NOE pumping.

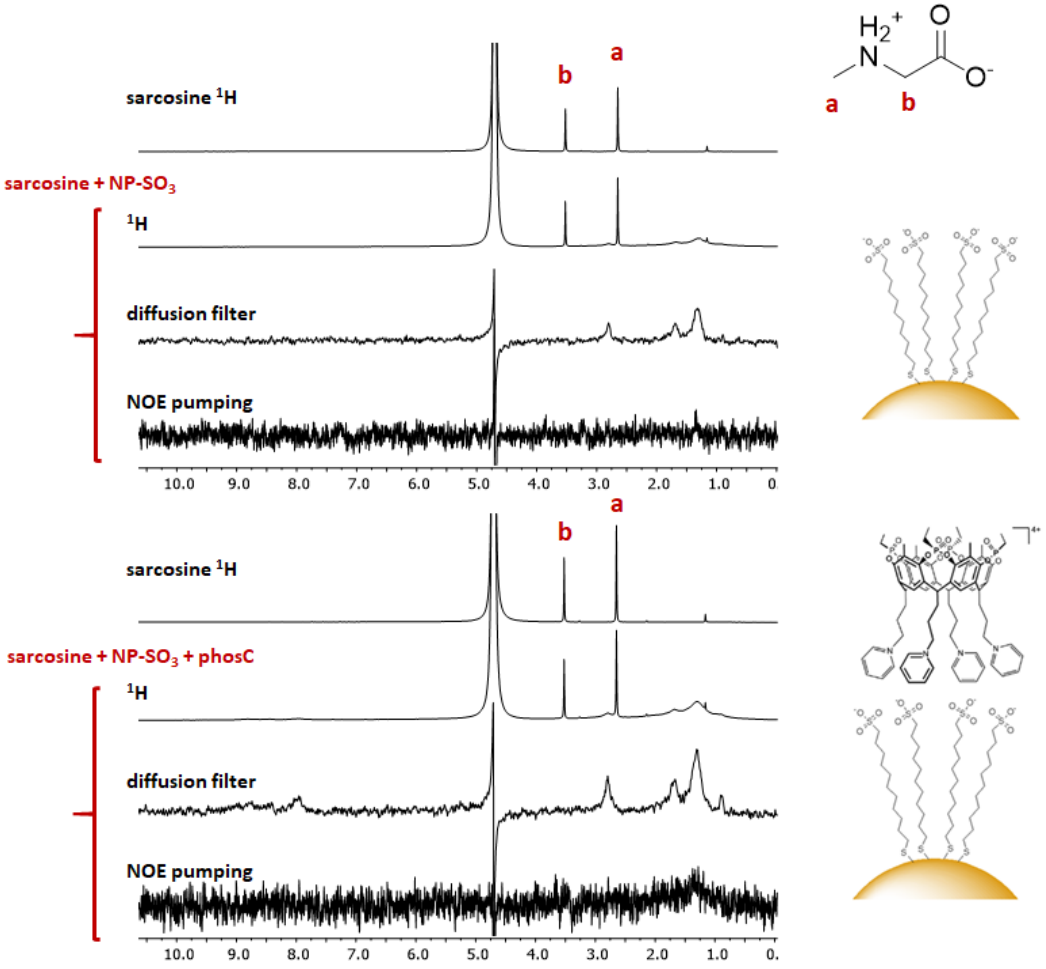

Figure 106: NOE pumping experiment for sarcosine detection. Sarcosine 1 mM, NP-SO_3 2 mM (in thiol) and phosphate buffer 10 mM (pD = 7) in D_2O; phosC absent above, 0.125 mM below

STD experiments were also tried for the detection of the analytes. At difference with NOE pumping experiments, they involve the continuous saturation of selected resonances on the receptor and provide consequently a greater sensitivity. Saturation of both the alkyl chains of the thiol monolayer and the pyridinium ions of the cavitand tails was tested to understand

which one was able to provide the greatest efficiency. In these experiments, at difference from the NOE pumping one, analyte signals could be detected. With both the analytes (phenNMe and sarcosine), saturation of the alkyl chains of the nanoparticle monolayer resulted to be the most efficient one in order to have the best signal to noise ratio for the analyte (Figure 107 and Figure 108).

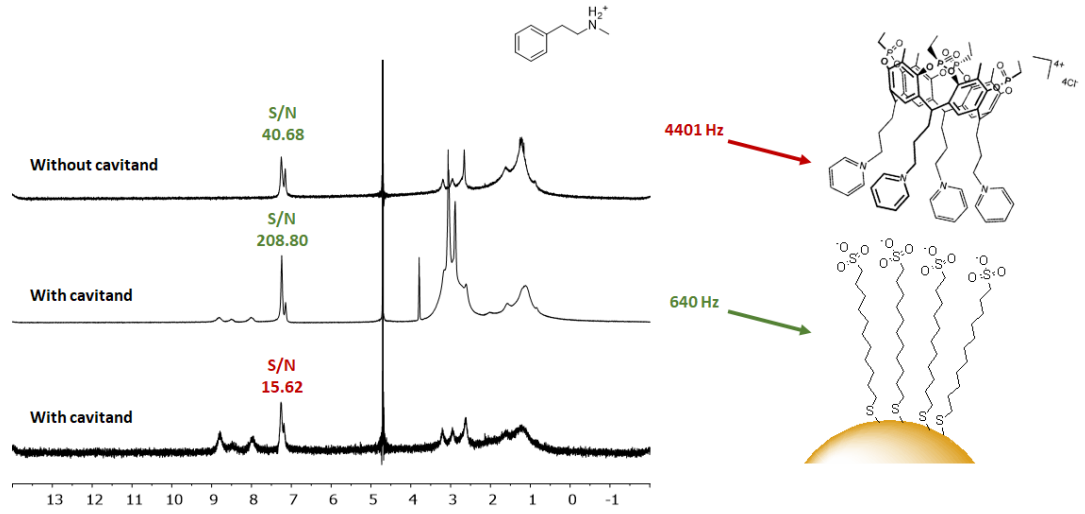

Figure 107: STD experiments for the detection of phenNMe. phenNMe 1 mM, NP-SO_3 2 mM, phosC 0.125 mM, phosphate buffer 10 mM (pD = 7) in D_2O; saturation on the monolayer and on the cavitand

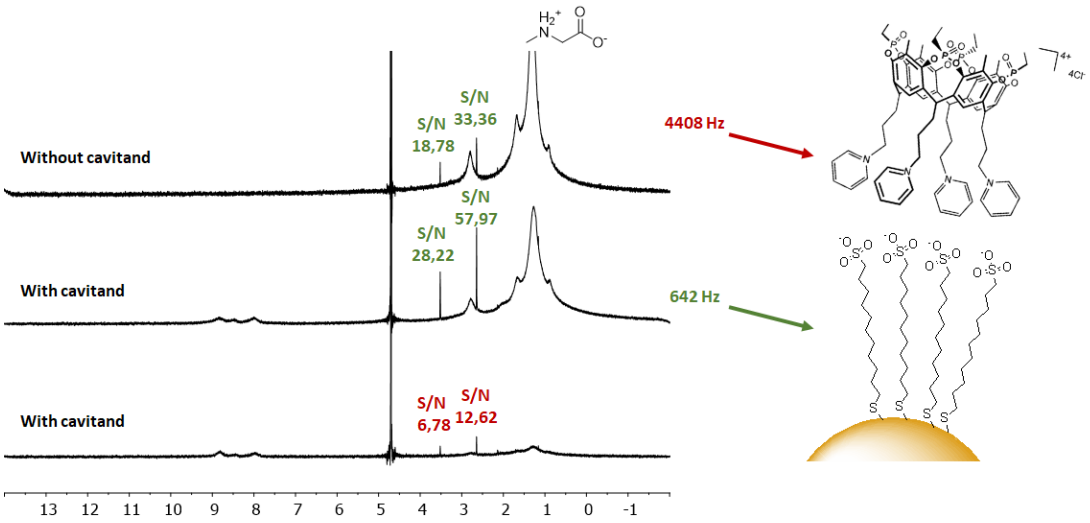

Figure 108: STD experiments for the detection of sarcosine. Sarcosine 1 mM, NP-SO_3 2 mM, phosC 0.125 mM, phosphate buffer 10 mM (pD = 7) in D_2O; saturation on the monolayer and on the cavitand

However, sensitivity of the sensing system featuring both the nanoparticles and the cavitand was much better than that of the sole nanoparticles. In addition, it should be noted that in the case of phenNMe the lineshape of the analyte in the STD spectra was not the same than that observed in the ^{1}H NMR one. This suggests that the signals obtained are not generated by the free analyte in solution (after saturation transfer and dissociation from the

nanoparticle) but form the analyte in the bound state, confirming the hypothesis of a high affinity of the sensing system for the analyte. To demonstrate that STD shows only signals from interacting molecules a set of experiments in presence of non-interacting species was performed. In these experiments an equimolar mixture of sarcosine (interacting molecule) and citrate (non-interacting molecule) were used. As can be seen in Figure 109, only signals from sarcosine are visible in the STD experiments.

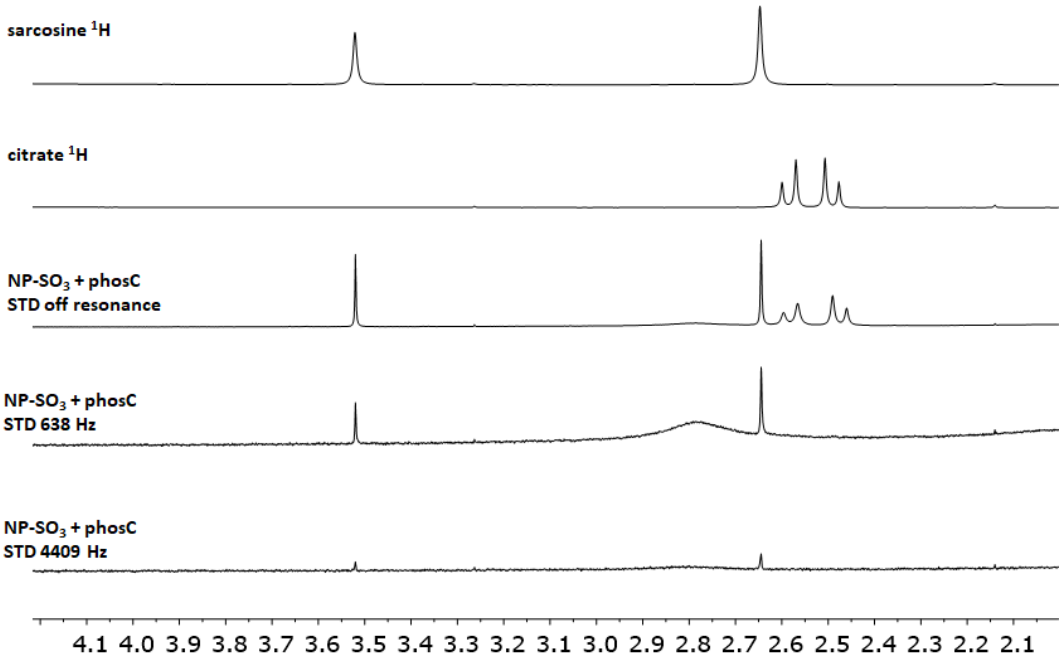

Figure 109: STD experiments on a mixture of sarcosine (1 mM) and citrate (1 mM) in phosphate buffer (10 mM). NPs 2 mM and phosC 0.125 mM in D_2O

STD experiments on phenNMe were also performed in presence of NP-SO_3 or NP-mix only. Comparing the spectra, which can be seen in Figure 110, it can be observed that, as already discussed, in the case of 100 % sulfonate nanoparticles (third spectrum, NP-SO_3) the aromatic signals of the analyte are shifted and have a different shape with respect to the ones in the first spectrum, where the analyte is free in phosphate buffer. On the other side, when mixed monolayer nanoparticles are employed, signals of the same shape and shift to those of the analyte in free state can be observed. This suggests that the neutral ligands of the monolayer prevent the analyte from interacting with the cavitand. It is possible that the PEG chains are filling the cavitand cavity, preventing it from being available for the analyte recognition. The analyte is therefore not included in the hydrophobic pocket and the signals remains identical to those in the free state. In both systems, with or without mixed monolayers, saturation of

the alkyl portion of the thiol chains proved to be much more effective than that of the aromatic region of the cavitand, leading to greater increase in s/n ratio of the analyte signals.

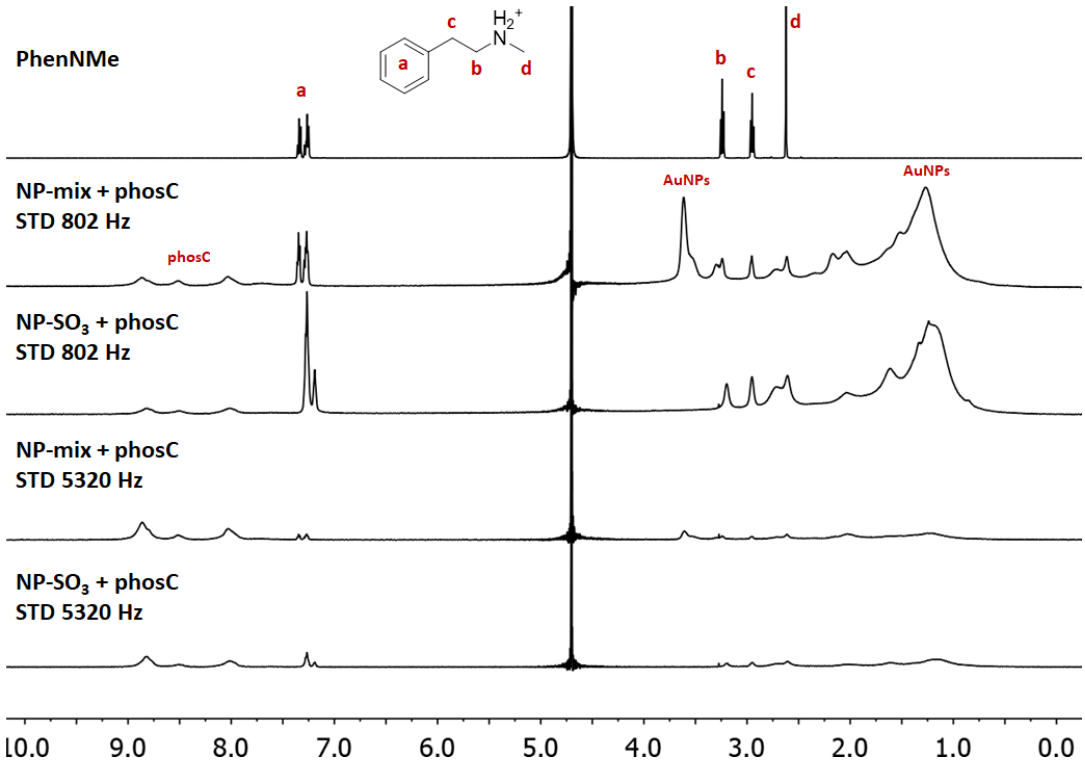

Figure 110: STD experiments; phenNMe 1 mM, NPs 2 mM (in thiol), phosC 0.125 mM and phosphate buffer 10 mM in D_2O. The first spectrum (on top) is a proton of phenNMe in phosphate buffer. The saturation frequency is reported on each spectrum.

Sensing through induced precipitation

Having demonstrated the interaction between phosC-functionalized NP-SO_3 nanoparticles and N-methylated ammonium ions, this system was tested also as a sensor for the visual detection of methylammonium dications. The idea was that a dicationic species interacting with cavitand-functionalized nanoparticles should crosslink them inducing precipitation (Figure 111). Of course, there is scarce interest for the detection of these molecules, but similar motifs are present on the surface of some protein (histones) whose detection is of interest as cancer biomarkers. Precipitation is an event which can be easily detected even visually by the operator, without the need of dedicated equipment, and would be usable as a strategy for the quick detection of dications and N-methylated proteins “in the field”. In addition, precipitation could be considered as an analyte concetration method, allowing subsequent more detailed analyses of the precipitate. Four dications were tested as sample

molecules (Figure 112), the first three were already studied by Pinalli group (University of Parma) and proved to be able to interact with phosC cavitand.

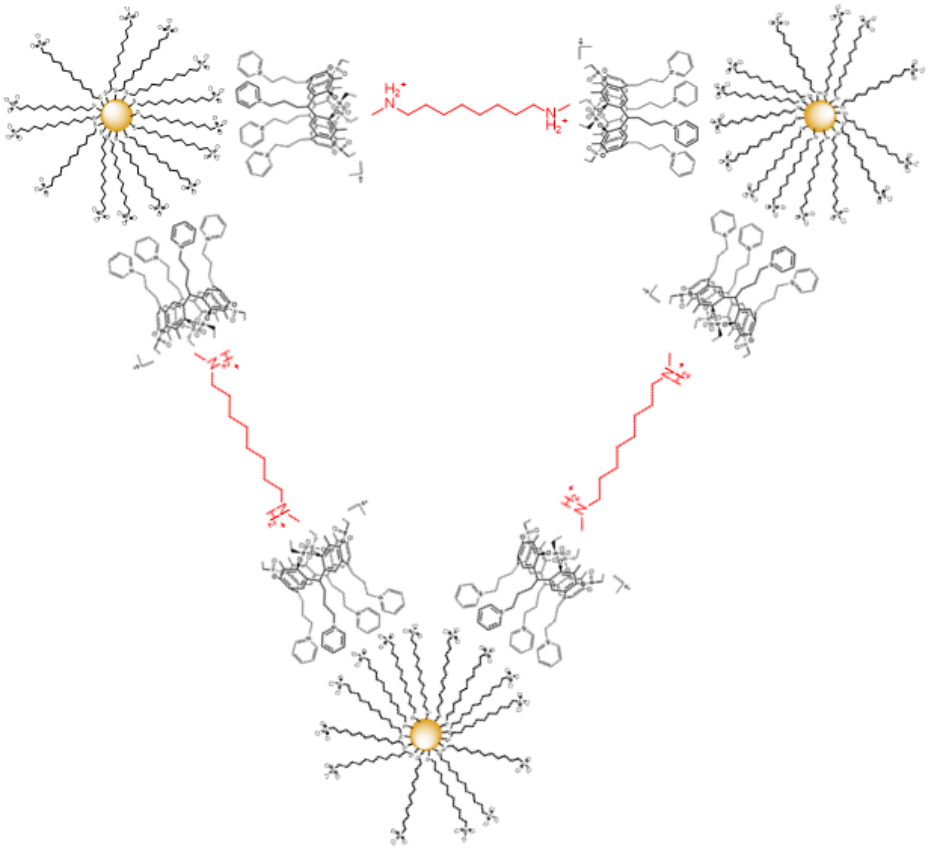

Figure 111: hypothetical dication-induced crosslinking

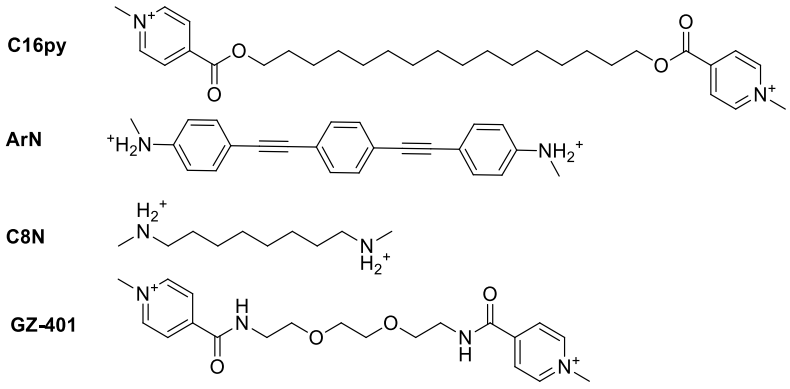

Figure 112: dicationic species tested to induce crosslinking.

These dicationic species were added as a solution in D_2O to the functionalized nanoparticles dispersion in substoichiometric amount (with respect to the cavitand). An excess of analyte would be undesirable to induce crosslinking because if the analytes saturate a large fraction of the cavitands, then the acquired free positive charges on the nanoparticle surface would

shield them from interacting with different nanoparticles. This would stabilize the colloid preventing the desired crosslinking and aggregation. Unfortunately, none of the tested analytes was able to induce precipitation, even after standing several days at room temperature. To better understand the interaction, the analytes were titrated by nanoparticles addition and followed by ^{1}H NMR. C8N and ArN were excluded from these experiments as in the first case signals were superimposed with the nanoparticles ones and the latter was not well solvated in water and always presented broad signals. The result of the titration of C16py with NP-SO_3 is reported in Figure 113. After the first addition of nanoparticles all the signals undergo a downfield shift, but the ones of the four aromatic protons adjacent to the pyridinium nitrogen split into two, indicating that a fraction of the analyte is interacting with both the terminal ionic headgroups while the other is bound with just one of them and exposes the other one to the water environment. Later, when the negative charges of the nanoparticles are in excess, these signals coalesced suggesting a situation where all the analytes are bound with both their ends.

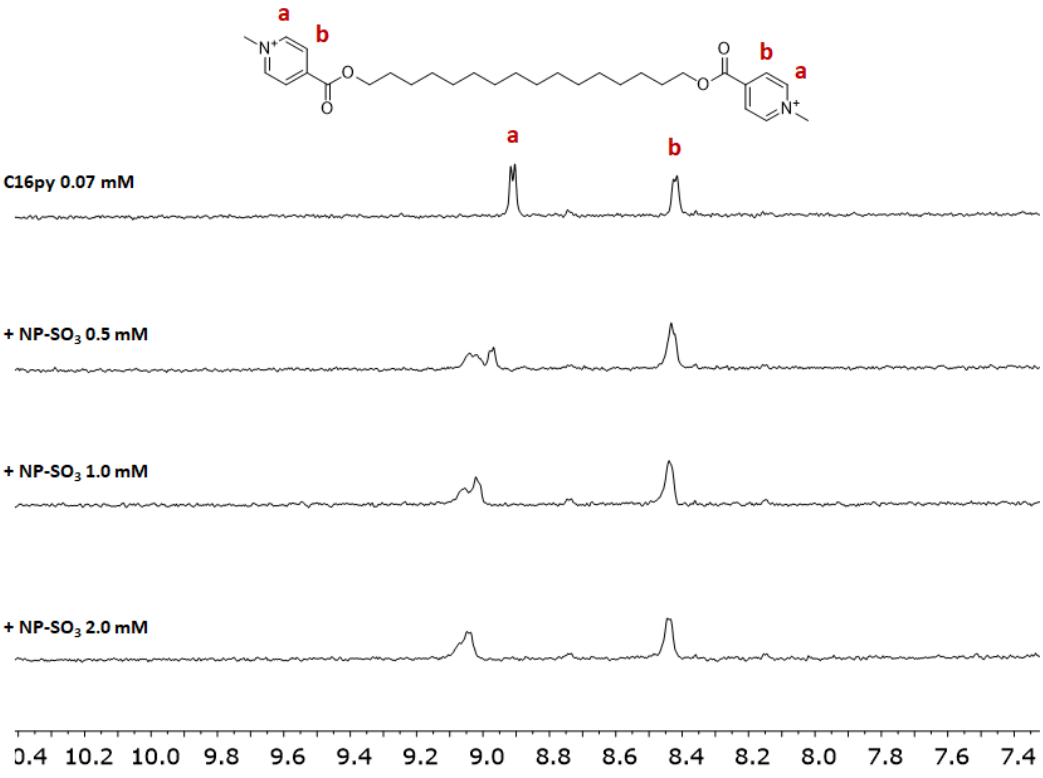

Figure 113: titration of C16py 0.07 mM with NP-SO_3 in D_2O.

Curiously, when the titration is performed with NP-mix (Figure 114) the aromatic protons signal splitting is always observed. Already after the first addition of nanoparticles the system seems to have reached equilibrium. Apparently, the presence of the neutral thiols in the monolayer disfavours the analyte from interacting with both its ends. As discussed in the

introduction the amide groups of the neutral thiols demonstrated to be able to form hydrogen bonds networks with water molecules, introducing them inside the monolayer. It is possible that, for the same reason, the internal part of the NP-mix monolayer results less hydrophobic, disfavouring the interaction with C16py alkyl chain and thus preventing it from interacting with both its extremities. When phosC is also present, all the signals become very broad and it is difficult to distinguish them from the superimposed cavitand ones (Figure 115). GZ-401 was therefore designed and synthesized to have a polar PEG-chain instead of an alkyl one. This PEG chain can be easily solvated in water and this could be enough to prevent its insertion inside the monolayer alkyl portion. With an analyte like this, bearing a hydrophilic chain which should prevent the partition of the molecule inside the inner hydrophobic part of the monolayer, it could in theory be possible to disfavour also the previously suggested binding mode of the cavitand, rotating it in the desired direction with the upper rim oriented toward the aqueous environment. As can be seen in Figure 116 and Figure 117, the experiments suggest that with an hydrophilic linker between the analyte charges there is no longer a preference for interacting with just one of the two extremities, and signal splitting is no longer observed. GZ-401 in the presence of NP-mix keeps showing very narrow and resolute peaks, suggesting that the environment in which the analyte is placed is much more flexible. This observation supports the previously suggested effect of the neutral thiols on the monolayer environment, making it more dynamic and water-solvated. This last situation would be, in theory, the ideal one to induce crosslinking of cavitand-functionalized nanoparticles as no significative direct interactions between analyte and nanoparticles were present. In this situation the interactions between cavitand and analyte would be the dominant ones. When NP-mix were present in combination with the cavitand, as can be seen in Figure 119, even if the aromatic signals of the analyte are superimposed with the ones of the cavitand tails, a significative signal broadening for GZ-401 can be observed. This must be caused by the binding of the analyte to the cavitand, as no broadening was detected with NP-mix alone (Figure 117). Unfortunately, no precipitation was observed.

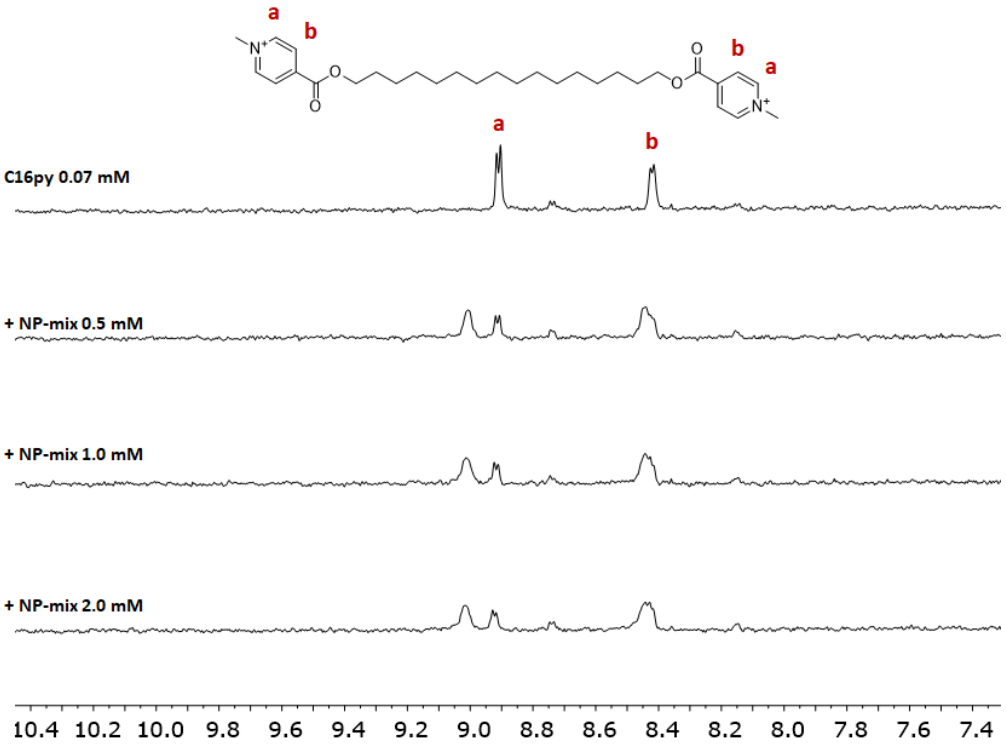

Figure 114: titration of C16py 0.07 mM with NP-mix in D_2O.

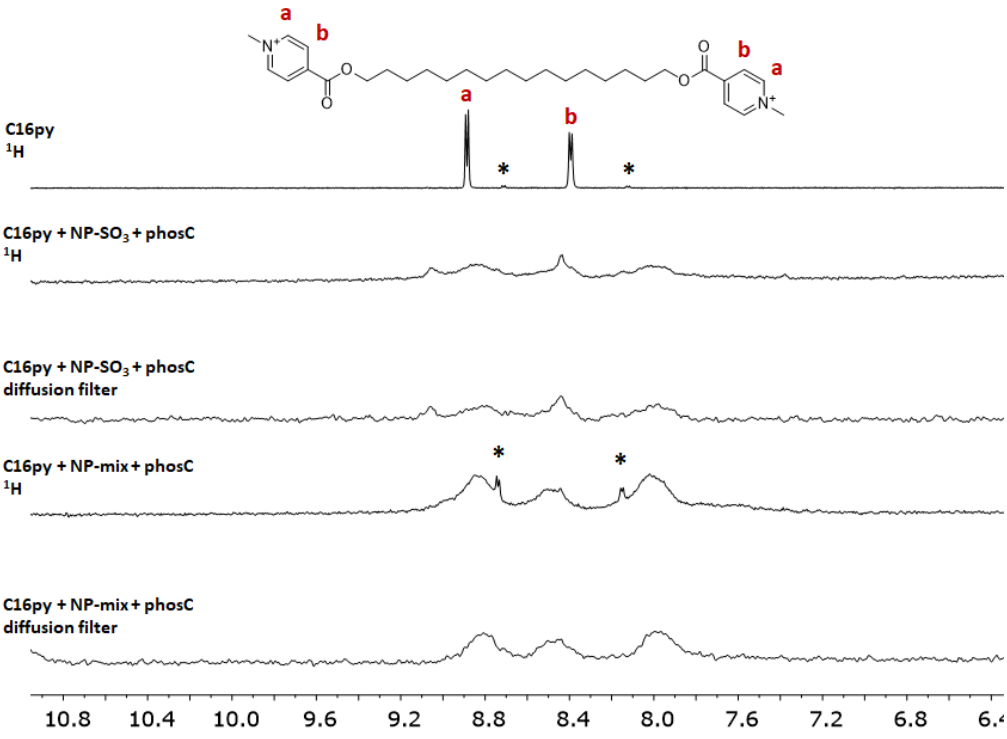

*Figure 115: C16py 0.0625 mM and, when present, NPs 2 mM and phosC 0.125 mM in D_2O; * marks impurities, probably an hydrolyzed byproduct of C16py*

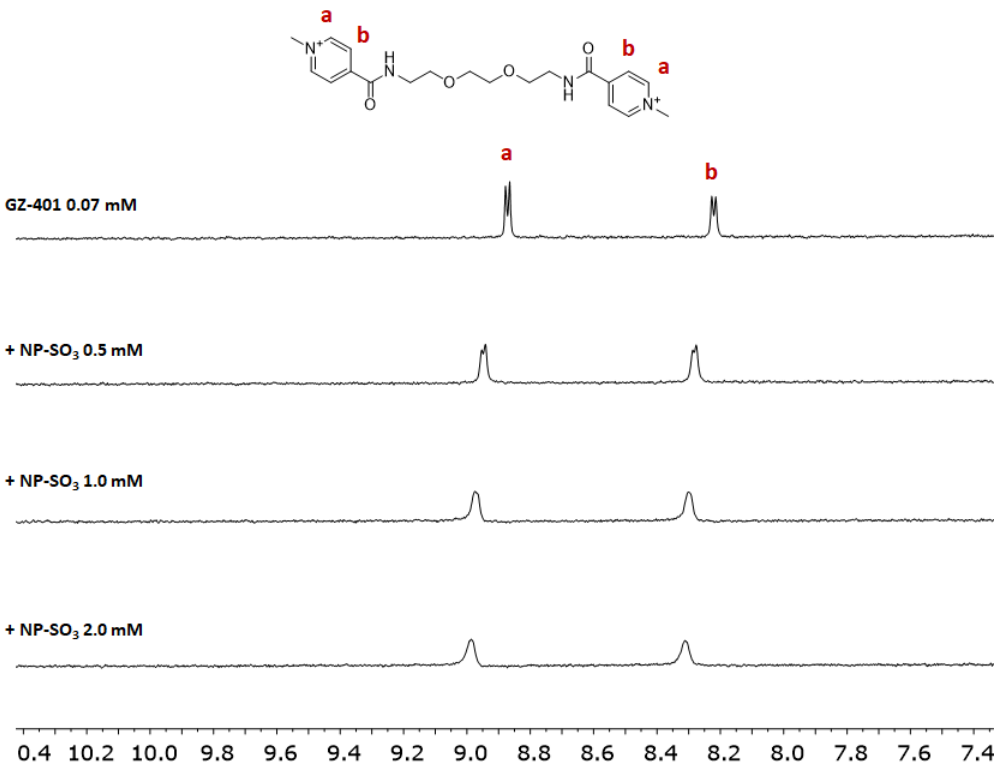

Figure 116: titration of GZ-401 0.07 mM with NP-SO_3 in D_2O.

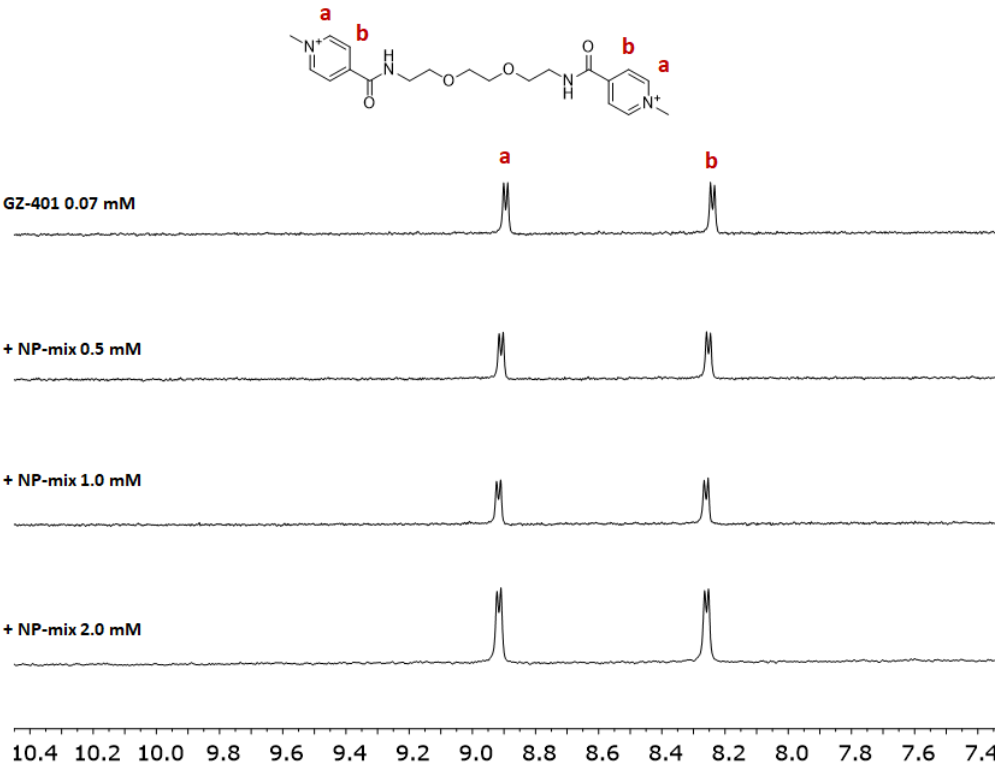

Figure 117: titration of GZ-401 0.07 mM with NP-mix in D_2O.

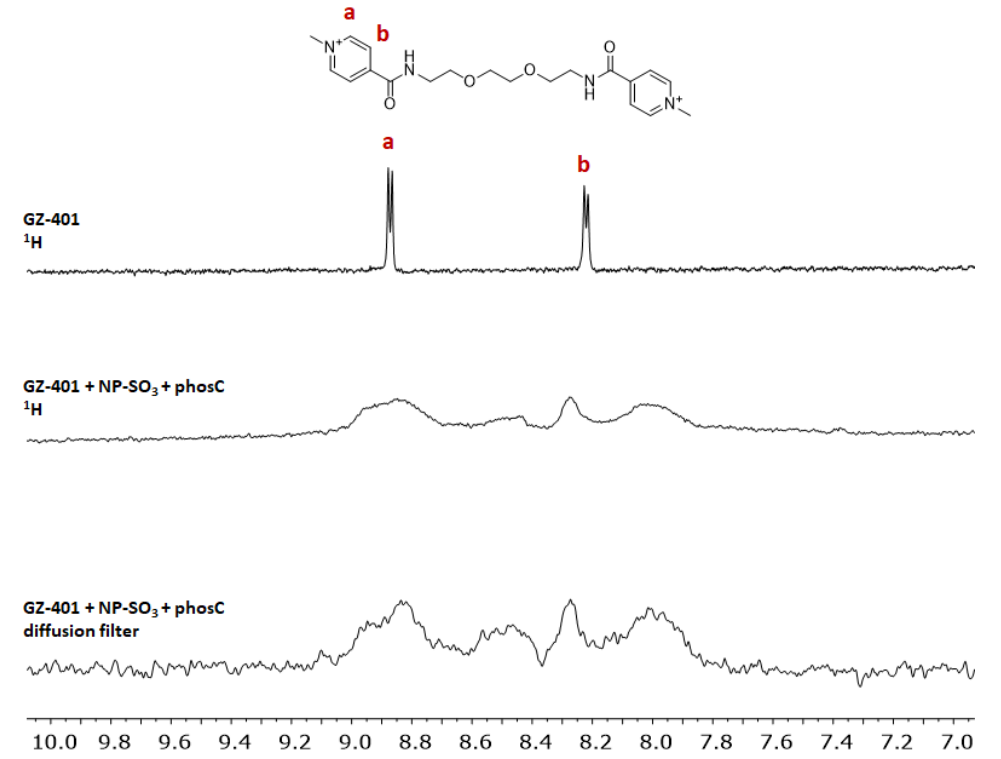

Figure 118: GZ-401 0.125 mM, NP-SO_3 2 mM, phosC 0.125 mM, D_2O

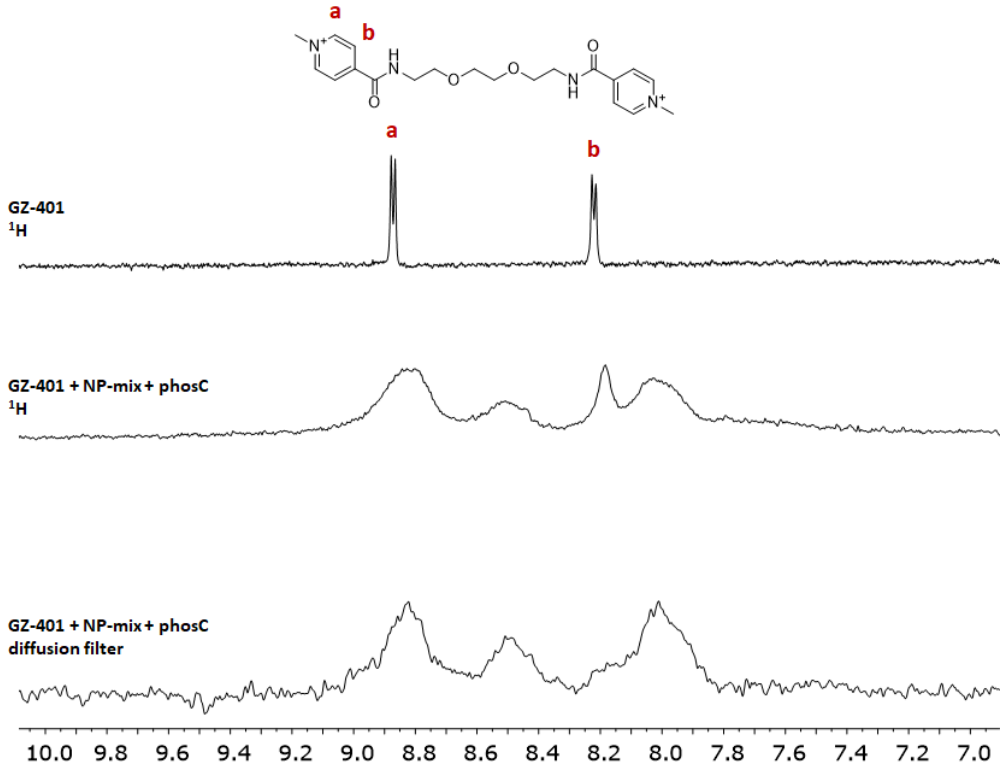

Figure 119: GZ-401 0.125 mM, NP-mix 2 mM, phosC 0.125 mM, D_2O

Conclusions

In summary, it has been possible to easily functionalize thiol-protected nanoparticles with cavitands by taking advantage of ionic interactions between charged thiols and charged tails on the lower rim. This strategy makes the (self-)assembly process extremely easy to perform, as it does not require any synthetic effort by the operator, and it could be even suitable for a high-throughput combinatorial synthesis approach. The interaction of the analytes with both free nanoparticles and cavitand-functionalized ones have been studied and a cavitand binding mode has been suggested. Apparently, the grafted cavitand exposes its lower rim to the aqueous environment. Though, the collected data are by no way sufficient for a definitive answer. The solvation and hydrophilicity properties of the nanoparticle monolayer can be tuned by using mixed thiols, where one is the ("active") charged one and the other (or others) is a neutral one bearing a hydrophilic portion directed toward the aqueous environment. By the use of mixed monolayer nanoparticles it was possible to strongly decrease the direct interaction between them and the analyte, allowing the cavitand binding site to be the predominant player in the supramolecular system binding properties. Unfortunately, it was not possible to use such system for the detection of sarcosine via NOE pumping NMR-chemosensing. However, it was possible to detect this molecule with STD experiments. The reason is likely the high affinity of the hybrids for the analytes, at least in the case of phenNMe, that prevents the effective recycling of the analyte in the monolayer and causes a relevant signal broadening. Other relevant limitations were found. The first and more relevant is that the monolayer of the nanoparticle is by itself a receptor for the target analyte class. This might reduce the selectivity of the sensing system, as other analytes with similar structure, i.e. phenethylamine derivatives, but devoid of the characteristic N-methylated head, could be still be recognized by the nanoparticles and detected. Finally, the need of a polyionic supramolecular receptor is by itself a limitation. In the case of cavitands, introduction of charged residues is a common strategy for making them water soluble, but it could not be easy to transfer such a strategy to other receptors, such as cucurbiturils as an example. It has not been possible to observe crosslinking-induced precipitation for the visual detection of dicationic analytes; NMR experiments however showed strong modifications that could be explained only by supposing an effective binding of the dications to the nanoparticles. Remarkably, such effects were by far more evident when the cavitand was added, suggesting a crucial role of this component. In theory, it is possible that a molecule similar to GZ-401 but having a longer and/or ramified PEG chain could induce it, but this would not be of practical relevance for analytical purposes and it has not been investigated.

3. NHC-protected gold nanoparticles

The realization of more selective and effective nanoparticle-based supramolecular receptors would receive a great benefit from new strategies capable to allowing control over the NPs ligand disposition in the monolayer.[74] The properties of the transient pocket-like binding sites formed on the surface of the nanoparticle do not depend only on the ligand structure itself, and designing a ligand having a good affinity for a target molecule doesn't necessarily translate into having an effective monolayer and thus an effective receptor for that analyte. The organization of the ligands needs to be controlled. As discussed in the introduction, NHC based monolayers could allow the creation of shorter and more rigid monolayers which could reflect in the creation of more uniform and controlled recognition pockets on the nanoparticle surface (Figure 120).

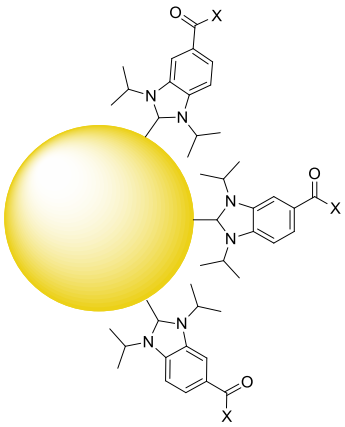

Figure 120: example of NHC-functionalized AuNPs, where X is a generic functional group

Currently, thiol-protected AuNPs for NMR-chemosensing are synthesized by a modified two-phases, two-steps Brust and Schiffrin procedure developed by Scrimin[11] (Figure 121) and described in the introduction.

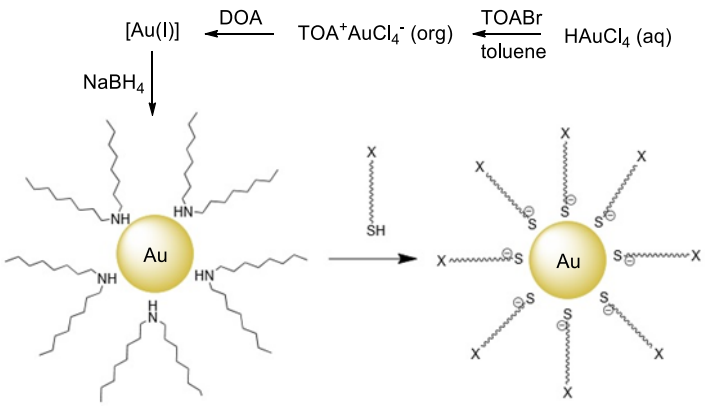

Figure 121: standard procedure for thiol-protected AuNPs synthesis

In particular, initially dioctylamine (DOA) coated nanoparticles are synthesized and then the thiol is attached in a second step by ligand exchange. Ideally, it would be convenient to develop a functionalization strategy to obtain NHC-protected AuNPs starting from the DOA-protected ones. To prepare a library of NHC ligands capable to endow the coated nanoparticles with molecular recognition abilities the benzimidazolium salt GZ-174 (Figure 122) was chosen and synthesized as carbene precursor. This molecule bears an exposed acid head group, which could conveniently be used to functionalize it further for the creation of the desired monolayer. The two isopropyl groups on the nitrogen atoms, as discussed in the introduction, should be sufficiently sterically demanding to keep the carbene stable against dimerization and, at the same time, not enough to prevent an efficient binding to the gold surface. The incorporation of a benzimidazole ring has been demonstrated to be important for the synthesis of more stable monolayers on gold surfaces, with respect to imidazolylidenes.

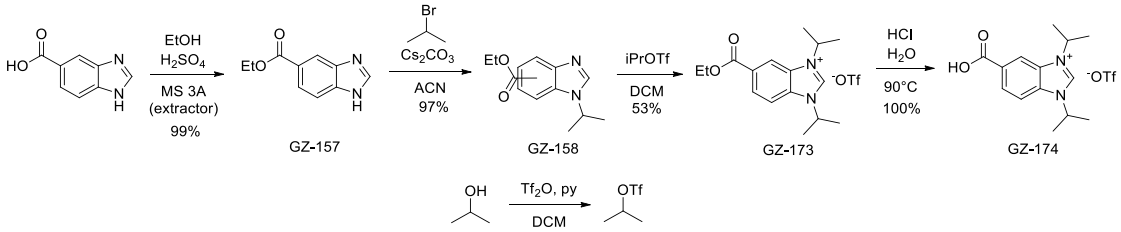

Figure 122: NHC precursor synthesis

The synthesis of the relative NHC-protected nanoparticles was explored following two different pathways: in the first case (Figure 123), the free carbene was synthesized via benzimidazolium deprotonation with a mixture of sodium hydride and potassium tert-butoxide, and this solution was then filtered and added to the dispersion of DOA-protected nanoparticles. In the second case (Figure 124), benzimidazolium salt and bases were added directly to the DOA-protected AuNPs dispersion producing the carbene in situ. In the first case nothing was obtained, while in the second case it was possible to obtain NHC-protected AuNPs. Unfortunately, these nanoparticles turned out to be unstable and, after only a single day, the dispersion turned red (indicating nanoparticles growth) with the formation of a black precipitate.

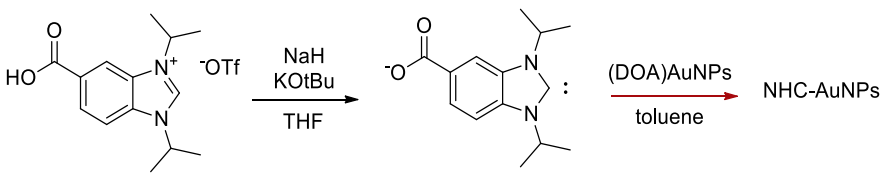

Figure 123: Attempted synthesis of NHC-AuNPs by ligand exchange with the free carbene

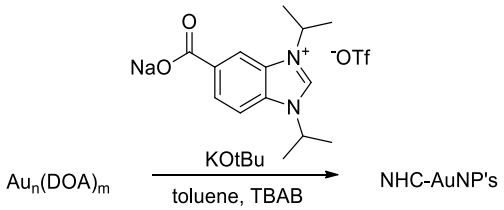

Figure 124: attempted synthesis of NHC-AuNPs by ligand exchange with in-situ formed carbene

In the end, none of the two strategies allowed to synthesize the desired AuNPs. The instability of the obtained colloids could be caused by a different and incompatible superficial structure between the DOA-protected and the NHC-protected ones. The ligand exchange reaction, apparently, can be performed with thiols but not carbenes. It is plausible that the NHCs atop binding mode does not allow a sufficient stabilization to the superficial features of the structures synthesized with the DOA-protected AuNPs synthetic procedure, which instead can effectively be stabilized by the formation of the staple motif with sulfur-based ligands. Thiolate ligands are also charged species while carbenes are neutral. While not of great interest for NMR-chemosensing applications, the ligand exchange procedure was tested also on 10 nm citrate-capped AuNPs in water by addition of a methanol solution of benzimidazolium salt (5 equiv.) and KOtBu (5 equiv.). The nanoparticles were left stirring overnight and then purified by dialysis (Amicon Ultra 100k membranes, 5000 rpm) 7 times with ultrapure water. However, once evaporated under vacuum, a gold mirror formed on the bottom of the flask. Neither starting from citrate-capped AuNPs it was possible to obtain stable NHC-protected nanoparticles. If the structural difference plays an important role in the colloid stability, then to synthesize stable NHC-protected NPs a different synthetic approach needs to be employed. The protocol followed is based on a single-step process where an Au(I) dicarbenic complex is reduced in water with sodium borohydride in presence of tetrachloroauric acid as supplementary Au ions source (Figure 125). This procedure was reported to produce stable NHC coated gold nanoparticles. [32]

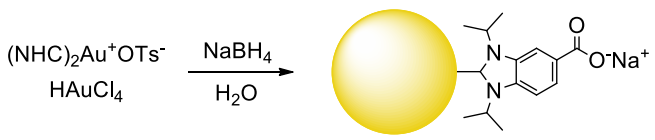

Figure 125: NHC-protected AuNPs synthesis by direct reduction of a mixture of Au(I) and Au(III)

The synthesis of this dicarbenic precursor is schematized in Figure 126. The complex is initially synthesized with the acid group protected as ethyl ester by in situ deprotonation of the benzimidazolium precursor (GZ-173) in presence of dimethylsulfidegold(I) chloride. Thanks to dimethylsulfide volatility, this species can be easily removed improving the yield of the

reaction. The Au-C bond is strong enough to sustain the hydrolysis conditions with sodium hydroxide in the following step and the target compound was produced in a reasonably high yield. This complex is stable and can be purified by column chromatography on silica.

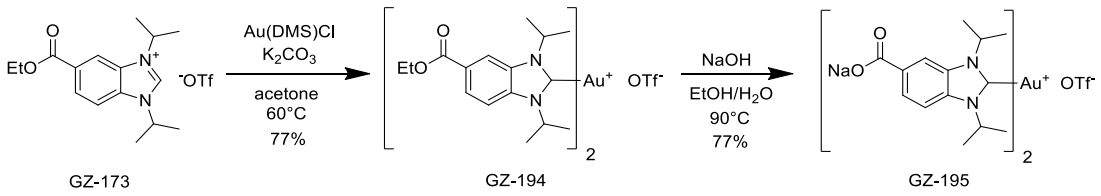

Figure 126: Synthesis of the dicarbenic gold complex

By direct reduction of this dicarbenic gold complex (GZ-195) in presence of additional Au(III), added as tetrachloraurate(III), it was possible to obtain nanoparticles of 1.7 nm of diameter which, this time, turned out to be stable in solution. This procedure, in contrast to the DOA-mediated one, is not optimized and relies on the interruption of the reduction reaction after 5 h, followed by purification by dialysis. The yield is very low and not comparable to the available synthetic strategies for thiol protected gold nanoparticles. While being much more stable than the previously synthesized ones, these nanoparticles still had stability issues. This issue can be noticed especially when the dispersion is dried, even if "mild" procedures, such as lyophilization, are employed. Leaking of dicarbenic Au(I) complex was always observed by ^{1}H NMR. In Figure 127 are reported the proton spectra recorded after sequential size exclusion chromatography purifications. All the benzimidazolium signals clearly become each time narrower, indicating a progressive detachment of the ligands from the nanoparticle surface. For comparison, a diffusion filter spectrum recorded in the same conditions is reported on the right. It is immediately obvious how different it is from the proton spectra on the left and how broad the signals of the surface-bound carbenes actually are. To explore the binding of the NHCs to the gold nanoparticle, the charge of the gold atoms which are bound to the ligands could in theory be determined by comparing the chemical shift of their carbenic carbon with the respective one of the dicarbenic gold(I) complex. Unfortunately, it has not been possible to record a ^{13}C spectrum of the organic monolayer, even after 25 h of acquisition time. Considering the instability of the system it was decided not to further increase the acquisition time.

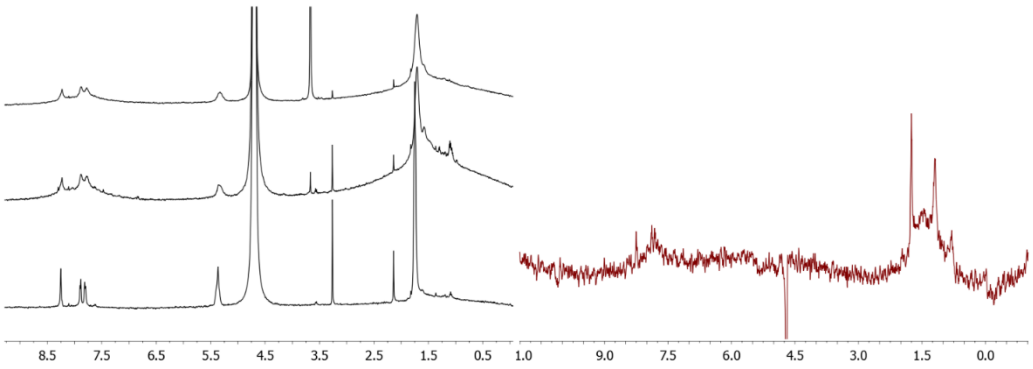

Figure 127: On the left ^{1}H NMR shows leaking of NHC gold(I) complex after sequential size exclusion chromatography (from the top to the bottom); the diffusion filter on the right shows the broad signals of the bound carbenes

Despite an effective nanoparticle synthetic methodology is still lacking and the instability of all the yet obtained dispersions, it is important also to develop a viable and flexible synthetic strategy for the carbene precursor, which should be easy and flexible enough to allow nanoparticle functionalization with a wide range of desirable function groups. However, despite having invested a lot of time on this aspect, I could not find the solution to this problem.

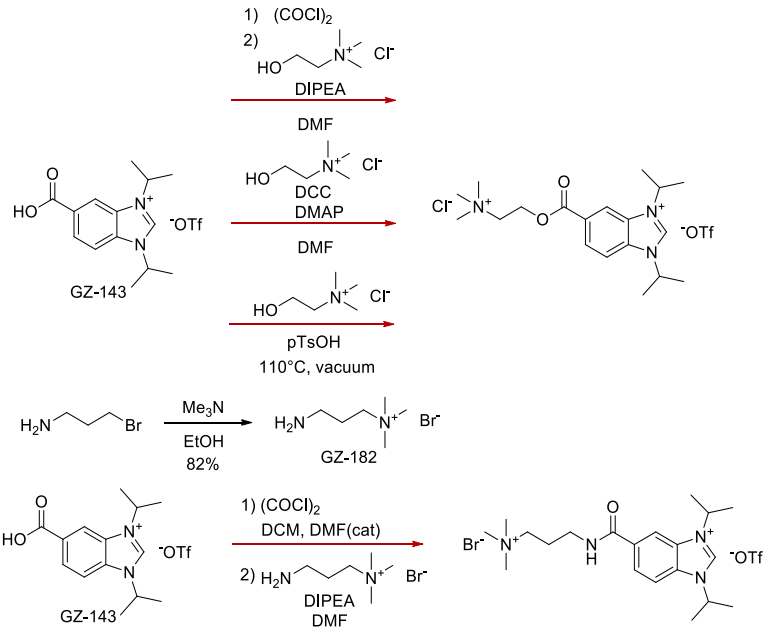

Figure 128: benzimidazolium functionalization tests, red arrows indicate reactions which didn't work

As a first test, due to the lacking of known cationic NHC-protected nanoparticles in literature, it was decided to functionalize a carbene with the positive charge of a trimethylammonium group. A direct functionalization was tried by ester coupling of the commonly available choline chloride on the benzimidazolium carbene precursor (Figure 128). Choline chloride

unfortunately turned out to be a really unreactive nucleophile. A functionalization through amide coupling was also tested (Figure 128) as amides are more stable toward hydrolysis than esters. A C_3 linker was chosen instead of a C_2 in the hope that an increased distance between the N-nucleophile and the positive charge would lead to an increase in reactivity. Different strategies were tested (Figure 128) but none worked. In all cases but acid transesterification (with choline chloride) benzimidazolium decomposition was observed. I also tried to synthesize a similar molecule by using the same moiety provided by choline chloride but employed this time as an electrophile (Figure 129). An alkyl bromide bearing the trimethylammonium charged head group was reacted with GZ-159 after deprotonation of its alcoholic groups with sodium hydride. This reaction also yielded no product.

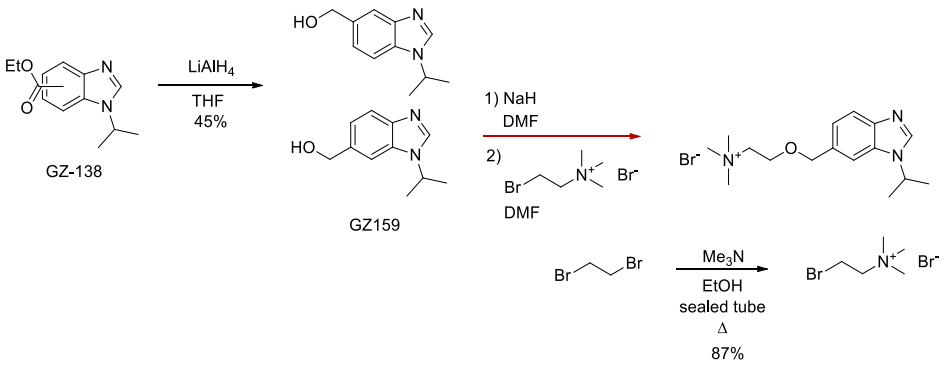

Figure 129: benzimidazole headgroup functionalization attempt

A new synthetic approach was followed leaving the benzimidazole ring second N-alkylation as the last step (Figure 129). Indeed, the results of the several failed attempts so far discussed (Figure 128 and Figure 129) suggested that the presence of two positive charges so close might be a problem, decreasing the stability of the desired carbene precursor. Again, choline chloride proved to be an unreactive nucleophile, even on neutral substrates (Figure 130). A C_2 spacer between a trimethylammonium ion and the ester group seems too short for the molecule to be stable. The idea of using a C_2 linker was therefore abandoned.

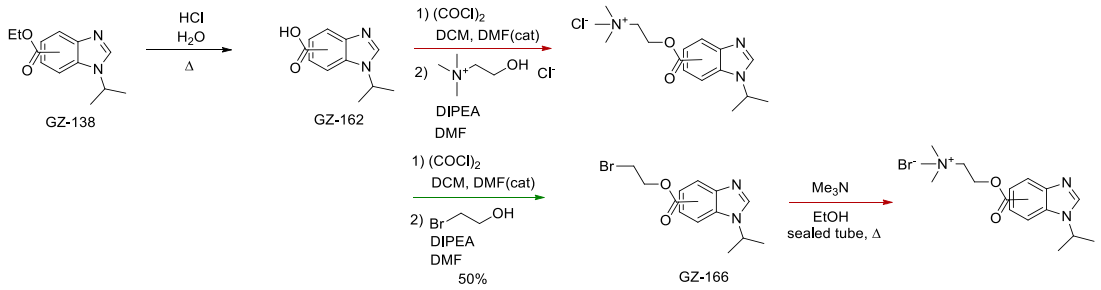

Figure 130: choline chloride is an unreactive nucleophile and choline esters seems to be too instable

The linker length was therefore increased of one unit. A C_3 linker seems finally to solve the reactivity issue and it was finally possible to install a positive charge via amide coupling (Figure 131). Unfortunately, the resulting benzimidazole couldn't be alkylated to benzimidazolium (Figure 132) anymore. Both isopropyl triflate and iodide were unable to react with this substrate.

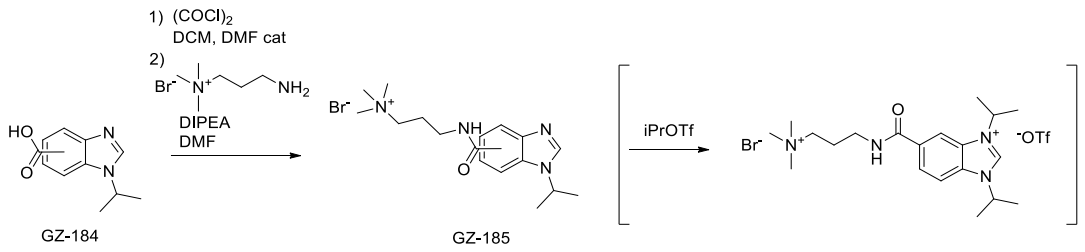

Figure 131: first attempt to the synthesis of a benzimidazolium salt with a trimethylammonium headgroup linked through a C3 spacer

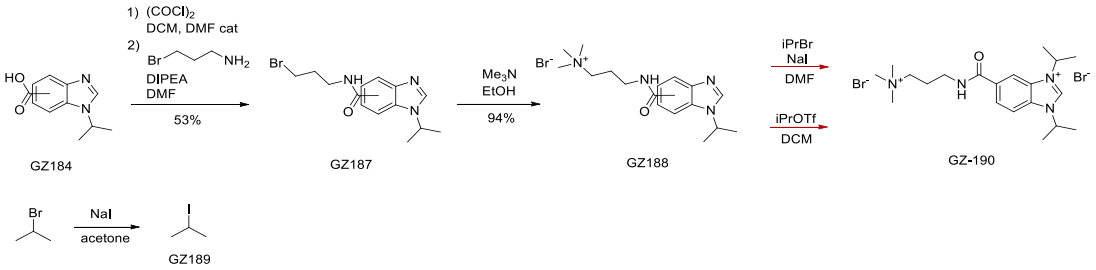

Figure 132: second attempt to the synthesis of a benzimidazolium salt with a trimethylammonium headgroup linked through a C3 spacer

Another way to obtain the desired molecule could be through a post functionalization approach of Au-NHC nanoparticles with a carbene ligand bearing a free acid group on the outer extremity. A mild amidation could be a suitable reaction for this scope but in order to be able to follow this route a synthetic strategy leading to stable NHC-protected nanoparticles is required. The NHC-protected nanoparticles previously described in this work are definitely not suitable for such post-functionalizations.

Conclusions

Unfortunately, it was not possible to synthesize stable NHC-protected AuNPs and, even when it was possible to isolate them, degradation was observed to rapidly occur. A "bottom-up" approach resulted in more stable colloids, which is not in agreement with what is reported in literature.[31] The ligand exchange reported in literature as "top-down" example, however, started from didodecyl sulfide-protected AuNPs, while in this work dioctylamine-protected

ones were employed. Apparently, while N,N-diisopropylbenzimidazolylidenes seems to be viable ligands for the functionalization of macroscopic surfaces, they are not so effective when used for the stabilization of colloids. Instability due to dicarbenic Au(I) complex leaking has been reported also in literature for smaller Au clusters.[90] The synthesis of the carbene precursor itself, which at first look it could seems straightforward, turned out to be quite difficult and these structures apparently seem not to be flexible enough to allow easy functionalization, even with simple and common functional groups.

4. SABRE parahydrogen hyperpolarization

Improving NMR sensitivity

A relevant problem of NMR-based techniques in chemical analysis is their intrinsic low sensitivity. Signal Amplification by Reversible Exchange (SABRE) is a technique which allows to hyperpolarize a wide range of molecules in a reversible process without the need of any chemical modification. The technique is based on the use of para-hydrogen (p-H_2), a molecule in which the nuclear spins are antiparallel in a singlet state, and a metal catalyst which can react with p-H_2 by oxidative addition (usually Ir^+ hydrogenation catalysts) and can bind the analyte. Reacting p-H_2 with the catalyst breaks its singlet state symmetry and generates an excess of polarization on the two hydride ligands, called hyperpolarization. Once generated, this hyperpolarization is transferred also between the resonances of the equatorial metal ligands through zero-quantum coherences. If the analyte of interest is coordinated to the metal in an equatorial position with respect to a p-H_2-originated hydride, then this species will also be hyperpolarized. The NMR spectrum is then recorded in a single acquisition and the enhancement in intensity of the analyte signals can be several orders of magnitude with respect to those obtained in a standard ^1H experiment.

Hyperpolarization catalyst

In order to be suitable for hyperpolarization transfer a catalyst should be able to rapidly react with hydrogen gas by oxidative addition and must be able to bind to the desired substrate to be hyperpolarized. The “standard” precatalyst (stdCat) which is usually chosen in literature for hyperpolarization experiments is an iridium(I) N-heterocyclic carbene complex (Figure 133).

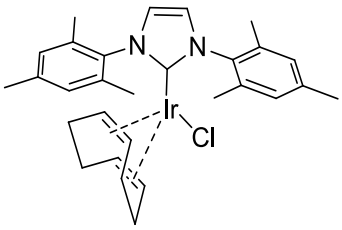

Figure 133: standard hyperpolarization (pre)catalyst "stdCat"

While being the go-to catalyst for these experiments, this compound is not commercially available and has to be synthesized. For this reason, I decided to evaluate a very similar compound (MeCat) which is in turn available in commerce.

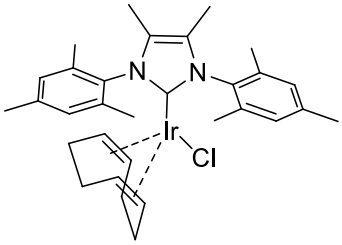

Figure 134: hyperpolarization (pre)catalyst employed in this work "MeCat"

This catalyst is identical to stdCat but have two methyl groups on the imidazole ring (Figure 134) and it was assumed to have a similar activity to the standard one. From a sterical point of view, the two methyl groups are in a position that should be far enough not to interfere with the iridium coordination sphere. The only effect that they could possibly have is an increase of the energetic barrier for the mesityl group rotation around the C-N bond. From an electronic point of view, the methylated imidazolilidene ligand is more electron rich thanks to the inductive effect of these two alkyl substituents, and this could have actually a beneficial effect on the ability to facilitate the oxidative addition of p-H_2 by stabilizing the Ir(III) product.

Para-hydrogen production

Natural ratio of p-hydrogen to o-hydrogen is 1:3, but the para state can be easily enriched by interaction with a spin catalyst at cryogenic temperatures. Lower temperatures increase the enrichment in p-H_2. With liquid nitrogen cooling, 50 % p-hydrogen is obtained. Paramagnetic impurities in activated charcoal or iron(III) oxide[91] are commonly used as spin catalyst. Initially, a Schlenk line was used for an "in batch" production of p-hydrogen by connecting to it a hydrogen generator (by electrolysis) with pressure regulation, a vacuum pump and a

cooled glass flask filled with the iron (III) oxide as spin catalyst. With this system it was possible to produce hydrogen gas enriched to 50 % in p-H_2 at 2 bar pressure, and it was used for the first set of preliminary experiments. An in-line apparatus for the continuous production of p-H_2 was then designed and built. The apparatus (Figure 135) has been homebuilt from copper tubing, standard brass tube fittings, manometers and ball valves. A coil obtained by bending the copper tubing was filled with iron oxide, hold in place by two pieces of cotton at the two extremities. A series of manual ball-valves allows the user to isolate the coil and to connect it to a nitrogen line, a vacuum pump, a hydrogen generator or to a quick-fit NMR tube adapter (apparatus schematized in Figure 136). Initially vacuum is pulled through the system and the coil is immersed in liquid nitrogen and left to reach thermal equilibrium. To remove traces of air (oxygen in particular) the system is purged by alternating vacuum pulling and nitrogen filling several times. In the end, nitrogen is finally displaced by hydrogen in the same way. When pressure stabilizes at 4.5 bar (set through the hydrogen generator) the para-hydrogen is ready to be spilled.

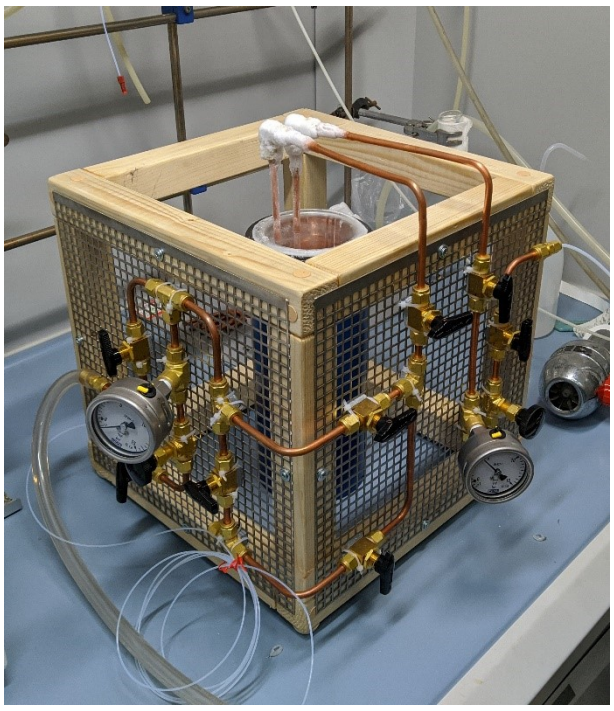

Figure 135: In line apparatus for the continuous production of p-hydrogen enriched gas

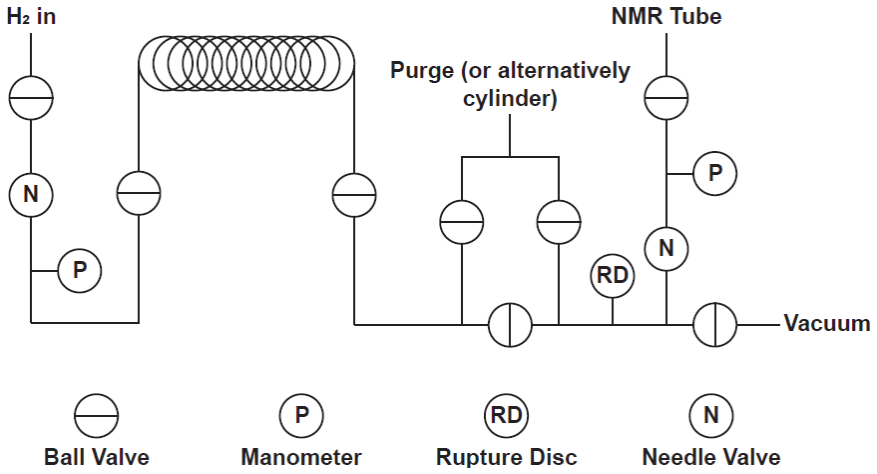

Figure 136: scheme of the in-line apparatus for p-H_2 production

This new system allowed a quicker and easier preparation and handling of p-H_2 enriched gas. As p-H_2 is metastable and can be stored at room temperature for several days, it is also possible to fill a canister with it and use it directly in the NMR room.

Coupling SABRE to NMR-chemosensing

The main problem of SABRE is the requirement for a reversible binding of the substrate to the hyperpolarization catalyst. This intrinsically limits the applicability of the techniques to a limited number of suitable analytes. Moreover, in a SABRE experiment, hyperpolarized signals are produced from each molecule which binds to the metal centre and designing a system which has the desired selectivity can be very difficult, limiting the applicability of the methodology for the analysis of complex mixtures. SABRE would have a much wider applicability if it was possible to circumvent the requirement for direct binding of the substrate to the metal centre. Hypothetically, by coupling this technique to nanoparticle assisted NMR-chemosensing it would be possible to differentiate the sensing system into two separate parts where one, based on SABRE, would be employed into signal enhancement while the other would act as selective receptor transferring the enhanced magnetization to the substrate. Such a goal could be achieved by co-functionalization of gold nanoparticles with an iridium hyperpolarization catalyst and ligands which can form selective binding pockets for the desired substrate. In this way, it should be possible to hyperpolarize the whole monolayer, which could then transfer its enhanced magnetization to the interacting analytes by NOE transfer, as already explained in the NOE-pumping chapter. With respect to the current NMR-chemosensing techniques, thanks to the great enhancement in magnetization that SABRE can provide, it is expected that such hybrid technique could enable

to greatly shrink the time requirements. An example of pyridine hyperpolarization by SABRE in methanol is shown in Figure 137. Hyperpolarized pyridine signals show an impressive intensity enhancement, from s/n = 54 in a standard ^{1}H experiment (1 scan) to s/n = 614 in the hyperpolarization experiment (1 scan).

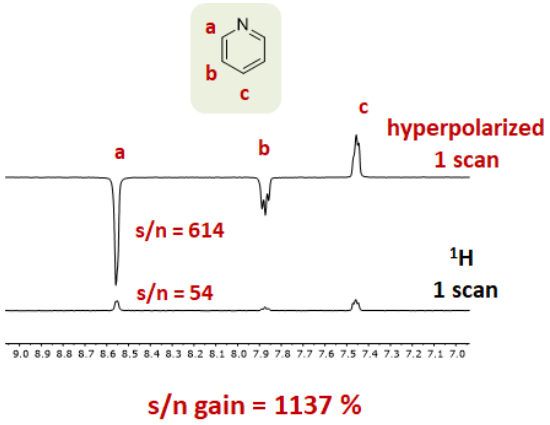

Figure 137: pyridine 1 mM, [MeCat] 50 µM, MeOD; hyperpolarized spectrum above (1 scan), ^{1}H below (1 scan). The spectra are in scale

As a first attempt, it was explored the possibility to load the iridium catalyst inside a monolayer by exploiting its hydrophobicity (Figure 138). A similar strategy was developed by Rotello for structurally related rhodium complexes. [7]

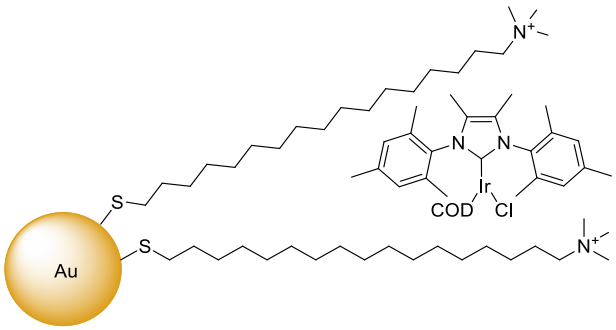

Figure 138: Iridium catalyst inserted in the monolayer of GZ-128 AuNPs by non-covalent hydrophobic interactions

Cationic nanoparticles with a C_{17} alkyl portion were chosen as they are soluble in water and they should have a "thick" hydrophobic region in which the complex should be able to fit. In order to load the catalyst into the nanoparticle monolayer, both the catalyst and the nanoparticles were dissolved in acetone and evaporated to dryness. After several attempts, it was determined that the most efficient procedure involved mixing 50 equivalents of catalyst with respect to the gold cores in acetone and then slowly removing the solvent by evaporation under a nitrogen stream. The loaded nanoparticles were then dissolved in water

and filtered to remove the excess catalyst not included in the monolayer. Broad catalyst signals appeared in the proton spectrum after the catalyst loading, confirming the nanoparticles functionalization (Figure 139).

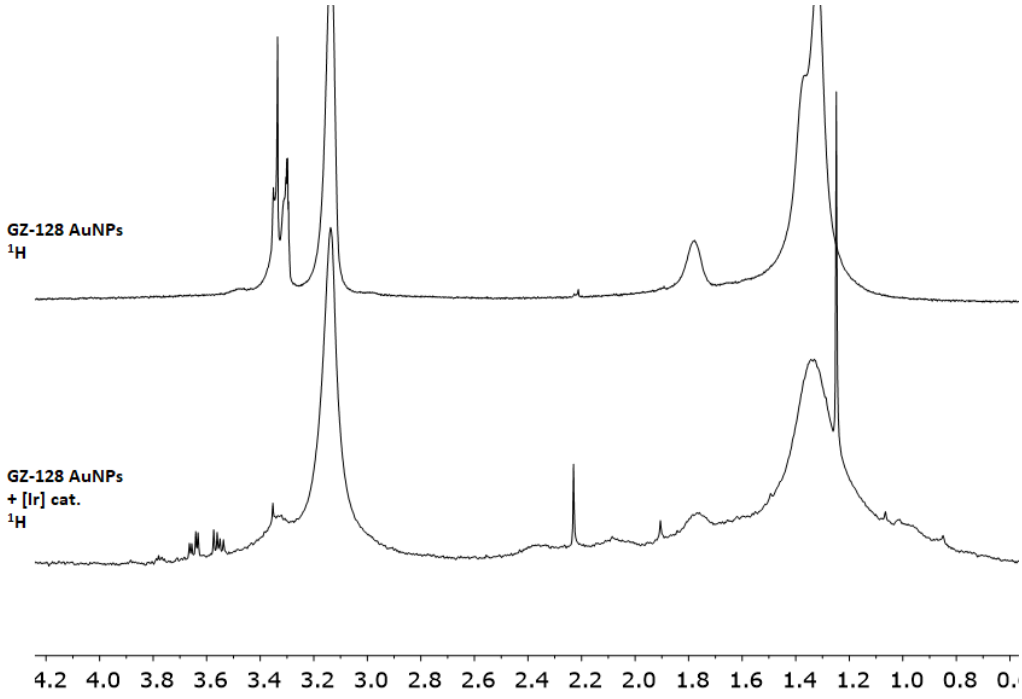

Figure 139: 1) cationic NPs ^1H spectrum, 2) cationic NPs (1 mM in thiol) + [MeCat] ^1H spectrum

The hyperpolarization experiment was performed in presence of both a molecule which interacts with the nanoparticle (homovanillic acid) and one which does not (phenylalanine). After the introduction of p-H_2 (50%, 2 bar) the NMR tube was rapidly shaken near the spectrometer magnet for around 10 seconds and introduced in the instrument. The hyperpolarized spectrum was immediately recorded in a single scan. The results of the experiment can be seen in Figure 140. Unfortunately, none of the signals is enhanced. A different monolayer was then tested for hyperpolarization. This time GZ-314 AuNPs were used, these nanoparticles are protected by a monolayer of thiols composed of a C11 alkyl chain connected to a triethylenglycol one through a squaramide linker. Squaramide linker could also act as ligand for the iridium catalyst through its carbonyls. The result (Figure 141) shows that neither in this case was possible to hyperpolarize the monolayer. The impossibility to detect signal enhancement could be caused by an effect of the nanoparticles on the interconversion of para-hydrogen into ortho-hydrogen, consuming the former and making it unavailable for the hyperpolarization of the sample.

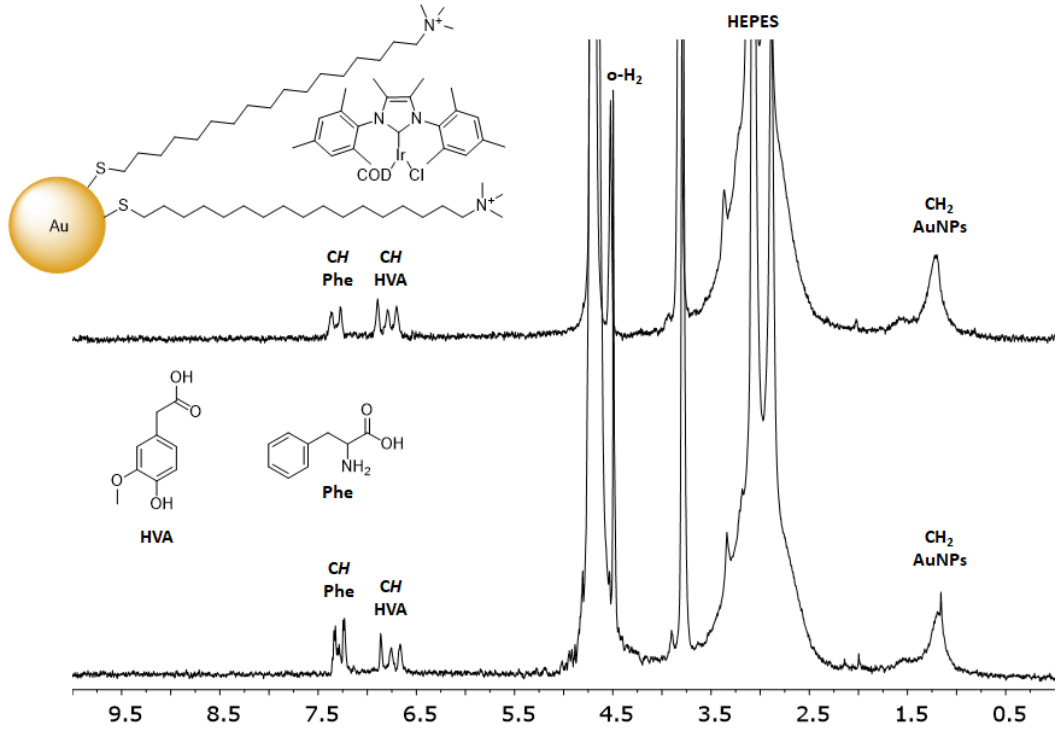

Figure 140: NPs 1 mM, [MeCat] 50 µM, homovanillic acid 1 mM and phenylalanine 1mM in D_2O; hyperpolarized above, ^1H below

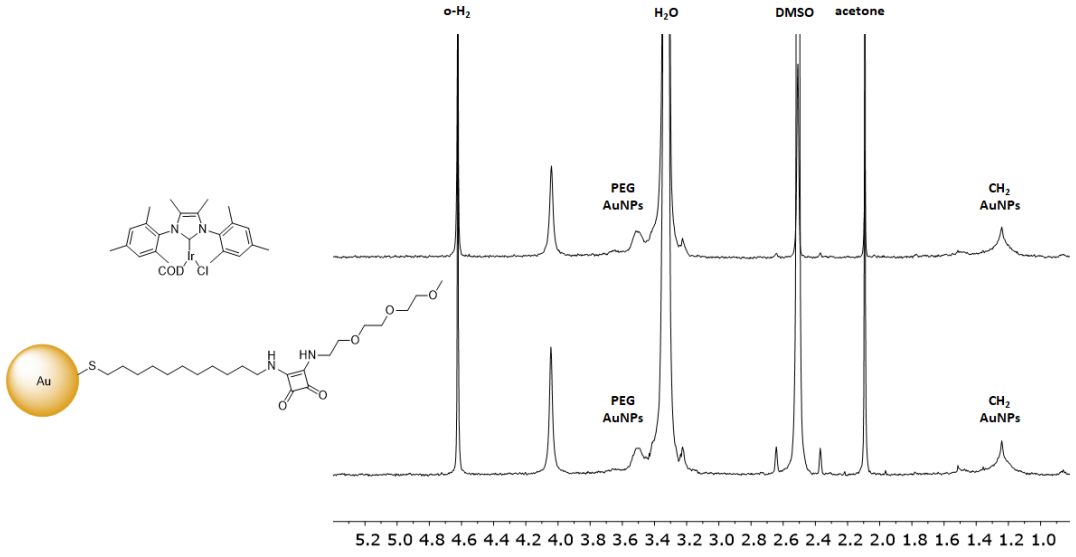

Figure 141: GZ-314 AuNPs 0.5 mM (in thiol) in deuterated DMSO, [MeCat] 50 µM, p-H_2 2.2 bar; hyperpolarized above

To determine if this effect exist and if it's relevant, GZ-128 AuNPs were mixed with para-hydrogen in absence of the iridium catalyst and proton spectra were acquired at regular intervals. The interconversion of para-hydrogen into ortho-hydrogen can be monitored by following the change in intensity of the singlet at 4.48 ppm, which is the signal of the o-H_2. If the nanoparticles act as spin catalyst, then this signal should increase over time. As can be

seen in Figure 142, the signal of the ortho-hydrogen remains basically unchanged even after 50 minutes, it can be concluded therefore that the consumption of para-hydrogen by the nanoparticles is negligible in the time scale of hyperpolarization experiments.

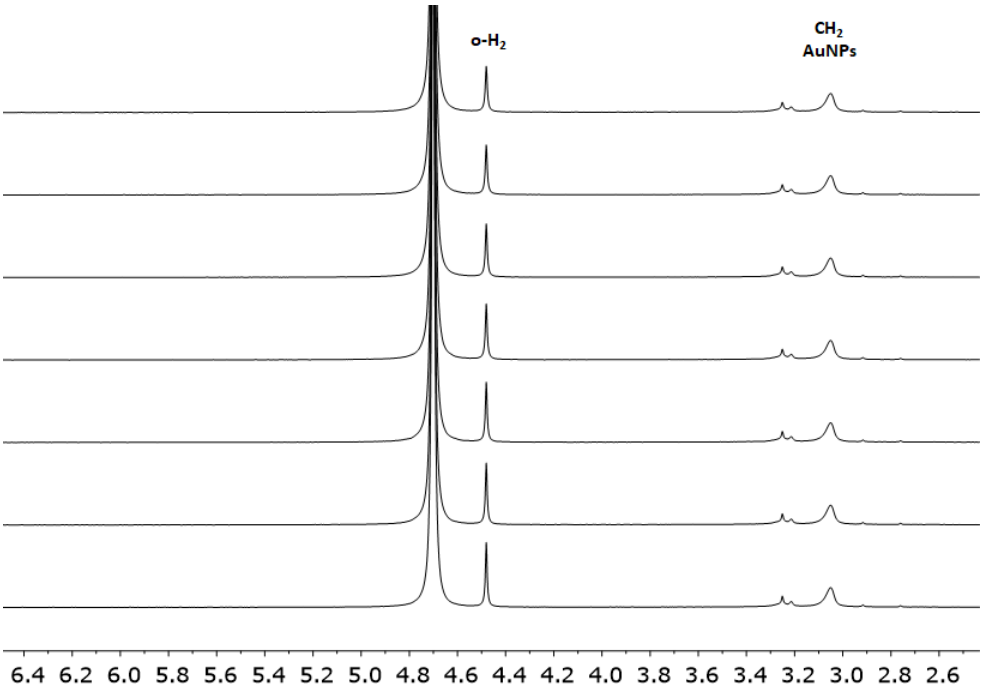

Figure 142: Cationic NPs and H_2 in D_2O, kinetics following the o-H_2 signal (ca. 4.5 ppm) from 0s (above) to 3000s (below), 500s increments; nanoparticles are not affecting the conversion of p-H_2 in o-H_2

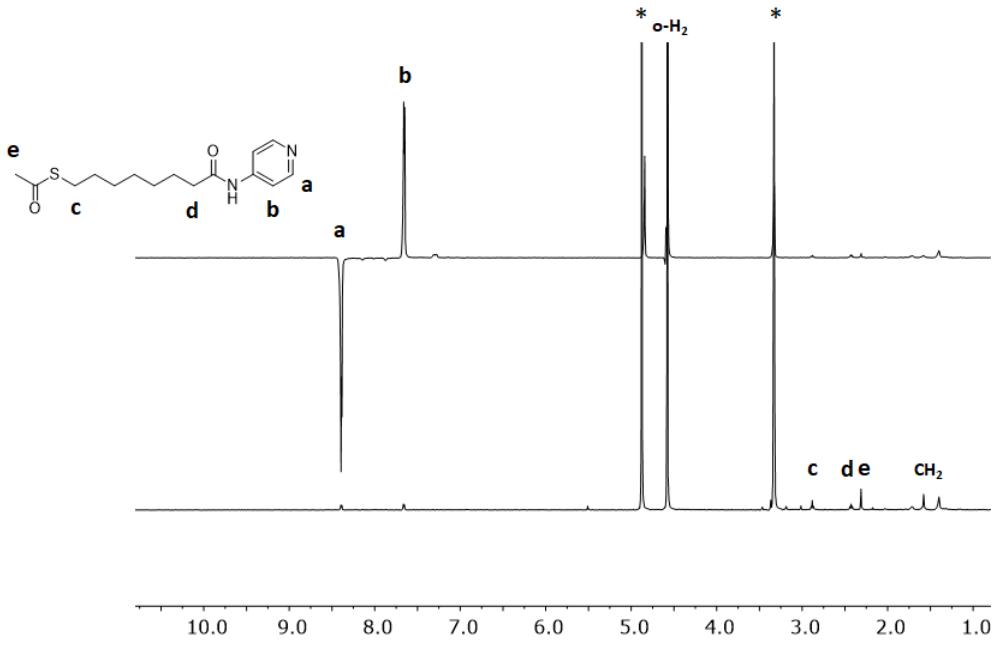

Figure 143: free GZ-373 (S-protected thiol) 1 mM, [MeCat] 50 µM, MeOD; hyperpolarized spectrum above, ^1H below (1 scan). The spectra are in scale

Nanoparticles bearing thiols exposing a pyridine, which can act as ligand for the catalyst were then synthesized and tested. Initially, hyperpolarization experiments were performed with the S-protected thiol only (GZ-373) to see if this species was able to bind to the catalyst and be hyperpolarized. As can be seen in Figure 143, the thiol is suitable for hyperpolarization experiments. This thiol was then used to synthesize GZ-383 nanoparticles. These nanoparticles turned out to have very broad signals indicating a very rigid monolayer, signals are so broad that they can't be seen unless the spectrum is recorded by averaging multiple scans (Figure 144). Hyperpolarization experiments were then performed but no change in signal intensity was detected even with these nanoparticles (Figure 145). Considering the strange behaviour of this monolayer, which seems to be very rigid, it was decided to synthesize nanoparticles with a mixed monolayer (GZ-375) where this active thiol is diluted with a neutral one terminated with a PEG chain. The amount of active thiol exchanged was 1/14 of the total thiols number. The scope of the mixed monolayer was to improve solubilization and ligand mobility, if the issue preventing hyperpolarization was the rigidity of the environment, this modification could solve it. No hyperpolarization was detected even in this case (Figure 146).

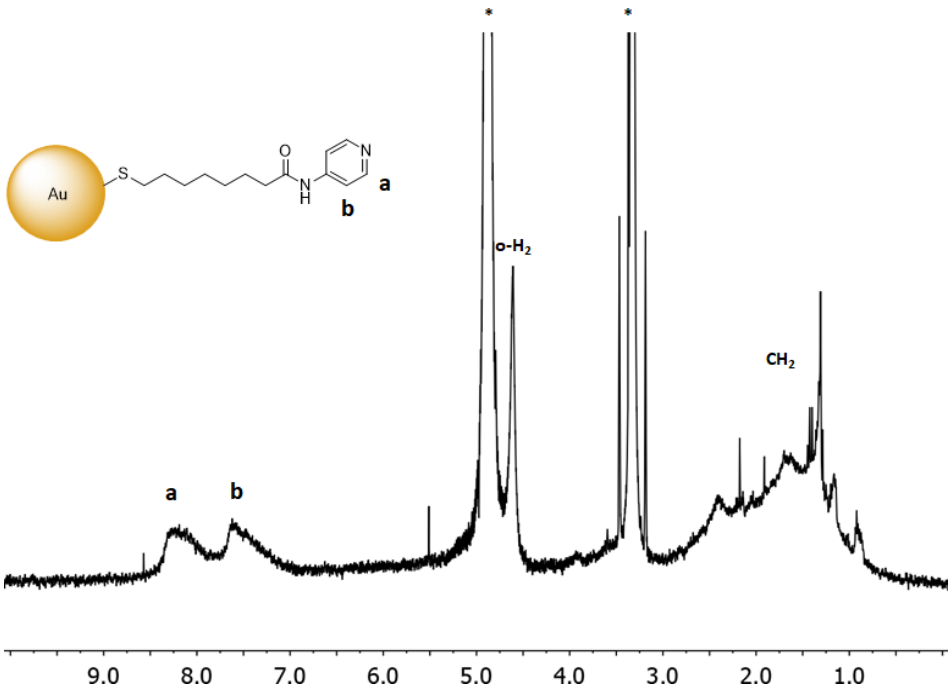

Figure 144: ^{1}H NMR spectrum of GZ-383 in D_2O

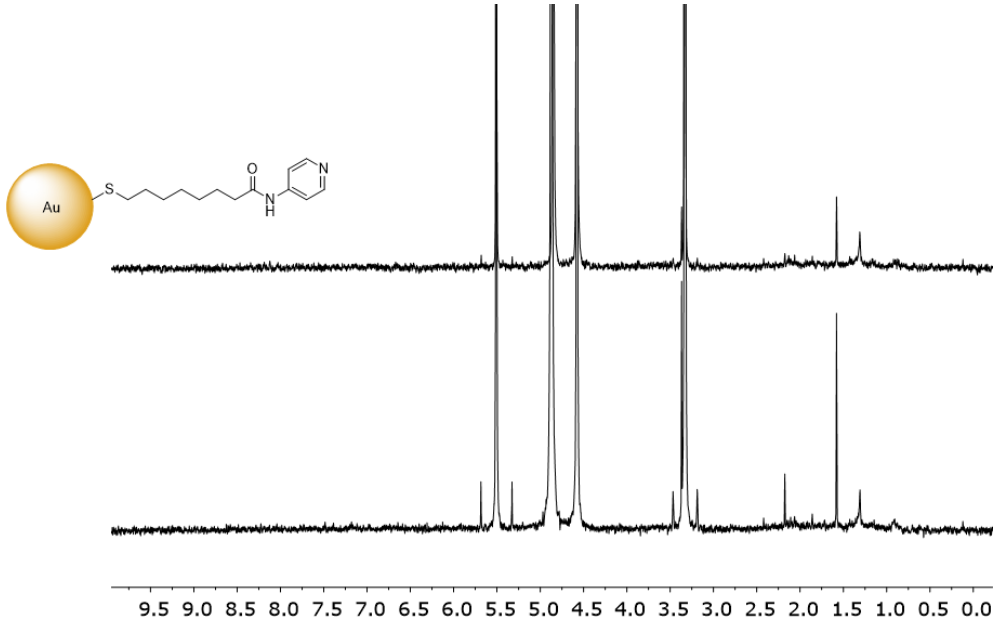

Figure 145: GZ-383 0.6 mM, [MeCat] 50 µM, MeOD; hyperpolarized spectrum above, ^{1}H below. The spectra are in scale. No AuNPs signals were detectable at these concentrations

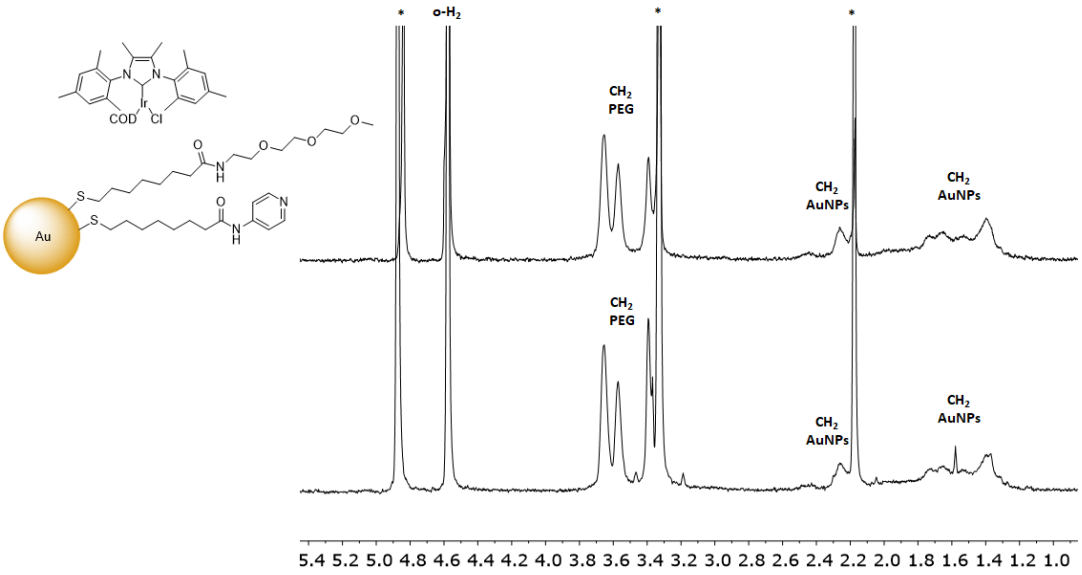

Figure 146: mixed NPs (GZ-375) 1 mM, [MeCat] 50 µM, p-H_2 2.2 bar; hyperpolarized spectrum above, ^{1}H below. Pyridine signals were not detectable at this concentration

The monolayer rigidity problem

A possible explanation for the impossibility to detect hyperpolarized signals could be that the environment is still too rigid and the short T2 relaxation time is affecting the decay rate of the magnetization, bringing it to a point where it is no longer detectable. To overcome this issue a nanoparticle with a more flexible and solvated monolayer would be required. A

possibility would be the introduction of a PEG chain between the alkyl chain and the pyridine moiety of the thiol (Figure 147). Such modification could provide enough flexibility to increase the T2 relaxation time of the system and allow the magnetization to be retained long enough for the hyperpolarized signals to be recorded.

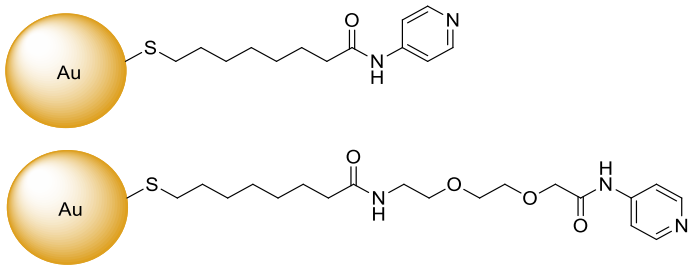

Figure 147: the introduction of a PEG chain should increase the flexibility of the monolayer, this nanoparticle will be synthesized in a future work

The axial ligand problem

As already discussed in the introduction, only the iridium ligands in the equatorial positions with respect to the hydrides are subjected to hyperpolarization. This fact is also confirmed by the absence of enhanced IMes signals in all the previously presented spectra. The less hindered position of the hyperpolarization catalyst, however, is the axial one, on the opposite side with respect to the bulky carbene. Depending on how the thiols self-organize on the gold nanoparticles, it is possible that the environment induces the pyridine coordination to this less hindered site. This would explain why it has never been possible to hyperpolarize the nanoparticle monolayer even when this featured a pyridine moiety. If this is the case, an effective solution to force the nanoparticle ligands to bind to at least one of the equatorial positions would be the substitution of the monodentate pyridine ligand with a bidentate one. Phenanthroline was therefore chosen and tested as substrate for hyperpolarization. The results of the experiment can be seen in Figure 148 and show a peculiar fact: the emerging hyperpolarized signals are different from those of free phenanthroline molecules which can be observed in a ^{1}H spectrum.

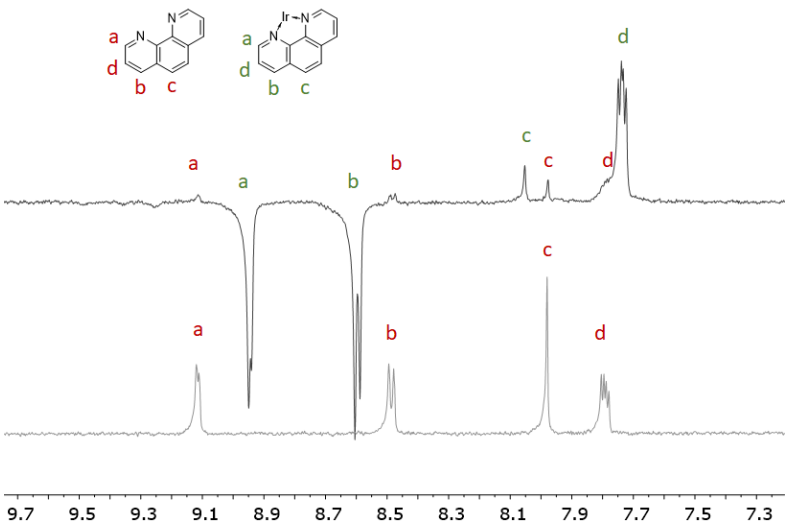

Figure 148: ^{1}H spectra of phenanthroline 1 mM, [MeCat] 25 µM, p-H_2 2.2 bar, 1 scan. Hyperpolarized spectrum above, ^{1}H below (1 scan)

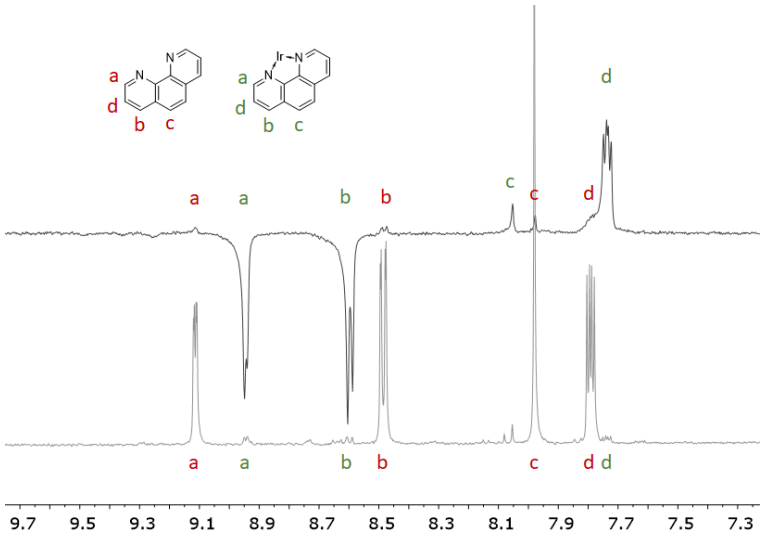

Figure 149: ^{1}H spectra of phenanthroline 1 mM, [MeCat] 25 µM, p-H_2 2.2 bar. Hyperpolarized spectrum above (1 scan), ^{1}H below (128 scans)

The appearance of different signals can be explained by the fact that this bidentate ligand is not in fast exchange with the iridium centre and the recorded signals of the free and bound ligands result to be discernible and not averaged between the two forms. Due to the slow ligand exchange kinetics the hyperpolarization is not transferred to free phenanthroline molecules, but it is retained on the bound ones. Due to the great hyperpolarization-derived signal enhancement, the signals of the bound ligand, which are not even detectable in a standard proton spectrum acquired in a single scan, become much more intense than those of the free ligand fraction. Indeed, just to barely detect these bound phenanthroline signals in a proton spectrum, 128 scans were needed (Figure 149, signals labelled in green).

Phenanthroline, thanks to its higher affinity for the iridium centre, could be a better ligand to ensure a stronger grafting of the catalyst to the nanoparticle surface. With this new knowledge, a new sensor for hyperpolarization has been designed combining the requisite for a flexible monolayer, discussed in the previous chapter, and the need of a bidentate ligand. This new nanoparticle (Figure 150) will be synthesized and tested in a future work.

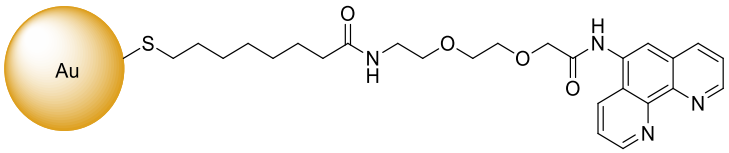

Figure 150: phenanthroline-based nanoparticle with flexible linker

SABRE reproducibility

One issue of the SABRE is that both the magnitude and the sign of hyperpolarized molecules signals are strongly affected by the magnetic field present when the p-H_2 gas is mixed in the sample (Figure 151).[92] An easy way to mix the sample in a magnetic field is to agitate the hydrogen-filled NMR tube around the spectrometer magnet. While this is a very easy and fast way to do it, it does not guarantee reproducibility of the experiments. The same signals will have different magnitude and sign depending on the exact position where the tube was agitated. This effect is illustrated in Figure 152 where the five spectra reported were recorded after agitation of the same exact sample in different positions around the spectrometer magnet.

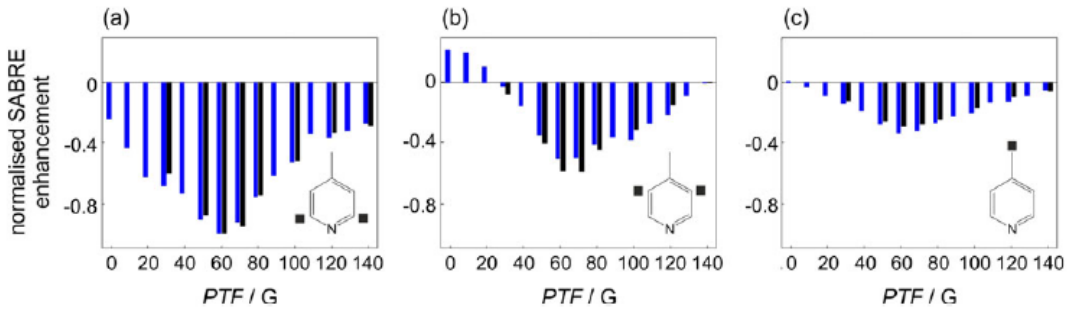

Figure 151: effect of the applied magnetic field during hydrogen addition on the recorded signals intensity and sign[92]

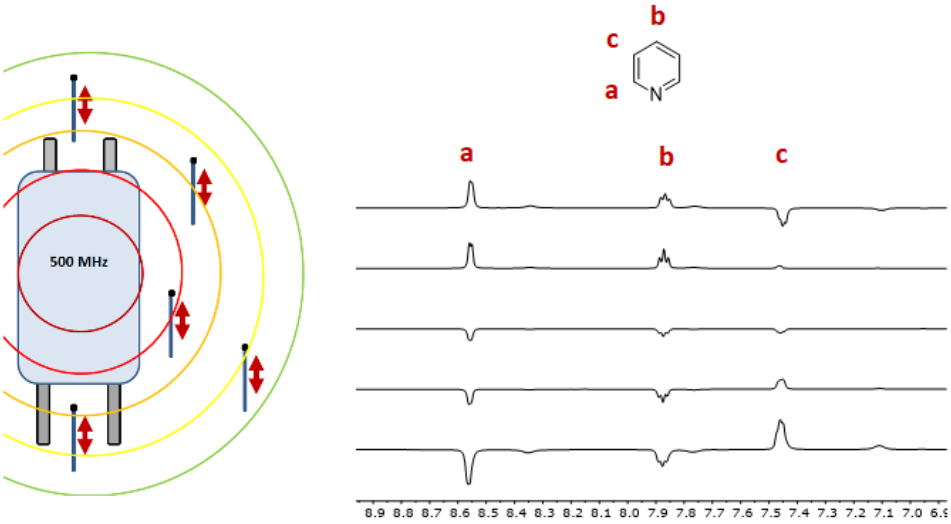

Figure 152: hyperpolarized ^{1}H spectra of pyridine; the hydrogen was mixed in the solution by manually shaking the tube in different position around the spectrometer magnet

This is clearly a big issue which needs to be addressed for the development of hyperpolarization-based NMR-chemosensing. In order to solve this reproducibility issue, which also affects the actual gain in signal intensity, a homogeneous magnetic field is needed. The required field strength depends on the exact nuclei that needs to be hyperpolarized, for ^{1}H a 60 G field is needed. The easiest way to create a homogeneous and reproducible field of the needed strength is to build a Halbach array with permanent magnets. 2.5 x 2.5 x 7.0 mm (grade N42) NdFeB magnets were used, as a simulation of the array field using these was already present in literature[92]. A 3D Halbach array was designed and parametrically modelled in Autodesk Fusion360 based on the published magnet spacings.

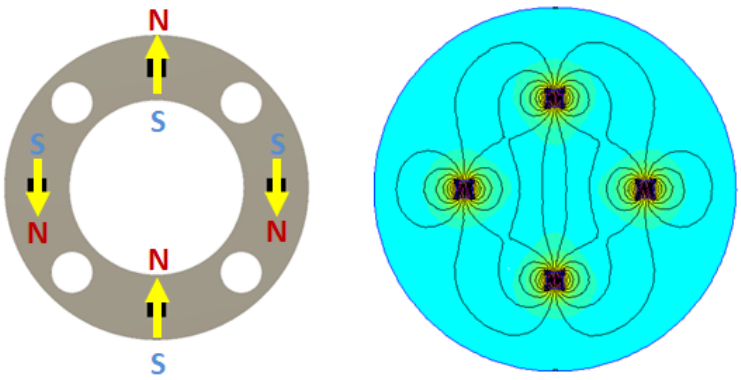

Figure 153: Halbach array slice

This array was 3D printed in PLA and assembled. A picture of the device can be seen in Figure 154 next to a section of its model.

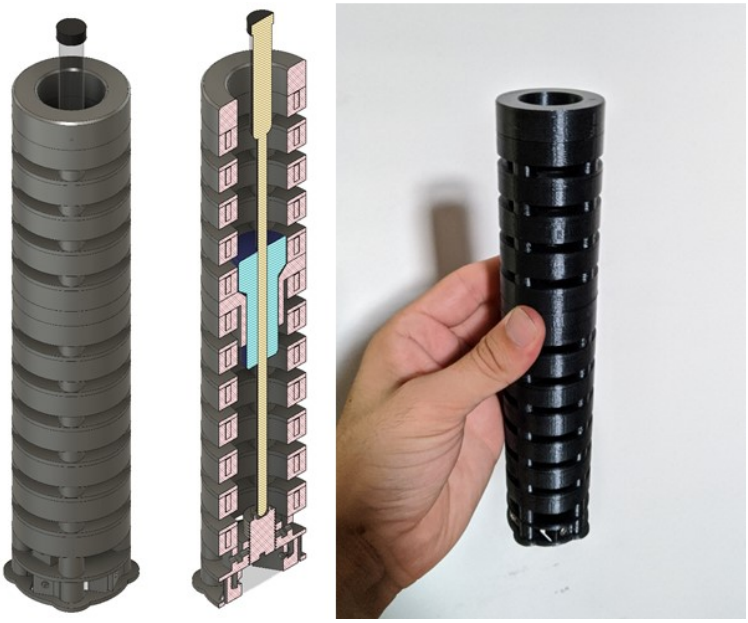

Figure 154: 60 G Halbach array magnet for ^{1}H hyperpolarization

The height of the NMR tube holder was designed to be finely tunable, in this way the tube can be placed at the correct depth for the NMR spectrometer in use. This removes the need of having to adjust the spinner position after the parahydrogen have been mixed, which would increase the risk of wasting magnetization due to relaxation during the operation. In this way, as soon as the tube is inserted and agitated in the device, it is ready to be immediately introduced in the spectrometer. This device effectively allowed the recording of perfectly reproducible results and it even increased further the signal enhancement recorded for both pyridine and phenanthroline (Figure 155 and Figure 156).

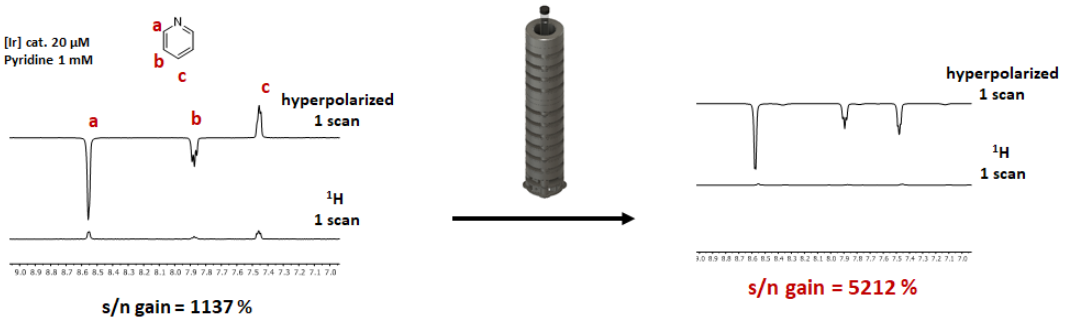

Figure 155: hyperpolarization experiments of pyridine 1 mM with [MeCat] 20 µM; the spectrum on the left was obtained by agitation of the sample near the spectrometer magnet while that on the right was obtained with the use of the 3D Halbach array

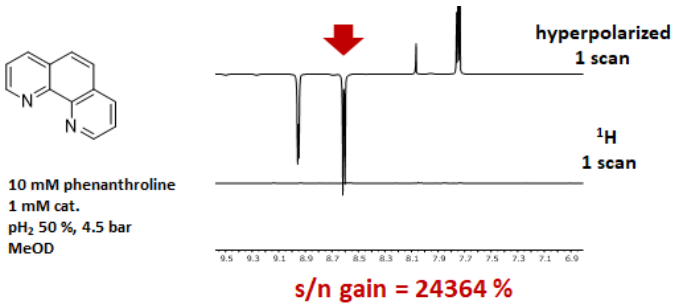

Figure 156: phenanthroline hyperpolarization experiment with the aid of the 3D Halbach array, spectra are in scale

Conclusions

The designed devices for on-demand p-H_2 production and mixing in a 60 G magnetic field greatly improved both performance and reproducibility of the experiments, enabling the realization of a complete platform for hyperpolarization experiments. Unfortunately, it has not been possible yet to hyperpolarize nanostructures for the development of hyperpolarization-based NMR-chemosensors. The results of these experiments allowed anyway to gain knowledge on the behaviour of such systems and suggested new strategies for reaching the final goal. Further work is needed for the development of a suitable monolayer for hyperpolarization. The next step will be focused on the increase of the monolayer mobility and the substitution of a monodentate ligand with a bidentate 1,10-phenanthroline-based one.

Experimental part

Standard procedures

All solvents and reactants were used as is without further purification. NMR spectra were recorded with a Bruker AV III 500 at 500.13 MHz for ^{1}H and 125.8 MHz for ^{13}C. TEM images were recorded with a Jeol 300 PX electron microscope. UV-Vis spectra were recorded with Cary 50 and Cary 100 spectrophotometer. Thermogravimetric analysis was performed with a Q5000 IR model TA, heating from 100°C to 1000°C in air. HRMS mass spectra were obtained with a Waters Xevo G2.S (Q-TOF) mass spectrometer (MeOH, 0.5% formic acid).

2-CTC resin swelling

The resin was left under agitation in DMF for 1h. Excess DMF was then removed without drying the resin.

First aminoacid coupling

To 2-CTC resin (loading = 1,35 mmol/g, 400 mg, 0.54 mmol, 1 equiv.) were added dry DMF (9 mL), DIPEA (0.8 mL, 4.59 mmol, 5.3 equiv.) and then Fmoc-L-Asp-OMe (320 mg, 0.87 mmol, 1.6 equiv.). The mixture was left at room temperature overnight under stirring. The solvent was then removed and the resin washed with 3 x 6 mL dry DMF.

Resin capping

To the resin was added dry DCM (7 mL), dry MeOH (7 mL) and DIPEA (0.5 mL) and the mixture was left under stirring for 1 h. The solvent was then removed and the resin washed with 3 x 6 mL dry DCM

Fmoc deprotection

20% 4-methylpiperidine in DMF (7 mL) was added to the resin, the mixture was stirred for 5 minutes and then the solvent was removed. The step was repeated a second time and then the resin was washed with 3 x 6 mL DMF.

Second and third aminoacid coupling

The desired Fmoc-L-AA-OH (1.08 mmol, 2 equiv.) was added to a glass vial, followed by dry DMF (2 mL), DIPEA (376 µL, 4 equiv.) and HBTU (409 mg, 2 equiv.). The mixture was manually stirred for 5 minutes and then added to the resin. The mixture was left under stirring at room temperature for 3 h for the second aminoacid or 7 h for the third aminoacid. The resin was then washed with 3 x 6 mL dry DMF.

Fmoc-L-Ala-OH * H_2O	356 mg
Fmoc-L-Gln-OH	398 mg
Fmoc-L-Leu-OH	382 mg
Fmoc-L-Phe-OH	418 mg
Fmoc-L-Pro-OH * H_2O	355 mg
Fmoc-L-Trp(Boc)-OH * H_2O	569 mg

Linker coupling

GZ-352_4 (236 mg, 1.08 mmol, 2 equiv.) was added to a glass vial, followed by dry DMF (2 mL), DIPEA (376 µL, 4 equiv.) and HBTU (409 mg, 2 equiv.). The mixture was manually stirred for 5 minutes and then added to the resin. The mixture was left under stirring at room temperature overnight. The resin was then washed with 3 x 6 mL dry DMF and 3 x 6 mL dry DCM.

Tripeptide cleavage

20% hexafluoroisopropanol in dry DCM (8 mL) was added to the resin and left under stirring at room temperature for 1 h. The liquid was recovered and evaporated. This step was repeated a second time. The resin was washed with 3 x 6 mL DCM. All the collected solution was evaporated and the solid/oil obtained was combined. The product does not require further purification.

Thioacetate deprotection

The desired tripeptide-linker-SAc (0.185 mmol, 1 equiv.) was added to a small round bottom flask under nitrogen atmosphere. Dry MeOH (2 mL) and sodium methoxide (30 mg, 0.555 mmol, 3 equiv.) were then added and the mixture was stirred for 2 h at room temperature. Some Amberlyst 15 hydrogen form resin was added to the resin and left standing for 20 min. The solution was then evaporated and the solid/oil used as is without further purification.

Boc deprotection

To the already deprotected thiol was added 50% TFA in DCM (4 mL) and the solution was left under stirring for 30 minutes and evaporated under reduced pressure. The product was used as is without further purification.

TEM analysis

A 0.5 mg/mL dispersion of gold nanoparticles in methanol was prepared and a drop of this was deposited on a carbon film on copper sample grid. The dispersion droplet was then dried by placing it in contact with a piece of paper.

TGA analysis

50 µL of a 20 mM stock solution (in D_2O) was placed in a platinum high-temperature crucible and it was evaporated at 80°C in open air. The analysis was performed after a drying step at 100°C for 20 minutes with a 10°C/min ramp from 100°C to 1000°C under air flow. The weight loss was calculated from an initial point after the drying treatment and a final one after the complete burning of the organic component at 850°C.

Synthetic procedures

AuNPs synthesis

A solution of $HAuCl_4 \cdot 3H_2O$ (50 mg, 0,13 mmol, 1 equiv.) in 0.5 mL of ultrapure H_2O was extracted with a solution of tetraoctylammonium bromide (172 mg, 0.31 mmol, 2.5 equiv.) in toluene (125 mL). The solution was poured in a 250 mL round bottom flask under nitrogen atmosphere and dioctylamine (755 µL, 2.5 mmol, 20 equiv.) was added. The solution was stirred for 2 h and then placed in an ice bath. A freshly prepared solution of $NaBH_4$ (47 mg, 1.3 mmol, 10 equiv.) in ultrapure H_2O (0.5 mL) was added and the dispersion was left under stirring for 2h. The water was removed with the aid of a separating funnel and the toluene phase was transferred back to a 250 mL round bottom flask in an ice bath under nitrogen atmosphere. A solution of the desired thiol (0.123 mmol, 2.5 equiv. with respect to an $Au_{180}SR_{70}$ average formula) in methanol (0.5 mL) was then added and the colloid was kept under stirring overnight. The suspension was then centrifugated and the nanoparticles were dispersed in ca. 2 mL of MeOH, sonicated with an ultrasonic bath and precipitated with diethyl ether. To collect them the dispersion was centrifugated for 5-8 min at 5000 rpm. This washing step was repeated three times. The nanoparticles were then purified three times by size exclusion chromatography on Sephadex LH-20 in methanol. The nanoparticles were then dried in vacuum and stored dry or as a 20 mM water stock solution in a freezer at -20°C.

Synthesis of GZ-416

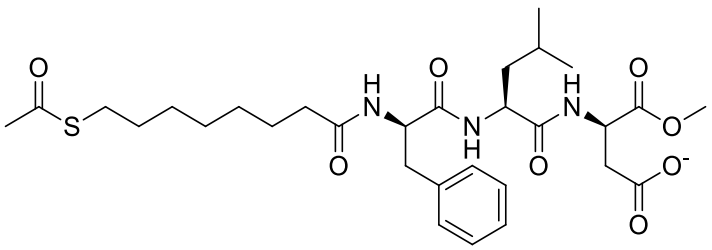

^{1}H NMR (500 MHz, MeOD): δ 7.31 – 7.17 (m, 5H, Ph Phe), 4.82 – 4.74 (m, 2H, C*H* Asp + C*H* Phe), 4.51 (dd, *J* = 9.2, 5.6 Hz, 1H, C*H* Leu), 3.72 (s, 3H, COOCH_3 Asp), 3.18 (dd, *J* = 14.0, 4.7 Hz, 1H, CH_2Phe), 2.93 – 2.81 (m, CH_2 Asp + CH_2SAc, 4H), 2.31 (s, CH_3S, 3H), 2.15 (t, *J* = 7.4 Hz, CH_2CON, 2H), 1.75 – 1.57 (m, C*H* Leu + CH_2 Leu, 3H), 1.56 – 1.42 (m, CH_2, 4H), 1.36 – 1.19 (m, CH_2, 4H), 1.19 – 1.09 (m, CH_2, 4H), 0.94 (2d, *J* = 6.4 Hz, CH_3 Leu, 6H).

^{13}C NMR (126 MHz, MeOD): δ 196.28 (1C, *C*OS), 174.70 (1C, *C*O linker), 173.00 (1C, *C*O Leu), 172.52 (1C, *C*O Phe), 172.41 (1C, *C*OOH Asp), 171.23 (1C, *C*OOMe Asp), 137.24 (1C, *C* Ph), 129.03 (2C, Ph), 128.07 (2C, Ph), 126.39 (1C, Ph), 54.30 (1C, *C*H Phe), 51.75 (1C, *C*H_3O), 51.66 (1C, *C*H Leu), 48.83 (1C, *C*H Asp), 40.65 (1C, *C*H_2 Leu), 37.51 (1C, *C*H_2 Phe), 35.44 (1C, *C*H_2CON), 35.36 (1C, *C*H_2 Asp), 29.31 (1C, *C*H_3COS), 28.52 (3C, *C*H_2SAc + 2*C*H_2), 28.33 (1C, *C*H_2), 28.24 (1C, *C*H_2), 25.44 (1C, *C*H_2), 24.39 (1C, *C*H Leu), 23.37 (1C, *C*H_2), 22.14 (1C, *C*H_3 Leu), 20.91 (1C, *C*H_3 Leu).

Synthesis of GZ-435

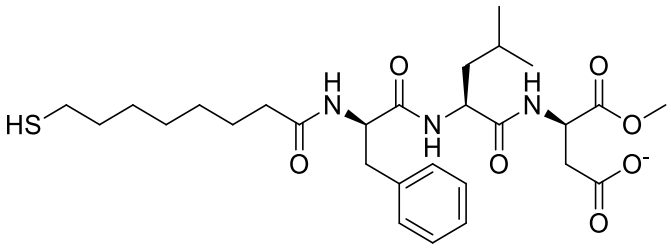

^{1}H NMR (500 MHz, MeOD): δ 4.76 – 4.63 (m, 2H, CH Asp + CH Phe), 4.46 (dd, *J* = 9.4, 5.4 Hz, 1H, CH Leu), 3.72 (s, 3H, CH3O), 3.25 – 3.19 (m, 1H, ½ CH2 Phe), 2.94 – 2.87 (m, 3H, ½ CH2 Phe + CH2SH), 2.79 – 2.59 (m, 2H, CH2 Asp), 2.15 (t, *J* = 7.4 Hz, 2H, CH2COON), 1.91 – 1.83 (m, ½ H, ½ CH Leu), 1.77 – 1.59 (m, 2H + ½ H, ½ CH Leu + CH2 Leu), 1.53 (p, *J* = 7.4 Hz, 1H, CH2), 1.46 (p, *J* = 7.8 Hz, 1H, CH2), 1.39 – 1.20 (m, 4H, 2 CH2), 1.19 – 1.09 (m, 2H, CH2), 0.98 (d, *J* = 6.4 Hz, 3H, CH3 Leu), 0.94 (d, *J* = 6.4 Hz, 3H, CH3 Leu)

^{13}C NMR (126 MHz, MeOD): δ 176.49 (1C, CO linker), 174.80 (1C, CO Leu), 172.78 (1C, CO Phe), 172.57 (1C, CO Asp), 172.53 (1C, COOMe Asp), 169.12, 137.35 (1C, quaternary C Ph), 128.93 (2C, Ph), 128.00 (2C, Ph), 126.30 (1C, Ph), 54.34 (1C, CH Phe), 51.44 (1C, CH Leu), 49.92 (1C, CH Asp), 40.49 (1C, CH2 Leu), 38.57 (1C, CH2 Asp), 37.24 (1C, CH2 Phe), 35.42 (1C, CH2CON), 29.28 (1C, CH2), 28.48 (3C, CH2), 28.18 (1C, CH2S), 24.37 (1C, CH2), 22.14 (1C, CH3 Leu), 20.65 (1C, CH3 Leu)

HRMS (ESI) m/z: 563.2642

Synthesis of GZ-417

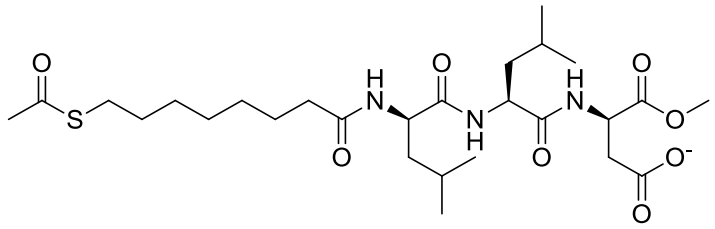

The product (324 mg) was collected as a viscous oil.

^{1}H NMR (500 MHz, MeOD): δ 4.77 (dd, *J* = 5.7 Hz, 1H, CH Asp), 4.48 (m, 2H, 2 C*H* Leu), 3.73 (s, 3H, C*H*$_3$O), 2.91 – 2.80 (m, 4H, C*H*$_2$SAc + C*H*$_2$ Asp), 2.31 (s, 3H, C*H*$_3$S), 2.25 (t, *J* = 7.3 Hz, 2H, C*H*$_2$COON), 1.76 – 1.53 (m, 8H, C*H*2 + C*H* Leu + C*H*$_2$ Leu), 1.42 – 1.30 (m, 6H, C*H*$_2$), 0.95 (4d, *J* = 6.1 Hz, 12H, C*H*$_3$ Leu)

^{13}C NMR (126 MHz, MeOD): δ 196.19 (1C, COS), 174.84 (1C, CO linker), 173.48 (1C, CO Leu), 173.00 (1C, CO Leu), 172.38 (1C, COOH Asp), 171.19 (1C, COOMe Asp), 51.67 (1C, OCH3), 51.61 (1C, CH Leu), 48.79 (1C, CH Asp), 40.58 (1C, CH2), 35.42 (1C, CH2 Asp), 35.39 (1C, CH2COON), 29.30 (1C, CH3S), 29.26 (1C, CH2), 28.69 (1C, CH2), 28.50 (2C, CH2SAc + CH2), 28.29 (1C, CH2), 25.52 (1C, CH2), 24.56 (1C, CH Leu), 24.39 (1C, CH Leu), 22.15 (2C, CH3 Leu), 20.83 (1C, CH3 Leu), 20.70 (1C, CH3 Leu).

Synthesis of GZ-442

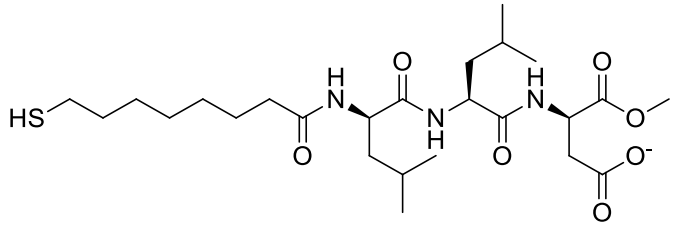

^{1}H NMR (500 MHz, MeOD): δ 4.70 – 4.65 (m, 1H, C*H* Asp), 4.49 – 4.42 (m, 2H, C*H* Leu), 3.72 (s, 3H, C*H*$_3$O), 2.75 (dd, J = 16.2, 5.7 Hz, 1H, C*H*$_2$ Asp), 2.60 (dd, J = 16.2, 5.0 Hz, 1H, C*H*$_2$ Asp), 2.26 (t, J = 7.5 Hz, 2H, C*H*$_2$COON), 1.81 – 1.53 (m, 10H, C*H*$_2$ + C*H* Leu), 1.47 – 1.29 (m, 6H, C*H*$_2$), 1.02 – 0.90 (m, 12H, C*H*$_3$ Leu).

^{13}C NMR (126 MHz, MeOD): δ 176.33 (1C, C=O), 174.96 (1C, C=O), 173.53 (1C, *C*=O), 172.84 (1C, *C*=O), 172.39 (1C, *C*=O), 51.66 (2C, *C*H Leu), 49.92 (1C, *C*H Asp), 40.59 (1C, *C*H$_2$ Leu), 40.20 (1C, *C*H$_2$ Leu), 38.51 (1C, *C*H$_2$ Asp), 35.42 (1C, *C*H$_2$CON), 33.73 (1C, *C*H$_2$), 28.75 (2C, *C*H$_2$), 28.49

(1C, *C*H_2), 27.87 (1C, *C*H_2), 24.57 (1C, *C*H_2), 24.57 (1C, *C*H Leu), 24.38 (1C, *C*H Leu), 22.14 (1C, *C*H_3 Leu), 22.12 (1C, *C*H_3 Leu), 20.59 (1C, *C*H_3 Leu), 20.47 (1C, *C*H_3 Leu).

HRMS (ESI) m/z: 530.2935 (M^-); calc. 530.2905

Synthesis of GZ-418

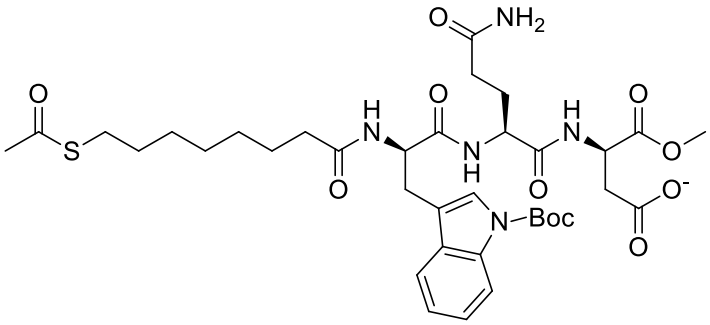

The product (275 mg) was collected as a beige solid.

^{1}H NMR (500 MHz, MeOD): δ 8.09 (d, J = 8.1 Hz, 1H, C*H* Trp), 7.65 (t, J = 8.1 Hz, 1H, C*H* Trp), 7.54 (s, 1H, C*H* Trp), 7.30 (t, J = 7.8 Hz, 1H, C*H* Trp), 7.23 (t, J = 7.5 Hz, 1H, C*H* Trp), 4.81 – 4.74 (m, 2H, C*H* Asp + C*H* Trp), 4.46 (dd, J = 8.6, 5.2 Hz, 1H, C*H* Gln), 3.73 (s, 3H, C*H*3O), 3.25 (m, 1H, ½ CH_2 Asp), 3.06 (m, 1H, ½ CH_2 Asp), 2.87 (t, 2H, CH_2 Trp), 2.80 (t, J = 7.4 Hz, 2H, CH_2SAc), 2.34 (t, J = 7.8 Hz, 2H, CH_2CON), 2.30 (s, 3H, CH_3S), 2.22 – 2.07 (m, 3H, CH_2 Gln + ½ CH_2 Gln), 2.03 – 1.89 (m, 1H, ½ CH_2 Gln), 1.68 (s, 9H, CH_3 Boc), 1.52 – 1.41 (m, 4H, CH_2), 1.27 – 1.05 (m, 6H, CH_2).

^{13}C NMR (126 MHz, MeOD): δ 196.26 (1C, *C*OS), 176.47 (1C, *C*O), 175.02 (1C, *C*O), 172.50 (1C, *C*O), 172.43 (1C, *C*O), 171.88 (1C, *C*O), 171.30 (1C, *C*O), 149.63 (1C, *C*=O Boc), 135.37 (1C, quaternary *C* Boc), 130.38 (1C, quaternary *C* Boc), 124.09 (1C, *C*H Boc), 123.95 (1C, *C*H Boc), 122.29 (1C, *C*H Boc), 118.84 (1C, *C*H Boc), 116.14 (1C, quaternary *C* Boc), 114.78 (1C, *C*H Boc), 83.43 (1C., quaternary C Boc), 53.11 (1C, *C*H Trp), 52.61 (1C, *C*H Gln), 51.70 (1C, *C*H_3O), 48.86 (1C, *C*H Asp), 35.45 (1C, *C*H_2 Trp), 35.35 (1C, *C*H_2 Gln), 30.91 (1C, *C*H_2CON linker), 29.24 (1C, *C*H_2 linker), 29.17 (1C, *C*H_3S), 28.47 (1C, *C*H_2 linker), 28.43 (1C, *C*H_2 linker, 28.40 (1C, *C*H_2 linker), 28.14 (1C, *C*H_2S linker), 27.65 (1C, *C*H_2 Gln), 27.12 (3C, *C*H_3 Boc), 26.92 (1C, *C*H_2 Asp), 25.30 (2C, *C*H_2 linker).

Synthesis of GZ-444

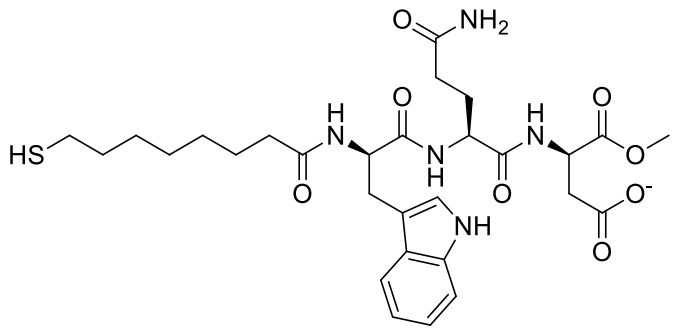

HRMS (ESI) m/z: 618.2599 (M^-); calc. 618.2603

Synthesis of GZ-420

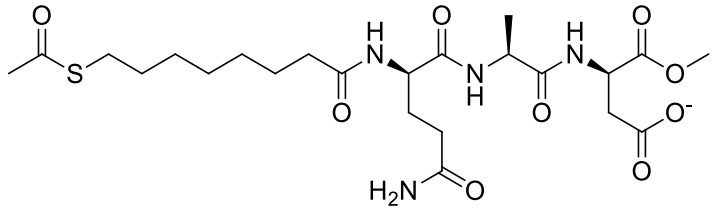

The product (178 mg) was collected as a beige solid.

^{1}H NMR (500 MHz, MeOD): δ 4.78 (t, J = 5.8 Hz, 1H, C*H* Asp), 4.41 (q, J = 7.1 Hz, 1H, C*H* Ala), 4.38 – 4.29 (m, 1H, C*H* Gln), 3.74 (s, 3H, CH_3O), 2.91 – 2.83 (m, 4H, CH_2SAc + CH_2 Asp), 2.37 – 2.30 (m, 5H, CH_3S + CH_2CON linker), 2.26 (t, J = 7.5 Hz, 2H, CH_2CONH$_2$ Gln), 2.13 – 1.91 (m, 2H, CH_2 Gln), 1.68 – 1.54 (m, 4H, CH_2), 1.39 (d, J = 7.2 Hz, 3H, CH_3 Ala), 1.43 – 1.30 (m, 6H, CH_2).

^{13}C NMR (126 MHz, MeOD): δ 196.28 (1C, *C*OS), 176.47 (1C, *C*=O), 174.92 (1C, *C*=O), 173.34 (1C, *C*=O), 172.55 (1C, *C*=O), 172.17 (1C, *C*=O), 171.32 (1C, *C*=O), 52.69 (1C, *C*H Gln), 51.63 (1C, *C*H$_3$O), 48.87 (2C, *C*H Asp + *C*H Ala), 35.40 (1C, *C*H$_2$ Asp), 35.35 (1C, *C*H$_2$ Gln), 31.09 (1C, *C*H$_2$CON), 29.28 (1C, *C*H$_2$), 29.13 (1C, *C*H$_3$S), 28.70 (1C, *C*H$_2$), 28.43 (2C, *C*H$_2$), 28.21 (1C, *C*H$_2$S), 27.49 (1C, *C*H$_2$ Gln), 25.32 (1C, *C*H$_2$), 16.57 (1C, *C*H$_3$ Ala).

Synthesis of GZ-445

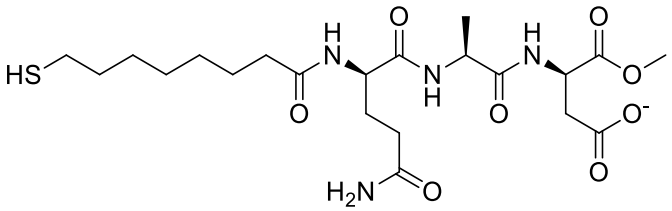

^{1}H NMR (500 MHz, D_2O) δ 4.37 – 4.23 (m, 3H, C*H* Gln + Ala + Asp), 3.68 (s, 3H, CH_3O), 2.68 (t, J = 7.2 Hz, 2H, CH_2SH), 2.60 (dd, J = 15.8, 4.4 Hz, 1H, CH_2 Asp), 2.50 (dd, J = 15.7, 8.6 Hz, 1H, CH_2 Asp), 2.31 (t, J = 7.6 Hz, 2H, CH_2CON), 2.23 (t, J = 7.4 Hz, 2H, CH_2 Gln), 2.13 – 1.99 (m, 1H, CH_2 Gln), 1.97 – 1.88 (m, 1H, CH_2 Gln), 1.62 (p, J = 7.3 Hz, 2H, CH_2), 1.54 (p, J = 7.2 Hz, 2H, CH_2), 1.34 (d, J = 7.1 Hz, 3H, CH_3 Ala), 1.37-1.22 (m, 6H, CH_2).

^{13}C NMR (126 MHz, D_2O) δ 178.83 (1C, *C*=O), 178.29 (1C, *C*=O), 177.77 (1C, *C*=O), 176.70 (1C, *C*=O), 173.62 (1C, *C*=O), 172.89 (1C, *C*=O), 53.08 (1C, *C*H), 52.80 (1C, *C*H_3O), 52.42 (1C, *C*H), 49.49 (1C, *C*H), 39.61 (1C, *C*H_2 Asp), 38.52 (1C, *C*H_2SH), 35.50 (1C, *C*H_2 Gln), 31.17 (1C, *C*H_2CON linker), 28.54 (1C, *C*H_2), 28.37 (1C, *C*H_2), 28.24 (1C, *C*H_2), 27.67 (1C, *C*H_2), 25.27 (1C, *C*H_2), 16.92 (1C, *C*H_3 Ala).

HRMS (ESI) m/z: 503.2187 (M^-); calc. 503.2181

Synthesis of GZ-458

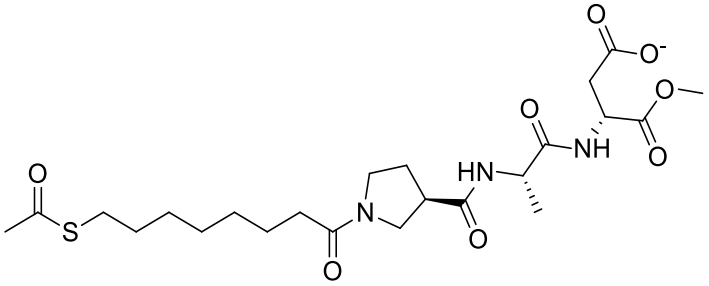

^{1}H NMR (500 MHz, MeOD): δ 4.76 (t, J = 5.5 Hz, 1H, CH Asp), 4.44 – 4.38 (m, 2H, C*H* Ala + C*H* Pro), 3.73 (s, 3H, CH_3O), 3.71 – 3.55 (m, 2H, CH_2 Pro), 2.87 (t, 2H, CH_2 Asp), 2.40 (m, 2H, CH_3COON), 2.32 (s, 3H, CH_3S), 2.23 (td, J = 8.3, 7.7, 3.4 Hz, 1H, ½ CH_2 Pro), 2.02 (dtd, J = 32.5, 10.3, 9.6, 6.2 Hz, 3H, CH_2 Pro + ½ CH_2 Pro), 1.66 – 1.54 (m, 4H, CH_2), 1.44 – 1.30 (m, 9H, CH_3 Ala + CH_2).

^{13}C NMR (126 MHz, MeOD): δ 196.19 (1C, *C*OS), 173.49 (1C, *C*=O), 173.44 (1C, *C*=O), 173.31 (1C, *C*=O), 172.52 (1C, *C*=O), 171.26 (1C, *C*=O), 59.88 (1C, *C*H Ala), 51.68 (1C, *C*H_3O), 48.85 (1C, *C*H Pro), 48.73 (1C, *C*H Asp), 47.40 (1C, *C*H2 Pro), 35.30 (1C, *C*H2 Asp), 33.93 (1C, *C*H_2CON),

29.50 (1C, *C*H$_2$ Pro), 29.38 (1C, *C*H$_2$), 29.20 (1C, *C*H$_3$COS), 28.86 (1C, *C*H$_2$), 28.65 (1C, *C*H$_2$), 28.29 (1C, *C*H$_2$), 24.40 (1C, *C*H$_2$), 24.28 (1C, *C*H$_2$ Pro), 16.29 (*C*H$_3$ Ala).

Synthesis of GZ-468

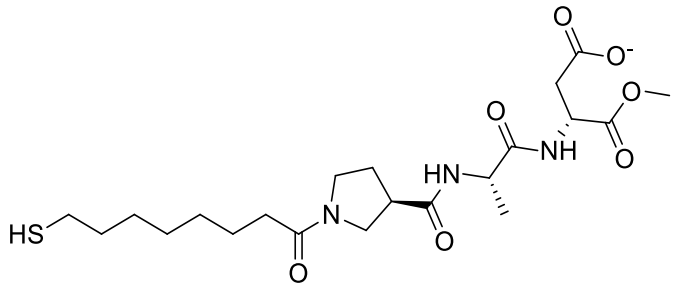

^{1}H NMR (500 MHz, MeOD) δ 4.73 – 4.63 (m, 1H, C*H* Asp), 4.46 – 4.38 (m, 2H, C*H* Ala + Pro), 3.72 (s, 3H, C*H*$_3$O), 3.68 (m, 1H, C*H*$_2$ Pro), 3.59 (m, 1H, C*H*$_2$ Pro), 2.91 – 2.85 (m, 2H, C*H*$_2$SH), 2.79 (dd, *J* = 16.3, 5.7 Hz, 1H, C*H*$_2$ Asp), 2.63 (dd, *J* = 16.3, 5.0 Hz, 1H, C*H*$_2$ Asp), 2.40 (t, *J* = 7.7 Hz, 2H, C*H*$_2$CON), 2.28 – 2.19 (m, 1H, C*H*$_2$), 2.14 – 2.06 (m, 2H, C*H*$_2$ + C*H*$_2$ Pro), 2.03 – 1.94 (m, 1H, C*H*$_2$ Pro), 1.67 – 1.54 (m, 4H, C*H*$_2$), 1.40 (d, *J* = 7.2 Hz, 3H, C*H*$_3$ Ala), 1.43 – 1.33 (m, 6H, C*H*$_2$).

^{13}C NMR (126 MHz, MeOD) δ 175.90 (1C, *C*O), 175.60 (1C, *C*O), 173.43 (1C, *C*O), 173.23, (1C, *C*O) 172.32 (1C, *C*O), 59.93 (1C, *C*H Ala), 51.40 (1C, *C*H$_3$O), 49.71 (1C, *C*H Asp), 48.99 (1C, *C*H Pro), 47.44 (1C, *C*H$_2$ Pro), 38.16 (1C, *C*H$_2$ Asp), 33.94 (1C, *C*H$_2$CON), 29.47 (1C, *C*H$_2$), 29.28 (1C, *C*H$_2$), 28.81 (1C, *C*H$_2$), 28.55 (1C, *C*H$_2$), 28.42 (1C, *C*H$_2$), 28.22 (1C, *C*H$_2$), 24.40 (1C, *C*H$_2$ Pro), 24.29 (1C, *C*H$_2$), 16.46 (1C, *C*H$_3$ Ala).

HRMS (ESI) m/z: 472.2118 (M^-); calc. 472.2123

Synthesis of GZ-459

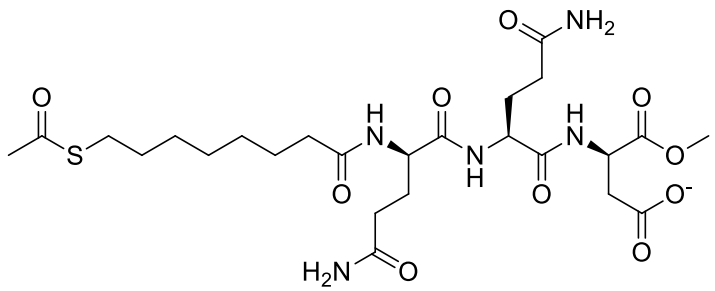

Synthesis of GZ-469

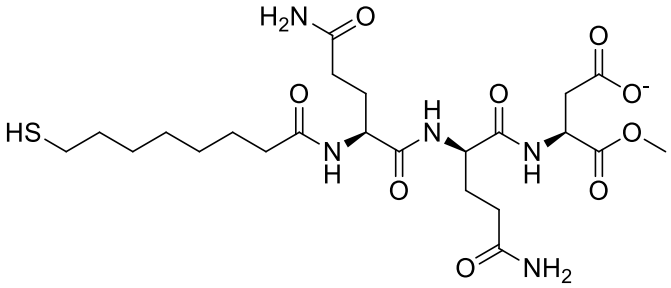

^{1}H NMR (500 MHz, MeOD) δ 4.74 – 4.66 (m, 1H, C*H* Asp), 4.44 (2d, *J* = 5.0 Hz, 1H, C*H* Gln), 4.35 – 4.28 (m, 1H, C*H* Gln), 3.72 (s, 3H, CH_3O), 2.88 (t, 3H, CH_2SH), 2.84 – 2.75 (m, 1H, CH_2 Asp), 2.60 (dd, *J* = 20.1, 4.1 Hz, 1H, CH_2 Asp), 2.37 (t, *J* = 7.5 Hz, 2H, CH_2CON), 2.26 (t, *J* = 7.6 Hz, 2H, CH_2 Gln), 2.15 – 1.90 (m, 2H, CH_2 Gln), 1.72 – 1.55 (m, 4H, CH_2), 1.47 – 1.33 (m, 6H, CH_2).

^{13}C NMR (126 MHz, MeOD) δ 176.44 (1C, *C*O), 176.40 (1C, *C*O), 176.32 (1C, *C*O), 174.99 (1C, *C*O), 172.66 (1C, *C*O), 172.51 (1C, *C*O), 171.86 (1C, *C*O), 53.12 (1C, *C*H Gln), 52.75 (1C, *C*H Gln), 51.42 (1C, *C*H_3O), 49.91 (1C, *C*H Asp), 38.42 (1C, *C*H_2 Asp), 35.34 (1C, *C*H_2 Gly),31.05 (1C, *C*H_2CON), 30.25 (1C, *C*H_2SH), 28.81 (1C, *C*H2), 28.49 (1C, *C*H_2), 27.90 (1C, *C*H_2), 27.64 (2C, *C*H_2 Gln), 27.16 (1C, *C*H_2), 25.36 (1C, *C*H_2).

HRMS (negative): 560.2404 (M^-); calc. 560.2396

Synthesis of GZ-498

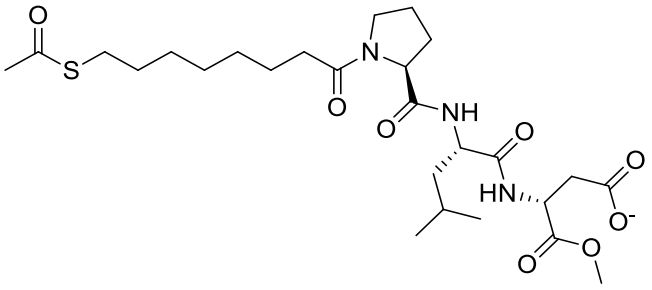

^{1}H NMR (500 MHz, MeOD): δ 4.77 (t, J = 5.8 Hz, 1H, C*H* Asp), 4.44 (m, 2H, C*H* Leu + C*H* Pro), 3.73 (s, 3H, CH_3O), 3.71 – 3.64 (m, 1H, 1/2 CH_2 Pro), 3.62 – 3.55 (m, 1H, 1/2 CH_2 Pro), 2.87 (m,, 2H, CH_2 Asp), 2.39 (t, 2H, CH_2CON), 2.31 (s, 3H, CH_3S), 2.22 (m, 1H, CH_2 Pro), 2.08 – 1.95 (m, 3H, CH_2 Pro), 1.81 – 1.70 (m, 1/2H, C*H* Leu), 1.69 – 1.55 (m, 7H, 3 CH_2 + 1/2 C*H* Leu), 1.43 – 1.29 (m, 6H, 3 CH_2), 0.96 (dd, J = 20.0, 6.5 Hz, 6H, CH_3 Leu).

^{13}C NMR (126 MHz, MeOD): δ 196.20 (1C, *C*OS), 173.59 (1C, *C*O), 173.42 (1C, *C*O), 173.17 (1C, *C*O), 172.43 (1C, *C*O), 171.21 (1C, *C*O), 59.98 (1C, *C*H Pro), 51.68 (1C, *C*H Leu), 51.59 (1C, *C*H_3O), 48.86 (1C, *C*H Asp), 47.40 (1C, *C*H_2 Pro), 40.12 (1C, *C*H_2 Leu), 35.56, 35.32, 33.98, 29.36, 29.28 (1C, CH_3S), 29.14 (1C, *C*H_2), 28.81 (1C, *C*H_2), 28.55 (1C, *C*H_2), 28.43 (1C, *C*H_2), 28.23 (1C, *C*H_2), 24.43 (1C, CH Leu), 24.39 (1C, CH_2), 24.31 (1C, CH_2), 22.09 (3C, *C*H_3 Leu), 20.59 (3C, *C*H_3 Leu).

Synthesis of GZ-499

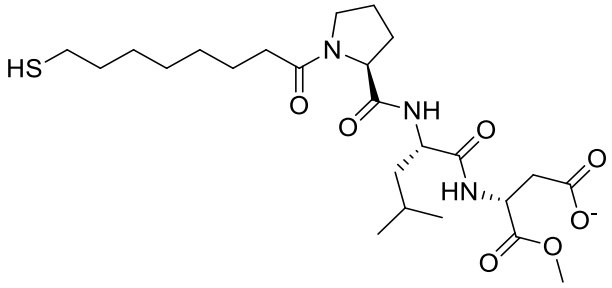

HRMS (ESI) m/z: (M^-); calc. 514.2592

GZ-438 (PheLeuAsp)

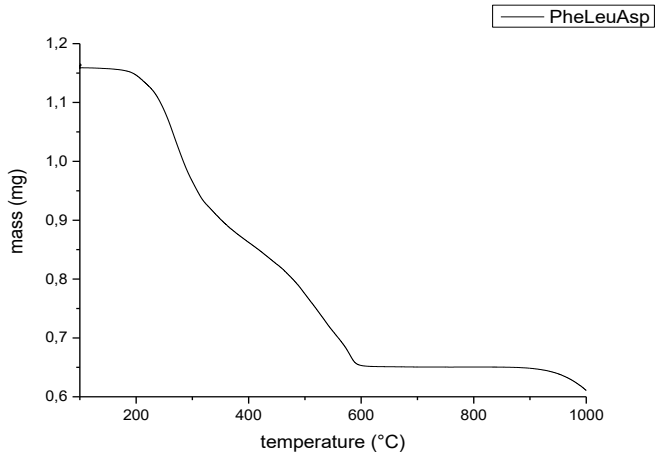

Figure 157: TGA analysis of GZ-438

TGA analysis: weight loss = 44.28 %

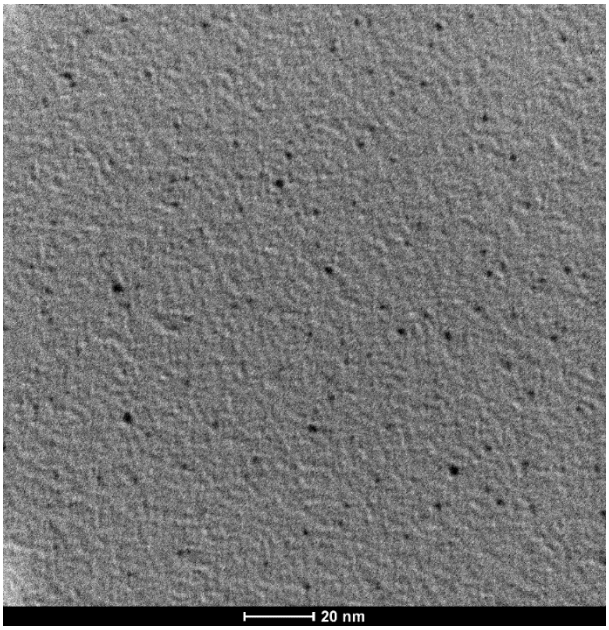

Figure 158: TEM analysis of GZ-438

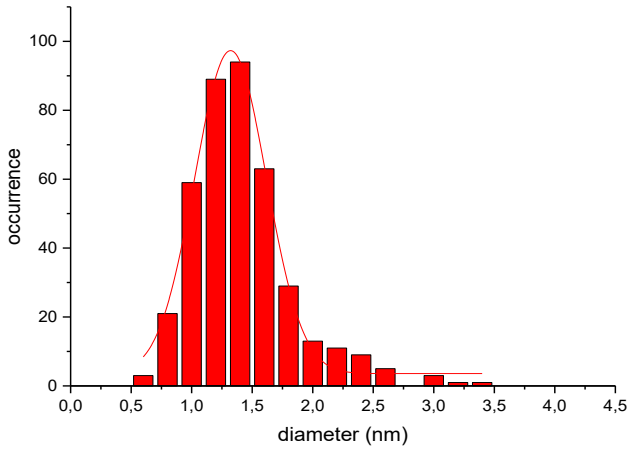

Figure 159: sizing of GZ-438

TEM analysis: diameter = 1.3 ± 0.3 nm

GZ-443 (LeuLeuAsp)

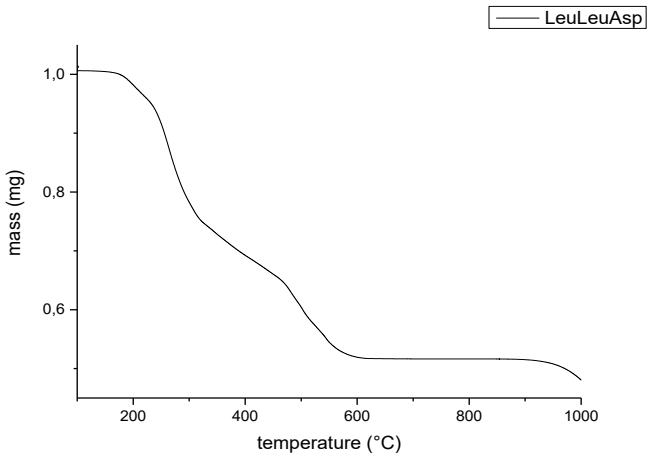

Figure 160: TGA analysis of GZ-443

TGA analysis: weight loss = 49.15 %

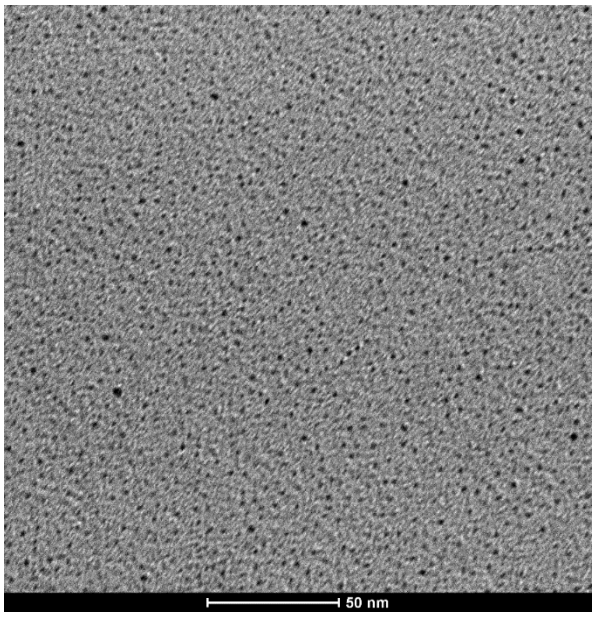

Figure 161: TEM analysis of GZ-443

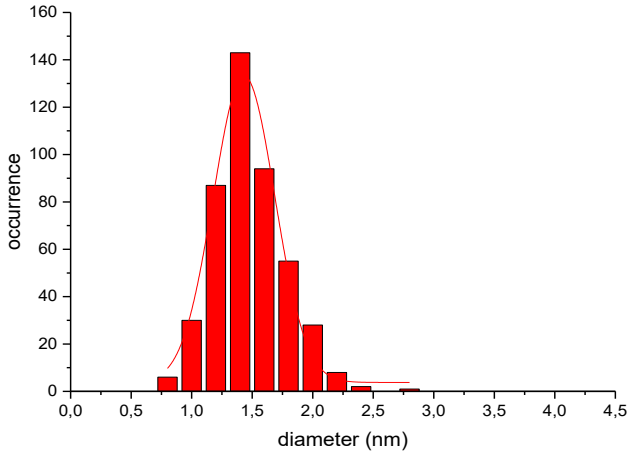

Figure 162: sizing of GZ-443

TEM analysis: diameter = 1.4 ± 0.3 nm

GZ-446 (TrpGlnAsp)

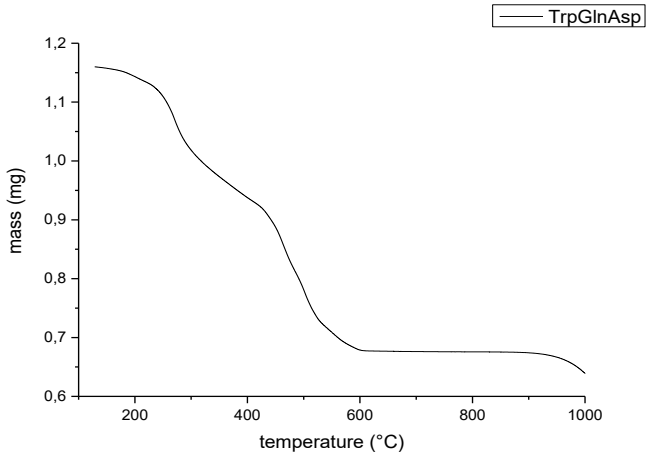

Figure 163: TGA analysis of GZ-446

TGA analysis: weight loss = 44.06 %

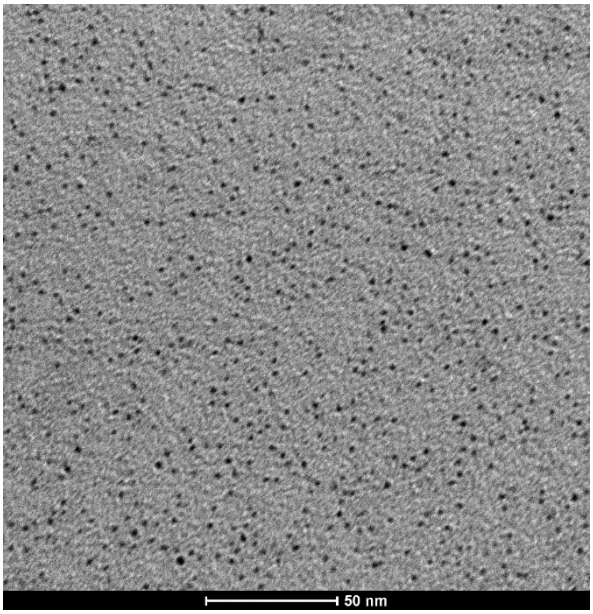

Figure 164: TEM analysis of GZ-446

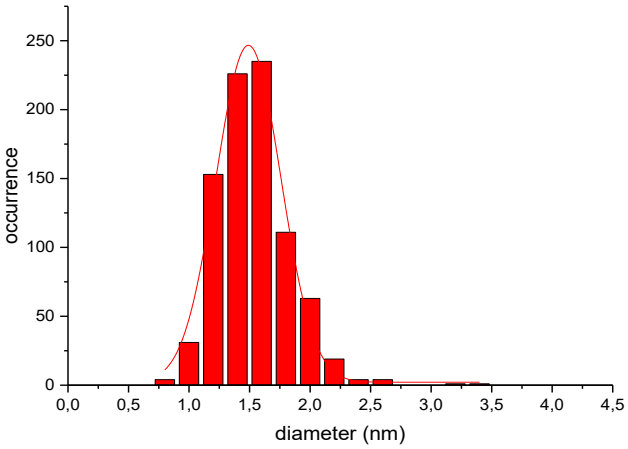

Figure 165: sizing of GZ-446

TEM analysis: diameter = 1.5 ± 0.3 nm

GZ-447 (GlnAlaAsp)

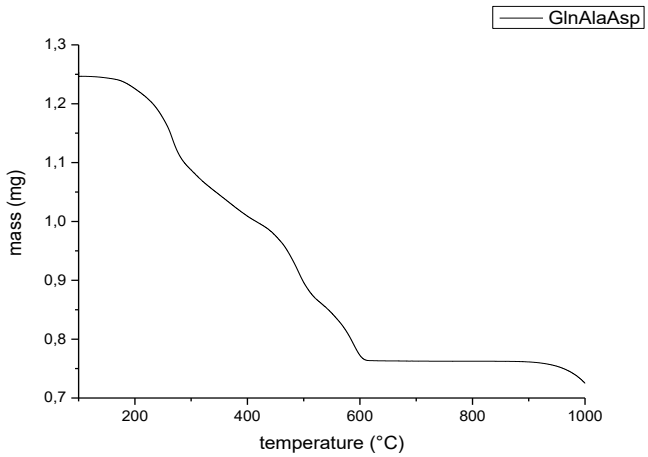

Figure 166: TGA analysis of GZ-447

TGA analysis: weight loss = 38.83 %

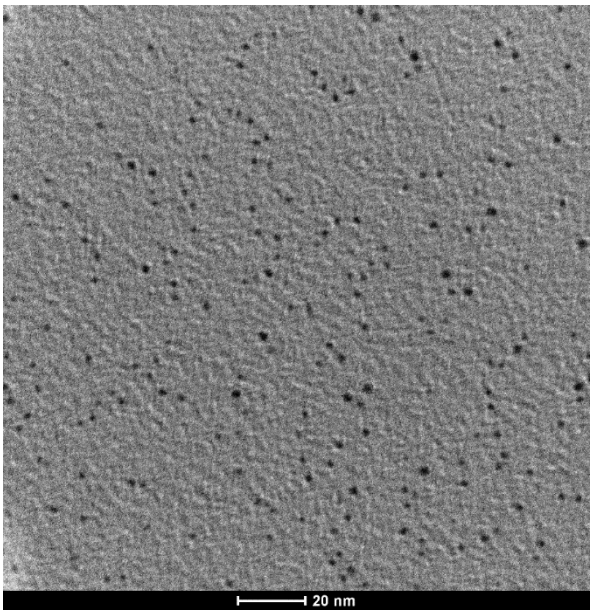

Figure 167: TEM analysis of GZ-447

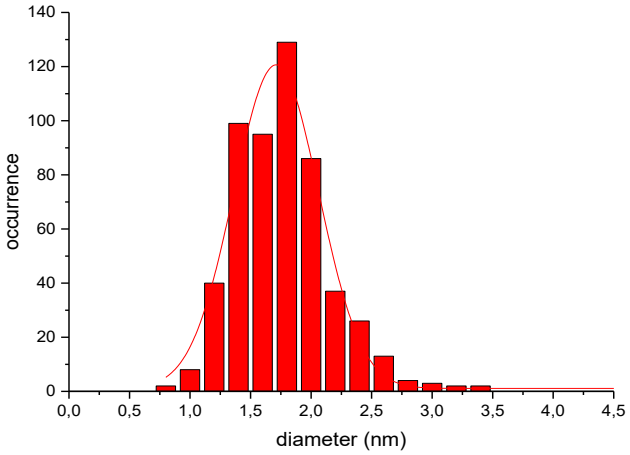

Figure 168: sizing of GZ-447

TEM analysis: diameter = 1.7 ± 0.4 nm

GZ-470 (ProAlaAsp)

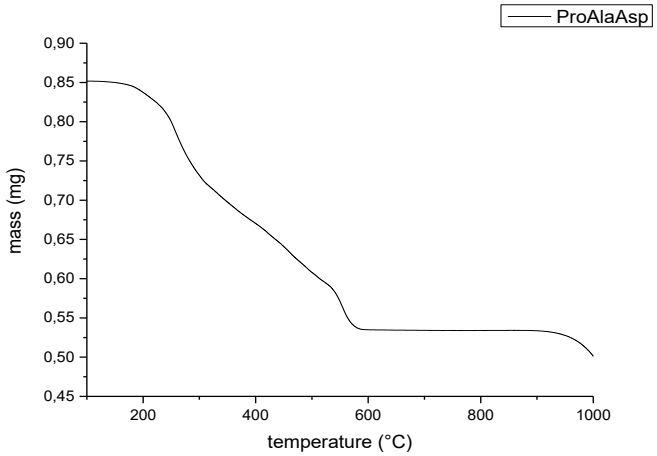

Figure 169: TGA analysis of GZ-470

TGA analysis: weight loss = 37.27 %

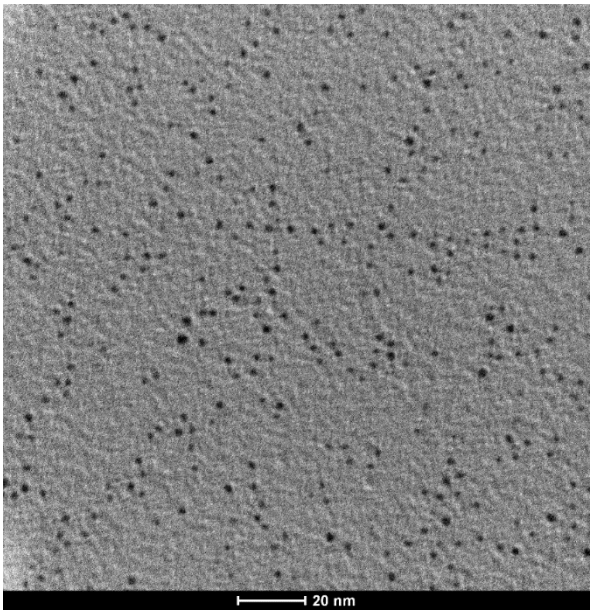

Figure 170: TEM analysis of GZ-470

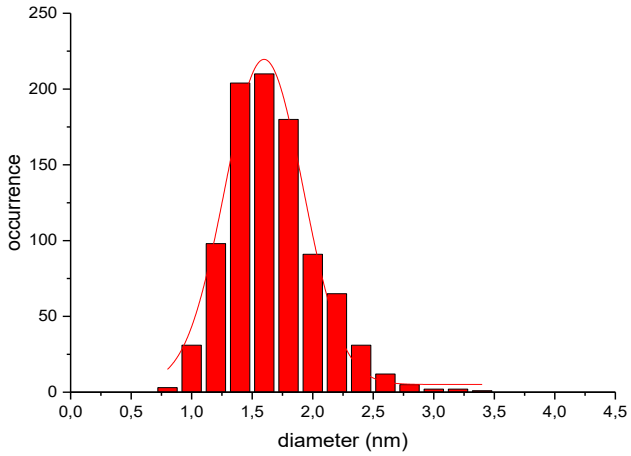

Figure 171: sizing of GZ-470

TEM analysis: diameter = 1.6 ± 0.3 nm

GZ-471 (GlnGlnAsp)

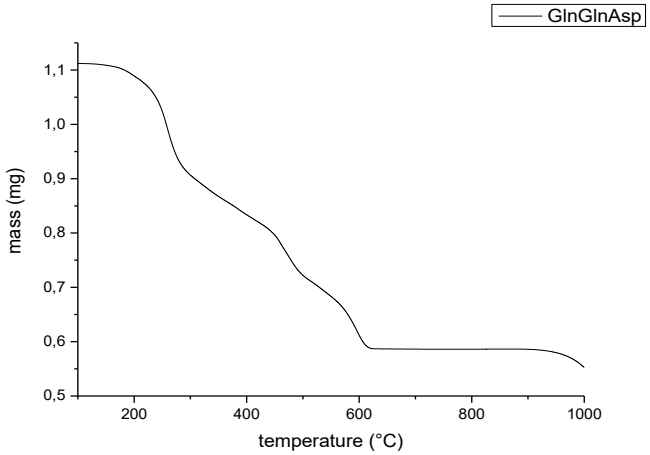

Figure 172: TGA analysis of GZ-471

TGA analysis: weight loss = 47.27 %

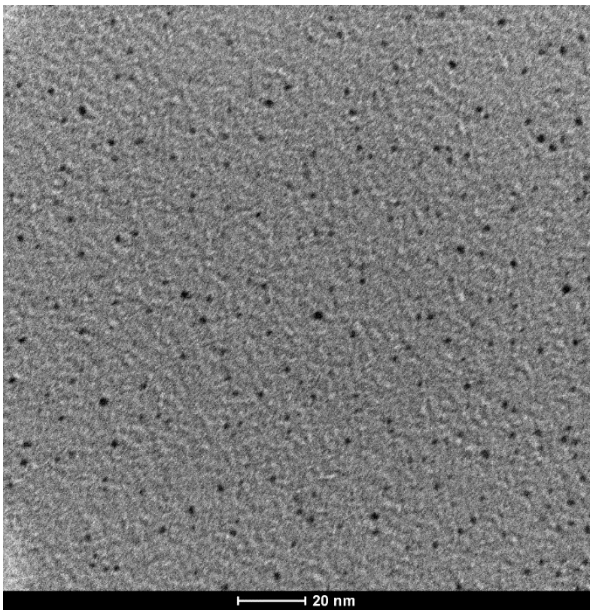

Figure 173: TEM analysis of GZ-471

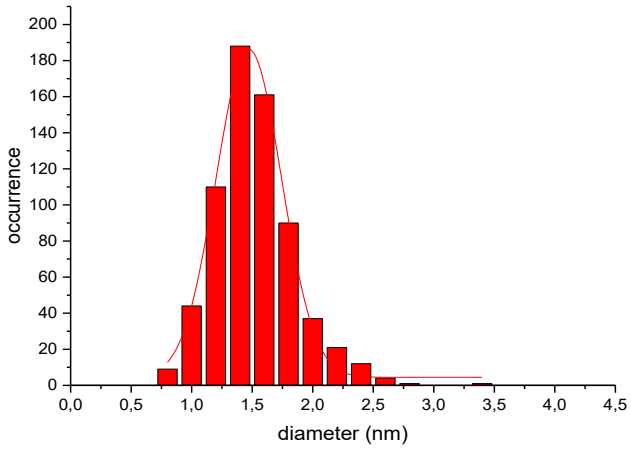

Figure 174: sizing of GZ-471

TEM analysis: diameter = 1.5 ± 0.3 nm

GZ-500 (ProLeuAsp)

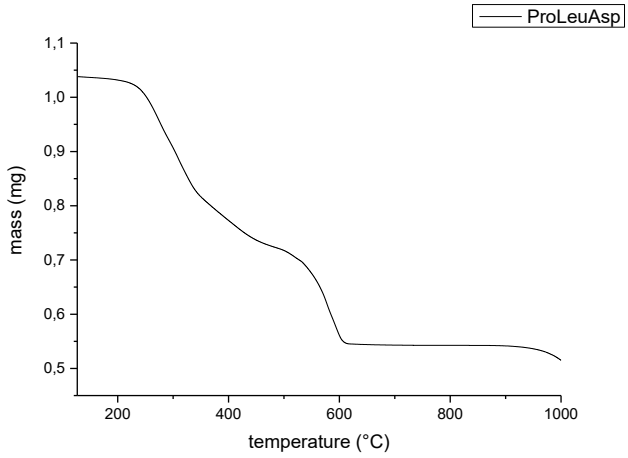

Figure 175: TGA analysis of GZ-500

TGA analysis: weight loss = 47.73 %

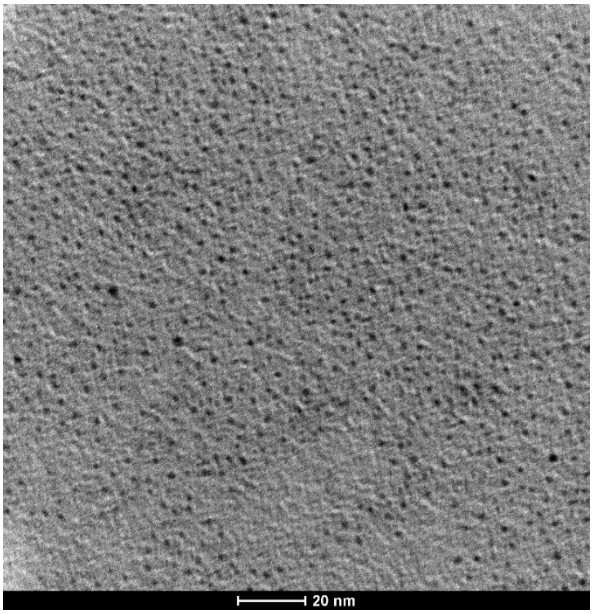

Figure 176: TEM analysis of GZ-500

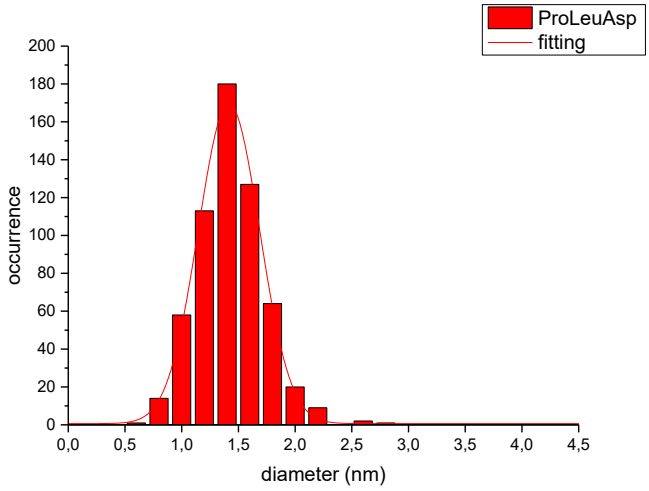

Figure 177: sizing of GZ-500

TEM analysis: average diameter = 1.4 ± 0.3 nm

Synthesis of citrate-capped AuNPs (10 nm)

In a 2-neck flask ultrapure H_2O (117 mL) was added and heated to reflux (100°C). A solution of sodium citrate (750 mg in 5 mL of ultrapure H_2O), one of silver nitrate (6.8 mg in 4 mL of ultrapure H_2O) and one of $HAuCl_4*3H_2O$ (50 mg in 0.5 mL of ultrapure water) were prepared. In a new vial were added: ultrapure water (5.6 mL) then citrate solution (1.657 mL) and silver

nitrate solution (0.250 mL). The vial was immersed in a warm water bath (30°C) and then the gold solution was added (0.500 mL). The solution was stirred for 5 min and then rapidly poured in the flask with boiling water. The solution was kept under reflux for 1h and then left to cool at room temperature. The solution can be stored in a fridge.

Synthesis of GZ-200

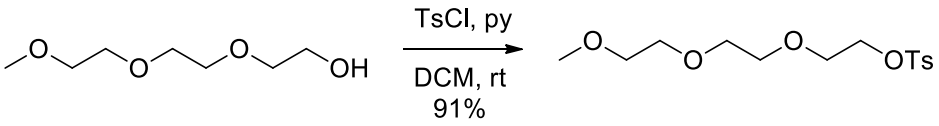

Triethylenglycol monomethylether (5.00 mL, 31.2 mmol, 1.0 equiv.), tosyl chloride (8.94 g, 46.9 mmol, 1.5 equiv.) and pyridine (3.79 mL, 466.9 mmol, 1.5 equiv.) were sequentially added to dry DCM (10 mL). The solution was stirred overnight at room temperature under nitrogen atmosphere and then evaporated. The residue was purified by flash column chromatography on silica (eluent: from DCM 100% to DCM:MeOH 1:1). The product (9.10 g, yield = 91%) was collected as a clear oil.

^{1}H NMR (500 MHz, MeOD) δ 7.80 (d, *J* = 8.0 Hz, 2H, C*H* Ar), 7.44 (d, *J* = 8.0 Hz, 2H, C*H* Ar), 4.16 (t, *J* = 4.5 Hz, 2H, CH_2OTs), 3.66 (t, *J* = 4.5 Hz, 2H, CH_2OMe), 3.60 – 3.56 (m, 4H, CH_2), 3.53 – 3.46 (m, 2H CH_2), 3.34 (s, 3H, CH_3O), 2.45 (s, 3H, CH_3Ar).

^{13}C NMR (126 MHz, MeOD) δ 145.10 (1C, *C*SO_3R), 133.09 (1C, *C* Ar), 129.82 (2C *C*H Ar), 127.73 (2C, *C*H Ar), 71.59 (1C, *C*H_2), 70.19 (1C, *C*H_2), 70.11 (1C, *C*H_2), 70.03 (1C, *C*H_2), 69.66 (1C, *C*H_2), 68.37 (1C, *C*H_2), 57.85 (1C, *C*H_3O), 20.41 (1C, Ar*C*H_3).

Synthesis of GZ-202

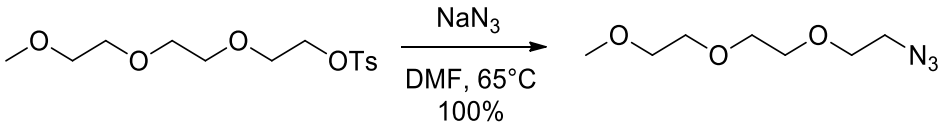

GZ-200 (9.10 g, 28.6 mmol, 1.0 equiv.) was dissolved in dry DMF (6 mL) and sodium azide (2.97 g, 45.7 mmol, 1.6 equiv.) was added. The mixture was stirred overnight at 65°C and then evaporated under reduced pressure. H_2O (10 mL) was added to the residue and the mixture was extracted with 3 x 20 mL DCM. The product (5.41 g, yield = 100%) was collected as a clear oil.

^{1}H NMR (500 MHz, $CDCl_3$) δ 3.52 – 3.44 (m, 8H, CH_2), 3.36 (t, *J* = 4.7 Hz, 2H, CH_2), 3.20 (m, 5H, CH_2 + CH_3O).

^{13}C NMR (126 MHz, $CDCl_3$) δ 71.72 (1C, *C*H_2), 70.45 (1C, *C*H_2), 70.43 (1C, *C*H_2), 70.36 (1C, *C*H_2), 69.83 (1C, *C*H_2), 58.69 (1C, *C*H_3O), 50.46 (1C, *C*H_2N_3).

Synthesis of GZ-204

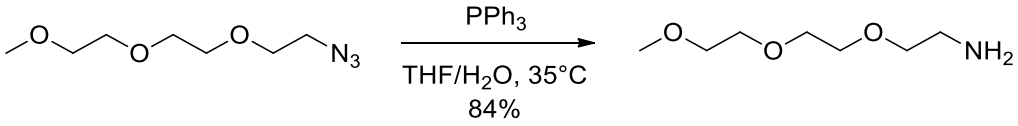

GZ-202 (5.41 g, 28.6 mmol, 1.0 equiv.) was dissolved in THF (40 mL), then were added triphenylphosphine (11.25 g, 42.9 mmol, 1.5 equiv.) and H_2O (4 mL). The mixture was stirred overnight at 35°C and then evaporated. The residue was purified by flash column chromatography on silica (eluent: from DCM 100% to MeOH 100%). The product (3.93 g, yield = 84%) was obtained as a yellowish oil.

^{1}H NMR (500 MHz, Chloroform-*d*) δ 3.09 – 3.04 (m, 4H, CH_2), 2.99 – 2.89 (m, 4H, CH_2), 2.79 (s, 3H, CH_3O), 2.28 (t, 2H, CH_2), 1.36 (t, 2H, CH_2).

^{13}C NMR (126 MHz, $CDCl_3$) δ 72.70 (1C, *C*H_2), 71.36 (1C, *C*H_2), 69.98 (1C, *C*H_2), 69.88 (1C, *C*H_2), 69.68 (1C, *C*H_2), 58.23 (1C, *C*H_3O), 41.17 (1C, *C*H_2NH_2).

Synthesis of GZ-253

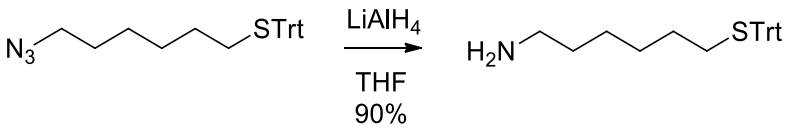

GZ-251 (819 mg, 2.04 mmol, 1.0 equiv.) was dissolved in dry THF (25 mL) and $LiAlH_4$ 1M in THF (3.06 mL, 3.06 mmol, 1.5 equiv.) was added dropwise under nitrogen atmosphere. The mixture was stirred overnight at room temperature.

^{1}H NMR (500 MHz, Chloroform-*d*) δ 7.48 (d, *J* = 7.9 Hz, 6H, C*H* Ar), 7.26 (t, *J* = 7.6 Hz, 6H, C*H* Ar), 7.18 (t, *J* = 7.2 Hz, 3H, C*H* Ar), 2.57 (t, *J* = 7.1 Hz, 2H, CH_2NH_2), 2.20 (t, *J* = 7.3 Hz, 2H, CH_2S), 1.43 (p, *J* = 7.3 Hz, 2H, CH_2), 1.34 (p, *J* = 7.5 Hz, 2H, CH_2), 1.32 – 1.21 (m, 2H, CH_2), 1.18 (p, *J* = 6.8 Hz, 2H, CH_2).

^{13}C NMR (126 MHz, $CDCl_3$) δ 145.14 (3C, *C*H Ar), 129.65 (6C, *C*H Ar), 127.87 (6C, *C*H Ar), 126.57 (3C, *C* Ar), 66.47 (1C, *C*H_2S), 42.02 (1C, *C*H_2NH_2), 33.44, 31.96, 28.83, 28.62, 26.45 (5C, *C*H_2).

Synthesis of GZ-255

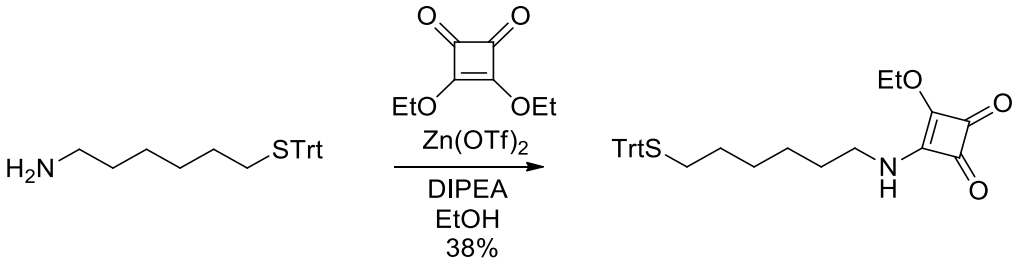

GZ-253 (400 mg, 1.06 mmol, 1.0 equiv.), 3,4-Diethoxy-3-cyclobutene-1,2-dione (236 µL, 1.60 mmol, 1.5 equiv.) and zinc triflate (77 mg, 0.21 mmol, 0.2 equiv.) were added to EtOH (7 mL) and the mixture was stirred overnight at room temperature. The solvent was evaporated under reduced pressure and the residue was purified by flash column chromatography on silica (eluent: DCM:MeOH 95:5). 200 mg of product (yield = 38%) were collected.

^{1}H NMR (500 MHz, Chloroform-*d*) δ 7.44 (d, *J* = 7.8 Hz, 6H, C*H* Ar), 7.30 (t, *J* = 7.6 Hz, 6H, C*H* Ar), 7.22 (t, *J* = 7.3 Hz, 3H, C*H* Ar), 4.78 (q, *J* = 7.3 Hz, 2H, CH_2CH_3), 3.39 (q, *J* = 6.9 Hz, 2H, CH_2S), 2.18 (t, *J* = 7.2 Hz, 2H, CH_2), 1.56 (p, *J* = 7.4 Hz, 2H, CH_2), 1.46 (t, *J* = 7.0 Hz, 3H, CH_3CH_2O), 1.41 (p, *J* = 7.4 Hz, 2H, CH_2), 1.35 – 1.17 (m, 4H, CH_2).

^{13}C NMR (126 MHz, $CDCl_3$) δ 189.86 (1C, *C*), 182.46 (1C, *C*), 177.45 (1C, *C*), 172.41 (1C, *C*), 145.02 (3C, Ar), 129.61 (6C, Ar), 127.87 (6C, Ar), 126.60 (3C, Ar), 69.73 (1C, *C*H_2), 66.48 (1C, *C*S), 44.76 (1C, *C*H_2), 31.86 (1C, *C*H_2), 30.34 (1C, *C*H_2), 28.46 (2C, *C*H_2), 25.93 (1C, *C*H_2), 15.94 (1C, *C*H_3).

Synthesis of GZ-257

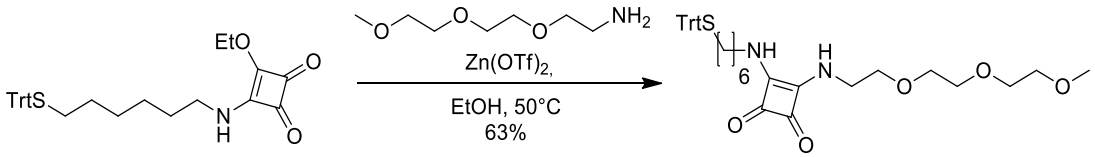

GZ-255 (200 mg, 4.00 mmol, 1.0 equiv.), GZ-232 (78.4 mg, 4.80 mmol, 1.2 equiv.) and zinc triflate (29 mg, 0.08 mmol, 0.2 equiv.) were added to EtOH (5 mL) and the mixture was stirred at 50°C for 5 days. Then DIPEA (200 µL) was added and the mixture was stirred for 1 more day at 75°C. The solvent was evaporated and the residue purified by flash column

chromatography on silica (eluent: gradient from DCM:MeOH 24:1 to 95:5). 156 mg of product (yield = 63%) were collected.

^{1}H NMR (500 MHz, Chloroform-*d*) δ 7.41 (d, *J* = 7.5 Hz, 6H, C*H* Ar), 7.27 (t, *J* = 7.7 Hz, 6H, C*H* Ar), 7.20 (t, *J* = 7.2 Hz, 3H, C*H* Ar), 3.82 (m, 2H, CH_2), 3.69 – 3.51 (m, 12H, CH_2), 3.36 (s, 3H, CH_3), 2.13 (t, *J* = 7.3 Hz, 2H, CH_2), 1.51 (p, *J* = 7.2 Hz, 2H, CH_2), 1.37 (p, *J* = 7.0 Hz, 2H, CH_2), 1.23 (m, 4H, CH_2).

^{13}C NMR (126 MHz, $CDCl_3$) δ 182.65 (2C, *C*O), 168.28 (1C, *C*N), 167.83 (1C, *C*N), 144.99 (3C, Ar), 129.57 (6C, Ar), 127.82 (6C, Ar), 126.55 (3C, Ar), 71.84, 70.61, 70.44, 70.19, 70.09, 66.41 (6C, *C*H_2 + *C*S), 58.91 (1C, *C*H_3O), 44.46, 43.96, 31.92, 31.02, 28.69, 28.54, 26.12 (7C, *C*H_2).

Synthesis of GZ-265

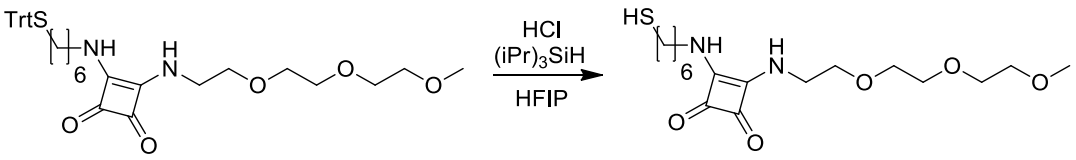

GZ-257 (77 mg, 0.125 mmol, 1.0 equiv.) was dissolved in 1,1,1,3,3,3-hexafluoroisopropanol (2 mL) and HCl 37% (0.2 mL) was added under nitrogen atmosphere. $(iPr)_3SiH$ (150 µL) was added and the solution stirred at room temperature for 4h. The mixture was evaporated and used as is for the AuNPs functionalization.

Synthesis of GZ-295

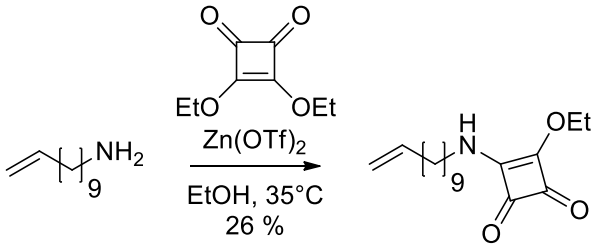

GZ-293 (400 mg, 2.36 mmol, 1 equiv.), 3,4-diethoxy-3-cyclobutene-1,2-dione (524 uL, 3.54 mmol, 1.5 equiv.) and zinc triflate (172 mg, 0.47 mmol, 0.2 equiv.) were dissolved in EtOH (10 mL) and left under stirring at 35°C for 13 days. The solvent was then evaporated under vacuum and the residue was extracted from water (25 mL) with 3 x 25 mL DCM. The product was purified by flash column chromatography on silica (eluent from DCM/MeOH 250/2 to 95/5). 162 mg of product were collected (yield = 26 %).

^{1}H NMR (200 MHz, Chloroform-*d*) δ 5.83 (ddt, *J* = 16.8, 10.1, 6.5 Hz, 1H, RC*H*=CH$_2$), 5.09 – 4.88 (m, 2H, C*H*2=CHR), 4.81 – 4.68 (m, 2H, OC*H*$_2$CH$_3$), 3.45 (q, *J* = 6.8 Hz, 2H, C*H*$_2$), 2.05 (q, *J* = 7.1, 6.4 Hz, 2H, C*H*$_2$), 1.76 – 1.07 (m, 15H, C*H*$_2$ + C*H*$_3$).

^{13}C NMR (50 MHz, $CDCl_3$) δ 189.96 (1C, *C*O), 182.66 (1C, *C*O), 177.53 (1C, *C* quat.), 172.64 (1C, *C* quat.), 139.35 (1C, *C*=C), 114.36 (1C, *C*=C), 69.83 (1C, *C*H$_2$O), 45.10, 33.98, 30.80, 29.58, 29.27, 29.10, 26.53 (9C, *C*H$_2$), 16.05 (1C, *C*H$_3$).

Synthesis of GZ-300

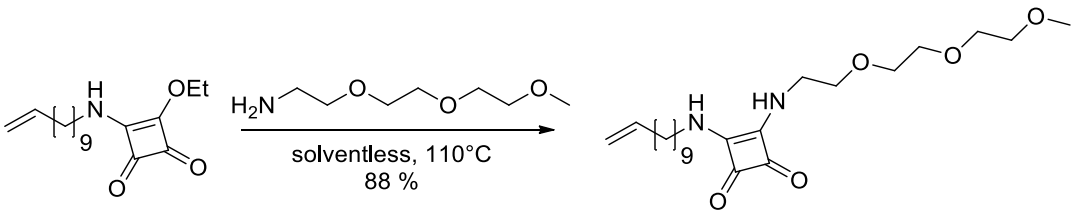

GZ-295 (162 mg, 0.61 mmol, 1 equiv.) and GZ-204 (125 mg, 0.76 mmol, 1.25 equiv.) were mixed in a sealed vial and stirred at 110°C for 5 days. The product was purified by flash column chromatography on silica (eluent DCM/MeOH 24/1 to 95/5). 220 mg of product were collected (yield = 88 %).

^{1}H NMR (500 MHz, Chloroform-*d*) δ 5.74 (ddt, *J* = 16.9, 10.2, 6.7 Hz, 1H, RC*H*=CH$_2$), 4.98 – 4.83 (m, 2H, C*H*$_2$=CHR), 3.79 (d, *J* = 6.2 Hz, 2H, C*H*$_2$N), 3.66 – 3.53 (m, 10H, C*H*$_2$), 3.51 – 3.46 (m, 2H, C*H*$_2$), 3.31 (s, 3H, C*H*$_3$O), 2.03 – 1.92 (m, 2H, C*H*$_2$), 1.57 (p, *J* = 7.1 Hz, 2H, C*H*$_2$), 1.35 – 1.18 (m, 12H, C*H*$_2$).

^{13}C NMR (126 MHz, $CDCl_3$) δ 182.45 (1C, *C*O), 182.22 (1C, *C*O), 168.10 (1C, *C* quat.), 167.91 (1C, *C* quat.), 139.04 (1C, *C*=C), 114.12 (1C, *C*=C), 71.83, 70.52, 70.46, 70.30, 70.16 (5C, *C*H$_2$O), 58.87 (1C, *C*H$_3$O), 44.61 (1C, *C*H$_2$N), 43.97 (1C, *C*H$_2$N), 33.74, 31.16, 29.49, 29.42, 29.28, 29.07, 28.86, 26.48 (8C, *C*H$_2$).

Synthesis of GZ-301

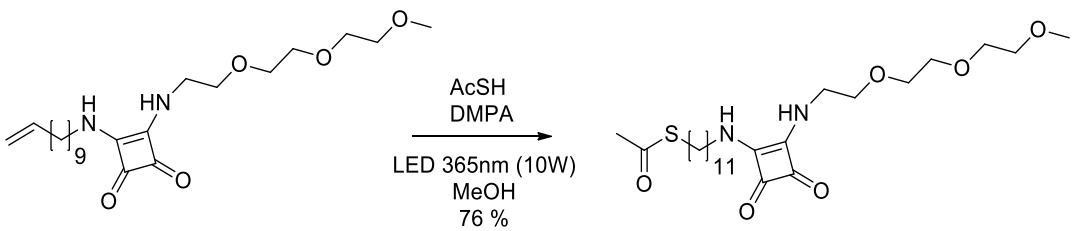

GZ-300 (200 mg, 0.49 mmol, 1 equiv.), thioacetic acid (328 uL, 4.48 mmol, 9.2 equiv.) and 2,2-dimethoxy-2-phenylacetophenone (12.7 mg, 0.049 mmol, 0.1 equiv.) were dissolved in previously degassed MeOH (2 mL). The solution was irradiated for 4 h with a 365nm LED (10W) under stirring. The solution was evaporated under reduced pressure and the product was purified by flash column chromatography on silica (eluent DCM/MeOH from 24/1 to 95/5). The product (180 mg, yield = 76 %) was collected as a yellowish solid.

^{1}H NMR (500 MHz, Chloroform-*d*) δ 3.77 (q, *J* = 5.6 Hz, 2H, C*H*$_2$N), 3.63 – 3.53 (m, 10H, C*H*$_2$), 3.52 – 3.46 (m, 2H, C*H*$_2$O), 3.30 (s, 3H, C*H*$_3$O), 2.78 (t, *J* = 7.3 Hz, 2H, C*H*$_2$S), 2.25 (s, 3H, C*H*$_3$S), 1.55 (p, *J* = 7.1 Hz, 2H, C*H*$_2$), 1.48 (p, *J* = 7.4 Hz, 2H, C*H*$_2$), 1.32 – 1.15 (m, 10H, C*H*$_2$).

^{13}C NMR (126 MHz, $CDCl_3$) δ 195.97 (1C *C*OS), 182.57 (1C, *C*O), 182.39 (1C, *C*O), 168.16 (1C, *C* quat.), 167.86 (1C, *C* quat.), 71.81, 70.56, 70.42, 70.23, 70.12 (5C, *C*H$_2$O), 58.85 (1C, *C*H$_3$O), 44.55 (1C, *C*H$_2$N), 43.93 (1C, *C*H$_2$N), 30.58, 29.50, 29.48, 29.44, 29.40, 29.27, 29.05, 28.74, 26.46 (9C, *C*H$_2$ + *C*H$_3$).

Synthesis of GZ-312

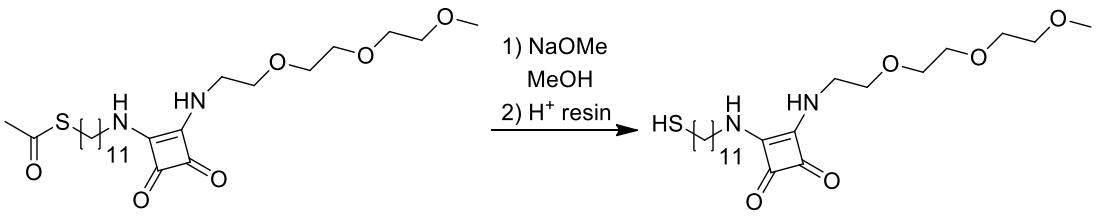

GZ-301 (59.8 mg, 0.123 mmol, 1 equiv.) was dissolved in dry MeOH (2 mL) and sodium methoxide (20 mg, 0.369 mmol, 3 equiv.) was added under nitrogen atmosphere. The solution was stirred at room temperature for 4 h then a spatula tip of Amberlyst H^+ resin was added and left standing in the solution for 20 minutes. The solution was used as is for the nanoparticles functionalization.

Synthesis of GZ-352

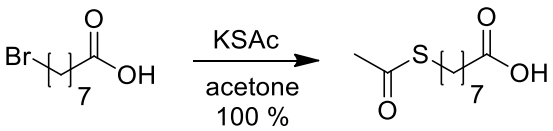

8-bromooctanoic acid (1.50 g, 6.72 mmol, 1 equiv.) and potassium thioacetate (1.15 g, 10.1 mmol, 1.5 equiv.) were added to acetone (50 mL) and stirred at 35°C overnight. The solvent

was evaporated under reduced pressure and to the residue water (30 mL) was added. The mixture was extracted with 3 x 30 mL DCM. The product was purified by flash column chromatography on silica (eluent: DCM/MeOH 95/5). The product (1.472 g, yield = 100 %) was collected as a beige solid.

^{1}H NMR (500 MHz, $CDCl_3$) δ 2.87 (t, *J* = 7.3 Hz, 2H, C*H*$_2$SAc), 2.36 (t, *J* = 7.5 Hz, 2H, C*H*$_2$COOH), 2.33 (s, 3H, C*H*$_3$S), 1.64 (p, *J* = 7.4 Hz, 2H, C*H*$_2$CH$_2$S), 1.58 (p, *J* = 7.6 Hz, 2H, C*H*$_2$CH$_2$COOH), 1.40 – 1.29 (m, 6H, C*H*$_2$).

^{13}C NMR (126 MHz, $CDCl_3$) δ 196.10 (1C, CH$_3$*C*OS), 179.99 (1C, *C*OOH), 33.98 (1C, *C*H$_2$), 30.63 (1C, *C*H$_2$S, 29.41 (1C, *C*H$_2$), 29.07 (1C, *C*H$_2$), 28.85 (1C, *C*H$_2$), 28.70 (1C, *C*H$_2$), 28.53 (1C, *C*H$_2$), 24.55 (1C, *C*H$_2$).

Synthesis of GZ-373

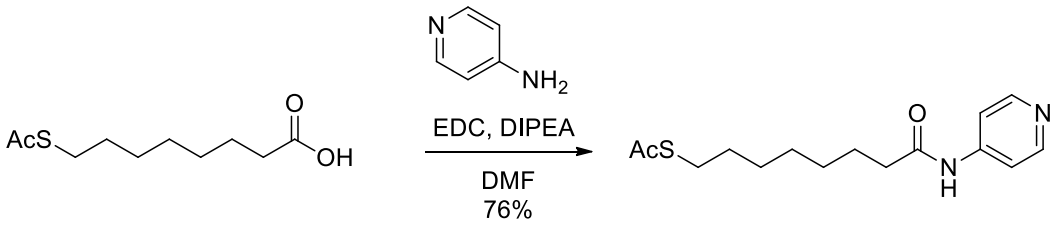

GZ-352 (250 mg, 1.15 mmol, 1.0 equiv.), 4-aminopyridine (108 mg, 1.15 mmol, 1.0 equiv.) and EDC hydrochloride (265 mg, 1.38 mmol, 1.2 equiv.) were diluted in dry DMF (3 mL) and DIPEA (501 µL, 2.88 mmol, 2.5 equiv.) was added. The solution was stirred overnight at room temperature. The solvent was evaporated and the residue purified by flash column chromatography on silica (eluent: gradient from DCM:MeOH 95:5 to 1:1 + 1% triethylamine). The product (257 mg, yield = 76%) was collected as a yellowish solid.

^{1}H NMR (500 MHz, Chloroform-*d*) δ 8.40 (d, *J* = 6.5 Hz, 2H, CH py), 7.57 (d, *J* = 6.5 Hz, 2H, CH py), 2.81 (t, *J* = 7.3 Hz, 2H, CH2SAc), 2.37 (t, *J* = 7.5 Hz, 2H, CH2COOH), 2.30 (s, 3H, CH3S), 1.67 (p, *J* = 7.4 Hz, 2H, CH2), 1.52 (p, *J* = 7.3 Hz, 2H, CH2), 1.36 – 1.23 (m, 6H, CH2).

^{13}C NMR (126 MHz, $CDCl_3$) δ 196.56 (1C, *C*OS), 173.06 (1C, *C*ON), 150.04 (2C, *C*H py), 146.14 (1C, *C* py), 113.78 (2C, *C*H py), 37.42 (1C, *C*H$_2$S), 30.66 (1C, *C*H$_2$), 29.36 (1C, *C*H$_2$), 29.00 (1C, *C*H$_2$), 28.95 (1C, *C*H$_2$), 28.68 (1C, *C*H$_2$), 28.47 (1C, *C*H$_2$), 25.18 (1C, *C*H$_2$).

Synthesis of GZ-373d

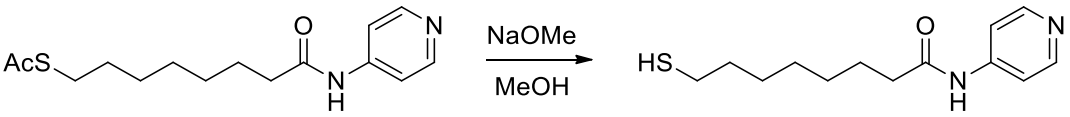

GZ-373 (36.2 mg, 0.123 mmol, 1.0 equiv.) and sodium methoxide (20 mg, 0.37 mmol, 3.0 equiv.) were dissolved in dry MeOH (2 mL) under nitrogen atmosphere. The solution was stirred for 2 h and then evaporated. The residue was used as is for the AuNPs functionalization.

^{1}H NMR (500 MHz, MeOD) δ 8.39 (d, *J* = 6.6 Hz, 2H, C*H* py), 7.66 (d, *J* = 6.5 Hz, 2H, C*H* py), 2.50 (t, *J* = 7.2 Hz, 2H, CH_2SH), 2.43 (t, *J* = 7.5 Hz, 2H, CH_2CON), 1.72 (p, *J* = 7.5 Hz, 2H, CH_2), 1.61 (p, *J* = 7.8, 7.2 Hz, 2H, CH_2), 1.48 – 1.35 (m, 6H, CH_2).

^{13}C NMR (126 MHz, MeOD) δ 174.12 (1C, *C*ON), 149.33 (1C, *C* py), 146.78 (2C, *C*H py), 113.61 (2C, *C*H py), 36.68 (1C, *C*H_2CON), 34.77 (1C, *C*H_2), 28.80 (1C, *C*H_2), 28.58 (1C, *C*H_2), 28.20 (1C, *C*H_2), 25.05 (1C, *C*H_2), 23.86 (1C, *C*H_2SH).

HRMS (ESI) m/z: 253.1393 ($M+H^+$); calc. 253.1370

Synthesis of GZ-375 (AuNPs)

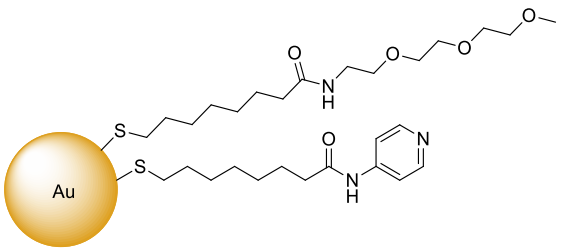

GZ-291 (20.45 mg, 2.47*10^{-5} mol (in thiols), 1.0 equiv.) was dissolved in 0.5 mL MeOD and GZ-373d (1.46 mg, 4.95*10^{-6} mol, 0.2 equiv.) was added. The dispersion was stirred overnight at room temperature under nitrogen atmosphere, then the AuNPs were purified by size exclusion chromatography (Sephadex LH-20, MeOH) x 3. 15.6 mg of AuNPs were collected.

By comparison of the CH_2CON integrals of the signals of the two different thiols after ligand stripping (by addition of a crystal of iodine to a dispersion of AuNPs ca. 1 mM in MeOD), the ratio of thiol pyridine/thiol TEG amide was determined to be 1/13.

TEM analysis: AuNPs diameter = 1.4 ± 0.3 nm

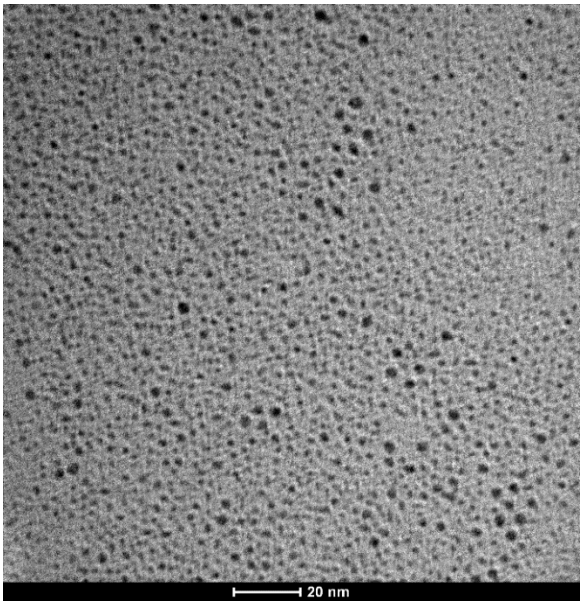

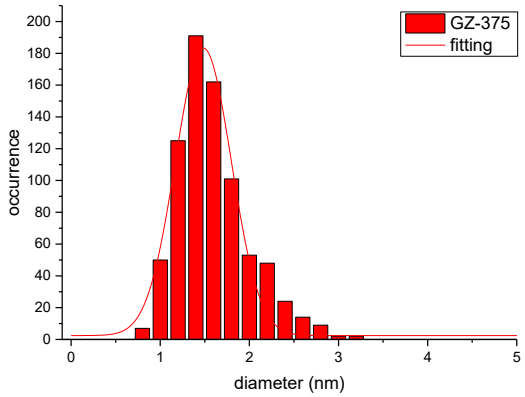

Figure 178: TEM analysis of GZ-375 AuNPs

Synthesis of GZ-399

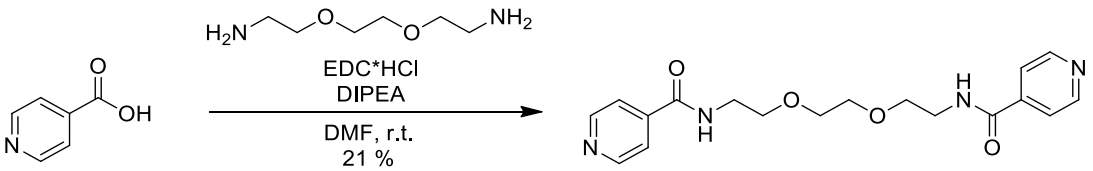

4-carboxypyridine (200 mg, 1.62 mmol, 2 equiv.), 1,8-diamino-3,6-dioxaoctane (119 µL, 0.81 mmol, 1 equiv.) and DIPEA (705 µL, 4.05 mmol, 5 equiv.) were added to dry DMF (2 mL). To the mixture EDC*HCl (372 mg, 1.94 mmol, 2.4 equiv.) was then added and the mixture was left under stirring in a nitrogen atmosphere at room temperature overnight. After evaporation under reduced pressure the product was purified by flash column

chromatography on silica (eluent: DCM/MeOH 85/15 to 8/2). 62 mg of product were collected (yield = 21 %).

Synthesis of GZ-401

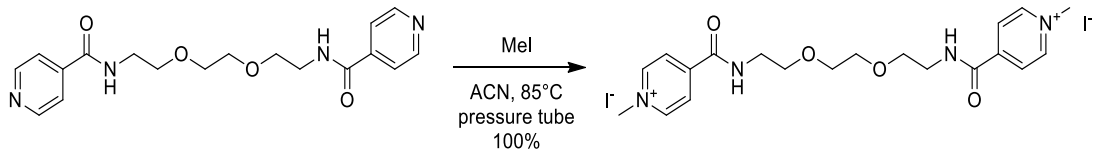

GZ-399 (62 mg, 0.17 mmol, 1 equiv.) was dissolved in CAN (100 µL) in a pressure tube. MeI (54 µL, 0.86 mmol, 5 equiv.) was added and the solution was left under stirring at 85°C overnight. The mixture was evaporated under reduced pressure and the product was obtained as a yellow solid (110 mg, yield 100 %).

^{1}H NMR (500 MHz, MeOD): δ 9.11 (d, J = 6.4 Hz, 4H, CHN), 8.43 (d, J = 6.3 Hz, 4H C*H*-CCON), 4.51 (s, 6H, C*H*$_3$N$^+$), 3.72 (t, J = 5.5 Hz, 4H, C*H*$_2$CH$_2$N), 3.70 (s, 4H, C*H*$_2$O), 3.63 (t, J = 5.5 Hz, 4H, C*H*$_2$N).

^{13}C NMR (126 MHz, MeOD): δ 162.87 (2C, *C*ON), 148.87 (2C, *C*CON), 146.47 (4C, *C*HN), 125.63 (4C, *C*HCCON), 69.97 (2C, *C*H$_2$), 68.69 (2C, *C*H$_2$), 47.85 (2C, *C*H$_3$), 39.97 (2C, *C*H$_2$N).

Synthesis of GZ-341 (NP-SO$_3$)

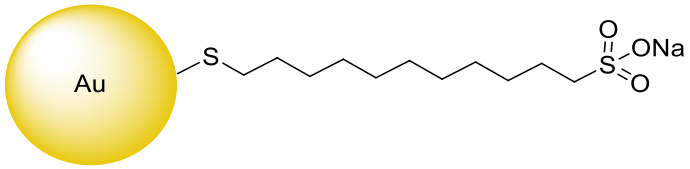

Thiol GZ-339 was added to the DOA-protected AuNPs. The nanoparticles were purified by 4 x precipitation from MeOH with Et$_2$O and then by size exclusion chromatography (Sephadex G-25 in H$_2$O) x 2. 36.9 mg of AuNPs were obtained.

MW (Au$_{180}$SR$_{70}$) = 55713

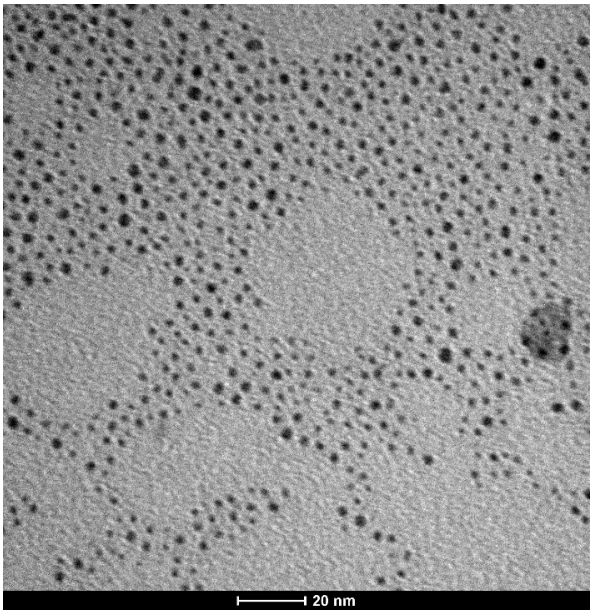

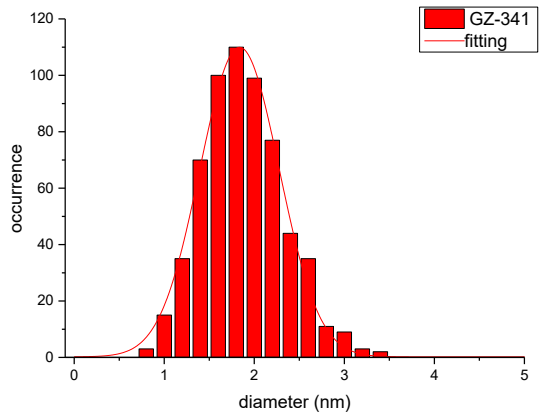

Figure 179: TEM analysis of GZ-341 (AuNP-SO_3)

TEM analysis: diameter = 1.8 ± 0.4 nm.

Synthesis of GZ-342 (NP-mix)

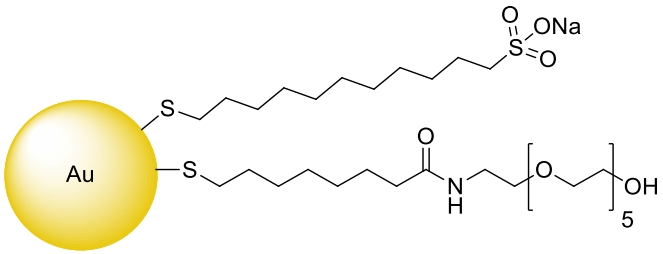

Nanoparticles were synthetized by addition of an equimolar mixture of thiols GZ-336 and GB-32 to the DOA-protected AuNPs. They were purified by precipitation from MeOH with Et_2O x

4 and then by size exclusion chromatography (Sephadex LH-20 in MeOH) x 2. 28.5 mg of AuNPs were obtained.

By comparison of the C*H*$_2$CON and C*H*$_2$SO$_3^-$ integrals of the two different thiols after ligand stripping (by addition of a crystal of iodine to a dispersion of AuNPs ca. 1 mM in MeOD), the ratio sulfonate thiol/PEG thiol resulted to be 1/1.123.

MW ($Au_{180}SR(SO_3^-)_{33}SR(PEG)_{37}$) = 61233

TGA analysis: diameter = 1.8 ± 0.4 nm

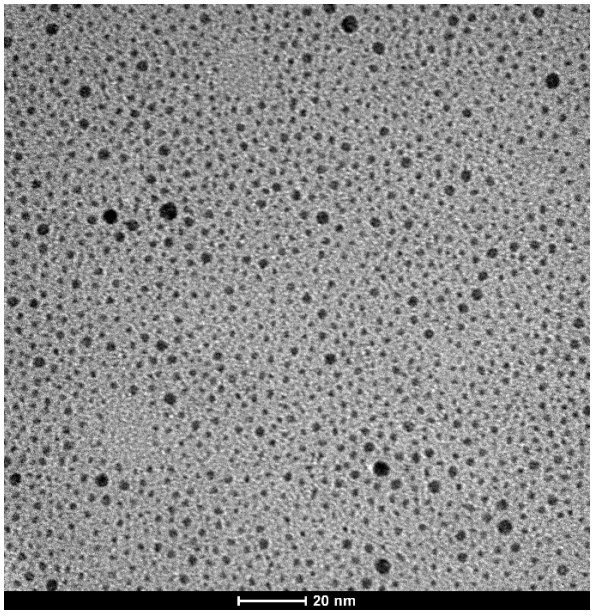

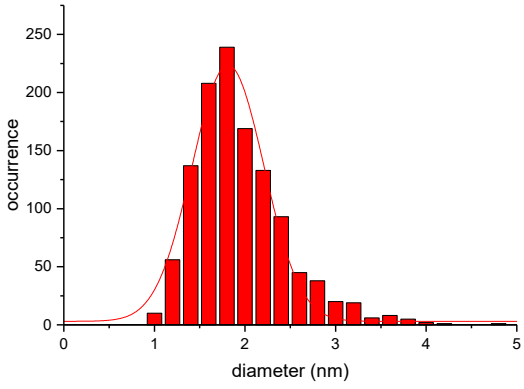

Figure 180: TEM analysis of GZ-342 (NP-mix)

Synthesis of GZ-157

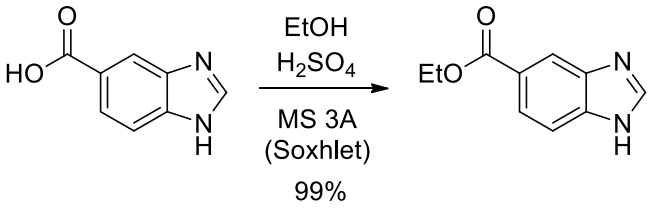

5-benzimidazolecarboxylic acid (1.50 g, 9.25 mmol, 1 equiv.) was dissolved in EtOH (38 mL) in a round bottom flask and H_2SO_4 96% (1.00 mL) was added dropwise. A Soxhlet extractor was filled with molecular sieves 3Å and was placed on the flask. The solution was refluxed overnight and then evaporated. The residue was neutralized with sat. $NaHCO_3$ and the mixture extracted with 3 x 40 mL EtOAc. The organic phase was evaporated with a rotavapor and the product was obtained as a yellowish oil (1,76 g, yield = 100%).

^{1}H NMR (500 MHz, $CDCl_3$) δ 10.64 (br, 1H, N*H*), 8.45 (s, 1H, C*H* imidazole), 8.35 (s, 1H, C*H* Ar), 8.02 (d, J = 8.5 Hz, 1H, C*H* Ar), 7.69 (d, J = 8.5 Hz, 1H, C*H* Ar), 4.40 (q, J = 7.1 Hz, 2H, OC$H_2$$CH_3$), 1.39 (t, J = 7.1 Hz, 3H, CH_3).

^{13}C NMR (126 MHz, $CDCl_3$) δ 167.37 (1C, *C*O), 143.26 (1C, Ar), 140.72 (1C, N*C*HN), 137.88 (1C, Ar), 125.16 (1C, Ar), 124.33 (1C, Ar), 118.23 (1C, Ar), 114.87 (1C, Ar), 61.15 (1C, *C*H_2), 14.34 (1C, *C*H_3).

Synthesis of GZ-158

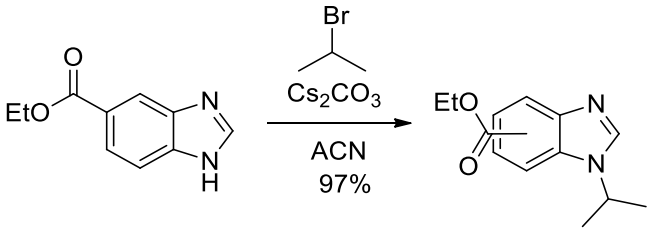

GZ-157 (1.50 g, 7.9 mmol, 1.0 equiv.), Cs_2CO_3 (3.58 g, 11.0 mmol, 1.4 equiv.) and isopropyl bromide (1.04 mL, 11.0 mmol, 1.4 equiv.) were added in sequence to ACN (45 mL) in a round bottom flask. The mixture was refluxed overnight and then evaporated with a rotavapor. H_2O (ca. 40 mL) was added to the residue and the mixture was extracted with 3 x 30 mL DCM. The organic phase was dried with sodium sulphate and evaporated with a rotavapor. The product (1.77 g, yield = 97%), a ca. 1:1 mixture of the two regioisomers, was collected as a yellowish oil.

^{1}H NMR (500 MHz, $CDCl_3$) δ 8.52 (s, 1H, NC*H*N), 8.51 (s, 1H, NC*H*N), 8.18 (s, 1H, C*H* Ar), 8.18 (s, 1H, C*H* Ar), 8.00 (dd, *J* = 8.6, 1.6 Hz, 1H, C*H* Ar), 7.98 (dd, *J* = 8.5, 1.6 Hz, 1H, C*H* Ar), 7.79 (dd, *J* = 8.5, 0.7 Hz, 1H, C*H* Ar), 7.42 (dd, *J* = 8.6, 0.6 Hz, 1H, C*H* Ar), 4.70 (p, *J* = 6.8 Hz, 1H, C*H* iPr), 4.64 (p, *J* = 6.8 Hz, 1H, C*H* iPr), 4.39 (q, *J* = 7.1 Hz, 2H, CH_2 Et), 4.39 (q, *J* = 7.1 Hz, 2H, CH_2 Et), 1.63 (s, 3H, CH_3 iPr), 1.62 (s, 3H, CH_3 iPr), 1.61 (s, 3H, CH_3 iPr), 1.60 (s, 3H, CH_3 iPr), 1.41 (t, *J* = 7.1 Hz, 3H, CH_3 Et), 1.40 (t, *J* = 7.1 Hz, 3H, CH_3 Et).

^{13}C NMR (126 MHz, $CDCl_3$) δ 166.53 (1C, *C*O), 166.44 (1C, *C*O), 146.95 (1C, Ar), 143.19 (1C, Ar), 142.79 (1C, Ar), 141.97 (1C, Ar), 136.08 (1C, Ar), 132.62 (1C, Ar), 124.38 (1C, Ar), 124.06 (1C, Ar), 123.55 (1C, Ar), 122.91 (1C, Ar), 122.02 (1C, Ar), 119.30 (1C, Ar), 112.14 (1C, Ar), 109.60 (1C, Ar), 60.53 (1C, *C*H_2 Et), 60.36 (1C, *C*H_2 Et), 47.62 (1C, *C*H iPr), 47.59 (1C, *C*H iPr), 22.09 (1C, *C*H_3 iPr), 21.93 (1C, *C*H_3 iPr), 14.00 (1C, *C*H_3 Et).

Synthesis of GZ-173

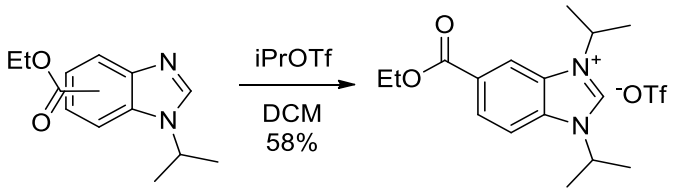

Dry isopropanol (361 µL, 4.71 mmol, 1.5 equiv.), dry pyridine (381 µL, 4.71 mmol, 1.5 equiv.) and triflic anhydride 1M in THF (5.02 mL, 5.02 mmol, 1.6 equiv.) were added sequentially in an ice bath under nitrogen atmosphere and constant stirring. After 90 minutes n-hexane (6 mL, previously dried with calcium hydride) was added to the solution. The mixture was then rapidly filtered on Celite and the filtrate added directly to a solution of GZ-158 (0.729 g, 3.14 mmol, 1.0 equiv.) in dry DCM (6 mL). The mixture was left under stirring overnight under nitrogen atmosphere in an ice bath. The mixture was then evaporated with a rotavapor and the residue purified through flash column chromatography on silica (eluent: gradient from DCM:MeOH 95:5 to 9:1). The product (770 mg, yield = 58%) was obtained as brown oil.

^{1}H NMR (500 MHz, $CDCl_3$) δ 9.69 (s, 1H, NC*H*N), 8.39 (s, 1H, C*H* Ar)), 8.22 (d, J = 8.8 Hz, 1H, C*H* Ar), 7.94 (d, J = 8.8 Hz, 1H C*H* Ar), 5.01 (2p, J = 6.7 Hz, 2H, C*H* iPr), 4.34 (q, J = 7.1 Hz, 2H CH_2 Et), 1.70 (2d, J = 6.8 Hz, 12H, CH_3 iPr), 1.33 (t, J = 7.1 Hz, 3H, CH_3 Et).

^{13}C NMR (126 MHz, $CDCl_3$) δ 164.83 (1C, *C*O), 140.46 (1C, N*C*HN), 133.75 (1C, Ar), 130.76 (1C, Ar), 129.39 (1C, Ar), 127.96 (1C, Ar), 115.30 (1C, Ar), 114.20 (1C, Ar), 61.97 (1C, *C*H_2 Et), 52.42 (1C, *C*H iPr), 21.70 (2C, *C*H_3 iPr), 21.59 (2C, *C*H_3 iPr), 14.14 (1C, *C*H_3 Et).

Synthesis of GZ-174

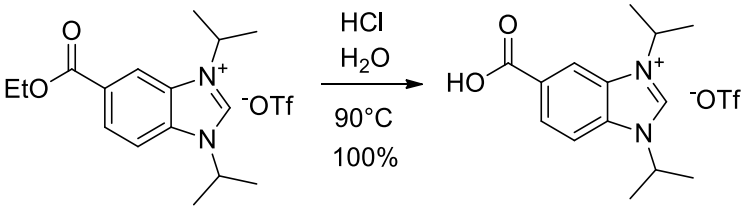

GZ-173 (500 mg) was dissolved in deionized water (20 mL) and HCl 37% (2.0 mL) was added. The solution was heated to 90°C and left under stirring overnight. The solution was evaporated and the product (467mg, yield = 100%) was obtained as a beige solid.

^{1}H NMR (500 MHz, MeOD) δ 9.75 (s, 1H, NC*H*N), 8.67 (s, 1H, C*H* Ar), 8.37 (d, J = 9.5 Hz, 1H, C*H* Ar), 8.16 (d, J = 8.7 Hz, 1H, C*H* Ar), 5.16 (2p, J = 6.7 Hz, 2H C*H* iPr), 1.79 (s, 6H, CH_3 iPr), 1.77 (s, 6H, CH_3 iPr).

^{13}C NMR (126 MHz, MeOD) δ 166.62 (1C, *C*O), 140.13 (1C, NCHN), 133.93 (1C, Ar), 131.17 (1C, Ar), 129.60 (1C, Ar), 127.59 (1C, Ar), 115.40 (1C, Ar), 113.81 (1C, Ar), 51.97 (1C, *C*H iPr), 51.80 (1C, *C*H iPr), 20.86 (1C, *C*H$_3$ iPr), 20.75 (1C, CH_3 iPr).

Synthesis of GZ-194

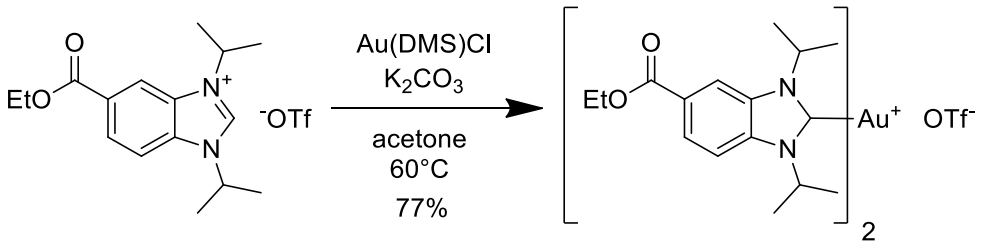

GZ-173 (153 mg, 0.36 mmol, 2.0 equiv), Au(DMS)Cl (53 mg, 0.18 mmol, 1.0 equiv.) and K_2CO_3 (90 mg, 0.65 mmol, 3.6 equiv.) were added to acetone (6 mL) in a round bottom flask. The mixture was stirred overnight at 60 °C and then filtered on Celite. The filtrate was evaporated and the residue was purified by flash column chromatography on silica (eluent: gradient to DCM:MeOH 95:5 to MeOH 100%). The product (124 mg, yield 77%) was obtained as a yellow solid.

^{1}H NMR (500 MHz, MeOD) δ 8.54 (s, 1H, C*H* Ar)), 8.20 (d, J = 8.7 Hz, 1H, Ar), 8.06 (d, J = 8.7 Hz, 1H, Ar), 5.55 (p, J = 7.0, 1H, C*H* iPr), 5.54 (p, J = 7.0, 1H, C*H* iPr), 4.47 (q, J = 7.1 Hz, 2H, CH_2 Et), 1.93 (d, J = 7.3 Hz, 6H, CH_3 iPr), 1.91 (d, J = 7.1 Hz, 6H, CH_3 iPr), 1.46 (t, J = 7.2 Hz, 3H, CH_3 Et).

^{13}C NMR (50 MHz, MeOD) δ 188.20 (1C, N*C*N), 164.63 (1C, *C*O), 134.26 (1C, Ar), 131.39 (1C, Ar), 125.74 (1C, Ar), 124.32 (1C, *C*H Ar), 113.05 (1C, *C*H Ar), 111.83 (1C, *C*H Ar), 60.20 (1C, *C*H_2 Et), 52.84 (1C, *C*H iPr), 52.36 (1C, *C*H iPr), 20.55 (2C, *C*H_3 iPr), 20.18 (2C, *C*H_3 iPr), 12.07 (1C, *C*H_3 Et).

Synthesis of GZ-195

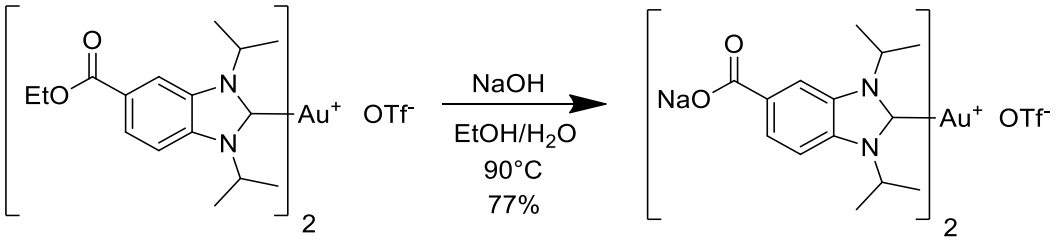

GZ-194 (124 mg, 0.14 mmol, 1.0 equiv.) was dissolved in a 1:1 mixture of EtOH:H_2O (8 mL) and then NaOH (17 mg, 0.42 mmol, 3.0 equiv) was added. The mixture was heated to 90 °C under stirring in a nitrogen atmosphere. After 1 hour the ethanol was evaporated under reduced pressure and the aqueous solution acidified to pH 1-2 with HCl 6M. The mixture was left in freezer at -20 °C for a few hours. The precipitate was washed with water and then it was dissolved in EtOH and evaporated under vacuum. The yellow oil was triturated with DCM and, after evaporation, the product (95 mg, yield = 77%) was collected as a beige solid.

^{1}H NMR (500 MHz, MeOD) δ 8.56 (s, 1H C*H* Ar), 8.22 (d, *J* = 8.7 Hz, 1H, C*H* Ar), 8.06 (d, *J* = 8.7 Hz, 1H, C*H* Ar), 5.55 (p, *J* = 7.0 Hz, 2H, C*H* iPr), 1.94 – 1.89 (2d, 12H, C*H*$_3$ iPr).

^{13}C NMR (126 MHz, MeOD) δ 189.31 (1C, N*C*N), 167.35 (1C, *C*O), 135.40 (1C, Ar), 132.53 (1C, Ar), 127.38 (1C, Ar), 125.77 (1C, Ar), 114.51 (1C, Ar), 112.91 (1C, Ar), 53.99 (1C, *C*H iPr), 53.67 (1C, *C*H iPr), 21.58 (1C, *C*H_3 iPr), 21.30 (1C, *C*H_3 iPr).

Synthesis of GZ-196 (NHC-AuNPs)

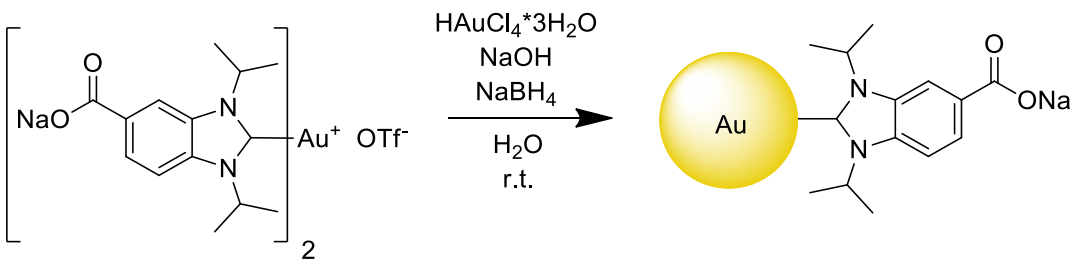

GZ-195 (40 mg, 0.045 mmol, 1.5 equiv.), $HAuCl_4*3H_2O$ (11.7 mg, 0.030 mmol, 1.0 equiv.) and NaOH (17 mg, 0.42 mmol, 14 equiv.) were dissolved in ultrapure water (3.4 mL) under stirring in a nitrogen atmosphere. A solution of sodium borohydride (19.3 g, 0.51 mmol, 17 equiv.) in ultrapure water (640 µL) was then added and the solution stirred at room temperature for 5h. The nanoparticles were purified by dialysis with Amicon Ultra 10kDa filters in a centrifuge (5000 rpm, 8 minutes). The nanoparticles were washed 3 times with ultrapure water. The dispersion was then purified by size exclusion chromatography in water (Sephadex G-25 resin). 2.9 mg of AuNPs were collected, but this colloid is not stable long term.

^{1}H NMR (500 MHz, MeOD): δ 8.74 – 8.63 (m, 4H, C*H*N), 7.83 – 7.73 (m, 4H, C*H*-CCON), 3.68 (m, 8H, CH_2), 3.59 (t, 4H, CH_2).

^{13}C NMR (126 MHz, MeOD): δ 166.40 (2C, *C*ON), 149.58 (4C, *C*H_2N) , 142.40 (2C, *C*-CON), 121.52 (4C, *C*H_2C-CON), 69.97 (2C, *C*H_2), 68.97 (2C, *C*H_2), 39.62 (2C, *C*H_2N).

Synthesis of GZ-187

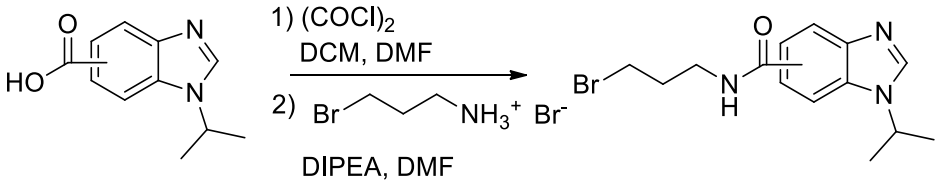

GZ-184 (106 mg, 0.52 mmol, 1.2 equiv.) was dissolved in dry DCM (2 mL) under nitrogen atmosphere. A drop of dry DMF was added followed by oxalyl chloride (72.7 µL, 0.86 mmol, 2.0 equiv.). The solution was stirred for 90 minutes and then evaporated with a rotavapor. The residue was dissolved in dry DMF (2 mL) under nitrogen atmosphere and then 3-bromopropanamine hydrobromide (94 mg, 0.43 mmol, 1.0 equiv.) was added followed by DIPEA (226 µL, 1.29 mmol, 3.0 equiv.). The solution was left under stirring overnight and then it was evaporated with a rotavapor. NaHCO3 5% (20 mL) was added to the residue which was then extracted with 3 x 20 mL EtOAc. 74 mg (yield = 53%) of product were collected.

Synthesis of GZ-159

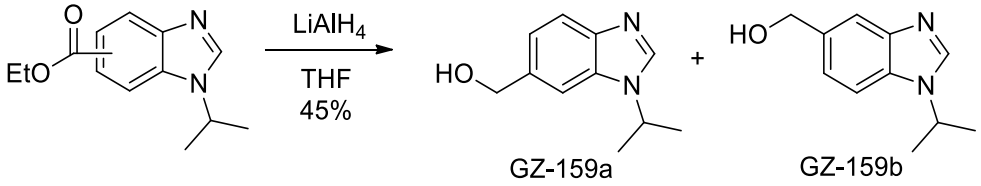

GZ-158 (400 mg, 1.70 mmol, 1.0 equiv.) was dissolved in dry THF (1 mL) under nitrogen atmosphere. To the solution was then added $LiAlH_4$ 1M in THF (3.4 mL, 3.40 mmol, 2.0 equiv.) and the solution was stirred overnight at room temperature. The mixture was then quenched by addition of EtOH (5 mL). EtOAc (5 mL) was added, the mixture was filtered and the filtrate evaporated. Aqueous $NaHCO_3$ was added and the mixture was extracted with 3 x 20 mL EtOAc. The organic phase was evaporated and the residue purified by flash column chromatography on silica (eluent: gradient from DCM:MeOH 95:5 to 9:1). GZ-159a (46 mg) and GZ-159b (99 mg) were collected as brown oils (for a 45% overall yield).

GZ-159a

^{1}H NMR (500 MHz, MeOD) δ 8.25 (s, 1H, NC*H*N), 7.65 (d, *J* = 8.3 Hz, 1H, C*H* Ar), 7.62 (s, 1H, C*H* Ar), 7.29 (d, *J* = 8.2 Hz, 1H, C*H* Ar), 4.79 – 4.75 (m, 3H, CH_2OH + C*H* iPr), 1.64 (s, 3H CH_3 iPr), 1.63 (s, 3H, CH_3 iPr).

^{13}C NMR (126 MHz, MeOD) δ 142.22 (1C, NC*H*N), 140.85 (1C, *C* Ar), 136.66 (1C, *C* Ar), 133.01 (1C, *C* Ar), 121.66 (1C, *C*H Ar), 118.57 (1C, *C*H Ar), 108.86 (1C, *C*H Ar), 64.14 (1C, *C*H_2OH), 47.87 (1C, *C*H iPr), 21.26 (2C, *C*H_3 iPr).

GZ-159b

^{1}H NMR (500 MHz, MeOD) δ 8.22 (s, 1H, NC*H*N), 7.70 (s, 1H, C*H* Ar), 7.53 (d, *J* = 8.3 Hz, 1H, C*H* Ar), 7.33 (d, *J* = 8.3 Hz, 1H, C*H* Ar), 4.73 (s, 2H, CH_2OH), 4.72 – 4.60 (m, 1H, C*H* iPr), 1.58 (s, 3H, CH_3 iPr), 1.57 (s, 3H, CH_3 iPr).

^{13}C NMR (126 MHz, MeOD) δ 142.93 (1C, NC*H*N), 140.95 (1C, *C* Ar), 136.01 (1C, *C* Ar), 132.29 (1C, *C* Ar), 122.36 (1C *C*H Ar), 117.30 (1C, *C*H Ar), 110.34 (1C, *C*H Ar), 64.11 (1C, *C*H_2OH), 47.94 (1C, *C*H iPr), 21.28 (2C, *C*H_3 iPr).

Bibliography

(1) Daniel, M. C.; Astruc, D. Gold Nanoparticles: Assembly, Supramolecular Chemistry, Quantum-Size-Related Properties, and Applications Toward Biology, Catalysis, and Nanotechnology. *Chem. Rev.* **2004**, *104* (1), 293–346. https://doi.org/10.1021/cr030698+.

(2) Dreaden, E. C.; Alkilany, A. M.; Huang, X.; Murphy, C. J.; El-Sayed, M. A. The Golden Age: Gold Nanoparticles for Biomedicine. *Chem. Soc. Rev.* **2012**, *41* (7), 2740–2779. https://doi.org/10.1039/c1cs15237h.

(3) Jin, R. Atomically Precise Metal Nanoclusters: Stable Sizes and Optical Properties. *Nanoscale* **2015**, *7* (5), 1549–1565. https://doi.org/10.1039/c4nr05794e.

(4) Wuithschick, M.; Birnbaum, A.; Witte, S.; Sztucki, M.; Vainio, U.; Pinna, N.; Rademann, K.; Emmerling, F.; Kraehnert, R.; Polte, J. Turkevich in New Robes: Key Questions Answered for the Most Common Gold Nanoparticle Synthesis. *ACS Nano* **2015**, *9* (7), 7052–7071. https://doi.org/10.1021/acsnano.5b01579.

(5) Polte, J. Fundamental Growth Principles of Colloidal Metal Nanoparticles - a New Perspective. *CrystEngComm* **2015**, *17* (36), 6809–6830. https://doi.org/10.1039/c5ce01014d.

(6) Wuithschick, M.; Witte, S.; Kettemann, F.; Rademann, K.; Polte, J. Illustrating the Formation of Metal Nanoparticles with a Growth Concept Based on Colloidal Stability. *Phys. Chem. Chem. Phys.* **2015**, *17* (30), 19895–19900. https://doi.org/10.1039/c5cp02219c.

(7) Polte, J.; Erler, R.; Thu, A. F.; Sokolov, S.; Ahner, T. T.; Rademann, K.; Emmerling, F.; Kraehnert, R. Nanoparticles Studied via in Situ Small. *ACS Nano* **2010**, *4* (2), 1076–1082.

(8) Brust, M.; Walker, M.; Bethell, D.; Schiffrin, D. J.; Whyman, R. Synthesis of Thiol-Derivatised Gold Nanoparticles In. *J. Chem. Soc. Chem. Commun.* **1994**, 801–802.

(9) Uehara, A.; Booth, S. G.; Chang, S. Y.; Schroeder, S. L. M.; Imai, T.; Hashimoto, T.; Mosselmans, J. F. W.; Dryfe, R. A. W. Electrochemical Insight into the Brust-Schiffrin Synthesis of Au Nanoparticles. *J. Am. Chem. Soc.* **2015**, *137* (48), 15135–15144. https://doi.org/10.1021/jacs.5b07825.

(10) Perala, S. R. K.; Kumar, S. On the Mechanism of Metal Nanoparticle Synthesis in the

Brust-Schiffrin Method. *Langmuir* **2013**, *29* (31), 9863–9873. https://doi.org/10.1021/la401604q.

(11) Manea, F.; Bindoli, C.; Polizzi, S.; Lay, L.; Scrimin, P. Expeditious Synthesis of Water-Soluble, Monolayer-Protected Gold Nanoparticles of Controlled Size and Monolayer Composition. *Langmuir* **2008**, *24* (8), 4120–4124. https://doi.org/10.1021/la703558y.

(12) Yang, Y.; Serrano, L. A.; Guldin, S. A Versatile AuNP Synthetic Platform for Decoupled Control of Size and Surface Composition. *Langmuir* **2018**, *34* (23), 6820–6826. https://doi.org/10.1021/acs.langmuir.8b00353.

(13) Negishi, Y.; Nakazaki, T.; Malola, S.; Takano, S.; Niihori, Y.; Kurashige, W.; Yamazoe, S.; Tsukuda, T.; Häkkinen, H. A Critical Size for Emergence of Nonbulk Electronic and Geometric Structures in Dodecanethiolate-Protected Au Clusters. *J. Am. Chem. Soc.* **2015**, *137* (3), 1206–1212. https://doi.org/10.1021/ja5109968.

(14) Chakraborty, I.; Pradeep, T. Atomically Precise Clusters of Noble Metals: Emerging Link between Atoms and Nanoparticles. *Chem. Rev.* **2017**, *117* (12), 8208–8271. https://doi.org/10.1021/acs.chemrev.6b00769.

(15) Häkkinen, H. The Gold-Sulfur Interface at the Nanoscale. *Nat. Chem.* **2012**, *4* (6), 443–455. https://doi.org/10.1038/nchem.1352.

(16) Lopez-Acevedo, O.; Akola, J.; Whetten, R. L.; Grönbeck, H.; Häkkinen, H. Structure and Bonding in the Ubiquitous Icosahedral Metallic Gold Cluster Au 144(SR) 60. *J. Phys. Chem. C* **2009**, *113* (13), 5035–5038. https://doi.org/10.1021/jp8115098.

(17) Fantuzzi, G.; Pengo, P.; Gomila, R.; Ballester, P.; Hunter, C. A.; Pasquato, L.; Scrimin, P. Multivalent Recognition of Bis- and Tris-Zn-Porphyrins by N-Methylimidazole Functionalized Gold Nanoparticles. *Chem. Commun.* **2003**, *3* (8), 1004–1005. https://doi.org/10.1039/b211544a.

(18) Boal, A. K.; Rotello, V. M.; Chemistry, J. M. S.; Weinheim, V. C. H. Fabrication and Self-Optimization of Multivalent Receptors on Nanoparticle Scaffolds. *J. Am. Chem. Soc.* **2000**, No. 9, 734–735.

(19) Tormena, C. F.; Evans, R.; Haiber, S.; Nilsson, M.; Morris, G. A. Matrix-Assisted Diffusion-Ordered Spectroscopy: Mixture Resolution by NMR Using SDSmicelles. *Magn. Reson. Chem.* **2010**, *48* (7), 550–553. https://doi.org/10.1002/mrc.2621.

(20) De Biasi, F.; Mancin, F.; Rastrelli, F. Nanoparticle-Assisted NMR Spectroscopy: A

Chemosensing Perspective. *Prog. Nucl. Magn. Reson. Spectrosc.* **2020**, *117*, 70–88. https://doi.org/10.1016/j.pnmrs.2019.12.001.

(21) Drechsler, U.; Erdogan, B.; Rotello, V. M. Nanoparticles: Scaffolds for Molecular Recognition. *Chem. - A Eur. J.* **2004**, *10* (22), 5570–5579. https://doi.org/10.1002/chem.200306076.

(22) Riccardi, L.; Gabrielli, L.; Sun, X.; De Biasi, F.; Rastrelli, F.; Mancin, F.; De Vivo, M. Nanoparticle-Based Receptors Mimic Protein-Ligand Recognition. *Chem* **2017**, *3* (1), 92–109. https://doi.org/10.1016/j.chempr.2017.05.016.

(23) Riccardi, L.; Decherchi, S.; Rocchia, W.; Zanoni, G.; Cavalli, A.; Mancin, F.; De Vivo, M. Molecular Recognition by Gold Nanoparticle-Based Receptors as Defined through Surface Morphology and Pockets Fingerprint. *J. Phys. Chem. Lett.* **2021**, *12* (23), 5616–5622. https://doi.org/10.1021/acs.jpclett.1c01365.

(24) Perrone, B.; Springhetti, S.; Ramadori, F.; Rastrelli, F.; Mancin, F. "NMR Chemosensing" Using Monolayer-Protected Nanoparticles as Receptors. *J. Am. Chem. Soc.* **2013**, *135* (32), 11768–11771. https://doi.org/10.1021/ja406688a.

(25) Gabrielli, L.; Rosa-Gastaldo, D.; Salvia, M. V.; Springhetti, S.; Rastrelli, F.; Mancin, F. Detection and Identification of Designer Drugs by Nanoparticle-Based NMR Chemosensing. *Chem. Sci.* **2018**, *9* (21), 4777–4784. https://doi.org/10.1039/c8sc01283k.

(26) Salvia, M. V.; Salassa, G.; Rastrelli, F.; Mancin, F. Turning Supramolecular Receptors into Chemosensors by Nanoparticle-Assisted "NMR Chemosensing." *J. Am. Chem. Soc.* **2015**, *137* (35), 11399–11406. https://doi.org/10.1021/jacs.5b06300.

(27) Sun, X.; Riccardi, L.; De Biasi, F.; Rastrelli, F.; De Vivo, M.; Mancin, F. Molecular-Dynamics-Simulation-Directed Rational Design of Nanoreceptors with Targeted Affinity. *Angew. Chemie - Int. Ed.* **2019**, *58* (23), 7702–7707. https://doi.org/10.1002/anie.201902316.

(28) Baquero, E. A.; Tricard, S.; Flores, J. C.; de Jesús, E.; Chaudret, B. Highly Stable Water-Soluble Platinum Nanoparticles Stabilized by Hydrophilic N-Heterocyclic Carbenes. *Angew. Chemie* **2014**, *126* (48), 13436–13440. https://doi.org/10.1002/ange.201407758.

(29) Macleod, M. J.; Johnson, J. A. PEGylated N - Heterocyclic Carbene Anchors Designed

To Stabilize Gold Nanoparticles in Biologically Relevant Media. **2015**, 1–4. https://doi.org/10.1021/jacs.5b02452.

(30) Bridonneau, N.; Hippolyte, L.; Mercier, D.; Portehault, D.; Desage-El Murr, M.; Marcus, P.; Fensterbank, L.; Chanéac, C.; Ribot, F. N-Heterocyclic Carbene-Stabilized Gold Nanoparticles with Tunable Sizes. *Dalt. Trans.* **2018**, *47* (19), 6850–6859. https://doi.org/10.1039/c8dt00416a.

(31) Gold, U.; Modi, N.; Man, R. W. Y.; Li, C.; Maclean, M. W. A.; Zenkina, O. V; Zamora, M. T.; Saunders, L. N.; Rousina-webb, A.; Nambo, M.; Crudden, C. M. Ultrastable Gold Nanoparticles Modified by Bidentate N - Heterocyclic Carbene Ligands. *J. Am. Chem. Soc.* **2018**, *140*, 1576–1579. https://doi.org/10.1021/jacs.7b08516.

(32) Salorinne, K.; Man, R. W. Y.; Li, C. H.; Taki, M.; Nambo, M.; Crudden, C. M. Water-Soluble N-Heterocyclic Carbene-Protected Gold Nanoparticles: Size-Controlled Synthesis, Stability, and Optical Properties. *Angew. Chemie - Int. Ed.* **2017**, *56* (22), 6198–6202. https://doi.org/10.1002/anie.201701605.

(33) Crudden, C. M.; Horton, J. H.; Ebralidze, I. I.; Zenkina, O. V.; McLean, A. B.; Drevniok, B.; She, Z.; Kraatz, H. B.; Mosey, N. J.; Seki, T.; Keske, E. C.; Leake, J. D.; Rousina-Webb, A.; Wu, G. Ultra Stable Self-Assembled Monolayers of N-Heterocyclic Carbenes on Gold. *Nat. Chem.* **2014**, *6* (5), 409–414. https://doi.org/10.1038/nchem.1891.

(34) Lucarini, M.; Franchi, P.; Pedulli, G. F.; Gentilini, C.; Polizzi, S.; Pengo, P.; Scrimin, P.; Pasquato, L. Effect of Core Size on the Partition of Organic Solutes in the Monolayer of Water-Soluble Nanoparticles: An ESR Investigation. *J. Am. Chem. Soc.* **2005**, *127* (47), 16384–16385. https://doi.org/10.1021/ja0560534.

(35) Kell, A. J.; Donkers, R. L.; Workentin, M. S. Core Size Effects on the Reactivity of Organic Substrates as Monolayers on Gold Nanoparticles. *Langmuir* **2005**, *21* (2), 735–742. https://doi.org/10.1021/la049016j.

(36) Wu, M.; Vartanian, A. M.; Chong, G.; Pandiakumar, A. K.; Hamers, R. J.; Hernandez, R.; Murphy, C. J. Solution NMR Analysis of Ligand Environment in Quaternary Ammonium-Terminated Self-Assembled Monolayers on Gold Nanoparticles: The Effect of Surface Curvature and Ligand Structure. *J. Am. Chem. Soc.* **2019**, *141* (10), 4316–4327. https://doi.org/10.1021/jacs.8b11445.

(37) Pezzato, C.; Lee, B.; Severin, K.; Prins, L. J. Pattern-Based Sensing of Nucleotides with

Functionalized Gold Nanoparticles. *Chem. Commun.* **2013**, *49* (5), 469–471. https://doi.org/10.1039/c2cc38058g.

(38) Pieters, G.; Pezzato, C.; Prins, L. J. Controlling Supramolecular Complex Formation on the Surface of a Monolayer-Protected Gold Nanoparticle in Water. *Langmuir* **2013**, *29* (24), 7180–7185. https://doi.org/10.1021/la304316z.

(39) Salvia, M. V.; Ramadori, F.; Springhetti, S.; Diez-Castellnou, M.; Perrone, B.; Rastrelli, F.; Mancin, F. Nanoparticle-Assisted NMR Detection of Organic Anions: From Chemosensing to Chromatography. *J. Am. Chem. Soc.* **2015**, *137* (2), 886–892. https://doi.org/10.1021/ja511205e.

(40) Gabrielli, L.; Rosa-Gastaldo, D.; Salvia, M. V.; Springhetti, S.; Rastrelli, F.; Mancin, F. Detection and Identification of Designer Drugs by Nanoparticle-Based NMR Chemosensing. *Chem. Sci.* **2018**, *9* (21), 4777–4784. https://doi.org/10.1039/c8sc01283k.

(41) Chen, A.; Shapiro, M. J. NOE Pumping: A Novel NMR Technique for Identification of Compounds with Binding Affinity to Macromolecules. *J. Am. Chem. Soc.* **1998**, *120* (39), 10258–10259. https://doi.org/10.1021/ja982152o.

(42) Rastrelli, F.; Jha, S.; Mancin, F. Seeing through Macromolecules: T2-Filtered NMR for the Purity Assay of Functionalized Nanosystems and the Screening of Biofluids. *J. Am. Chem. Soc.* **2009**, *131* (40), 14222–14224. https://doi.org/10.1021/ja904737r.

(43) Lepre, C. A.; Moore, J. M.; Peng, J. W. Theory and Applications of NMR-Based Screening in Pharmaceutical Research. *Chem. Rev.* **2004**, *104* (8), 3641–3675. https://doi.org/10.1021/cr030409h.

(44) Meyer, B.; Peters, T. NMR Spectroscopy Techniques for Screening and Identifying Ligand Binding to Protein Receptors. *Angew. Chemie - Int. Ed.* **2003**, *42* (8), 864–890. https://doi.org/10.1002/anie.200390233.

(45) De Biasi, F.; Rosa-Gastaldo, D.; Sun, X.; Mancin, F.; Rastrelli, F. Nanoparticle-Assisted NMR Spectroscopy: Enhanced Detection of Analytes by Water-Mediated Saturation Transfer. *J. Am. Chem. Soc.* **2019**, *141* (12), 4870–4877. https://doi.org/10.1021/jacs.8b13225.

(46) Dalvit, C.; Pevarello, P.; Tato, M.; Veronesi, M.; Vulpetti, A.; Sundström, M. Identification of Compounds with Binding Affinity to Proteins via Magnetization

Transfer from Bulk Water. *J. Biomol. NMR* **2000**, *18* (1), 65–68. https://doi.org/10.1023/A:1008354229396.

(47) De Biasi, F.; Rosa-Gastaldo, D.; Mancin, F.; Rastrelli, F. Hybrid Nanoreceptors for High Sensitivity Detection of Small Molecules by NMR Chemosensing. *Chem. Commun.* **2021**, *57* (24), 3002–3005. https://doi.org/10.1039/d0cc07559k.

(48) Hövener, J. B.; Schwaderlapp, N.; Lickert, T.; Duckett, S. B.; Mewis, R. E.; Highton, L. A. R.; Kenny, S. M.; Green, G. G. R.; Leibfritz, D.; Korvink, J. G.; Hennig, J.; Von Elverfeldt, D. A Hyperpolarized Equilibrium for Magnetic Resonance. *Nat. Commun.* **2013**, *4*, 1–5. https://doi.org/10.1038/ncomms3946.

(49) Ardenkjær-Larsen, J. H.; Fridlund, B.; Gram, A.; Hansson, G.; Hansson, L.; Lerche, M. H.; Servin, R.; Thaning, M.; Golman, K. Increase in Signal-to-Noise Ratio of >10,000 Times in Liquid-State NMR. *Proc. Natl. Acad. Sci. U. S. A.* **2003**, *100* (18), 10158–10163. https://doi.org/10.1073/pnas.1733835100.

(50) Kovtunov, K. V.; Pokochueva, E. V.; Salnikov, O. G.; Cousin, S. F.; Kurzbach, D.; Vuichoud, B.; Jannin, S.; Chekmenev, E. Y.; Goodson, B. M.; Barskiy, D. A.; Koptyug, I. V. Hyperpolarized NMR Spectroscopy: D-DNP, PHIP, and SABRE Techniques. *Chem. - An Asian J.* **2018**, *13* (15), 1857–1871. https://doi.org/10.1002/asia.201800551.

(51) Bowers, C. Russell, D. P. W. Parahydrogen and Synthesis Allow Dramatically Enhanced Nuclear Alignment. *J. Am. Chem. Soc.* **1987**, *109*, 5541–5542.

(52) Bowers, C. R.; Weitekamp, D. P. Physical Review Letters 24. **1986**, *57* (21).

(53) Natterer, J.; Bargon, J. Para-Hydrogen Induced Polarization (PHIP). *Prog. Nucl. Magn. Reson. Spectrosc.* **1997**, *31*, 293–315.

(54) Golman, K.; Axelsson, O.; Jóhannesson, H.; Månsson, S.; Olofsson, C.; Petersson, J. S. Parahydrogen-Induced Polarization in Imaging: Subsecond 13C Angiography. *Magn. Reson. Med.* **2001**, *46* (1), 1–5. https://doi.org/10.1002/mrm.1152.

(55) Adams, R. W.; Aguilar, J. A.; Atkinson, K. D.; Cowley, M. J.; Elliott, P. I. P.; Duckett, S. B.; Green, G. G. R.; Khazal, i. G.; Lopez-Serrano, J.; Williamson, D. C. Sensitivity by Polarization Transfer. *Science (80-.).* **2009**, *323* (March), 1708–1711.

(56) Atkinson, K. D.; Cowley, M. J.; Duckett, S. B.; Elliott, P. I. P.; Green, G. G. R.; López-Serrano, J.; Khazal, I. G.; Whitwood, A. C. Para-Hydrogen Induced Polarization without Incorporation of Para-Hydrogen into the Analyte. *Inorg. Chem.* **2009**, *48* (2), 663–670.

https://doi.org/10.1021/ic8020029.

(57) Adams, R. W.; Duckett, S. B.; Green, R. A.; Williamson, D. C.; Green, G. G. R. A Theoretical Basis for Spontaneous Polarization Transfer in Non-Hydrogenative Parahydrogen-Induced Polarization. *J. Chem. Phys.* **2009**, *131* (19). https://doi.org/10.1063/1.3254386.

(58) Barskiy, D. A.; Shchepin, R. V.; Tanner, C. P. N.; Colell, J. F. P.; Goodson, B. M.; Theis, T.; Warren, W. S.; Chekmenev, E. Y. The Absence of Quadrupolar Nuclei Facilitates Efficient 13C Hyperpolarization via Reversible Exchange with Parahydrogen. *ChemPhysChem* **2017**, *18* (12), 1493–1498. https://doi.org/10.1002/cphc.201700416.

(59) Theis, T.; Truong, M. L.; Coffey, A. M.; Shchepin, R. V.; Waddell, K. W.; Shi, F.; Goodson, B. M.; Warren, W. S.; Chekmenev, E. Y. Microtesla SABRE Enables 10% Nitrogen-15 Nuclear Spin Polarization. *J. Am. Chem. Soc.* **2015**, *137* (4), 1404–1407. https://doi.org/10.1021/ja512242d.

(60) Shchepin, R. V.; Goodson, B. M.; Theis, T.; Warren, W. S.; Chekmenev, E. Y. Toward Hyperpolarized 19F Molecular Imaging via Reversible Exchange with Parahydrogen. *ChemPhysChem* **2017**, *18* (15), 1961–1965. https://doi.org/10.1002/cphc.201700594.

(61) Zhivonitko, V. V.; Skovpin, I. V.; Koptyug, I. V. Strong 31P Nuclear Spin Hyperpolarization Produced via Reversible Chemical Interaction with Parahydrogen. *Chem. Commun.* **2015**, *51* (13), 2506–2509. https://doi.org/10.1039/c4cc08115c.

(62) Olaru, A. M.; Burt, A.; Rayner, P. J.; Hart, S. J.; Whitwood, A. C.; Green, G. G. R.; Duckett, S. B. Using Signal Amplification by Reversible Exchange (SABRE) to Hyperpolarise 119Sn and 29Si NMR Nuclei. *Chem. Commun.* **2016**, *52* (100), 14482–14485. https://doi.org/10.1039/c6cc07109k.

(63) Lloyd, L. S.; Adams, R. W.; Bernstein, M.; Coombes, S.; Duckett, S. B.; Green, G. G. R.; Lewis, R. J.; Mewis, R. E.; Sleigh, C. J. Utilization of SABRE-Derived Hyperpolarization to Detect Low-Concentration Analytes via 1D and 2D NMR Methods. *J. Am. Chem. Soc.* **2012**, *134* (31), 12904–12907. https://doi.org/10.1021/ja3051052.

(64) Crabtree, R. H.; Felkin, H.; Morris, G. E. Cationic Iridium Diolefin Complexes as Alkene Hydrogenation Catalysts and the Isolation of Some Related Hydrido Complexes. *J. Organomet. Chem.* **1977**, *141* (2), 205–215. https://doi.org/10.1016/S0022-328X(00)92273-3.

(65) Cowley, M. J.; Adams, R. W.; Atkinson, K. D.; Cockett, M. C. R.; Duckett, S. B.; Green, G. G. R.; Lohman, J. A. B.; Kerssebaum, R.; Kilgour, D.; Mewis, R. E. Iridium N-Heterocyclic Carbene Complexes as Efficient Catalysts for Magnetization Transfer from Para -Hydrogen. *J. Am. Chem. Soc.* **2011**, *133* (16), 6134–6137. https://doi.org/10.1021/ja200299u.

(66) Eshuis, N.; Van Weerdenburg, B. J. A.; Feiters, M. C.; Rutjes, F. P. J. T.; Wijmenga, S. S.; Tessari, M. Quantitative Trace Analysis of Complex Mixtures Using SABRE Hyperpolarization. *Angew. Chemie - Int. Ed.* **2015**, *54* (5), 1481–1484. https://doi.org/10.1002/anie.201409795.

(67) Tennant, T.; Hulme, M. C.; Robertson, T. B. R.; Sutcliffe, O. B.; Mewis, R. E. Benchtop NMR Analysis of Piperazine-Based Drugs Hyperpolarised by SABRE. *Magn. Reson. Chem.* **2020**, *58* (12), 1151–1159. https://doi.org/10.1002/mrc.4999.

(68) Reile, I.; Eshuis, N.; Hermkens, N. K. J.; Van Weerdenburg, B. J. A.; Feiters, M. C.; Rutjes, F. P. J. T.; Tessari, M. NMR Detection in Biofluid Extracts at Sub-MM Concentrations: Via Para -H2 Induced Hyperpolarization. *Analyst* **2016**, *141* (13), 4001–4005. https://doi.org/10.1039/c6an00804f.

(69) Ratajczyk, T.; Gutmann, T.; Bernatowicz, P.; Buntkowsky, G.; Frydel, J.; Fedorczyk, B. NMR Signal Enhancement by Effective SABRE Labeling of Oligopeptides. *Chem. - A Eur. J.* **2015**, *21* (36), 12616–12619. https://doi.org/10.1002/chem.201501552.

(70) Štěpánek, P.; Sanchez-Perez, C.; Telkki, V. V.; Zhivonitko, V. V.; Kantola, A. M. High-Throughput Continuous-Flow System for SABRE Hyperpolarization. *J. Magn. Reson.* **2019**, *300*, 8–17. https://doi.org/10.1016/j.jmr.2019.01.003.

(71) Delcambre S., Nonnenmacher Y., H. K. *Dopamine Metabolism and Reactive Oxygen Species Production. In: Buhlman L. (Eds) Mitochondrial Mechanisms of Degeneration and Repair in Parkinson's Disease*; Springer, Ed.; 2016.

(72) Park, J. R.; Eggert, A.; Caron, H. Neuroblastoma: Biology, Prognosis, and Treatment. *Hematol. Oncol. Clin. North Am.* **2010**, *24* (1), 65–86. https://doi.org/10.1016/j.hoc.2009.11.011.

(73) Schweisguth, O. Excretion of Catecholamine Metabolites in Urine of Neuroblastoma Patients. *J. Pediatr. Surg.* **1968**, *3* (1 PART 2), 118–120. https://doi.org/10.1016/0022-3468(68)90993-7.

(74) Zanoni, G. Sviluppo Di Nanorecettori Supramolecolari Autoassemblati per La Rilevazione Di Metaboliti Della Dopamina, Università degli studi di Padova, 2018.

(75) Verly, I. R. N.; van Kuilenburg, A. B. P.; Abeling, N. G. G. M.; Goorden, S. M. I.; Fiocco, M.; Vaz, F. M.; van Noesel, M. M.; Zwaan, C. M.; Kaspers, G. J. L.; Merks, J. H. M.; Caron, H. N.; Tytgat, G. A. M. 3-Methoxytyramine: An Independent Prognostic Biomarker That Associates with High-Risk Disease and Poor Clinical Outcome in Neuroblastoma Patients. *Eur. J. Cancer* **2018**, *90*, 102–110. https://doi.org/10.1016/j.ejca.2017.11.025.

(76) Sreekumar, A.; Poisson, L. M.; Rajendiran, T. M.; Khan, A. P.; Cao, Q.; Yu, J.; Laxman, B.; Mehra, R.; Lonigro, R. J.; Li, Y.; Nyati, M. K.; Ahsan, A.; Kalyana-Sundaram, S.; Han, B.; Cao, X.; Byun, J.; Omenn, G. S.; Ghosh, D.; Pennathur, S.; Alexander, D. C.; Berger, A.; Shuster, J. R.; Wei, J. T.; Varambally, S.; Beecher, C.; Chinnaiyan, A. M. Metabolomic Profiles Delineate Potential Role for Sarcosine in Prostate Cancer Progression. *Nature* **2009**, *457* (7231), 910–914. https://doi.org/10.1038/nature07762.

(77) Hopkinson, M. N.; Richter, C.; Schedler, M.; Glorius, F. An Overview of N-Heterocyclic Carbenes. *Nature* **2014**, *510* (7506), 485–496. https://doi.org/10.1038/nature13384.

(78) Heinemann, C.; Müller, T.; Apeloig, Y.; Schwarz, H. On the Question of Stability, Conjugation, and "Aromaticity" in Imidazol-2-Ylidenes and Their Silicon Analogs. *J. Am. Chem. Soc.* **1996**, *118* (8), 2023–2038. https://doi.org/10.1021/ja9523294.

(79) Zhukhovitskiy, A. V.; Mavros, M. G.; Van Voorhis, T.; Johnson, J. A. Addressable Carbene Anchors for Gold Surfaces. *J. Am. Chem. Soc.* **2013**, *135* (20), 7418–7421. https://doi.org/10.1021/ja401965d.

(80) Hahn, F. E.; Jahnke, M. C. Heterocyclic Carbenes: Synthesis and Coordination Chemistry. *Angew. Chemie - Int. Ed.* **2008**, *47* (17), 3122–3172. https://doi.org/10.1002/anie.200703883.

(81) Kuhn, N.; Al-Sheikh, A. 2,3-Dihydroimidazol-2-Ylidenes and Their Main Group Element Chemistry. *Coord. Chem. Rev.* **2005**, *249* (7–8), 829–857. https://doi.org/10.1016/j.ccr.2004.10.003.

(82) DiBenedetto, S. A.; Facchetti, A.; Ratner, M. A.; Marks, T. J. Molecular Self-Assembled Monolayers and Multilayers for Organic and Unconventional Inorganic Thin-Film

Transistor Applications. *Adv. Mater.* **2009**, *21* (14–15), 1407–1433. https://doi.org/10.1002/adma.200803267.

(83) Ranieri, A.; Monari, S.; Sola, M.; Borsari, M.; Battistuzzi, G.; Ringhieri, P.; Nastri, F.; Pavone, V.; Lombardi, A. Redox and Electrocatalytic Properties of Mimochrome VI, a Synthetic Heme Peptide Adsorbed on Gold. *Langmuir* **2010**, *26* (23), 17831–17835. https://doi.org/10.1021/la103744x.

(84) Koh, S. J. Strategies for Controlled Placement of Nanoscale Building Blocks. *Nanoscale Res. Lett.* **2007**, *2* (11), 519–545. https://doi.org/10.1007/s11671-007-9091-3.

(85) Love, J. C.; Estroff, L. A.; Kriebel, J. K.; Nuzzo, R. G.; Whitesides, G. M. *Self-Assembled Monolayers of Thiolates on Metals as a Form of Nanotechnology*; 2005; Vol. 105. https://doi.org/10.1021/cr0300789.

(86) Inayeh, A.; Groome, R. R. K.; Singh, I.; Veinot, A. J.; de Lima, F. C.; Miwa, R. H.; Crudden, C. M.; McLean, A. B. Self-Assembly of N-Heterocyclic Carbenes on Au(111). *Nat. Commun.* **2021**, *12* (1), 1–9. https://doi.org/10.1038/s41467-021-23940-0.

(87) MacLeod, M. J.; Johnson, J. A. PEGylated N-Heterocyclic Carbene Anchors Designed to Stabilize Gold Nanoparticles in Biologically Relevant Media. *J. Am. Chem. Soc.* **2015**, *137* (25), 7974–7977. https://doi.org/10.1021/jacs.5b02452.

(88) Pinalli, R.; Suman, M.; Dalcanale, E. Cavitands at Work: From Molecular Recognition to Supramolecular Sensors. *European J. Org. Chem.* **2004**, No. 3, 451–462. https://doi.org/10.1002/ejoc.200300430.

(89) Pinalli, R.; Brancatelli, G.; Pedrini, A.; Menozzi, D.; Hernández, D.; Ballester, P.; Geremia, S.; Dalcanale, E. The Origin of Selectivity in the Complexation of N-Methyl Amino Acids by Tetraphosphonate Cavitands. *J. Am. Chem. Soc.* **2016**, *138* (27), 8569–8580. https://doi.org/10.1021/jacs.6b04372.

(90) Rodríguez-Castillo, M.; Lugo-Preciado, G.; Laurencin, D.; Tielens, F.; van der Lee, A.; Clément, S.; Guari, Y.; López-de-Luzuriaga, J. M.; Monge, M.; Remacle, F.; Richeter, S. Experimental and Theoretical Study of the Reactivity of Gold Nanoparticles Towards Benzimidazole-2-Ylidene Ligands. *Chem. - A Eur. J.* **2016**, *22* (30), 10446–10458. https://doi.org/10.1002/chem.201601253.

(91) Sundararajan, K.; Sankaran, K.; Ramanathan, N.; Gopi, R. Production and Characterization of Para-Hydrogen Gas for Matrix Isolation Infrared Spectroscopy. *J.*

Mol. Struct. **2016**, *1117*, 181–191. https://doi.org/10.1016/j.molstruc.2016.03.068.

(92) Richardson, P. M.; Jackson, S.; Parrott, A. J.; Nordon, A.; Duckett, S. B.; Halse, M. E. A Simple Hand-Held Magnet Array for Efficient and Reproducible SABRE Hyperpolarisation Using Manual Sample Shaking. *Magn. Reson. Chem.* **2018**, *56* (7), 641–650. https://doi.org/10.1002/mrc.4687.

(93) Overhauser, A. W. Polarization of Nuclei in Metals. *Phys. Rev.* **1953**, *92* (2), 411–415. https://doi.org/10.1103/PhysRev.92.411.

(94) Craik, D. J.; Higgins, K. A.; Kneen, M. M.; Munro, S. L. A.; Waterman, K. J. Determining the Conformation of a Ligand Bound to an Enzyme - Application of NMR Spectroscopy in Drug Design. *J. Chem. Educ.* **1991**, *68* (3), 258–261. https://doi.org/10.1021/ed068p258.

(95) Viegas, A.; Manso, J.; Nobrega, F. L.; Cabrita, E. J. Saturation-Transfer Difference (STD) NMR: A Simple and Fast Method for Ligand Screening and Characterization of Protein Binding. *J. Chem. Educ.* **2011**, *88* (7), 990–994. https://doi.org/10.1021/ed101169t.

Appendix I

Nuclear Overhauser Effect (NOE)

The Nuclear Overhauser Effect (NOE), discovered originally by Albert W. Overhauser in 1953[93], is the change in intensity of a resonance when its spin equilibrium is perturbed by a spatially close (< 5 Å) second resonance. This second resonance can be perturbed by rf irradiation leading to an increase (positive NOE) or decrease (negative NOE) of the former signal intensity. This change in signal intensity provides valuable structural, conformational and recognition ability information.[44,94,95] The magnitude of the NOE is evaluated as relative intensity change with respect to an off-resonance spectrum, where the sample is irradiated at a frequency where none of the resonances are affected (i_0).

$$NOE = \frac{i - i_0}{i_0}$$

Errore. L'origine riferimento non è stata trovata. shows the case of two homonuclear spins (-1/2 nuclei) I and S not sharing a scalar coupling between them but being spatially close enough to interact via dipolar coupling. Populations of the αβ and βα are equal at the equilibrium state while αα state will be more populated than ββ as its energy is lower.

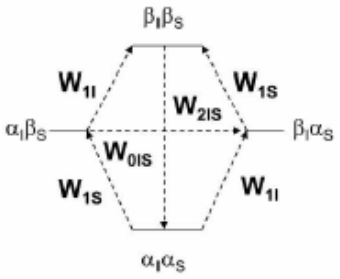

Figure 181: Energy level diagram for a two homonuclear spin system (-1/2 nuclei I and S)

W is the transition probability between two spin states. Only the two cross relaxation pathways αα-ββ (double quantum transitions) and αβ-βα (zero quantum transitions) are responsible for the NOE.

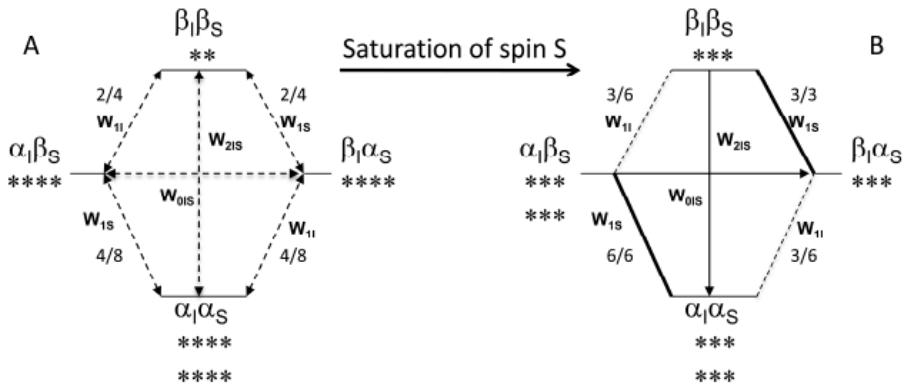

*Figure 182: A) equilibrium state; B) saturation state. * represent spin populations*

If S resonance is saturated then the spin populations of the system are equalized so that $\alpha_I\alpha_S = \alpha_I\beta_S$ and $\beta_I\alpha_S = \beta_I\beta_S$. The system will reach equilibrium again through W_{0IS} and W_{2IS} transitions. W_2 transition, while recovering the population differences across S transitions, will increase the population difference across the two I transitions. I resonance intensity will therefore be enhanced, leading to a positive NOE (for small molecules). W_0 process, at the other end, will result in a decrease in population difference across I transitions leading to a negative NOE (large molecules). It is therefore the dominating pathway between W_0 and W_2 to determine the sign of the NOE.

$$f_1(S) = \left(\frac{\gamma_S}{\gamma_I}\right) * \left(\frac{W_2 - W_0}{W_0 + 2W_1^I + W_2}\right)$$

Where γ_S and γ_I are the magnetogyric ratio of the two spins. The probability of the two transitions W_0 and W_2 is correlated to the spectral density *J* at the Larmor frequency ($\omega \approx 0$ for W_0, $\omega = 2\omega_0$ for W_2). The spectral density of a specie in random rotation at a frequency ω, assuming it to be spherical, is given by the equation:

$$J(\omega) = \frac{2_c}{1 + \ \omega^2\tau_c^2}$$

Hence, the spectral density starts with a maximum at ω = 0 and the decreases with the frequency, the steepness of such decrease depends on the correlation time (τ_c), which is high for large molecules and small for smaller ones. Shorter correlation times causes a larger frequency distribution. Consequently:

- For small molecules $\omega\ \tau_c << 1$ so W_2 is the dominant pathway leading to positive NOE

- For large molecules $\omega \tau_c >> 1$ so W_0 is the dominant pathway leading to negative NOE
- For intermediate sizes $\omega \tau_c \approx 1$ the NOE is ≈ 0 and the actual sign depends on the frequency of the spectrometer

This is supported by the fact that the more rapidly the molecules are tumbling the higher it is the probability to generate higher frequencies.